

UNIVERSITY OF CALIFORNIA,
IRVINE

Nitrogen Containing Secondary Organic Aerosols: Experiments and Air Quality Simulations

DISSERTATION

submitted in partial satisfaction of the requirements
for the degree of

DOCTOR OF PHILOSOPHY

in Chemistry

by

Julia Montoya-Aguilera

Dissertation Committee:
Professor Sergey Nizkorodov, Chair
Professor Barbara Finlayson-Pitts
Professor Ann Marie Carlton

2020

DEDICATION

A mi familia. To my family.

TABLE OF CONTENTS

	Page
LIST OF FIGURES.....	v
LIST OF TABLES.....	ix
ACKNOWLEDGMENTS	x
VITA	xii
ABSTRACT OF THE DISSERTATION	xvii
CHAPTER 1: INTRODUCTION	
1.1: Atmospheric aerosols	1
1.2: Effect of relative humidity on SOA properties	3
1.3: Organic nitrogen in SOA	5
CHAPTER 2: EFFECT OF RELATIVE HUMIDITY ON THE FORMATION OF LOW-NO _x TOLUENE SECONDARY ORGANIC AEROSOL	
2.1: Introduction	7
2.2: Experimental Methods	10
2.3: Results and Discussion.....	12
2.4: Conclusions	25
CHAPTER 3: SECONDARY ORGANIC AEROSOL FROM INDOLE OXIDATION	
3.1: Introduction	27
3.2: Experimental methods	33
3.3: Modeling methods	45
3.4: Experimental results.....	50
3.5: Modeling results	83
3.6: Conclusions	90
CHAPTER 4: AMMONIA UPTAKE BY SECONDARY ORGANIC AEROSOL	
4.1: Background	92
4.2: Experimental methods	96
4.3: Modeling methods	100
4.4: Experimental results	109
4.5: Model predictions for the SoCAB.....	117
4.6: Model predictions for the continental US	129
4.7: Conclusions	148

CHAPTER 5: EFFECT OF HUMIDITY ON AMMONIA AND AMINE UPTAKE BY SECONDARY ORGANIC AEROSOL	
5.1: Background	152
5.2: Experimental methods	156
5.3: Results	160
5.4: Conclusions	171
CHAPTER 6: SUMMARY AND CONCLUSIONS	
6.1: Research goals	173
6.2: Goal 1: Studying the effect of RH on SOA particle formation	174
6.3: Goal 2: Investigate the formation of SOA from a N-containing VOC	175
6.4: Goal 3: Investigate NOC formation in SOA particles via SOA uptake of ammonia (NH ₃) and dimethylamine (DMA)	177
6.5: Conclusions	179
REFERENCES	181

LIST OF FIGURES

	Page
Figure 2.1 HRMS spectra obtained in negative ion mode and positive ion mode	13
Figure 2.2 Combined abundance of all peaks as a function of the number of carbon atoms in negative mode and positive mode	15
Figure 2.3 Estimated volatility distribution for the compounds observed in low-NO _x SOA samples in the negative and positive ion modes at low and high RH	18
Figure 2.4 Examples of particle mass concentration measurements by SMPS	19
Figure 3.1 Chemical structures, common names, molecular formulas, and nominal molecular weights for indole and its oxidized derivatives discussed in this work	29
Figure 3.2 Decay of the ¹³ C isotopic ion of protonated indole as a function of time	35
Figure 3.3 Plot comparing the mass of SOA material collected as determined from SMPS calculations and weighing	37
Figure 3.4 Filters containing indole+OH SOA, indole+O ₃ SOA, and indole+NO ₃ SOA particles	39
Figure 3.5 UV-Vis absorption spectra for sample of indole + O ₃ SOA at 25% RH extracted multiple times	40
Figure 3.6 Summary of modifications made to the UCI-CIT model	48
Figure 3.7 Mass spectra of the chamber VOC compounds before and after photooxidation of indole	51
Figure 3.8 Time-dependent signals of ions that were produced and then removed	52
Figure 3.9 Time-dependent signals of ions that were removed	54
Figure 3.10 The mass concentration of indole, the mass concentration of particles, and the wall loss-corrected mass concentration of particles over time	56
Figure 3.11 Nano-DESI and DART mass spectra of indole photooxidation SOA plotted as a function of the molecular weights	58
Figure 3.12 Distribution of the number of C atoms in the indole photooxidation SOA compounds	61

Figure 3.13 The N/C ratio of indole SOA compounds.....	62
Figure 3.14 Wavelength-dependent MAC of indole+NO ₃ SOA for different starting concentrations of indole	63
Figure 3.15 Wavelength-dependent MAC of indole+OH SOA.....	64
Figure 3.16 Wavelength-dependent MAC of indole+OH SOA, indole+OH+NO _x SOA, indole+O ₃ SOA, and indole+NO ₃ SOA generated at different RH.....	66
Figure 3.17 <i>k</i> values calculated from MAC of indole+OH SOA prepared in a chamber under low and high NO _x conditions.....	67
Figure 3.18 <i>k</i> values calculated from MAC of indole+O ₃ SOA prepared in a chamber under different RH.....	68
Figure 3.19 <i>k</i> values calculated from MAC of indole+NO ₃ SOA prepared in a chamber under different RH.....	69
Figure 3.20 Measured <i>k</i> for indole+NO ₃ SOA generated in a glass OFR reactor at various RH.....	70
Figure 3.21 Indole+NO ₃ SOA: AMS Families vs RH.....	71
Figure 3.22 AMS families that followed the same trend with RH as <i>k</i> vs RH	71
Figure 3.23 AMS families that followed opposite trend with RH to <i>k</i> vs RH	72
Figure 3.24 HPLC-PDA chromatogram of indole photooxidation SOA	73
Figure 3.25 Comparison between measured PDA absorption spectra at selected retention time (RT) from an indole+OH SOA sample and reference spectra	74
Figure 3.26 HPLC-PDA chromatogram of indole+O ₃ SOA sample and indole+NO ₃ SOA sample generated at low RH.....	75
Figure 3.27 Tentative mechanism for the formation of observed chromophores in the photooxidation of indole	82
Figure 3.28 The 24-hour average gas-phase indole concentrations.....	84
Figure 3.29 Twenty-four-hour average concentrations (μg m ⁻³) of total SOA.....	85
Figure 3.30 Domain-wide average SOA concentrations.....	87
Figure 3.31 Gas-phase indole concentrations.....	88

Figure 3.32 Domain wide average SOA concentrations	89
Figure 4.1 The modeling approach for the reactive uptake of ammonia by secondary organic aerosol.....	103
Figure 4.2 Plots showing the particle mass concentration over time under low RH.....	111
Figure 4.3 Plots showing the N:C ratio of the particle composition over time for limonene/O ₃ SOA and n-hexadecane/OH SOA generated under low RH and toluene/OH SOA generated under 54% RH.....	112
Figure 4.4 DART mass spectra of limonene/O ₃ SOA samples generated under low RH conditions in the absence of NH ₃ and in the presence of NH ₃	114
Figure 4.5 DART mass spectra of toluene/OH SOA samples generated under low RH conditions in the absence of NH ₃ and in the presence of NH ₃	115
Figure 4.6 DART mass spectra of n-hexadecane/OH SOA samples generated under low RH, collected onto filters, and then aged in the presence of H ₂ O and NH ₃	116
Figure 4.7 Domain wide average concentrations of NH ₃ and PM _{2.5}	118
Figure 4.8 24-hour average concentrations of SOA in the reference case.....	118
Figure 4.9 24-hour average concentrations of NH ₃ and PM _{2.5}	121
Figure 4.10 24-hour average concentrations of HNO ₃ and H ₂ SO ₄	124
Figure 4.11 24-h average concentrations of particulate NO ₃ ⁻ , NH ₄ ⁺ , and SO ₄ ²⁻	126
Figure 4.12 Daily, spatially-averaged NH ₃ concentrations for different uptake coefficient scenarios for the winter period and summer period.....	130
Figure 4.13 Spatial distribution of time-averaged NH ₃ concentrations for winter and summer.....	132
Figure 4.14 . Spatial distribution of time-averaged HNO ₃ concentrations for winter and summer.....	134
Figure 4.15 Spatial distribution of time-averaged NH ₄ ⁺ concentrations for winter and summer.....	136
Figure 4.16 Spatial distribution of time-averaged NO ₃ ⁻ concentrations for winter and summer.....	138

Figure 4.17 Spatial distribution of time-averaged SO_4^{2-} concentrations for winter and summer.....	138
Figure 4.18 Spatial distribution of time-averaged SOA concentrations for winter and summer.....	140
Figure 4.19 Spatial distribution of the difference in time-averaged biogenic SOA concentrations, IEPOX-derived SOA concentrations, particle pH, and IEPOX concentrations between the $\gamma = 10^{-3}$ case and the base case during the summer.....	142
Figure 4.20 Daily, spatially averaged concentrations of particle-phase H^+ in winter and summer, IEPOX in winter and summer, and IEPOX-derived SOA in winter and summer.....	144
Figure 4.21 Daily, spatially-averaged concentrations of different scenarios for $\text{PM}_{2.5}$ in the winter and summer, and PM_{10} in the winter and summer	145
Figure 4.22 Spatial distribution of time-averaged $\text{PM}_{2.5}$ concentrations for winter and summer.....	147
Figure 4.23 Spatial distribution of time-averaged biogenic SOA fraction of total $\text{PM}_{2.5}$ for the winter and summer.....	147
Figure 5.1 Particle number concentration and particle mass concentration for toluene/OH SOA at low RH exposed to DMA	161
Figure 5.2 Particle number concentration and particle mass concentration for d-limonene/ O_3 SOA at low RH exposed to DMA.....	162
Figure 5.3 Elemental ratios of d-limonene ozonolysis SOA particles when exposed to NH_3 and DMA	163
Figure 5.4 d-Limonene ozonolysis SOA exposed to DMA at varying RH.....	164
Figure 5.5 Plots showing the H:C, O:C, and N:C ratios as a function of time for α -cedrene ozonolysis SOA particles exposed to DMA at varying RH	165
Figure 5.6 Toluene photooxidation SOA exposed to DMA at varying RH	166
Figure 5.7 Nitrogen-containing families plotted versus time for LIM/ O_3 SOA, CED/ O_3 SOA, and TOL/OH SOA exposed to DMA under low RH.....	167
Figure 5.8 Elemental ratios plotted versus time for LIM/ O_3 SOA, CED/ O_3 SOA, and TOL/OH SOA exposed to DMA under low RH.....	169

LIST OF TABLES

	Page
Table 2.1 The five most abundant compounds observed in the low- and high-RH low-NO _x toluene SOA samples.....	14
Table 2.2 Summary of SMPS experiments	21
Table 2.3 Most common mass differences in the HRMS of low-NO _x toluene SOA.....	23
Table 3.1 Particle effective density measured by AAC and SMPS.....	45
Table 3.2 Summary of assigned PTR-ToF-MS peaks	55
Table 3.3 Monomer and dimer peaks with the largest peak abundance observed in DART-MS and nano-DESI-HRMS spectra.....	60
Table 3.4 Proposed chromophores from indole+NO ₃ SOA, indole+O ₃ SOA, and indole+OH SOA generated at low RH	75
Table 4.1 Domain-averaged NH ₃ concentrations and PM _{2.5} mass concentrations	119
Table 5.1 Table listing the 15 most prominent N-containing peaks and their families for LIM/O ₃ SOA, CED/O ₃ SOA, and TOL/OH SOA after exposure to DMA	168
Table 5.2 Uptake coefficients and increase in moles of N in the particles after exposure to NH ₃ and DMA.....	171

ACKNOWLEDGMENTS

I am currently sitting at my desk slowly making progress on this dissertation while nearly eight months pregnant wondering to myself how I got here. I say this partly in jest. I have some idea of how I got here and the many people who helped me along the way, but I apologize in advance to those I forget to thank.

I would like to begin by thanking the professors at Cal State State Los Angeles who encouraged me to start on my research journey, as well as the MORE (Minority Opportunities in REsearch) programs for providing structured guidance and support of my undergraduate research and development. I would also like to thank Prof. Krishna Foster for giving me my first research opportunity in her laboratory. I am thankful for all the time Prof. Foster invested in my growth as a researcher and for her sincere belief that I was capable of continuing in my scientific education after my undergraduate studies.

I would like to express my gratitude to my PhD advisor, Professor Sergey Nizkorodov for his immense support of my growth as a scientific researcher these past five years. I would also like to thank him for allowing me to be “a true academic”, a testament to his patience. Moreover, I also want to thank the Nizkorodov group members, past and present, for contributing to a friendly lab atmosphere that I enjoyed being a part of.

I would like to thank my committee member Professor Barbara Finlayson-Pitts for all the support and guidance she provided as the Chair of my PhD Advancement Committee, as well as for her willingness to serve on my thesis committee. I would also like to thank my committee member Professor Ann Marie Carlton for sharing her wisdom when I needed help with scientific and non-scientific worries, for serving on my advancement panel, and for willing to serve again in my thesis committee.

Moreover I am thankful to our collaborators. Professor Donald Dabdub (UCI, Department of Mechanical and Aerospace Engineering) and his students Dr. Jeremy Horne and Dr. Shupeng Zhu who carried out all the modeling simulations for the indole SOA and NH_3 uptake projects (Ch. 3 and 4). We worked closely with Professors Alex and Julia Laskin (Purdue University, Department of Chemistry), and their postdoc Dr. Peng Lin to obtain and discuss the high resolution mass spectroscopy data included in the toluene SOA and indole SOA work (Ch. 2 and 3). Professor Yinon Rudich (Weizmann Institute of Science, Department of Earth and Planetary Sciences) and his postdoc Dr. Quanfu He carried out advanced spectroscopy experiments to study the absorption and scattering of indole SOA particles (Ch. 3).

I am grateful for the various fellowships that supported me throughout my entire PhD. UCI's Competitive EDGE Summer Research Program provided financial support during my first summer at UCI in 2015, which allowed me to start graduate research early. The NSF Bridge to the Doctorate Fellowship funded the first two years of my PhD, and the NSF Graduate Research Fellowship Program funded the last three. I am immensely grateful for this support and the protected time they provided.

Last but not least I would like to thank my family, specially my husband, my parents, and my siblings for their love, understanding, and support while I completed my graduate studies over these challenging, but worthwhile past five years.

VITA

Julia Montoya-Aguilera

Education:

PhD, Chemistry, University of California, Irvine, Irvine CA	2020
M.S., Chemistry, University of California, Irvine, Irvine, CA	2018
B.S., Chemistry, California State University, Los Angeles, Los Angeles, CA	2015

Research and Work Experience:

February 2020 – Present: South Coast Air Quality Management District, Diamond Bar, CA

Air Quality Specialist, Science and Technology Advancement

Supervisor: Dr. Payam Pakbin

- Our team conducts air quality monitoring needed to support the efforts of Assembly Bill (AB) 617. AB 617 aims to reduce emissions of and exposure to air pollutants in environmental justice communities.

June 2015 - Present: University of California, Irvine, CA

Graduate Research Assistant, Atmospheric Chemistry Laboratory

PI: Prof. Sergey Nizkorodov

- My PhD project aims to investigate the effects of ammonia (NH_3) on secondary organic aerosol (SOA) formation and composition. Systematic chamber studies are conducted and particle growth is monitored via a scanning mobility particle sizer (SMPS). SOA particles are analyzed via time-of-flight aerosol mass spectrometry (ToF-AMS) to elucidate their chemical composition and determine whether NH_3 actively participates in the formation and aging of SOA, in particular by identifying nitrogen-containing compounds. By working closely with atmospheric modelers, the results of these studies help us predict the role of NH_3 in SOA formation for a particular region, and consequently expand our understanding of SOA on climate and air quality.

June 2012– June 2015: California State University, Los Angeles, CA

Undergraduate Research Assistant, Physical Chemistry Laboratory

PI: Prof. Krishna Foster

- The research objective was to determine the efficiency of pyrene and benzo[a]pyrene, two polycyclic aromatic hydrocarbons (PAHs), to sensitize singlet oxygen and study their potential effect on the oxidizing capacity in the lower atmosphere. The experimental method relied on UV-VIS spectroscopy to monitor the PAH concentration, a Nd:YAG pulsed laser to excite the PAH, and an oscilloscope to track the production and decay of singlet oxygen.

June–August 2014: Oregon State University, OR

Undergraduate Research Assistant, Inorganic Chemistry Laboratory

PI: Prof. Doug Keszler

- The research focus was to determine whether rare earth (f-orbital) metal oxides exhibit different properties than transition metal oxides. The project consisted of synthesizing and depositing Holmium clusters to make thin film metal oxides. Characterization of metal clusters and metal oxide thin films involved training with infrared (IR) spectrometry, Raman spectroscopy, small and wide x-ray scattering (SWAXS), dynamic light scattering (DLS), ellipsometry, and temperature desorption- mass spectrometry (TPD-MS).

Publications:

Julia Montoya-Aguilera, Nujhat N. Ali, Lauren T. Fleming, Quanfu He, Peng Lin, Alexander Laskin, Julia Laskin, Yinon Rudich, Donald Dabdub, and Sergey A. Nizkorodov (*in preparation*) Optical properties of secondary organic aerosol from atmospheric photooxidation of indole by OH, O₃, and NO₃

Jeremy R. Horne, Shupeng Zhu, **Julia Montoya-Aguilera**, Mallory L. Hinks, Lisa M. Wingen, Sergey A. Nizkorodov and Donald Dabdub (2018) Reactive uptake of ammonia by secondary organic aerosols: Implications for air quality, *Atmos. Environ.*, 189, 1-8 <https://doi.org/10.1016/j.atmosenv.2018.06.021>

Julia Montoya-Aguilera, Mallory L. Hinks, Paige K. Aiona, Lisa M. Wingen, Jeremy R. Horne, Shupeng Zhu, Donald Dabdub, Alexander Laskin, Julia Laskin, Peng Lin and Sergey A. Nizkorodov (2018) Reactive uptake of ammonia by biogenic and anthropogenic organic aerosols, *ACS Symposium Series*, Vol. 1299, Chapter 7, pp 127-147 in "Multiphase Environmental Chemistry in the Atmosphere", Hunt S., Laskin A., Nizkorodov S.A. Eds., ISBN13: 9780841233638 <https://doi.org/10.1021/bk-2018-1299.ch007>

Shupeng Zhu, Jeremy R. Horne, **Julia Montoya-Aguilera**, Mallory L. Hinks, Sergey A. Nizkorodov, and Donald Dabdub (2018). Modeling reactive ammonia uptake by secondary organic aerosol in CMAQ: application to continental US, *Atmos. Chem. Phys.*, 18, 3641-3657 <https://doi.org/10.5194/acp-18-3641-2018>

Mallory L. Hinks, **Julia Montoya-Aguilera**, Lucas Ellison, Peng Lin, Alexander Laskin, Julia Laskin, Manabu Shiraiwa, Donald Dabdub and Sergey A. Nizkorodov (2018). Effect of relative humidity on the yield and composition of secondary organic aerosol from oxidation of toluene, *Atmos. Chem. Phys.*, 18, 1643-1652 <https://doi.org/10.5194/acp-18-1643-2018>

Julia Montoya-Aguilera, Jeremy R. Horne, Mallory L. Hinks, Lauren T. Fleming, Veronique Perraud, Peng Lin, Alexander Laskin, Julia Laskin, Donald Dabdub, and Sergey A. Nizkorodov (2017). Secondary Organic Aerosol from Atmospheric Photooxidation of Indole. *Atmos. Chem. Phys.*, 17, 11605-11621 <https://dx.doi.org/10.5194/acp-17-11605-2017>

Presentations - Oral:

2019 **Julia Montoya-Aguilera**, Natalie R. Smith, Shupeng Zhu, Donald Dabdub, and Sergey A. Nizkorodov. A Laboratory and Modeling Investigation of the Effects of Ammonia and Amine Uptake on SOA Composition and Its Potential Impacts on Air Quality. Presented at the 37th Annual Conference of the American Association for Aerosol Research in Portland, OR.

2018 **Julia Montoya-Aguilera**, Natalie Smith, Shupeng Zhu, Donald Dabdub, and Sergey Nizkorodov. Effects of Ammonia Uptake on SOA Composition and Its Potential Impacts on Air Quality. Presented at the AirUCI Retreat in Lake Arrowhead, CA.

2018 **Julia Montoya-Aguilera**, Jeremy R. Horne, Mallory L. Hinks, Lauren T. Fleming, Veronique Perraud, Peng Lin, Alexander Laskin, Julia Laskin, Donald Dabdub, and Sergey Nizkorodov. *Formation, Composition, and Air Quality of Indole SOA*. Presented at The 20th Annual Peter B. Wagner Memorial Award in Reno, NV.

2017 **Julia Montoya**. *How the National Science Foundation Has Impacted my Life*. Presented at This Is What a Scientist/Engineer Looks Like in Irvine, CA.

2017 Mallory L. Hinks, **Julia Montoya**, Jeremy R. Horne, Sergey A. Nizkorodov, and Donald Dabdub. *The Ammonia Puzzle: Interactions with Particles and Impacts on Air Quality*. Presented at the Science and Societal Impacts of Air Quality and Climate Issues: Past, Present and Future Symposium in Irvine, CA.

- 2017 **Julia Montoya**, Donald Dabdub, Mallory L. Hinks, Jeremy R. Horne, and Sergey A. Nizkorodov. *The Role of Ammonia: Interactions with Particles and Impacts on Air Quality*. Presented at the Air Quality in a Changing World EPA STAR Program Meeting in Research Triangle Park, NC.
- 2015 **Julia Montoya** and Sergey Nizkorodov. *Effects of Ammonia on SOA Formation and Composition*. Presented at the 2015 Summer Research Symposium in Irvine, CA.
- 2015 **Julia Montoya**, Geovani Montoya, Dong Zhang, Matthias Selke, and Krishna Foster. *Identification of Pyrene as a Sensitizer of Singlet Oxygen in the Lower Atmosphere*. Presented at the 23rd Annual Cal State L.A. Student Symposium on Research, Scholarship and Creative Activity in Los Angeles, CA.
- 2015 **Julia Montoya**, Matthew Hardy, and Doug Keszler. *Hydrophilicity of Holmium Oxide Thin Films: Characterization of Ho-cluster Solution and Thin Films*. Presented at the MORE Programs Seminar in Los Angeles, CA.

PRESENTATIONS - Poster:

- 2019 **Julia Montoya-Aguilera**. Formation and Properties of Nitrogen-Containing Organic Compounds in Secondary Organic Aerosol (SOA). Presented at the 37th Annual Conference of the American Association for Aerosol Research in Portland, OR.
- 2019 **Julia Montoya-Aguilera**, Natalie R. Smith, Mallory L. Hinks, Jeremy R. Horne, Shupeng Zhu, Donald Dabdub, and Sergey Nizkorodov. Ammonia and Amine Uptake by SOA Leads to Nitrogen-Containing Organic Compounds (NOC) Formation in SOA Particles. Presented at the 2019 Gordon Research Conference on Atmospheric Chemistry in Newry, ME.
- 2019 **Julia Montoya-Aguilera**, Natalie R. Smith, Mallory L. Hinks, Jeremy R. Horne, Shupeng Zhu, Donald Dabdub, and Sergey A. Nizkorodov. A Laboratory and Modeling Investigation on the Effects of NH₃ and Amine Uptake on SOA Composition and its Potential Impacts on Air Quality. Presented at the 36th Annual Informal Symposium on Kinetics and Photochemical Processes in the Atmosphere (ISKPPA) in Riverside, CA.
- 2018 **Julia Montoya-Aguilera**, Mallory Hinks, Jeremy Horne, Shupeng Zhu, Donald Dabdub, and Sergey Nizkorodov. *A Laboratory and Modeling Investigation on the Effects of Ammonia Uptake on SOA Composition and Its Potential Impacts on Air Quality*. Presented at the 10th International Aerosol Conference (IAC) in St. Louis, MO.
- 2017 **Julia Montoya**, Jeremy R. Horne, Mallory L. Hinks, Lauren T. Fleming, Veronique Perraud, Peng Lin, Alexander Laskin, Julia Laskin, Donald Dabdub, and Sergey Nizkorodov. *Secondary Organic Aerosol (SOA) from Photooxidation of Indole*. Presented at The Third Sino-European School on Atmospheric Chemistry (SESAC III) in Shanghai, China.
- 2017 **Julia Montoya-Aguilera**, Jeremy R. Horne, Mallory L. Hinks, Lauren T. Fleming, Veronique Perraud, Peng Lin, Alexander Laskin, Julia Laskin, Donald Dabdub, and Sergey Nizkorodov. *Secondary Organic Aerosol (SOA) from Photooxidation of Indole*. Presented at the Gordon Research Conference on Atmospheric Chemistry in Newry, ME.
- 2017 **Julia Montoya**, Mallory L. Hinks, Sergey A. Nizkorodov, Jeremy R. Horne, and Donald Dabdub. *Effects of Ammonia on SOA Formation and Composition*. Presented at the NSF-GRFP Symposium: Training for Tomorrow in Irvine, CA.
- 2017 **Julia Montoya**, Jeremy R. Horne, Mallory L. Hinks, Lauren T. Fleming, Veronique Perraud, Peng Lin, Alexander Laskin, Julia Laskin, Donald Dabdub, and Sergey Nizkorodov. *Secondary Organic*

- Aerosol (SOA) from Photooxidation of Indole*. Presented at the 34th Informal Symposium on Kinetics and Photochemical Processes in the Atmosphere (ISKPPA) in San Diego, CA.
- 2016 **Julia Montoya**, Mallory L. Hinks, Sergey A. Nizkorodov, Jeremy R. Horne, and Donald Dabdub. *Effects of Ammonia on SOA Formation and Composition*. Presented at the 2016 Society for Advancement of Chicanos/Hispanics and Native Americans in Science (SACNAS) Conference in Long Beach, CA.
- 2016 **Julia Montoya**, Mallory L. Hinks, Sergey A. Nizkorodov, Jeremy R. Horne, and Donald Dabdub. *Effects of Ammonia on SOA Formation and Composition*. Presented at the International Global Atmospheric Chemistry (IGAC) Project 2016 Science Conference in Breckenridge, CO.
- 2014 **Julia Montoya**, Geovani Montoya, Dong Zhang, Matthias Selke, and Krishna Foster. *Identification of Pyrene as a Sensitizer of Singlet Oxygen in the Lower Atmosphere*. Presented at the 2014 Society for Advancement of Chicanos/Hispanics and Native Americans in Science (SACNAS) National Conference in Los Angeles, CA.
- 2014 **Julia Montoya**, Matthew Hardy, and Doug Keszler. *Characterization of Ho-cluster Solution and Thin Film*. Presented at the CSMC Undergraduate Student Symposium in Corvallis, OR.
- 2014 **Julia Montoya**, Geovani Montoya, Dong Zhang, Matthias Selke, and Krishna Foster. *Identification of Pyrene as a Sensitizer of Singlet Oxygen in the Lower Atmosphere*. Presented at the MORE Programs Symposium in Los Angeles, CA.
- 2013 **Julia Montoya**, Geovani Montoya, Dong Zhang, Matthias Selke, and Krishna Foster. *Identification of Pyrene as a Sensitizer of Singlet Oxygen in the Lower Atmosphere*. Presented at the MORE Programs Symposium in Los Angeles, CA.
- 2013 **Julia Montoya** and Krishna Foster. *Identification of Benzo[a]pyrene-1,6-dione as a Sensitizer of Singlet Oxygen in the Lower Atmosphere*. Presented at the MORE Programs Symposium in Los Angeles, CA.
- 2013 Delmy Escobar, **Julia Montoya**, and Vincent Espinoza. *Pollution in Central LA and Central SB Valley: Monitoring NO₂ and O₃*. Presented at the CSULA Honors College Symposium in Los Angeles, CA.
- 2012 Maria Vazquez, **Julia Montoya**, and Krishna Foster. *Reduced Phosphorus Oxyanions Speciation in Ancient Rocks*. Presented at MORE Programs Symposium in Los Angeles, CA.

Awards and Fellowships:

- 2018: Peter B. Wagner Memorial Award in Atmospheric Sciences, 3rd place
- 2017-2020: NSF-GRFP Fellowship
- 2017: Ford Foundation Pre-doctoral Fellowship - Honorable Mention
- 2017: Associated Graduate Students (AGS) Travel Grant
- 2017: Carl Storm Underrepresented Minority (CSURM) Fellowship
- 2015-2017: Louis Stokes Alliance for Minority Participation Bridge-to-the-Doctorate (LSAMP-BD) Fellowship
- 2015-2016: Chemistry at the Space-Time Limit (CaSTL) Diversity Fellowship
- 2014-2015: Dean's List
- 2013-2015: NIH Minority Access to Research Careers-Undergraduate Student Training for Academic Research (MARC U*STAR) Fellowship
- 2013-2014: Rashad E. Razouk Chemistry Scholarship
- 2012-2013: NIH RISE Scholarship
- 2012-2013: Dean's List

2011-2012: Dean's List
2010-2011: Dean's List
2009-2010: General Education Honors

ABSTRACT OF THE DISSERTATION

Nitrogen Containing Secondary Organic Aerosols: Experiments and Air Quality Simulations

By

Julia Montoya-Aguilera

Doctor of Philosophy in Chemistry

University of California, Irvine, 2020

Professor Sergey Nizkorodov, Chair

Secondary organic aerosol (SOA) is a large fraction of particulate matter (PM) worldwide and remains a large source of uncertainty in global models that aim to predict the radiative forcing contribution of PM. The properties of SOA are susceptible to change during transport in the atmosphere in response to different environmental conditions, such as sunlight, temperature, relative humidity (RH), and interaction with other atmospheric species. My research investigated the effects on the physical properties and chemical composition of SOA resulting from the exposure of SOA to common environmental species, such as ammonia, amines, and water vapor mixing ratios.

My first project examined the effect of RH on the chemical composition of SOA formed from low-NO_x toluene oxidation. We found that the particle mass loading decreased by nearly an order of magnitude when RH increased from < 2 to 75–90 % for low-NO_x toluene SOA, but this effect was much smaller for high-NO_x toluene SOA. Mass spectrometry revealed a significant reduction in the fraction of oligomers present in the SOA generated at 75 % RH compared to SOA generated under dry conditions in the low-NO_x toluene SOA. The observed

increase in the oligomer fraction and particle mass loading under dry conditions were attributed to the enhancement of condensation reactions which produce water and oligomers from smaller compounds in low-NO_x toluene SOA. These results indicate the mass yield of toluene SOA in the atmosphere depends on NO_x concentrations and RH.

Another focus of my research was to explore the reactive uptake of reduced nitrogen compounds by SOA. Currently, *inorganic* nitrogen contribution to PM is represented in air quality models, but the contribution of nitrogen *organic* compounds (NOC) to PM is missing. We found that the reactive uptake of NH₃ or dimethylamine (DMA) by low-NO_x SOA (toluene, cedrene, or limonene) did not change SOA particle mass but did change particle composition and color due to the formation of NOC. Air quality model simulations showed that inclusion of this new chemistry significantly reduces gas-phase NH₃ and can therefore affect particle pH and reduce the formation of inorganic PM.

An additional study exploring the formation of NOC in SOA consisted of generating SOA from a N-containing biogenic precursor (indole). This study found that indole oxidation by OH, O₃ or NO₃ efficiently produces brown SOA. Overall, this PhD work highlights the effects that RH can have on SOA formation, as well as the novel chemistry and important properties of NOC in the atmospheric environment.

CHAPTER 1

Introduction

1.1 Atmospheric aerosols

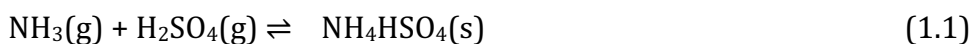
The term “aerosol” refers to a mixture of solids or liquids suspended in a gas by Brownian motion that prevents sedimentation to the ground. Aerosols are ubiquitous in the atmosphere and have far reaching effects at the local, regional, and global scales. The phrase “particulate matter”, which is often used interchangeably with aerosols, refers to only the solid or liquid (i.e., the particle) component of the aerosol. Particulate matter (PM) is of great interest to study because it has been shown to impact public health (Poschl and Shiraiwa, 2015), visibility, and Earth’s climate (Ravishankara et al., 2015; Schneidemesser et al., 2015).

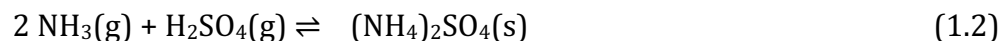
When it comes to exploring the relationship between PM and adverse health effects, it is useful to characterize PM by size, because inhaled particles of different size deposit in different sections of the respiratory system. PM₁₀ refers to PM with a diameter of 10 µm or less; PM_{2.5} includes PM with a diameter of 2.5 µm or less. For perspective, the width of a human hair ranges from ~50-100 µm (Wei et al., 2005; Wolfram, 2003). Both PM sizes are currently regulated in the US by the Environmental Protection Agency, which sets the National Ambient Air Quality Standards for PM and five other criteria air pollutants known to adversely affect human health and the environment. When inhaled, PM₁₀ can make its way down into the larynx, however smaller PM_{2.5} can travel further into the lungs (Finlayson-Pitts and Pitts, 2000; Yeh et al., 1996). One of the earlier studies that drew attention to the toxicity of PM looked at correlations between increased mortality and pollution in six different cities in the US consisting of Portage, WI, Topeka, KA, Watertown, MS, St. Louis, MI,

Harriman, TN, and Steubenville, OH (Dockery et al., 1993). The study found that air pollutants, specifically PM_{2.5} and sulfates, were strongly correlated with increased mortality. Currently, air pollution regulations for PM are based on particle size and mass concentration, however there is increasing discussion of whether these parameters (as opposed to chemical composition, particle number, and surface area) are the best measures of PM toxicity.

PM can measurably impact the radiative forcing (RF) on the Earth's climate and can also decrease visibility (IPCC, 2013). Most particles are weakly-absorbing and strongly-scattering, thus contributing to a net cooling effect on climate (i.e., negative RF), but a subset of particles are strongly light-absorbing in the ultraviolet and visible range of the solar spectrum effectively contributing to a warming effect on climate (i.e., positive RF). In a report published by the Intergovernmental Panel on Climate Change (IPCC), the net RF of natural and anthropogenic atmospheric species were quantified relative to the RF in the year 1750 (IPCC, 2013). Greenhouse gases such as CO₂, CH₄, and halocarbons clearly contribute a net positive RF. On the other hand, the net effect of aerosols and their precursors on climate is less understood with a net RF value spanning both the negative and positive ranges (-0.77-0.23 W m⁻²), due to the large error bars associated with these estimates (IPCC, 2013; Bellouin et al., 2019).

In terms of chemical composition, aerosols can be broadly classified into inorganic and organic. Inorganic aerosols primarily consist of ammonium nitrate and ammonium sulfate salts formed in the atmosphere from through acid/base chemistry (Eqns. 1.1-1.3)





Organic aerosols are further classified by the mechanism of their formation into primary and secondary. Primary organic aerosols (POA) and primary inorganic aerosols (PIA) are directly emitted into the atmosphere from their sources such as biomass burning, wind-driven suspension of soil and dust, sea-spray, volcanic eruptions, and biological species. Secondary inorganic aerosols (SIA) are formed by reactions 1.1-1.3 and the relative contribution of nitrate and sulphate varies by location (Pilinis and Seinfeld, 1987; Tang et al., 2004). Secondary organic aerosols (SOA) are formed in the atmosphere when volatile organic compounds (VOCs) are oxidized by OH, O₃, NO₃ into less volatile compounds and undergo gas to particle conversion. Unlike SIA that have only a few chemical components, the resulting SOA are chemically complex, are less understood relative to inorganic aerosol, and are the focus of the research discussed throughout this thesis.

This dissertation focuses on three under-investigated aspects of SOA chemistry: the effect of relative humidity on the chemical composition of SOA, the effect of ammonia and amines on the chemical composition of SOA, with emphasis on the formation of nitrogen containing compounds, and the chemistry of SOA from unexplored VOC precursors such as indole. The relevant background for each topic and the motivations for the experiments are described in detail at the beginning of corresponding chapters. A brief summary of the chapter goals are described below.

1.2 Effect of relative humidity on SOA properties

The majority of laboratory-based SOA experimental studies have been conducted under low relative humidity (RH) conditions, yet water is known to affect both the chemical and physical properties of SOA and it remains critical to understand the extent of these effects. The presence of water can affect the physical properties of SOA such as viscosity, particle size, and particle mass as well as its chemical properties such as particle acidity and molecular composition. The physical and chemical properties of SOA are understandably linked; therefore when water affects one parameter of SOA other parameters are often also affected. For example, water can act as a plasticizer for SOA particles, making them less viscous and thereby indirectly affecting reactive gas uptake, diffusion rates of gases, and the rate of SOA growth (Renbaum-Wolff et al., 2013; Perraud et al., 2012; Shiraiwa and Seinfeld, 2012). Moreover, aerosol liquid water (ALW) has a strong effect on the acidity of particles and therefore affects acid-catalyzed processes occurring in particles (Jang et al., 2002). The effects of the presence and absence of water on SOA can be illustrated at both RH extremes by studying SOA solvated in water to mimic cloud conditions. For example, going from supersaturated conditions to dry conditions has been demonstrated to speed up reactions that lead to the formation of nitrogen- and sulfur-containing light-absorbing compounds (Nguyen et al., 2012). Moreover under supersaturated conditions, aqueous chemistry occurring in cloud and fog droplets promotes the conversion of small water-soluble molecules into nonvolatile products that would not form in the absence of liquid water (Herrmann et al., 2015).

Chapter 2 explores how RH affects the chemical composition of SOA formed from the OH oxidation of toluene. This study also discusses how the chemical composition and volatility

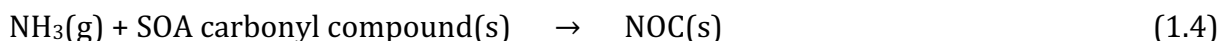
distribution of the SOA compounds influences the amount of SOA formed (mass yield) under low and high RHs.

1.3 Organic nitrogen in SOA

Inorganic nitrogen contribution to PM (Eqns. 1.1-1.3) is well represented in air quality models. Less understood and missing from models is the contribution of nitrogen-containing organic compounds (NOC) to PM. NOC can be highly light-absorbing in the visible range and may therefore contribute a positive RF on climate. Another consequence of NOC formation in SOA is that NOC are less efficient than ammonia at neutralizing acids in particles.

One obvious route for the production of NOC in SOA is via the oxidation of a N-containing VOC. Nitrogen-containing aromatic compounds based on pyrrole, pyridine, imidazole, indole, diazines, purines, etc., have been detected in biomass burning emissions (Laskin et al., 2009). Chapter 3 describes the first experimental study of the SOA generation from indole, a N-containing VOC emitted from plants and animal waste. The study also investigates the light-absorbing properties of the NOC produced in the indole SOA. Furthermore, results are presented from an airshed modeling study that explored the potential contribution of indole SOA to PM_{2.5} mass concentrations at the regional scale.

A second potential pathway for the incorporation of NOC into SOA is through reactions of SOA with NH₃ (Eqn. 1.4). Ammonia is predominantly emitted from agriculture (e.g., fertilizer use) and is the most abundant basic gas in the atmosphere.



Previous laboratory experiments have shown that exposure of SOA to NH_3 can lead to 'browning' of SOA (Mang et al., 2008) by a mechanism involving the reaction of NH_3 with carbonyls in the SOA that lead to a loss of one or more water molecules (Aiona et al., 2017; Kampf et al., 2016). This proposed mechanism is similar to the Maillard reaction that is responsible for the browning of certain foods after cooking. Few studies have attempted to quantify the uptake coefficient of NH_3 on SOA particles (Liu et al., 2015), a useful parameter for translating laboratory results into modeling studies. Chapter 4 describes our study of NH_3 uptake by various SOA, as well as the results from an exploratory modeling study that investigated the potential impact of NH_3 uptake by SOA on $\text{PM}_{2.5}$ mass concentrations at the regional and continental scale. Lastly, a similar mechanism for the incorporation of NOC into SOA may be through the reactions of SOA with other reduced nitrogen compounds present in the atmosphere, such as amines. Chapter 5 discusses experiments investigating the uptake of dimethylamine by various SOA leading to NOC formation, as well as the dependence of this uptake on RH.

CHAPTER 2

Effect of Relative Humidity on the Formation of Low-NO_x Toluene

Secondary Organic Aerosol

Portions of this chapter were reproduced under the Creative Commons Attribution 4.0 License from:

Hinks, M.L.; Montoya-Aguilera, J.; Ellison, L.; Lin, P.; Laskin, A.; Laskin, J.; Shiraiwa, M.; Dabdub, D.; Nizkorodov, S.A., Effect of relative humidity on the composition of secondary organic aerosol from the oxidation of toluene, *Atmospheric Chemistry and Physics*, **18** (2018) 1643-1652.

2.1 Introduction

Secondary organic aerosol (SOA) is an important component of atmospheric particulate matter. It is formed in the atmosphere via the oxidation of volatile organic compounds (VOCs) by common atmospheric oxidants such as O₃, OH, and NO₃ (Seinfeld and Pandis, 2016). The SOA formation mechanisms depend in a complex way on physical environmental parameters such as solar irradiance, temperature, and relative humidity (RH). They also depend on the type of oxidant, the concentration of VOC precursors, which govern RO₂ concentrations, and NO_x levels, which determine the fate of the RO₂ radicals. The RH controls the amount of available water in the system and therefore affects processes in which water acts as a reactant, product, or solvent in several ways. Firstly, gaseous water can directly participate in the VOC oxidation reactions. For example, it is well known to react with carbonyl oxide intermediates in the ozonolysis of alkenes (Finlayson-Pitts and Pitts Jr., 2000). Additionally, aerosol liquid water (ALW) present in hygroscopic particles can lead to the hydrolysis of organic compounds and other particle-phase reactions involving or

catalyzed by water (Ervens et al., 2011). ALW also has a strong effect on the acidity of particles and therefore affects acid-catalyzed processes occurring in particles (Jang et al., 2002). Furthermore, water can act as a plasticizer for SOA particles, making them less viscous and thus affecting the rate of their growth (Renbaum-Wolff et al., 2013; Perraud et al., 2012; Shiraiwa and Seinfeld, 2012). Under supersaturated conditions, aqueous chemistry occurring in cloud and fog droplets promotes the conversion of small water-soluble molecules into nonvolatile products that would not form in the absence of liquid water (Herrmann et al., 2015). Finally, dissolved SOA compounds may undergo more efficient photodegradation in water (Bateman et al., 2011; Nguyen et al., 2012; Romonosky et al., 2015, 2017; Zhao et al., 2017) compared to dry particles (Kourtchev et al., 2015).

Chemical composition is an important characteristic of SOA because it may determine the climate- and health-relevant properties of particles. The effect of RH on the chemical composition of particles has been studied for several types of biogenic SOA (Nguyen et al., 2011; Zhang et al., 2011; Riva et al., 2016; Harvey et al., 2016). For example, Nguyen et al. (2011) examined high-NO_x isoprene SOA formed under high- and low-RH conditions and found that the high-RH samples contained fewer oligomers than the low-RH samples. Zhang et al. (2011) investigated the effect of RH on the composition of high-NO_x isoprene SOA and found that oligoesters present in the SOA were suppressed at higher RH, while the formation of organosulfates was enhanced. Riva et al. (2016) studied the effect of RH on SOA made from oxidized isoprene hydroxyhydroperoxide (ISOPOOH) and found that increasing RH led to an increase in the abundance of some oligomers while decreasing the abundance of other oligomers. Harvey et al. (2016) investigated the effect of RH on 3-hydroxypropanal

ozonolysis SOA and found that increasing RH resulted in a decrease in SOA yield and a decrease in oligomerization.

The effect of RH on SOA formed from monoaromatic compounds, such as benzene, toluene, *m*-xylene, and 1,3,5-trimethylbenzene (TMB), has been studied. Most of these studies focused on the effect of RH on SOA yield (Edney et al., 2000; Zhou et al., 2011; Cocker III et al., 2001; Kamens et al., 2011; Cao and Jang, 2010; Faust et al., 2017; Liu et al., 2017; Jia and Xu, 2017) and not the chemical composition of SOA particles. The comparison between different experiments is complicated by the fact that some experiments are done in the presence of hygroscopic seed particles, where ALW may be playing a role; others are done with seed particles containing strong acids, which favor acid-catalyzed chemistry, and others without seed particles. For toluene SOA produced in presence of hygroscopic seed particles, the yield is generally found to be larger under high-RH conditions (Zhou et al., 2011; Kamens et al., 2011; Faust et al., 2017; Liu et al., 2017; Jia and Xu, 2017) because additional organic compounds are produced by the aqueous photochemistry of small highly soluble compounds, such as glyoxal, partitioned in ALW. However, Cao and Jang (2010) observed a negative correlation between RH and SOA yield for low-NO_x experiments; i.e., lower RH resulted in higher SOA yields.

In the experiments done without seed particles, the acid catalysis and chemistry occurring in ALW do not contribute to the particle growth. However, this does not rule out the possibility that RH may affect the SOA chemical composition and yield by mechanisms other than those mentioned above. Indeed, White et al. (2014) investigated the effect of RH on the composition of toluene SOA produced under high-NO_x conditions without seed particles and observed higher toluene SOA yields at elevated RH and higher yields of photooxidation

products. In this work, we studied the composition of low-NO_x toluene SOA formed under dry and humid conditions in the absence of seed particles. We observed a significant negative correlation between RH and low-NO_x SOA from toluene SOA mass loading and a strong RH dependence on SOA molecular composition. We attribute this effect to the more extensive oligomerization of SOA compounds driven by condensation reactions under dry conditions. The reduction in the fraction of oligomeric compounds under humid conditions is predicted to partly counteract the previously observed enhancement in the toluene SOA yield driven by the ALW chemistry in deliquesced inorganic seed particles.

2.2 Experimental Methods

SOA was generated by the photooxidation of toluene in a 5 m³ smog chamber surrounded by a bank of UV-B lights. Before each experiment, the chamber was humidified to the desired RH by flowing purified air through a Nafion humidifier (PermaPure). The temperature (± 1 °C) and RH (± 2 % RH) inside the chamber were monitored with a Vaisala HMT330 probe. No seed aerosol was used. Hydrogen peroxide (H₂O₂) was introduced to the chamber by injecting a measured volume of aqueous H₂O₂ (30 wt %) into a bulb where it was evaporated and carried into the chamber by a flow of purified air over a period of 30 min. The majority of the experiments were done under low-NO_x conditions with concentrations of NO and NO_y being below the 1 ppb detection limit of the NO_y analyzer (Thermo Scientific 42i-Y). In the high-NO_x experiments, gaseous NO (1000 ppm in N₂; Praxair) was added to achieve a total NO concentration of 300 ppb. Toluene (Fisher Scientific; ACS grade) was introduced into the chamber by evaporating a measured volume of liquid toluene into a stream of air over a period of 5 min, which resulted in a toluene mixing ratio of either 300 or 1000 ppb. Following

the addition of gaseous reactants into the chamber, the UV lamps were turned on, photolyzing the H_2O_2 and resulting in a steady-state OH concentration of $1 \times 10^6 \text{ molec cm}^{-3}$ (determined in a separate experiment from the rate loss of a VOC in the presence of OH). These high concentrations of toluene were chosen in order to produce a sufficient amount of SOA to collect for offline analysis. Throughout each experiment, particle concentrations were monitored with a scanning mobility particle sizer equipped with a condensation particle counter (SMPS model 3080; CPC model 3775; TSI Inc.). We used an effective SOA particle density of 1.4 g cm^{-3} to convert the SMPS measurements into particle mass concentration (Sato et al., 2007; Ng et al., 2007). The concentration of toluene in the chamber was tracked with a proton-transfer reaction time-of-flight mass spectrometer (PTR-ToF-MS; Ionicon 8000). The observed decrease in the toluene concentration (typically $\sim 40 \%$) was the same under low- and high-RH conditions.

SOA samples were collected onto Teflon filters for offline analysis by nanospray desorption electrospray ionization–high-resolution mass spectrometry (nano-DESI–HRMS). The filters were sealed and frozen immediately after the sample collection to avoid decomposition of less stable compounds, as observed for example by Krapf et al. (2016). The SOA filter samples were brought to room temperature and immediately analyzed in both positive and negative ion modes using an LTQ Orbitrap mass spectrometer (Thermo Corp.) with a resolving power of 10^5 at m/z 400 equipped with a custom-built nano-DESI source (Roach et al., 2010a, b). The advantage of nano-DESI is in minimizing the time in which the sample is exposed to the solvent, thus minimizing solvolysis reactions. Mass spectra of the solvent and blank filters were recorded as controls. Mass spectra of the samples with the highest signal-to-noise ratio were clustered together, and the m/z axis was calibrated internally with respect to known

SOA products. The solvent and impurity peaks were discarded. The peaks were assigned formulas, $C_cH_hO_oN_nNa+0-1$ or $C_cH_hO_oN-n$, constrained by valence rules (Kind and Fiehn, 2007) and elemental ratios (c, h, o, and n refer to the number of corresponding atoms in the ion). The resulting ion formulas were converted into formulas of the corresponding neutral species. All data reported below refer to the formula and molecular weights of the neutral species.

2.3 Results and Discussion

The mass spectra of a low-RH sample (< 2 % RH) and a high-RH sample (75 % RH) are shown in Fig. 2.1 plotted as a function of the molecular weight of the neutral compounds. The mass spectra obtained in the positive and negative ion modes represent the SOA compounds ionizable in these modes and are not expected to be identical (Walser et al., 2008). The low- NO_x mass spectrum shown in Fig. 2.1 is qualitatively similar to the low- NO_x mass spectrum of toluene SOA discussed in a previous study in which it was prepared in a different smog chamber but analyzed by the same nano-DESI instrument (Lin et al., 2015).

As shown in Fig. 2.1, the increase in RH resulted in a visible reduction in the overall peak abundance for both ion modes due to the fact that the high-RH sample had a much lower particle mass during the SOA generation (see below), and thus there was less material on the substrate. There was also a reduction in the number of observed peaks. For example, the positive mode mass spectrum in Fig. 2.1 contains 665 peaks at low RH but only 285 peaks at high RH; the corresponding peak numbers are 276 and 90 for the negative ion mode. Despite this reduction in peak abundance and number, the major observed peaks in the mass spectra remained the same. Table 2.1 lists the five most abundant peaks for both the low- and high-

RH samples observed in the positive and negative modes. The fact that the major peaks are similar between the low- and high-RH samples suggests that the major products are produced by a similar mechanism that is not too sensitive to RH. It is of course still possible that the distribution of different structural isomers within each peak could be affected by humidity, but the nano-DESI method used here would be blind to this effect because it cannot separate isobaric isomers.

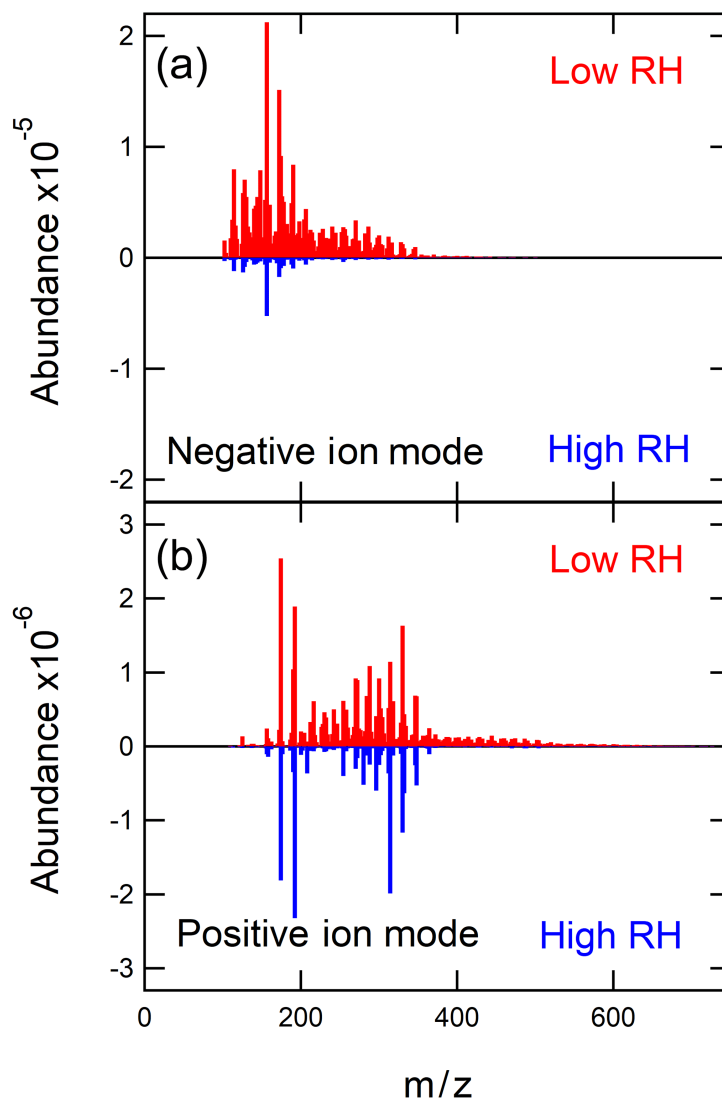


Figure 2.1. High-resolution mass spectra obtained in negative ion mode **(a)** and positive ion mode **(b)**. The red upward-pointing mass spectra represent the low-NO_x SOA sample made under low RH (< 2 %) and the blue inverted mass spectra represent the low-NO_x SOA sample made under high RH (75 %).

Table 2.1. The five most abundant compounds observed in the low- and high-RH low-NO_x toluene SOA samples. In positive ion mode, the most abundant species differed by one compound in the low- and high-RH experiments, and hence the table contains six formulas. In negative ion mode, the same five most abundant peaks were observed at the low and high RH.

Nominal mass	Formula	Low RH	High RH
Positive ion mode		Normalized peak abundance	
174	C ₇ H ₁₀ O ₅	1	1
192	C ₇ H ₁₂ O ₆	0.74	0.86
330	C ₁₄ H ₁₈ O ₉	0.64	0.78
314	C ₁₄ H ₁₈ O ₈	0.45	0.50
288	C ₁₂ H ₁₆ O ₈	0.43	0.11
332	C ₁₄ H ₂₀ O ₉	0.17	0.27
Negative ion mode		Normalized peak abundance	
156	C ₇ H ₈ O ₄	1	1
172	C ₇ H ₈ O ₅	0.71	0.86
174	C ₇ H ₁₀ O ₅	0.43	0.78
190	C ₇ H ₁₀ O ₆	0.40	0.50
114	C ₅ H ₆ O ₃	0.38	0.27

While the major oxidation products were similar at low and high RH, the less abundant products were much more strongly affected by RH. Specifically, the abundances of some high-molecular-weight compounds were visibly reduced at high RH (Fig. 2.1), suggesting that either the gas-phase oligomer formation is suppressed by water vapor or the particle-phase oligomer formation is suppressed by ALW. (An alternative explanation is that oligomers hydrolyze after partitioning into the particle, but the amount of ALW in the particles might be too small to sustain efficient hydrolysis.) To better quantify this effect, Fig. 2.2 shows the combined peak abundances as a function of the number of carbon atoms (n_c) in each molecule. Monomer compounds containing $n_c = 7$ and dimer compounds with $n_c = 14$ clearly dominate the distribution. In fact, the combined abundance of dimers ($n_c = 14$) represents the highest peak in the distribution in the positive ion mode. Many larger compounds with n_c up to 32 also appear in the mass spectrum, and these minor compounds are the ones most affected by RH.

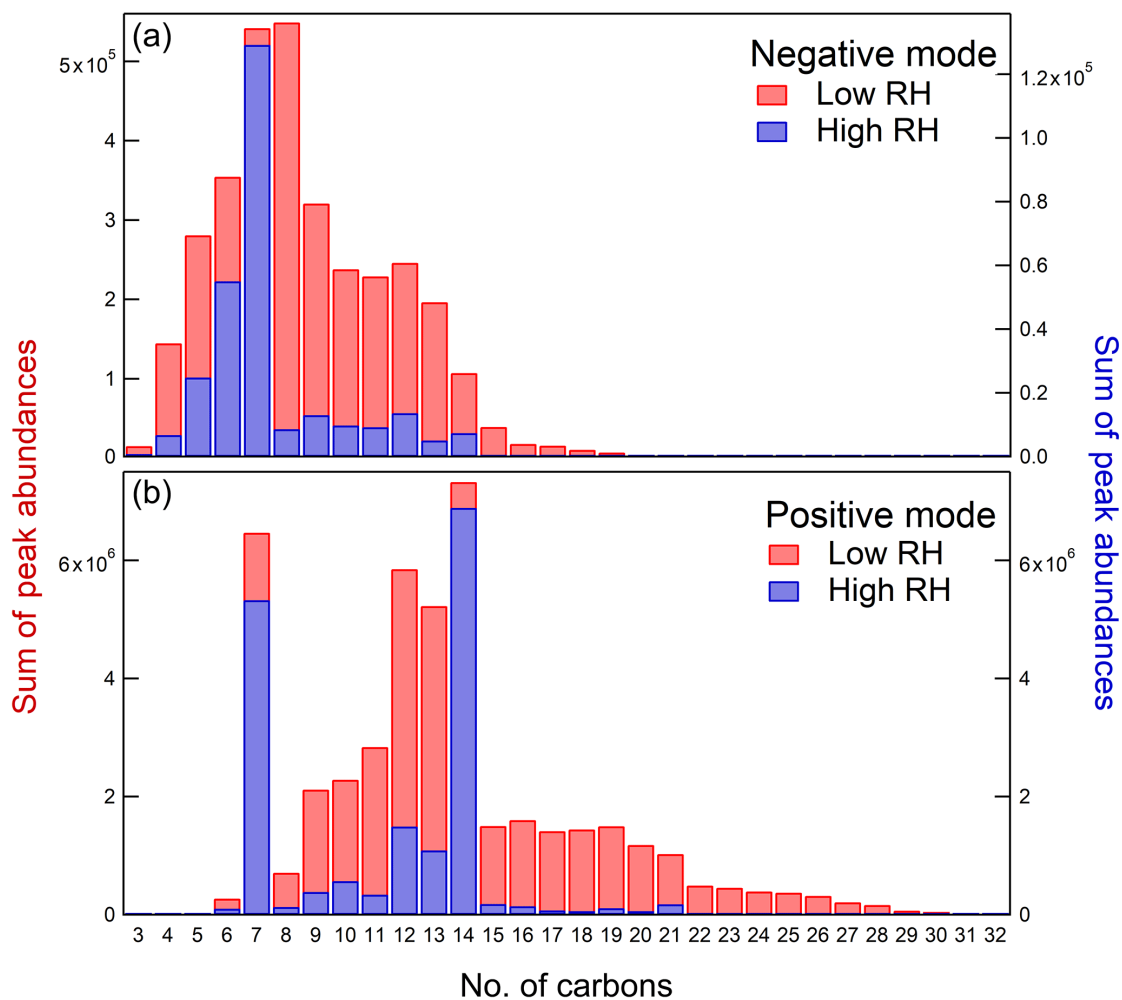


Figure 2.2. Combined abundance of all peaks as a function of the number of carbon atoms in negative mode **(a)** and positive mode **(b)**. The data for the low-RH sample are shown in red and the data for the high-RH sample are shown in blue. The samples were prepared under low- NO_x conditions.

When comparing the low-RH sample to the high-RH sample, there is a significant decrease in combined peak abundance for molecules with $n_c > 7$ under high-RH conditions (except for the $n_c = 14$ dimers). Because these higher-molecular-weight oligomers tend to have lower volatility (Li et al., 2016), they play an important role in the formation and growth of aerosol particles. With the lower fraction of oligomers produced under high-RH conditions, the population of the oxidation products becomes more volatile on average, which should result in a lower SOA yield.

To better illustrate the possible effect of RH on the yield of condensable oxidation products, the volatility distributions were estimated for the low-NO_x toluene SOA compounds using the “molecular corridor” approach (Li et al., 2016; Shiraiwa et al., 2014). This parameterization was developed specifically for atmospheric organic compounds containing oxygen, nitrogen, and sulfur (Li et al., 2016), and it makes it possible to estimate the pure compound vapor pressure, C_0 , from the elemental composition derived from high-resolution mass spectra (Lin et al., 2016; Romonosky et al., 2017). C_0 is related to the more commonly used effective saturation mass concentration, $C^* = \gamma \times C_0$, where γ is the activity coefficient (Pankow, 1994). C_0 becomes equal to C^* under the assumption of an ideal thermodynamic mixing. The C_0 values were calculated for each compound observed in the positive and negative ion mode mass spectra. Note that the molecular corridor approach only predicts C_0 (i.e., for pure compound); it does not attempt to predict C^* , so there is no need to assume a value for the activity coefficient. The values were binned in equally spaced bins of the base-10 logarithm of C_0 as is commonly done in the volatility basis set (VBS; Donahue et al., 2006). The contribution of each compound to its volatility bin was taken to be proportional to its relative abundance in the mass spectrum.. A previous study looking at the ESI detection of standards in an SOA mixture demonstrated that while their ion intensities were suppressed to a different extent in the mixture (as opposed to in a pure solvent), the ion intensities remained proportional to the mass concentration of the individual compounds in the complex mixture (Nguyen et al., 2013). This is a considerable approximation because even for a series of carboxylic acids the ESI detection sensitivities can vary by several orders of magnitude within the same sample (Bateman et al., 2012). However, this approximation may

still be useful for comparing distributions for the same types of SOA produced and analyzed under the same experimental conditions (Romonosky et al., 2017).

Figure 2.3 shows the resulting distribution of the SOA compounds by volatility. Under typical ambient conditions, compounds with C_0 above $\sim 10 \mu\text{g m}^{-3}$, i.e., the ones falling above the $\log(C_0) = 1$ bin, should exist primarily in the gaseous phase. Some of these more volatile compounds were detected in the negative ion mode. They may correspond to carboxylic acids that adsorbed to the filter during sampling or were trapped in the SOA. Less volatile compounds were preferentially observed in the positive ion mode. In both positive and negative ion modes, the compounds falling in the lower volatility bins were visibly suppressed at high RH. For example, the high-RH to low-RH ratio of the combined peak abundances for the compounds falling below $\log(C_0) = 1$ is 0.3 in the positive ion mode and 0.05 in the negative ion mode.

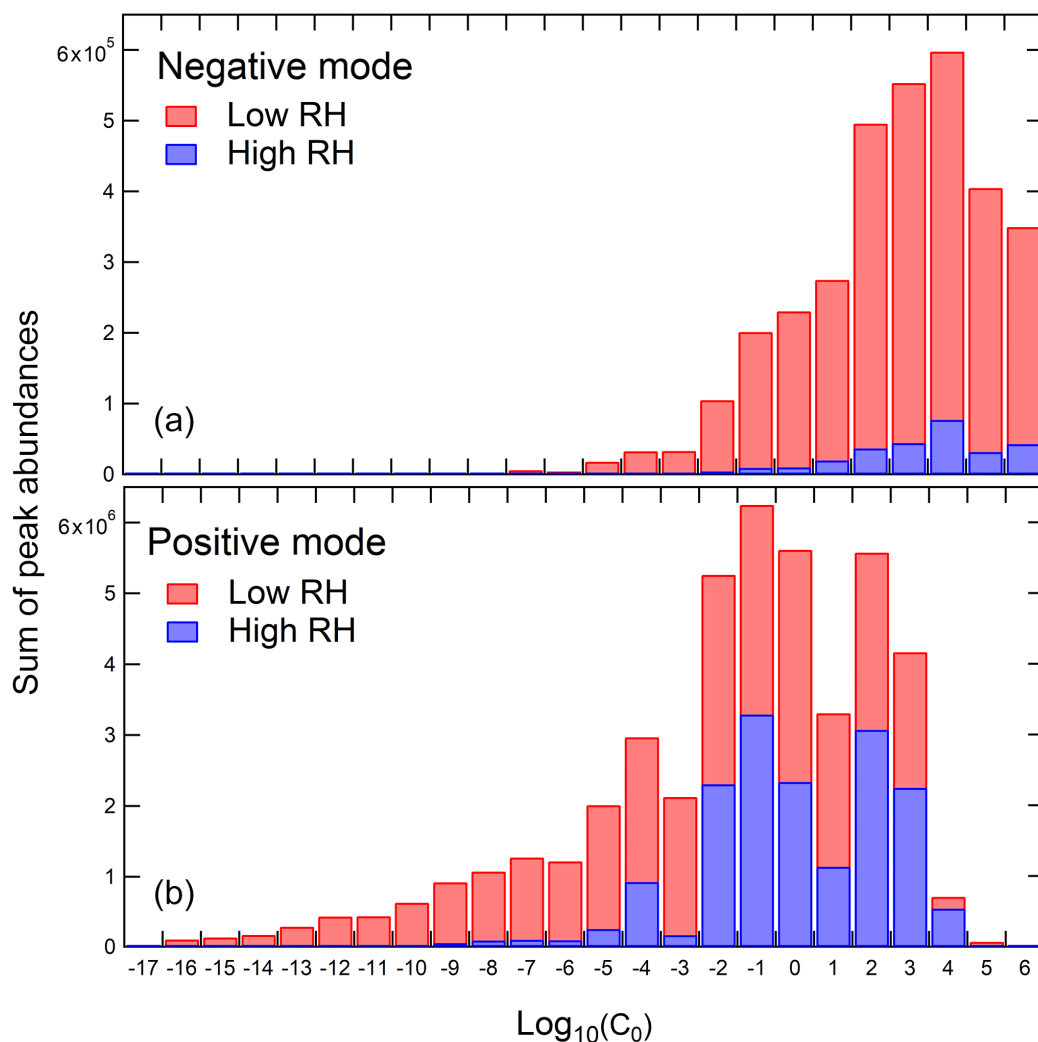


Figure 2.3. Estimated volatility distribution for the compounds observed in low-NO_x SOA samples in the negative **(a)** and positive **(b)** ion mode at low (red bars) and high (blue bars) RH. The height of each bar is proportional to the total ESI abundance of compounds falling within the volatility bin. In order to investigate whether the decrease in oligomers affects the SOA mass loading, we

carried out additional experiments in which the particle mass concentration was tracked with the SMPS at different RH. The SMPS data were corrected for particle wall-loss effects assuming an effective first-order rate constant for the loss of mass concentration of $9.3 \times 10^{-4} \text{ min}^{-1}$, which was measured in a separate experiment (the rate constant was assumed to be independent of particle size). The SMPS experiments were performed under both low-NO_x and high-NO_x conditions. A summary of these experiments is presented in

Table 2.2. Representative examples of the wall-loss-corrected particle mass concentration as a function of photooxidation reaction time are shown in Fig. 2.4 for both the low-NO_x and the high-NO_x toluene SOA systems.

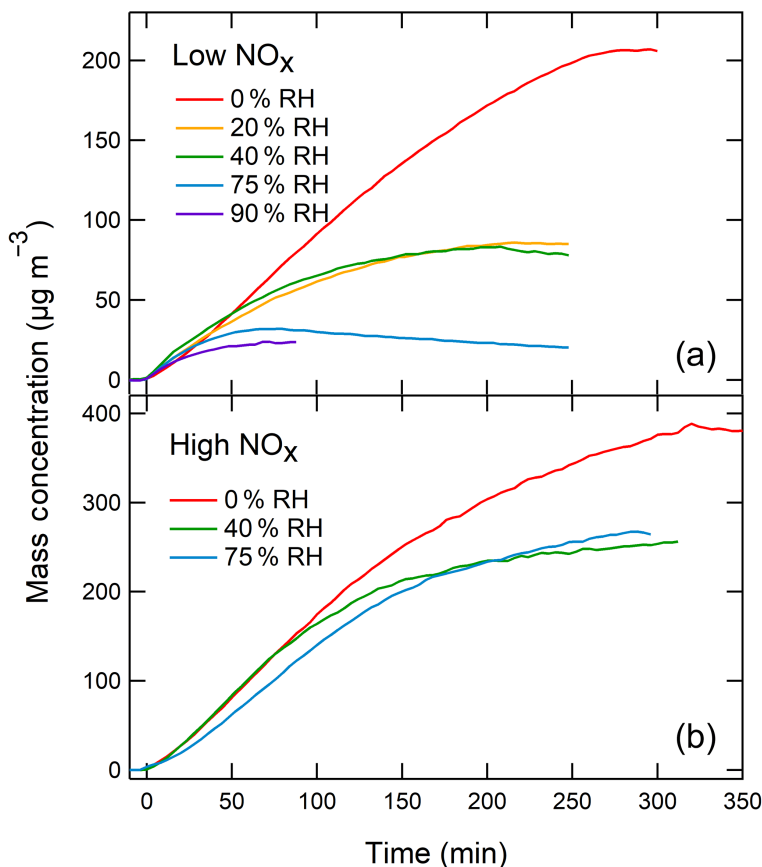


Figure 2.4. Examples of particle mass concentration measurements by SMPS (corrected for wall loss) as a function of photooxidation time under low-NO_x **(a)** and high-NO_x **(b)** conditions. Under high-NO_x conditions, there was a small difference in the maximum mass concentration achieved under < 2, 40, and 75 % RH (less than a factor of 2), but under low-NO_x conditions the difference was substantially larger. For the low-NO_x system, the wall-loss-corrected particle mass concentration decreased by a factor of 8 over the range of RHs studied. The effect was reproducible as essentially the same mass concentration was observed in experiments repeated on different days under the same initial conditions.

Combining the measured particle mass concentrations with the toluene concentration measurements from PTR-ToF-MS makes it possible to estimate the apparent SOA yields, which are listed in the last column of Table 2.2. Under high-NO_x conditions, the yield decreased from ~ 27 to ~ 19 % as RH increased from < 2 to 77 %. Under low-NO_x conditions, the yields dropped from 15 to 2 % for the same change in RH. We note that the previously reported SOA yields from toluene SOA formed in the presence of ammonium sulfate seed aerosol displayed the opposite trend, with the yield being higher (~ 30 %) under low-NO_x conditions and lower under high-NO_x conditions (~ 19 %; Ng et al., 2007). Hildebrandt et al. (2009) noted that the yields in the toluene SOA system are highly sensitive to the oxidation conditions, including the type of UV lights used in photooxidation and the seed aerosol concentration. Furthermore, the wall-loss effects are especially prominent in the toluene SOA system (Zhang et al., 2014). We attribute the difference in the absolute values of yields between our experiments and experiments by Ng et al. (2007) to the difference in the experimental design, likely due to the lack of seed particles in our experiment and lower OH-oxidation rate of toluene.

Table 2.2. Summary of SMPS experiments. The uncertainties included in this table are based on 1 standard deviation in the data for repeated experiments.

Initial RH	No. of experiments	NO _x ppm	Toluene ppm	H ₂ O ₂ ppm	SOA from SMPS μg m ⁻³	Wall-loss-corrected SOA μg m ⁻³	SOA yield (%)
Low NO _x – high toluene							
< 2	4	–	1.0	2.0	180 ± 20	210 ± 20	15 ± 2
20 ± 3	2	–	1.0	2.0	76 ± 4	87 ± 6	6.2 ± 0.5
43	1	–	1.0	2.0	74	84	5.9
76 ± 1	4	–	1.0	2.0	27 ± 7	28 ± 7	2.0 ± 0.5
89 ± 1	2	–	1.0	2.0	25 ± 8	26 ± 9	1.9 ± 0.6
Low NO _x – lower toluene							
< 2	1	–	0.3	0.6	23	27	5.5
75	1	–	0.3	0.6	8	9	2.2
High NO _x – high toluene							
< 2	1	0.3	1.0	2.0	330	390	27
43	1	0.3	1.0	2.0	210	260	18
77	1	0.3	1.0	2.0	230	270	19

The differences between the low- and high-RH systems cannot be explained by the hygroscopic growth of particles at elevated RH. Throughout the experiment, the SMPS sampled air directly from the chamber. Each experiment lasted many hours, which allowed the sheath flow in the SMPS to approach the RH of the chamber air. Therefore, the particles sized by the SMPS contained some ALW and would appear larger than their dry size. If the organic mass in particles did not change at different RH levels, we would have observed an *increase* as opposed to a decrease in the measured particle mass concentration. With a typical hygroscopic growth factor (the ratio of particle diameters in humidified and dry air) for SOA of 1.1 at 85 % RH (Varutbangkul et al., 2006), the increase in the apparent mass concentration would have been by a factor of about 1.3. Instead, the mass concentration decreased by almost a factor of 8 at higher RHs. The strong dependence of the low-NO_x toluene SOA mass loading on RH is therefore not an artifact of the SMPS measurements.

We cannot rule out the possibility that the mass loading of SOA was affected by the enhanced wall loss of more water-soluble compounds under high-RH conditions. Indeed, the chamber wall effects are expected to be stronger for the slowly reacting toluene compared to monoterpenes that are oxidized much faster (Pierce et al., 2008). Furthermore, in the absence of seed particles, toluene SOA aerosol growth takes longer, making the wall-loss effects larger (Kroll et al., 2007; Zhang et al., 2014). It is conceivable that the products of the low-NO_x oxidation of toluene are more water soluble than the products of the high-NO_x oxidation of toluene. This would result in a stronger effect of RH on the mass loading of low-NO_x SOA because these products would be more efficiently absorbed by the wetted chamber walls. Distinguishing the wall-loss effects from the effect of water on the distribution of oligomers would require more careful chamber measurements of SOA yields over a broad range of concentrations and in the presence of seed aerosol (to suppress the wall-loss effects).

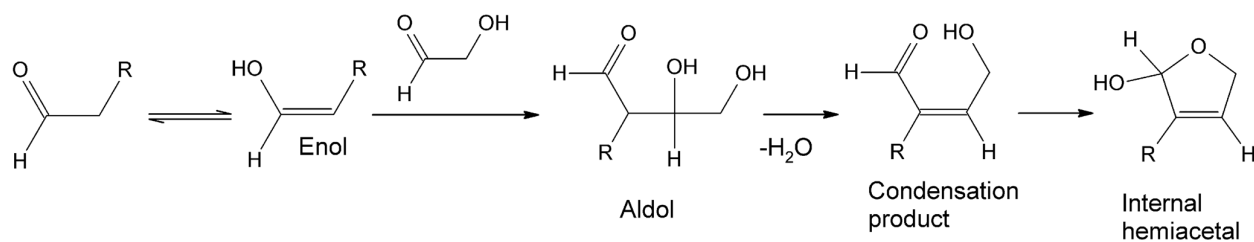
A possible chemical explanation for the observed RH effect is that there are chemical reactions in the system that directly involve water and change the chemical composition of the particles, thereby affecting their growth rate. Previous studies have shown that RH can affect the composition and potential yield of SOA by altering the fraction of low-volatility oligomers in SOA. Increased RH could suppress the oligomerization occurring by condensation reactions (i.e., reactions between monomers that produce water as a by-product) by shifting the reaction equilibrium toward the monomers as discussed in Nguyen et al. (2011). Conversely, increased RH could promote the hydrolysis of oligomers after they are produced in the gas phase and partition into wet particles. As pointed out above, the latter mechanism is less likely due to the low ALW content of the organic particles.

To investigate the mechanism, we examined the frequency of occurrence of mass differences (corresponding to molecular fragments) between the peaks in the high-resolution mass spectra. Table 2.3 lists the most common mass differences in all four mass spectra.

Table 2.3. Most common mass differences in the high-resolution mass spectra of low-NO_x toluene SOA (in the order of decreasing frequency of occurrence).

Positive ion mode		Negative ion mode	
Low RH	High RH	Low RH	High RH
C ₂ H ₂ O	CH ₂	C	O
CH ₂ O	O	C ₂ H ₂ O	CH ₂ O
C	CH ₂ O	O	C
CH ₂	C ₂ H ₂ O	CH ₂ O	C ₂ H ₂ O
O	C	CH ₂	CH ₂
C ₃ H ₄ O ₂	CO	CO	C ₂ H ₂

The most frequently observed mass difference in the low-RH sample was C₂H₂O, and its frequency of occurrence dropped in the high-RH sample. It is possible that C₂H₂O results from the oligomerization chemistry of glycolaldehyde (C₂H₄O₂), which can react by an aldol condensation mechanism with compounds containing a carbonyl group (Scheme 2.1). Glycolaldehyde has been observed previously in the oxidation of toluene (White et al., 2014; Yu et al., 1997), likely as an oxidation product of methylglyoxal. The mass difference corresponding to H₂O was not amongst the most common and therefore not listed in Table 2.3; however, it became more prevalent in the high-RH sample, consistent with hydration reactions. Anhydrides, commonly found in toluene SOA (Bloss et al., 2005; Forstner et al., 1997; Sato et al., 2007), may undergo hydrolysis, which adds an H₂O unit to the formula.



Scheme 2.1. An aldol condensation reaction involving glycolaldehyde that results in the addition of $\text{C}_2\text{H}_2\text{O}$ to the formula of the aldehyde co-reactant.

We additionally tested whether oligomeric compounds occurring in low-RH toluene SOA can be produced by either simple addition or condensation of monomer compounds occurring in high-RH toluene SOA. If simple addition is responsible for the oligomerization, we would expect to see peaks in the low-RH mass spectrum with molecular weights equal to the sum of two peaks from the high-RH mass spectrum. If condensation is responsible for the oligomerization, we would expect to see peaks in the low-RH mass spectrum with molecular weights equal to the sum of two peaks from the high-RH mass spectrum minus the mass of water (the same relationship would hold in reverse for oligomers undergoing hydrolysis in the particle). In positive ion mode, the fraction of peaks that could be matched by the addition reactions was 69 %, while the fraction of peaks matched by the condensation reactions was 83 %. These numbers were 62 and 69 %, respectively, for negative ion mode. This suggests that condensation reactions (that remove water) are more likely to be responsible for the enhanced oligomer formation under dry conditions. This conclusion is similar to the one reached in the study of the effect of RH on oligomerization in high- NO_x isoprene SOA (Nguyen et al., 2011).

2.4 Conclusions

This study demonstrates that the composition of low-NO_x toluene SOA depends on RH when it is produced in smog chamber experiments without seed particles. Oligomers produced by condensation reactions were observed in higher concentrations in the mass spectra of toluene SOA produced under low RH and were suppressed under high RH conditions. Additionally, the mass loading of low-NO_x toluene SOA was reduced under high RH conditions. The plausible reason for the suppression of SOA mass loading at high RH is the change in the SOA chemical composition that favors lower molecular weight, more volatile compounds. The reduction of dimers and trimers in the high RH samples suggests that low-volatility oligomers are not forming in toluene SOA under low-NO_x conditions, which means particle growth is suppressed and mass loading is reduced.

In previous studies on the effect of RH on SOA yield from toluene in the presence of hygroscopic seed (Zhou et al., 2011; Kamens et al., 2011; Faust et al., 2017; Liu et al., 2017; Jia and Xu, 2017), an opposite effect was observed in which the SOA yield increased at high RH. This was attributed to the aqueous partitioning and subsequent reactions in ALW of smaller photooxidation products, such as glyoxal (Faust et al., 2017). Our results suggest that the increase in the SOA yield due to the ALW-supported chemistry is at least partly counteracted by the lower yield of oligomers under high-RH conditions. While it is not straightforward to compare experiments done with and without seed aerosol in different smog chambers, the ALW-supported chemistry enhancement of the yield appears to be a more important effect.

It is conceivable that the effect of RH on the SOA yield is a common feature of all low-NO_x aromatic SOA, all of which should contain aldehyde compounds capable of oligomerization

by condensation reactions. If this is the case, the production of SOA from naturally emitted aromatic compounds (indole, benzyl acetate, benzaldehyde, etc.), which exist in low-NO_x environments, would be strongly modulated by the ambient relative humidity. This definitively warrants further investigation.

CHAPTER 3

SECONDARY ORGANIC AEROSOL FROM INDOLE OXIDATION

Portions of this chapter were reproduced under the Creative Commons Attribution 4.0 License from:

Montoya-Aguilera, J.; Horne, J.R.; Hinks, M.L.; Fleming, L.T.; Perraud, V.; Lin, P.; Laskin, A.; Laskin, J.; Dabdub, D.; Nizkorodov, S.A., Secondary organic aerosol from atmospheric photooxidation of indole, *Atmospheric Chemistry and Physics*, **17** (2017) 11605-11621.

3.1 Introduction

Atmospheric particulate matter (PM) absorbs and scatters solar radiation and is responsible for diminished visibility in urban areas and for global changes in climate. A key component of PM is secondary organic aerosol (SOA). While air quality model prediction capabilities have improved in recent years, disagreements between SOA predictions and measurements remain (Couvidat et al., 2013; Heald et al., 2005; Hodzic et al., 2010; Jiang et al., 2012; Volkamer et al., 2006). Discrepancies may result from incorrect or incomplete parameterizations of mechanisms for known SOA precursors, as well as from unaccounted precursors of SOA. Atmospheric researchers have investigated in detail the SOA generated from oxidation of basic anthropogenic and biogenic volatile organic compounds (VOCs), such as isoprene, monoterpenes, saturated hydrocarbons, and aromatic hydrocarbons. Much less is known about SOA from nitrogen-containing VOCs, even though such VOCs are also common in the atmospheric environment and can potentially provide significant additional pathways for SOA formation. For example, photooxidation of amines could serve as a

possible SOA source (Atkinson et al., 1987; Price et al., 2014; Silva et al., 2008; Tuazon et al., 1984; Tuazon et al., 1994).

Heterocyclic nitrogen-containing aromatic compounds based on pyrrole, pyridine, imidazole, indole, diazines, purines, etc., have been detected in biomass burning emissions (Laskin et al., 2009). Such compounds can also be emitted by vegetation, for example, indole is produced by wide variety of plants (Cardoza et al., 2003; De Boer et al., 2004; Gols et al., 1999; McCall et al., 1993; Turlings et al., 1990; Zhuang et al., 2012). Indole is emitted in response to physical or herbivore-induced stress (Erb et al., 2015; Frey et al., 2004; Misztal et al., 2015; Niinemets et al., 2013; Schmelz et al., 2003; Turlings et al., 2004) and during flowering events (Gentner et al., 2014). Once emitted, indole performs critical roles in plant ecology, for example, in attracting pollinators (Zito et al., 2015). For decades, indole and its derivatives (Fig. 3.1) have been utilized in agriculture, dyes, perfumes, and pharmaceutical applications. One of the better-known derivatives of indole is indigo dye (also known as indigotin), which is used to dye jeans to their characteristic deep blue color.

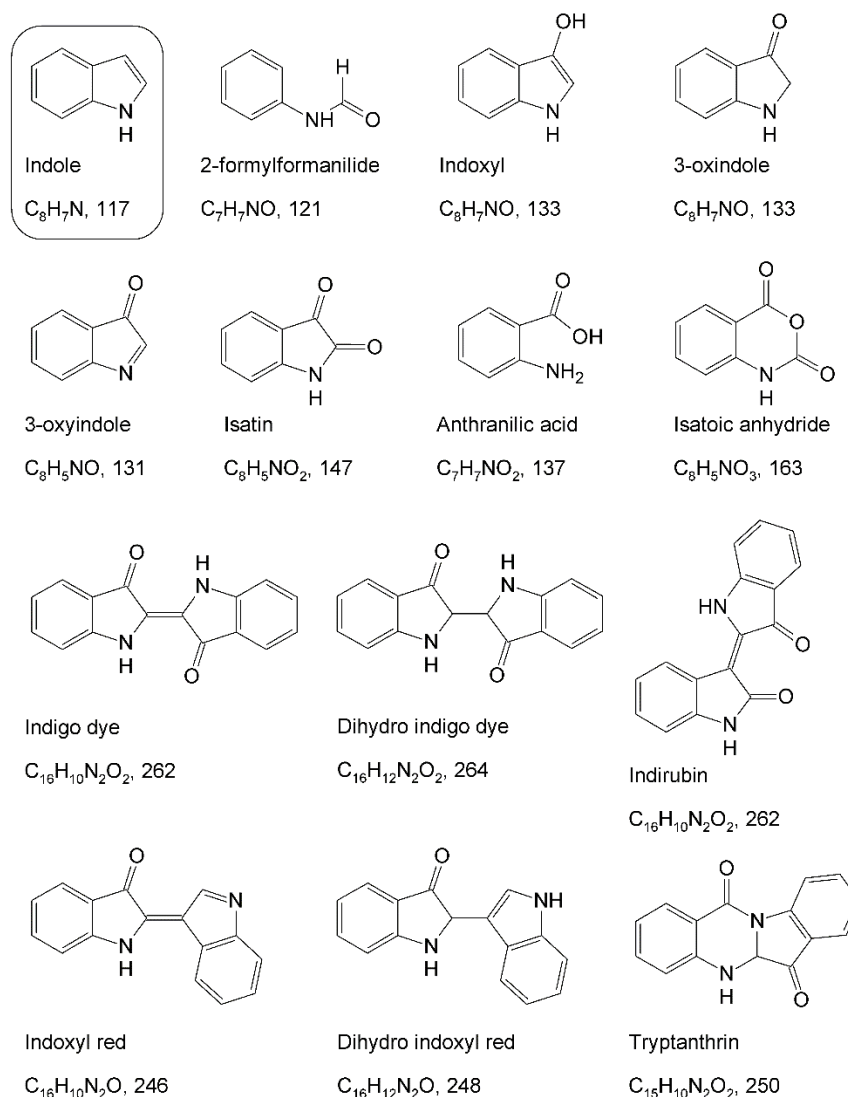


Figure 3.1. Chemical structures, common names, molecular formulas, and nominal molecular weights for indole and its oxidized derivatives discussed in this work.

Studies of maize plants under stress revealed that indole acts as an aerial priming agent, released before terpenoids (Erb et al., 2015; Schmelz et al., 2003). For example, Schmelz et al. (2003) examined insect induced volatile emissions in *Zea Mays* seedlings and demonstrated direct positive relationships between jasmonic acid levels and both sesquiterpene and indole volatile emissions. Additionally, they showed that indole can reach maximal emission levels during nocturnal herbivory and concluded that indole could

function as an early morning signal for parasitoids and predators searching for insect hosts and prey. Niinemets et al. (2013) found evidence that quantitative relationships exist between the severity of biotic stress and induced volatile emissions, in addition to the previously demonstrated dose-response relationships for abiotic stresses. Erb et al. (2015) showed that herbivore induced indole emissions in maize plants precede the release of mono-, homo-, and sesquiterpenes, supporting the conclusion that indole is involved in the airborne priming of terpenoids. Different plant stress mechanisms typically elicit release of the same ubiquitous stress volatile, such as indole, and more stress-specific mono- and sesquiterpene blends (Erb et al., 2015; Gentner et al., 2014; Niinemets et al., 2013; Schmelz et al., 2003).

Emissions of indole have also been well correlated with monoterpene emissions during flowering events (Gentner et al., 2014). In the San Joaquin Valley, an agricultural region in California, indole was measured at 4.72-17.74 $\mu\text{g m}^{-3}$, which was comparable to or greater than β -myrcene concentrations, the dominant monoterpene in this study (Gentner et al., 2014). The authors stressed the need for future laboratory and modeling studies on the SOA formation potential of indole and other novel compounds identified in their study. A later study by Misztal et al. (2015) used a combination of laboratory experiments, ambient measurements, and emissions modeling to show that plants emit a wide variety of benzenoid compounds (including indole) to the atmosphere at substantial rates, and that current VOC inventories underestimate biogenic benzenoid emissions. They concluded that emissions of benzenoids from plants are likely to increase in the future due to changes in the global environment and stressed that atmospheric chemistry models should account for this potentially important precursor of SOA.

An additional source of indole is the microbial processing of L-tryptophan in the intestine or feces of livestock animals (Le et al., 2005). In concentrated animal feeding operations (CAFOs), indole is primarily emitted from animal waste (Yuan et al., 2017) and can contribute significantly to the malodors in cattle feedyards and swine facilities (Feilberg et al., 2010; Wright et al., 2005). Indole has been measured in cattle facilities or during the land application of cattle manure, with emission rates of 0.002 – 9.41 $\mu\text{g m}^{-2} \text{min}^{-1}$ (Parker, 2008; Woodbury et al., 2015; Cai et al., 2015) and concentrations of 2.4 – 32.6 $\mu\text{g m}^{-3}$ (0.5 - 6.8 ppb; Parker, 2008). The range of emission rates and concentrations of indole detected in swine facilities or during the land application of swine slurry were 0.13-2.67 $\mu\text{g m}^{-2} \text{min}^{-1}$ (Le et al., 2005; Cai et al., 2015; Parker et al., 2013; Bongiorno et al., 2004) and 0.07-500 $\mu\text{g m}^{-3}$ (0.01 - 100 ppb; Hobbs et al., 1997; Zahn et al., 2001; Jo et al., 2015; Osaka et al., 2018), respectively. Emissions of indole from animal husbandry were not included in this study but should be considered when modeling areas with active animal husbandry facilities.

Despite the importance of indole in the atmospheric environment, few studies exist on the mechanism of its photooxidation. Gas-phase oxidation of indole by OH, O₃, and NO₃ was previously studied by Atkinson et al. (1995). They found that indole reacts with OH and NO₃ at collision-limited rates, with rate constants of $1.5 \times 10^{-10} \text{ cm}^3 \text{ molec}^{-1} \text{ s}^{-1}$ and $1.3 \times 10^{-10} \text{ cm}^3 \text{ molec}^{-1} \text{ s}^{-1}$, respectively. The rate for the reaction of indole with O₃ (rate constant of $5 \times 10^{-17} \text{ cm}^3 \text{ molec}^{-1} \text{ s}^{-1}$) and the rate of direct photolysis were found to be too low to compete with the OH and NO₃ reactions. Atkinson et al. (1995) observed 2-formylformanilide (Fig. 3.1) as the major primary product of oxidation of indole by both O₃ and OH. Oxidation of indole was also studied by Iddon et al. (1971) in γ -irradiated aqueous solutions, where oxidation by OH was the dominant reaction mechanism. The reaction produced 3-oxoindole, indoxyl red,

indirubin, indigo dye, and eventually resulted in a trimer of 3-oxoindole and two indole molecules as the major products.

Previously, the formation of SOA from indole has not been investigated. One of the motivations for investigating indole SOA is that it may possess unusual optical properties. Many of the indole-derived products are brightly colored and have distinctive absorption bands in visible spectrum. If these products are formed during atmospheric oxidation of indole and partition into aerosol particles, they could contribute to the pool of organic light-absorbing species. Such organic compounds that absorb radiation strongly in the near-UV and visible spectral ranges are collectively known as “brown carbon” in the atmospheric literature (Andreae and Gelencser, 2006; Laskin et al., 2015). Examples include secondary aerosols generated by photooxidation of polycyclic aromatic compounds and primary aerosols produced by biomass burning. The chemical composition of the aerosol depends on the source. For example, nitroaromatic compounds are known to be major chromophores in biomass burning aerosols produced by flaming combustion, while humic-like substances are emitted from smoldering fires. It is important to characterize known sources of light-absorbing aerosols and to account for missing sources in order to better predict the effect of aerosols on global temperatures.

This chapter describes a series of experiments and model simulations on the formation of SOA via the oxidation of indole by OH, O₃, and NO₃. The molecular composition of indole SOA and the effect of relative humidity on its optical properties were explored using smog-chamber and flow reactor experiments. These results were incorporated into an airshed model with detailed SOA chemistry to estimate the effect of indole on the total SOA and on the light-absorbing components of SOA. The model predicted that indole can measurably

contribute to SOA loading even in urban environments, where anthropogenic emissions dominate over biogenic ones, such as the South Coast Air Basin of California (SoCAB). Furthermore, we showed that indole SOA contains unique strongly-absorbing compounds and can contribute to decreased visibility, especially under plant-stressed conditions or during flowering events.

3.2 Experimental Methods

3.2.1 Smog Chamber Experiments

SOA was generated in a 5 m³ Teflon chamber at different levels of relative humidity (RH <2, 25, 50%; measured by a Vaisala HMT333 probe). No inorganic seed aerosol was used to avoid interference with off-line mass-spectrometric analysis of SOA. Indole (99% purity, Sigma-Aldrich) was dissolved in methanol (LC-MS grade, 99.9% purity, Honeywell) and was evaporated into the chamber to obtain an initial mixing ratio of 200 parts per billion by volume (ppbv), which is equivalent to 960 µg m⁻³. While 200 ppb of indole was used in most experiments to collect sufficient mass for analysis, several experiments were done at lower mixing ratios (50 ppbv and 100 ppbv) to test the dependence of indole SOA optical properties on the starting indole mixing ratios. The injector and inlet lines were heated to 70°C to minimize losses of indole on the injector surfaces. At room temperature, the reported vapor pressure of indole is 0.012 mmHg (Das et al., 1993), which is equivalent to ~ 16 parts per million by volume (ppmv). Therefore, most of the injected indole should have remained in the gas phase although some of it could remain adsorbed to the injection line and chamber wall surfaces, contributing to the variability in the SOA yield (the concentration of indole in the chamber was observed to decline even without reaction, consistent with first order loss

on the chamber walls, Figure 3.2). In the ozonolysis experiments, O₃ was introduced to achieve a mixing ratio of 1 ppmv. In the nitrate radical experiments, NO₃ was generated in the chamber by introducing O₃ and NO in a small excess of the 2:1 ratio (500 ppbv O₃ and 200 NO ppbv). In the photooxidation experiments, hydrogen peroxide was introduced into the chamber by evaporation of a 30 wt% solution of H₂O₂ in water (Fisher Scientific) into a flow of clean air to achieve an initial mixing ratio of 2 ppmv. UV-B lamps were turned on to initiate the photooxidation, which led to an [OH] of $\sim 1.4 \times 10^6$ molec cm⁻³ (see below). The content of the chamber was mixed with a fan for 10 min following the injection. In some of the photooxidation experiments, complete mixing was achieved only after the lamps were turned on as evidenced by the measured indole concentrations continuing to increase in the initial photooxidation period. Although mixing was not fast, it was faster than the timescale of the reaction, so it should not have affected the SOA mass yield calculations.

The OH concentration was estimated from the rate of loss of indole (measured using the ¹³C isotopic ion of protonated indole observed at *m/z* 119 a proton-transfer-reaction time-of-flight mass spectrometer) shown in Figure 3.2. The slope translates into [OH] $\sim 1.4 \times 10^6$ molec cm⁻³. The shaded region denotes the time when the chamber lamps were on.

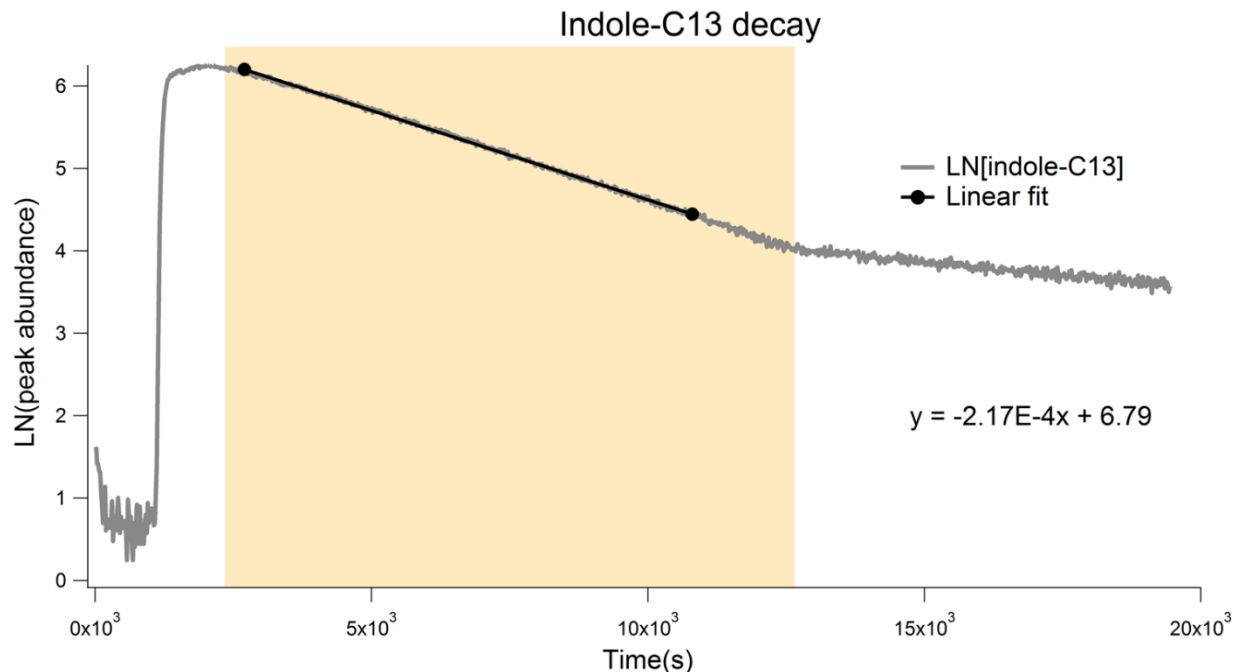


Figure 3.2: Decay of the ^{13}C isotopic ion of protonated indole as a function of time used to estimate the OH concentration in the chamber. Data range used for fit was from 45-180 minutes.

Throughout the experiment, size and number concentration of particles were monitored with a scanning mobility particle sizer (SMPS; TSI 3936) equipped with a condensation particle counter (CPC; TSI 3775). A proton-transfer-reaction time-of-flight mass spectrometer (PTR-ToF-MS; Ionicon model 8000) monitored the decay of indole, as well as the formation of volatile photooxidation products. The PTR-ToF-MS had a resolving power of $m/\Delta m \sim 5 \times 10^3$ and was operated with the following settings: drift tube temperature of 60 °C, drift tube voltage of 600 V, field strength of ~ 135 Td, and inlet flow of 0.2 SLM. The chemical composition of the SOA particles was probed with a Time-of-Flight Aerosol Mass Spectrometer (ToF-AMS) operated in both the V-mode (provides higher signal, but lower resolution) and W-mode (provides less signal, but higher resolution) ion flight paths. The ToF-AMS data were analyzed using SQUIRREL 1.62A software with PIKA 1.22A. When the SOA particles reached a peak concentration in the chamber, the polydispersed particles were

collected on one Teflon filter (47 mm diameter, Millipore FGLP04700) at 20 L min⁻¹ for 2-3 hours. One filter was collected per each chamber run; therefore, each replicate sample was collected from a separate experiment run under the same conditions. The amount of the collected SOA material on each filter was estimated from SMPS data assuming 100% collection efficiency by the filters and SOA density of 1.4 g cm⁻³. The density of indole SOA is unknown, but the adopted value of 1.4 g cm⁻³ is similar to the reported range of densities of 1.47–1.55 g cm⁻³ for SOA prepared from another bicyclic aromatic compound, naphthalene (Chan et al., 2009; Chen et al., 2016). In addition, densities of known indole oxidation products, for example isatin (1.47 g cm⁻³), anthranilic acid (1.40 g cm⁻³), indigo dye (1.20 g cm⁻³), isatoic anhydride (1.52 g cm⁻³), and 3-oxindole (1.20 g cm⁻³), range from 1.2 to 1.5 g cm⁻³, suggesting that 1.4 g cm⁻³ should be a reasonable guess for indole SOA. For comparison, the mass of collected SOA material on each filter was also determined by weighing using a microbalance (Sartorius ME5F, +/- 0.001 mg). When comparing the SOA mass calculated from SMPS to the weighed mass, the weighed mass was often higher, as can be seen in Figure 3.3. Possible reasons for this discrepancy in mass include that the SMPS does not work well at high concentrations, SMPS was not recently calibrated, and/or incorrect particle density assumed. Unfortunately, the experiments of indole photooxidation carried out at low RH and used in the SOA yield calculations were done early in the study and relied solely on SMPS estimations for the collected mass. In all other experiments, the mass was determined by weighing rather than SMPS measurements.

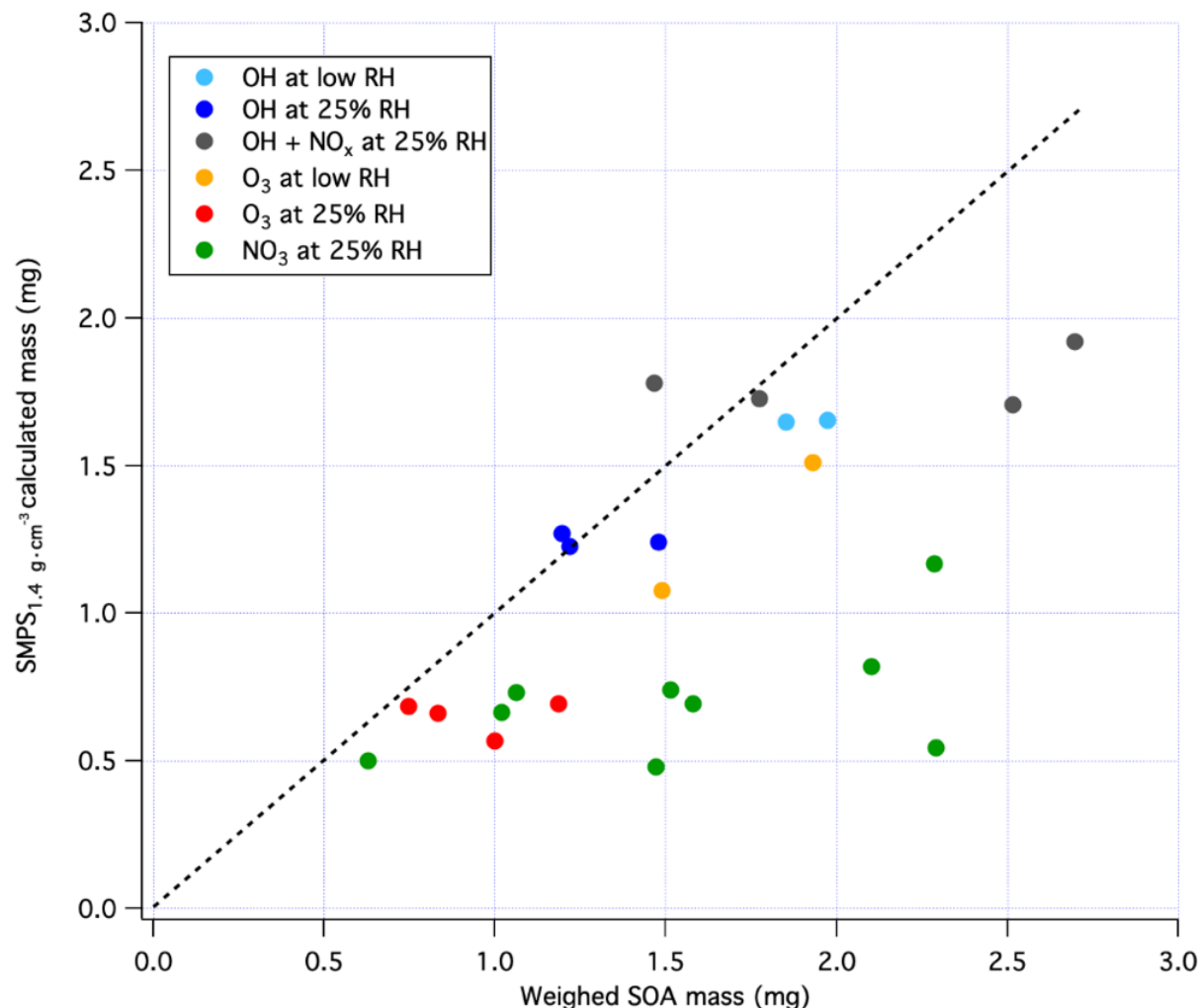


Figure 3.3. Plot comparing the mass of SOA material collected as determined from SMPS calculations (y-axis) and weighing (x-axis). The dashed line has a slope of 1, which denotes agreement between the two measurements.

The SOA yield in the early indole+OH SOA experiments was calculated from Eq. (3.1).

$$Yield = \frac{\Delta SOA}{\Delta VOC} \quad (3.1)$$

The increase in the mass concentration of particles, ΔSOA , was obtained from SMPS measurements (since we began weighing in later experiments) and corrected for the particle wall loss. The change in the mass concentration of indole, ΔVOC , was equated to the initial indole concentration because PTR-ToF-MS measurements suggested complete removal of

indole during the photooxidation. The wall loss correction was done by assuming a first-order particle size independent loss of particle mass concentration (PM)

$$\frac{dPM}{dt} = \text{Source}(t) - \text{Loss}(t) = \text{Source}(t) - k_w \times PM \quad (3.2)$$

where the $\text{Source}(t)$ and $\text{Loss}(t)$ are time dependent production and removal rates for the particles. The effective first-order rate constant $k_w = 0.00090 \text{ min}^{-1}$ was determined in a separate experiment in which indole SOA was produced, the lamps were turned off, and mass concentration of SOA was followed with the SMPS for 10 hours without collecting SOA on filters. In the experiment used to calculate k_w , the RH in the chamber was low. At higher RHs, greater wall loss would be expected (Huang et al., 2018). Using the known k_w , we could determine $\text{Source}(t)$ from the actual measured PM concentration in every experiment.

$$\text{Source}(t) = \frac{dPM}{dt} + k_w \times PM \quad (3.3)$$

The corrected PM concentration (i.e. the hypothetical PM concentration that would be achieved if the wall loss was absent) was calculated from:

$$PM_{corrected}(t) = PM(t = 0) + \int_0^t \text{Source}(t)dt \quad (3.4)$$

The integration of data was carried out numerically in Excel.

After collecting SOA on a filter, the color of the filter depended on the oxidant and amount of SOA collected, and could be brown, yellow-green, or even black in appearance. Examples of filter photographs are given in Fig. 3.4.

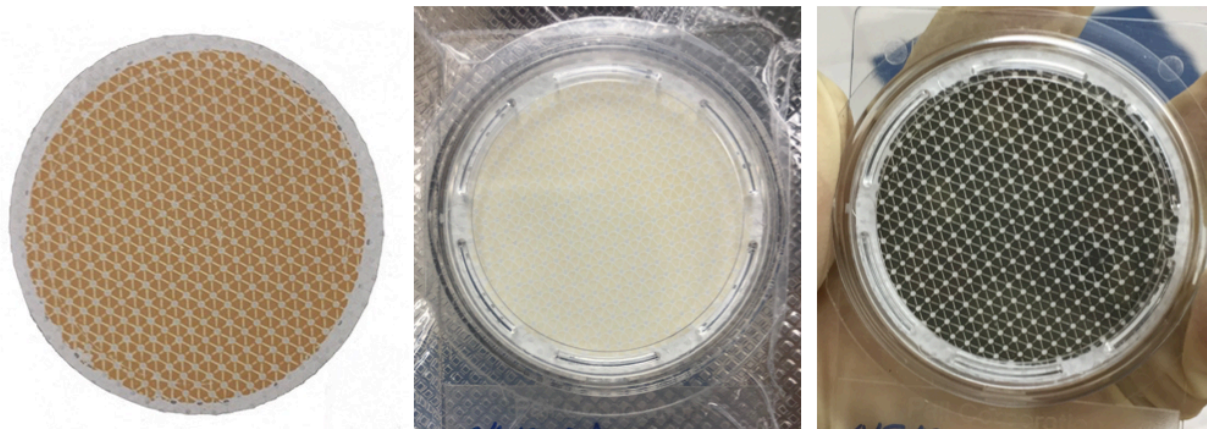


Figure 3.4. Filters containing indole+OH SOA (left), indole+O₃ SOA (middle), and indole+NO₃ SOA (right) particles.

One half of the filter sample was extracted in methanol (LC-MS grade, 99.9% purity, Honeywell) and shaken vigorously on a shaker for five minutes. The filter color changed from the initial brown or yellow-green to white suggesting most of the light-absorbing compounds were extracted. More quantitative extraction efficiency tests, in which the same filter was extracted multiple times, suggested that the initial extraction removed >95% of the filter material (see Fig. 3.5). The SOA methanol extract was analyzed by UV-Vis spectrophotometry in a dual beam spectrophotometer (Shimadzu UV-2450), with pure methanol used as reference.

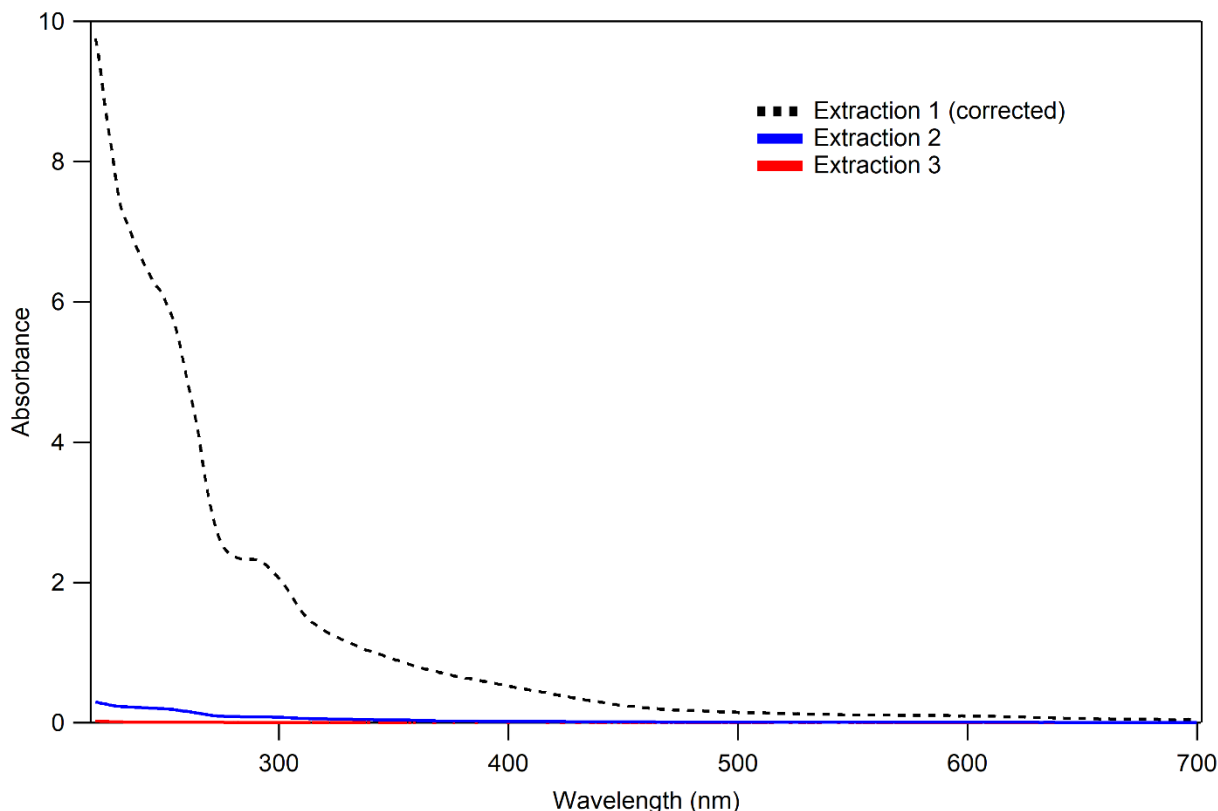


Figure 3.5. UV-Vis absorption spectra for sample of indole + O₃ SOA at 25% RH extracted multiple times. The solution obtained from the first extraction saturated the detector. Therefore, the solution was diluted by a factor of 10, and the absorption values were multiplied by 10 to generate the effective absorbance shown as the dotted trace. Across the UV-Vis spectrum, the absorbance of extraction 1 was 20-30 times higher than that of extraction 2, suggesting that the first extraction extracted >95% of the soluble material.

The wavelength-dependent mass absorption coefficient (MAC) was calculated for indole SOA from the base-10 absorbance, A_{10} , of an SOA extract, the path length, b (cm), and the solution mass concentration, C_{mass} (g cm⁻³):

$$MAC(\lambda) = \frac{A_{10}^{solution}(\lambda) \times \ln(10)}{b \times C_{mass}} \quad (3.5)$$

The main uncertainty in the calculated MAC values comes from the uncertainty of the mass concentration, which arises from uncertainties in the SMPS measurement of aerosol mass

concentration (Fig. 3.3), filter collection efficiency, and solvent extraction efficiency. We estimate that MAC values should be accurate within a factor of 2 (Romonosky et al., 2015a). The imaginary part of the refractive index, k , which describes the absorptive properties the particle material was calculated from MAC values using equation 3.6. As discussed earlier, the indole SOA density, ρ , was assumed to be 1.4 g cm^{-3} .

$$k(\lambda) = \frac{MAC(\lambda) \times \rho \times \lambda}{4\pi} \quad (3.6)$$

The second half of the filter was used for direct analysis in real-time mass spectrometry (DART-MS) measurements. The filter half was extracted in the same way with acetonitrile (LC-MS grade, 99.9 % purity, Honeywell). Assuming a complete extraction of the SOA material, the mass concentration of $0.03\text{--}0.22 \text{ mg mL}^{-1}$ was much lower than the solubility of 19 mg mL^{-1} reported for isatin in acetonitrile (Liu et al., 2014). (We elected to use different solvents for UV-vis and DART-MS because methanol afforded measurements deeper in the UV region and acetonitrile gave cleaner background spectra in DART-MS.) Aliquots from the acetonitrile SOA extracts were transferred onto a clean stainless- steel mesh, dried in air, and manually inserted between the DART ion source and mass spectrometer inlet. The DART-MS consisted of a Xevo TQS quadrupole mass spectrometer (Waters) equipped with a commercial DART ion source (Ion-Sense, DART SVP with Vapur® Interface). It was operated with the following settings: 350 V grid electron voltage, 3.1 L min^{-1} He gas flow, 350°C He gas temperature, and 70°C source temperature. The samples were analyzed with DART-MS in both positive and negative ion modes. Background spectra from the pure solvent were also collected and subtracted from the DART mass spectra.

Additional sample filters were analyzed via nanospray desorption electrospray ionization high-resolution mass spectrometry (nano-DESI-HRMS) and high-performance liquid chromatography, coupled to photodiode array spectrophotometry and high-resolution mass spectrometry (HPLC-PDA-HRMS). The former method provides a spectrum of the entire mixture without prior separation; it is useful for providing an overview of the types of compounds present in SOA. The latter method is suited for advanced detection of individual light-absorbing components in SOA (Lin et al., 2015a, b; Lin et al., 2016). Both methods employ an LTQ-Orbitrap mass spectrometer (Thermo Corp.) with a resolving power of 10^5 at m/z 400, sufficient for unambiguous characterization of SOA constituents.

For the HPLC-PDA-HRMS measurements, one-quarter of the filter was extracted using 350 μ L acetonitrile (CH_3CN , gradient grade, $\geq 99.9\%$ purity) and the change in filter color from colored to white suggested that most light-absorbing compounds were extracted into the solution. Separation of the SOA extract was achieved with a Scherzo SM-C18 column (Imtakt USA). The gradient elution protocol included a 3 min hold at 10 % of CH_3CN , a 45 min linear gradient to 90 % CH_3CN , a 16 min hold at this level, a 1 min return to 10 % CH_3CN , and another hold until the total scan time of 90 min. The column was maintained at 25°C and the sample injection volume was 8 μ L. The UV-vis spectrum was measured using the PDA detector over the wavelength range of 250 to 700 nm. The ESI settings were positive ionization mode, +4.5 kV spray potential, 35 units of sheath gas flow, 10 units of auxiliary gas flow, and 8 units of sweep gas flow.

The HRMS data analysis was performed by methods summarized by Romonosky et al. (2015b). Briefly, the mass spectra were clustered together, the m/z axis was calibrated internally with respect to expected products of photooxidation, and the peaks were assigned

to formulas $C_cH_hO_oN_nNa^{+0-1}$ or $C_cH_hO_oN_n^-$ constrained by valence rules and typical elemental ratios (c, h, o, n refer to the number of corresponding atoms in the ion). These were then converted to formulas of the corresponding neutral species, obtained by removing Na or H from the observed positive ion formulas or adding H to the negative ion formulas. The HPLC-PDA-HRMS analysis was done as described in Lin et al. (2015b, 2016).

3.2.2 Oxidation Flow Reactor Experiments

Oxidation flow reactor experiments were conducted by Professor Yinon Rudich and Dr. Qunafu He in order to obtain more information regarding the optical properties of indole SOA particles. SOA was generated in three different oxidation flow tube reactors (OFRs) without seed aerosol to simulate indole oxidation initiated by OH radical, O_3 , and NO_3 radical. These experiments were done by our collaborators in the Weizmann Institute of Science. Pure indole (99% purity, Sigma-Aldrich) was placed in a bubbler and was introduced into the OFRs by a gentle N_2 flow to obtain an initial mixing ratio of 200 ppbv. SOA generation through OH oxidation of indole was done in a potential aerosol mass (PAM) OFR. A total flow of 4.2 L min^{-1} of N_2 and 0.3 L min^{-1} O_2 at RH of 36–38% was used in the PAM with a corresponding residence time of 184 s. The OH concentration was varied by changing the UV light intensity. To simulate SOA formation in the presence of NO_x , 1%, 2%, and 4% N_2O were added to the PAM chamber as NO_x source (Lambe et al., 2017), with corresponding NO_x concentration of 133, 669, and 2425 ppbv (Model T200, Teledyne, USA). The OH exposures were regulated to $\sim 4.2 \times 10^{11} \text{ molecules cm}^{-3} \text{ s}$ which were determined by measuring the decay of the SO_2 (Model 49i, Thermo Fisher Scientific, USA). Due to the limitation of the lamp power, the OH exposures were controlled to $\sim 3.1 \times 10^{11} \text{ molecules cm}^{-3} \text{ s}$ for experiments conducted with 4.0% N_2O . SOA generation from ozonolysis of indole under dry conditions

was performed in a glass OFR (20 L in volume) with an initial O₃ concentration of 20 ppm. High O₃ concentration was used due to the short residence time of the glass reactor (~20 minutes at the total flow of 1.0 L min⁻¹). To simulate NO₃ oxidation of indole, N₂O₅ synthesized from NO₂ reaction with ozone was used as the source of NO₃ radical. NO₃ radical was produced by thermal decomposition of N₂O₅ which was carried out by pure nitrogen from a N₂O₅ crystal cold trap. SOA production was achieved in a glass OFR (OFR, L:70 cm, ID: 7 cm) where we mixed the N₂O₅ (~ 1 ppm) and other gases. Particles were produced by homogeneous nucleation and condensation following NO₃ oxidation. The relative humidity in the OFR was set to <5%, 25%, 51%, and 76% to examine how the RH affects the aerosol optical properties. For all of the experiments, particle size distribution was monitored by the SMPS and an HR-ToF-AMS operated alternatively in V mode and W mode was employed to probe the chemical composition of the generated aerosols.

Assuming that the SOA particles are spherical and non-porous, the particle effective density was calculated by comparing the aerodynamic diameter (obtained from the aerosol aerodynamic classifier, AAC) and the mobility diameter (measured by SMPS). The particle effective density ($\rho_{\text{eff}} = \frac{d_{\text{Aero}}}{d_{\text{m}}} \rho_0$), which is the aerodynamic diameter (d_{Aero}) divided by the mobility diameter (d_{m}) was obtained from optical measurements. The average of the measured effective densities (1.21 g/cm³; see Table 3.1) was used as an independent approach (from the method described in section 3.2.1) to calculate k .

Table 3.1. Particle effective density measured by AAC and SMPS. The standard deviation (STD) corresponds to one sigma.

Oxidation type	RH	N ₂ O	Effective Density g/cm ³	STD g/cm ³
OH oxidation	38.2	0	1.33	0.02
	37.1	1%	1.15	0.01
	37.6	2%	1.17	0.01
	37.6	4%	1.31	0.01
NO ₃ oxidation	<5%	0%	1.29	0.01
	21%	0%	1.13	0.05
	51%	0%	1.24	0.03
	76%	0%	1.18	0.06
O ₃ oxidation	<5%	0%	1.05	0.03

The complex refractive index of the aerosols can be retrieved by measuring the extinction cross section of several different sizes of particles and followed by fitting a theoretical Mie curve to the measured extinction cross sections at each specific wavelength (Riziq et al., 2007; Lang-Yona et al., 2009; Washenfelder et al., 2013). To measure the optical cross section of the size-selected particles, aerosol from the OFR was sampled, passed through a VOCs denuder and a drier, size selected with an AAC, and directed into the broadband cavity-enhanced spectrometer (BBCES) system (two broadband channels which span the 360–390 and 385–425 nm spectral regions) while counted by the CPC. Notably, another BBCES system which spans the wavelength range of 315–345 and 380–700 nm was employed for measuring light extinction of particle from O₃ oxidation of indole.

3.3 Modeling Methods

Air quality simulations were performed by Professor Donald Dabdub and Dr. Jeremy Horne to complement laboratory experiments and to assess the formation of indole SOA from photooxidation in a coastal urban area. The University of California, Irvine, and California Institute of Technology (UCI-CIT) regional airshed model with a state-of-the-art chemical

mechanism and aerosol modules was used in this study. The model domain utilized 4970 computational cells (five vertical layers with 994 cells per layer) with a 5 km × 5 km horizontal grid size and encompassed the SoCAB, including the Pacific Ocean on the western side, heavily populated urban areas around Los Angeles, and locations with a high density of plant life such as the Angeles National Forest on the eastern side. The model included spatially and temporally resolved emissions and typical meteorological conditions for this region. The emission inventory used in this study was based on the 2012 Air Quality Management Plan (AQMP) provided by the South Coast Air Quality Management District (SCAQMD, 2013). Boundary and initial conditions were based on historical values. Simulations were performed for a 3-day summer episode. Two days of model spin-up time were used to reduce the influence of initial conditions and allow sufficient time for newly added emissions to drive changes in air quality. Results shown below are for the third day of the simulations.

The UCI-CIT model utilizes an expanded version of the Caltech atmospheric chemical mechanism (CACM; Dawson et al., 2016; Griffin et al., 2002a, b, 2005) and has been used in numerous other studies to simulate air quality in the SoCAB (Carreras-Sospedra et al., 2006; Carreras-Sospedra et al., 2010; Chang et al., 2010; Nguyen and Dabdub, 2002). The CACM includes a comprehensive treatment of SOA known as the Model to Predict the Multiphase Partitioning of Organics (MPMPO) (Griffin et al., 2003, 2005). MPMPO is a fully coupled aqueous-organic equilibrium-partitioning-based model and is used to calculate gas-particle conversion of secondary organic species. The SIMPOL.1 group-contribution method of Pankow and Asher (2008) was used to calculate vapor pressures of SOA species for use in MPMPO. Activity in both the aqueous and organic phases was determined using the UNIFAC

model of Hansen et al. (1991). Henry's law constants were calculated according to the group contribution method of Suzuki et al. (1992). Several studies have used the UCI-CIT model to investigate SOA formation, dynamics, reactivity, and partitioning phase preference in the SoCAB (Carreras-Sospedra et al., 2005; Chang et al., 2010; Cohan et al., 2013; Dawson et al., 2016; Griffin et al., 2002b; Vutukuru et al., 2006). For a more detailed description of recent model developments incorporated into the UCI-CIT model and its SOA modules, the reader is referred to Dawson et al. (2016).

For the present study, the chemical mechanism was modified from the base case version to include species and processes shown in Fig. 3.6. Two new gas-phase species were added: indole and one representative oxidation product, indigo dye. Because of the high mass yield of indole SOA, with most of the products ending up in the particle phase, any reasonable indole oxidation product with a low vapor pressure would be suitable. We elected to use indigo dye ($C_{16}H_{10}O_2N_2$) because it is a very common derivative of indole and because its formula was reasonably close to the average formula of SOA compounds determined from nano-DESI ($C_{15}H_{11}O_3N_2$). One new gas-phase reaction was added, which forms gas-phase indigo dye via oxidation of gas-phase indole by hydroxyl radical. Lastly, indigo dye was also added to the model as a new SOA species. Gas-phase indigo dye was assumed to partition into the aerosol phase based on its calculated vapor pressure and Henry's law constant. We did not experimentally determine the viscosity of indole SOA, therefore this partitioning does not take into account indole SOA viscosity. After the modifications described here, the model contained a total of 202 gas-phase species, 607 gas-phase reactions, and 18 SOA species. Each SOA species was sorted into eight distinct size bins based on particle diameter, up to a maximum of 10 μm . The activity coefficient of indigo dye was assumed to be 1.

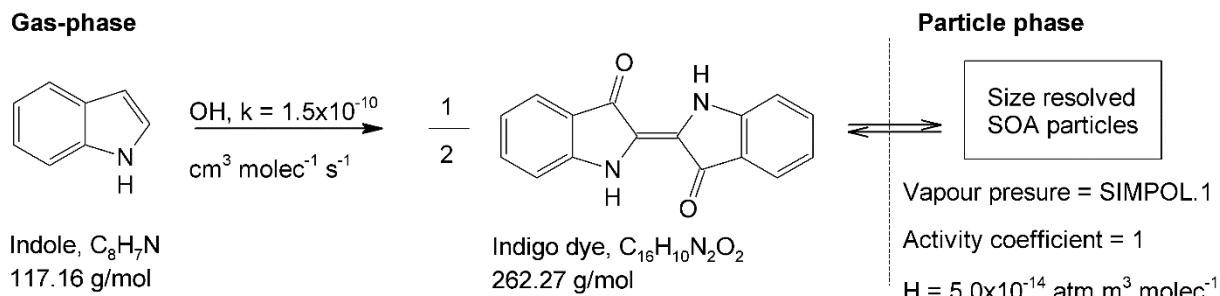


Figure 3.6. Summary of modifications made to the UCI-CIT model chemical mechanism and aerosol modules. In the simulation that included oxidation by NO₃ an additional similar reaction was added with the indole + NO₃ rate constant of 1.3×10^{-10} cm³ molec⁻¹ s⁻¹.

Because gas-phase indole was not included in the base case emissions inventory, its emission rate was estimated based on available literature data. As discussed in the introduction section, emissions of indole have been shown to be well correlated to emissions of monoterpenes in a variety of plant species (Erb et al., 2015; Gentner et al., 2014; Niinemets et al., 2013). However, most existing data were obtained from controlled laboratory experiments and emissions of indole at the regional scale are not well constrained. In this work, emissions of gas-phase indole were added to the base case emissions inventory by using a ratio to “BIOL”, an existing gas-phase species in the emission inventory. BIOL is representative of lumped biogenic monoterpenes and contains spatially and temporally resolved emissions in the base case inventory. Therefore, the spatiotemporal distribution of indole emissions follows that of BIOL, with the magnitude of the emissions set to a given percentage of BIOL emissions. Please note that no emissions of indole derived from agriculture and animal husbandry activities were added in the model. In addition, no direct emissions of gas-phase indigo dye were added to the model. Because of the uncertainty and episodic nature of gas-phase indole emissions, simulations were performed with a range of

possible emission factors to determine the sensitivity of indole SOA formation to gas-phase indole emissions.

Five scenarios were considered for model calculations. The first scenario had zero emissions of gas-phase indole. This scenario will be referred to as the “base case” and serve as the reference scenario to which the other scenarios are compared to determine changes in air quality. The second, third, and fourth scenarios had emissions of gas-phase indole set to 5, 10, and 25 % of BIOL emissions, referred herein as “low”, “medium”, and “high” emissions, respectively. When averaged over the entire simulation domain, the corresponding average emission factors for indole were 0.25, 0.51, and 1.27 $\mu\text{g m}^{-2} \text{h}^{-1}$, respectively. A comparable emission factor of 0.6 $\mu\text{g m}^{-2} \text{h}^{-1}$ for indole was used in a previous study of Misztal et al. (2015), in which indole emissions under average stress conditions were incorporated in the MEGAN 2.1 biogenic VOC emissions model to estimate total global emissions. Therefore, the medium emission scenario considered in this study should be representative of the emissions of indole under average stress conditions, while the high emission scenario is more likely to represent episodic emission events such as those during springtime flowering or herbivore infestation.

The focus of this modeling work was to study the formation of SOA from the photooxidation of indole by OH, in order to complement the experimental data reported in this work. While the SOA formation from oxidation of indole by NO_3 was not experimentally studied prior to the modeling, the reaction of indole with NO_3 is fast and may provide an additional source of indole SOA. The fifth and final scenario explored the potential impact of including an additional oxidation pathway for gas-phase indole via reaction with NO_3 . This scenario corresponds to the high emission scenario with one new gas-phase reaction included in the

model in addition to those described previously. For this new reaction, it is assumed that gas-phase indole reacts with NO_3 to produce indigo dye, the same representative oxidation product assumed for the reaction of gas-phase indole with hydroxyl radical. A rate constant of $1.3 \times 10^{-10} \text{ cm}^3 \text{ molec}^{-1} \text{ s}^{-1}$ was used following Atkinson et al. (1995). No other changes were made to the model or its inputs in this scenario.

3.4 Experimental results

The initial focus of this research was to explore the formation and composition of SOA produced from indole photooxidation, and therefore this SOA system is discussed in more detail throughout this chapter than the other two, i.e., indole produced via O_3 and NO_3 oxidation. Indole oxidation by OH is likely to be the dominant oxidation pathway of indole in the SoCAB during the daytime due to the high rate constant (on the order of $10^{-10} \text{ cm}^3 \text{ molec}^{-1} \text{ s}^{-1}$) of this reaction. These initial experiments resulted in SOA that was highly absorbing in the UV-Vis spectrum, and therefore follow up experiments focused on further exploring the optical properties of indole+OH SOA, indole+ NO_3 SOA, and indole+ O_3 SOA.

3.4.1 Gas-phase oxidation products of indole + OH SOA

The PTR-ToF mass spectrum of indole before photooxidation (Figure 3.7) was dominated by the protonated indole at m/z 118.067 (the m/z values cited in the text correspond to the measured m/z values; the corresponding exact m/z values are listed in Table 3.2). After photooxidation, a few other prominent peaks appeared.

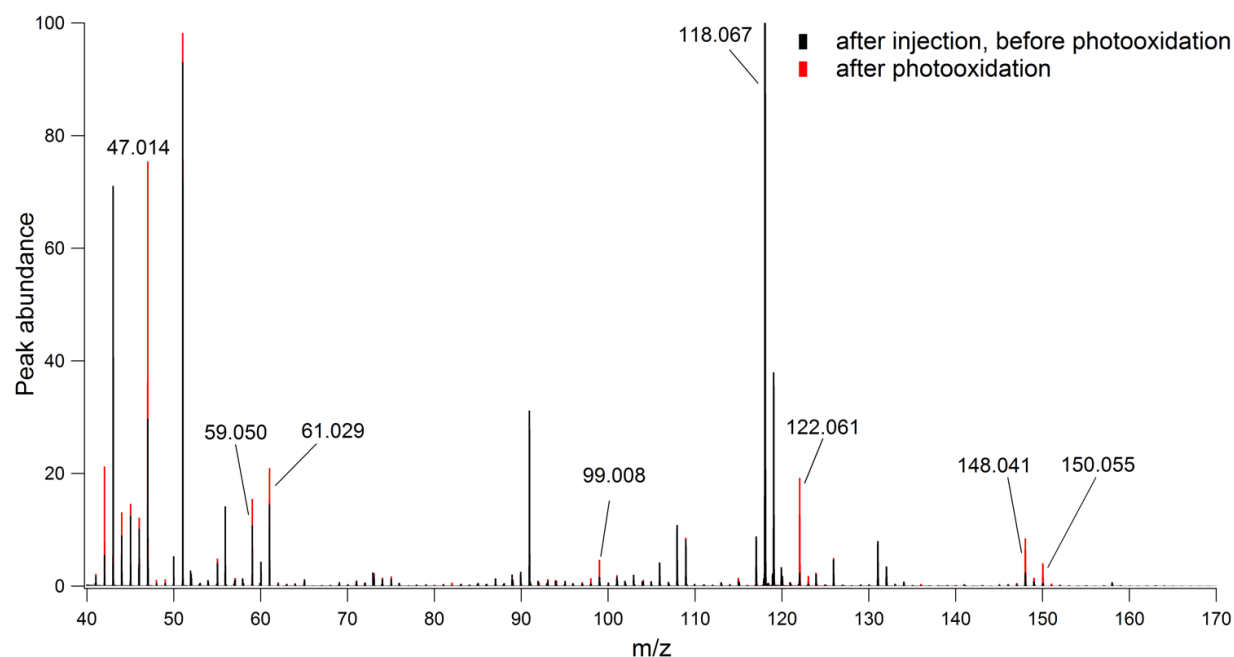


Figure 3.7: Mass spectra of the chamber VOC compounds before and after photooxidation of indole

Figures 3.8 and 3.9 show the time-dependence profiles of several peaks of interest detected by PTR-ToF-MS during the photooxidation of indole, and Table 3.2 contains their proposed assignments. Peaks at m/z 120.072, 131.062, and 132.050 (Figure 3.9) appeared simultaneously with indole injection, suggesting that the indole sample contained small amounts (<2%) of indoline, diazanaphthalene, and 3-oxyindole impurities, respectively, which may have contributed to SOA formation. From the ions that first appeared and then were consumed during photooxidation (Figure 3.8), the one at m/z 122.061 had the largest peak abundance. It corresponds to protonated 2-formylformanilide $[M+H]^+$ ion (Figure 3.1), a major gas-phase product of indole oxidation by OH (Atkinson et al., 1995). Another significant product was detected at m/z 148.041 and was tentatively assigned to the $[M+H]^+$ ion from isatin (Figure 3.1). Isatin also was observed as an abundant peak in both DART(+) and nano-DESI(+) mass spectra, suggesting that it can partition between the gas and particle phases. Smaller peaks produced and then consumed in photooxidation included indoxyl,

benzotrile, and phenylamine. A few peaks at smaller m/z grew during the photooxidation including cyanic acid, acetaldehyde, acetone, and acetic acid.

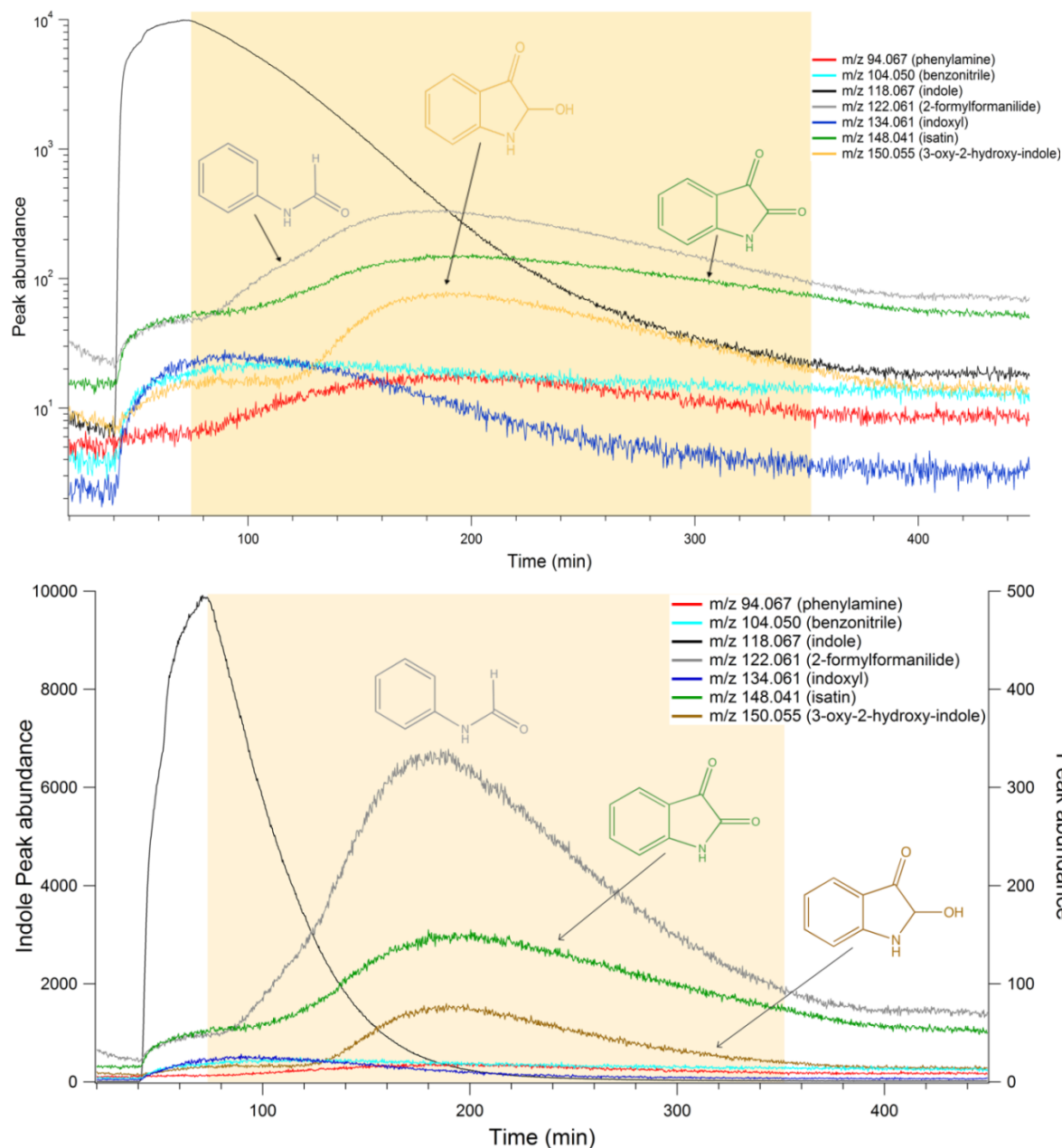


Figure 3.8: Time-dependent signals of ions that were produced and then removed. Shaded region denotes the time when the chamber lamps were on. The top panel shows data on the log scale and the bottom panel shows data on the linear scale.

Segments of the sampling line for PTR-ToF-MS were not heated, and the time dependence the observed in Figs. 3.8 and 3.9 may be complicated by the adsorption equilibria on the

sampling tube surfaces. For example in Fig. 3.8, the unusual time dependence for m/z 150.055 (yellow trace) and m/z 148.041 (green trace) was reproducible, and likely resulted from delayed passage of these compounds through the sampling lines. However, the time dependence makes it possible to sort observed compounds into ones produced by the UV radiation from the chamber lamps, and ones that are less affected (or not affected at all) by the UV radiation. This particular plot shows compounds that clearly went up when the UV lamps were on; their removal at later time is from secondary photooxidation or photolysis.

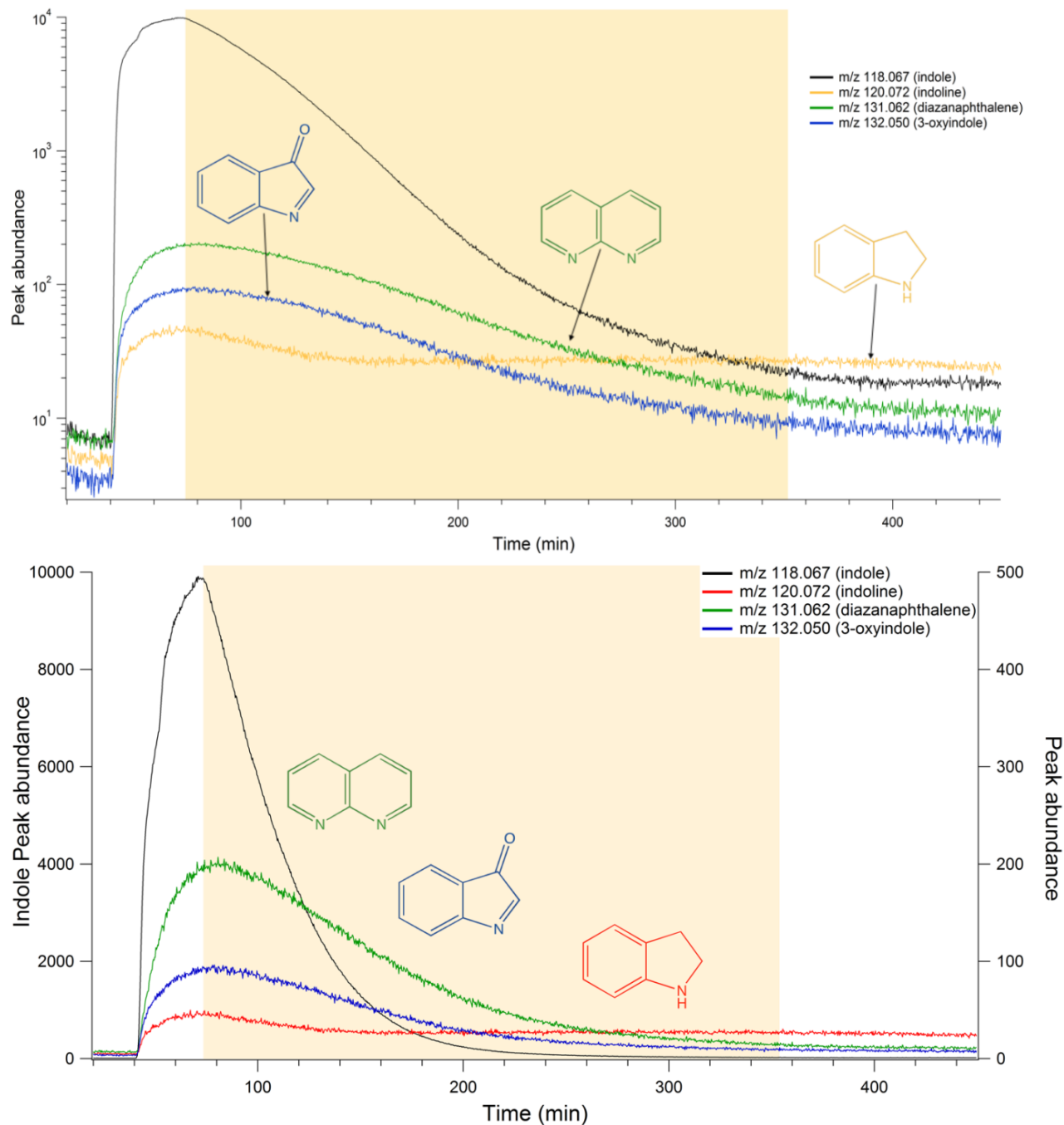


Figure 3.9: Time-dependent signals of ions that were removed during photooxidation. Shaded region denotes the time when the chamber lamps were on. The top panel shows data on the log scale and the bottom panel shows data on the linear scale. Indoline and diazanaphthalene were likely present in the indole sample to begin with, as impurities.

Table 3.2. Summary of assigned PTR-ToF-MS peaks

Calibrated m/z	Exact m/z	Ion Formula	Neutral Formula	Possible Assignment	Behavior
44.014	44.0131	CH ₂ NO ⁺	HOCN	cyanic acid	produced
45.034	45.0335	C ₂ H ₅ O ⁺	C ₂ H ₄ O	acetaldehyde	produced
46.029	46.0287	CH ₄ NO ⁺	CH ₃ NO	nitrosomethane	produced
47.014	47.0128	CH ₃ O ₂ ⁺	HCOOH	formic acid	produced
59.050	59.0491	C ₃ H ₇ O ⁺	C ₃ H ₆ O	acetone	produced
61.029	61.0284	C ₂ H ₅ O ₂ ⁺	C ₂ H ₄ O ₂	acetic acid	produced
90.950	90.9477	FeO ₂ H ₃ ⁺	H ₂ O·FeO	produced in ion source	
94.067	94.0651	C ₆ H ₈ N ⁺	C ₆ H ₇ N	phenylamine (aniline)	produced then removed
98.026	98.0237	C ₄ H ₄ NO ₂ ⁺	C ₄ H ₃ NO ₂	maleimide	produced
99.008	99.0077	C ₄ H ₃ O ₃ ⁺	C ₄ H ₂ O ₃	maleic anhydride	produced
104.050	104.0495	C ₇ H ₆ N ⁺	C ₆ H ₅ CN	benzonitrile	produced then removed
118.067	118.0651	C ₈ H ₈ N ⁺	C ₈ H ₇ N	indole	removed
120.072	120.0808	C ₈ H ₁₀ N ⁺	C ₈ H ₉ N	indoline (impurity)	removed
122.061	122.0600	C ₇ H ₈ NO ⁺	C ₇ H ₇ NO	2-formylformanilide	produced then removed
131.062	131.0604	C ₈ H ₇ N ₂ ⁺	C ₈ N ₆ N ₂	diazanaphthalene (impurity)	removed
132.050	132.0444	C ₈ H ₆ NO ⁺	C ₈ H ₅ NO	3-oxyindole	removed
134.061	134.0600	C ₈ H ₈ NO ⁺	C ₈ H ₇ NO	indoxyl	produced then removed
148.041	148.0393	C ₈ H ₆ NO ₂ ⁺	C ₈ H ₅ NO ₂	isatin	produced then removed
150.055	150.0550	C ₈ H ₈ NO ₂ ⁺	C ₈ H ₇ NO ₂	3-oxy-2-hydroxy-indole	produced then removed

3.4.2 Yield of indole + OH SOA

Figure 3.10 illustrates the time dependence of mass concentrations of indole and particulate matter in a typical chamber experiment. The particles had a geometric mean diameter of approximately 0.3 μm when the filter collection started. The terminal wall-loss corrected mass concentration of particles (Fig. 3.10) was higher than the initial concentration of indole, suggesting that the SOA yield, defined by Eq. (3.1), was high. A high SOA yield suggests that most of the oxidation products of indole end up in the particle phase, indicating that indole is an effective precursor for SOA.

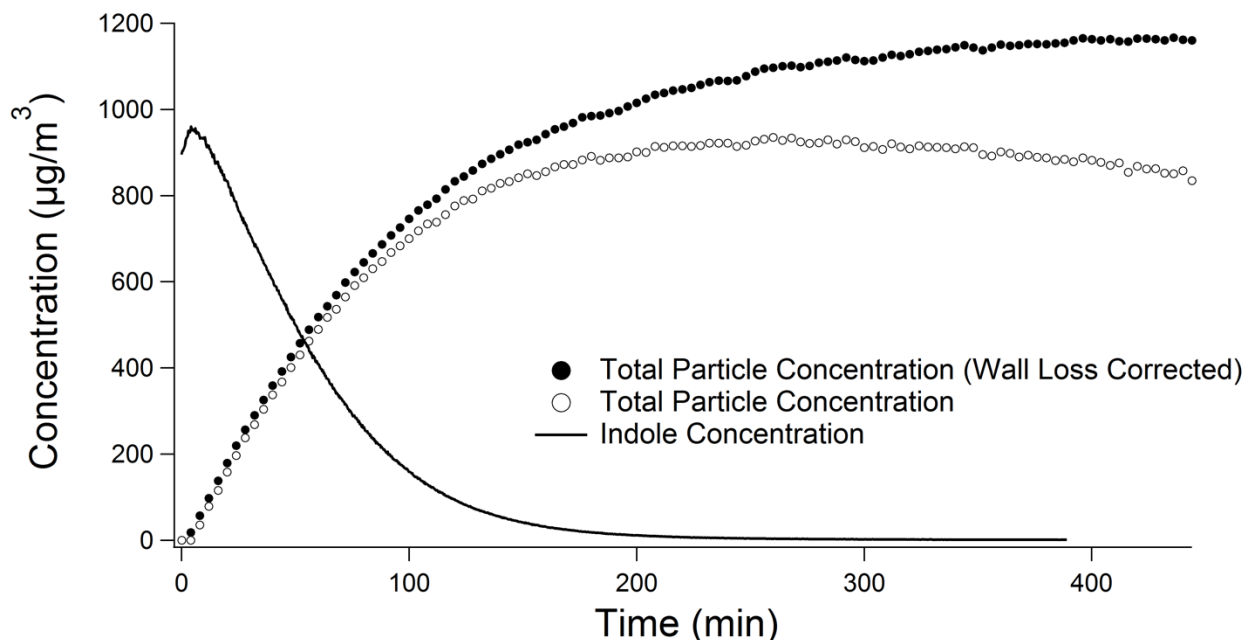


Figure 3.10. The mass concentration of indole (solid trace), the mass concentration of particles (open circles), and the wall loss-loss-corrected mass concentration of particles (solid circles) over time. Indole was not yet fully mixed in the chamber by the time photooxidation started at $t=0$, resulting in an apparent initial rise in the measured indole concentration.

For five experiments repeated under the same conditions on separate days, the SOA yields calculated from Eq. (3.1) were 1.21, 1.10, 0.86, 1.77, and 1.46 with an average of 1.3 ± 0.3 . We normally obtain much more reproducible yields for more volatile precursors, such as monoterpenes; it is not clear why the yield of indole SOA is so variable. Indole oxidation products could be lost to the walls reducing the apparent yield and contributing to its scatter. However, this effect is probably minor given that the apparent yield is quite high. The yield is higher than that for SOA formed from another bicyclic aromatic compound, naphthalene, which has a reported yield range of 0.04-0.73 under low- NO_x conditions (Chan et al., 2009; Chen et al., 2016). The high yield suggests that the major fraction of indole oxidation products ends up in the particle phase at the concentrations used in this work. The yield of 1.3 would require that, on average, at least two oxygen atoms should add to the indole during

oxidation ($C_8H_7N \rightarrow C_8H_7NO_{2.2}$), which is quite reasonable and qualitatively consistent with mass spectrometric observations.

3.4.3 Composition of indole + OH SOA

We used two offline MS methods (DART and nano-DESI) and both negative (-) and positive (+) ion modes to characterize the SOA composition to detect a broader range of compounds than possible with a single method. Figure 3.11 shows the DART and nano-DESI mass spectra of indole SOA in both positive and negative modes. The high resolving power of nano-DESI-HRMS afforded unambiguous formula assignments for all peaks up to m/z 500, and the molecular weights (MWs) of the neutral compounds could be determined from the corresponding ion formulas. About half of the ions observed in nano-DESI (+) mass spectra were $[M+Na]^+$ adducts, and the remaining compounds were protonated ions, $[M+H]^+$. The DART mass spectra were acquired on a triple quadrupole mass spectrometer with only unity mass resolution. As a result, only the nominal m/z values for the observed peaks could be determined. It was assumed that the dominant mechanism of ionization was protonation ($[M+H]^+$ ions formed; nominal MW = nominal $m/z - 1$) in the positive ion mode and deprotonation ($[M-H]^-$ ions formed; nominal MW = nominal $m/z + 1$) in the negative ion mode (Nah et al., 2013). For ease of comparison, all the mass spectra were plotted as function of the exact mass of the corresponding neutral compounds.

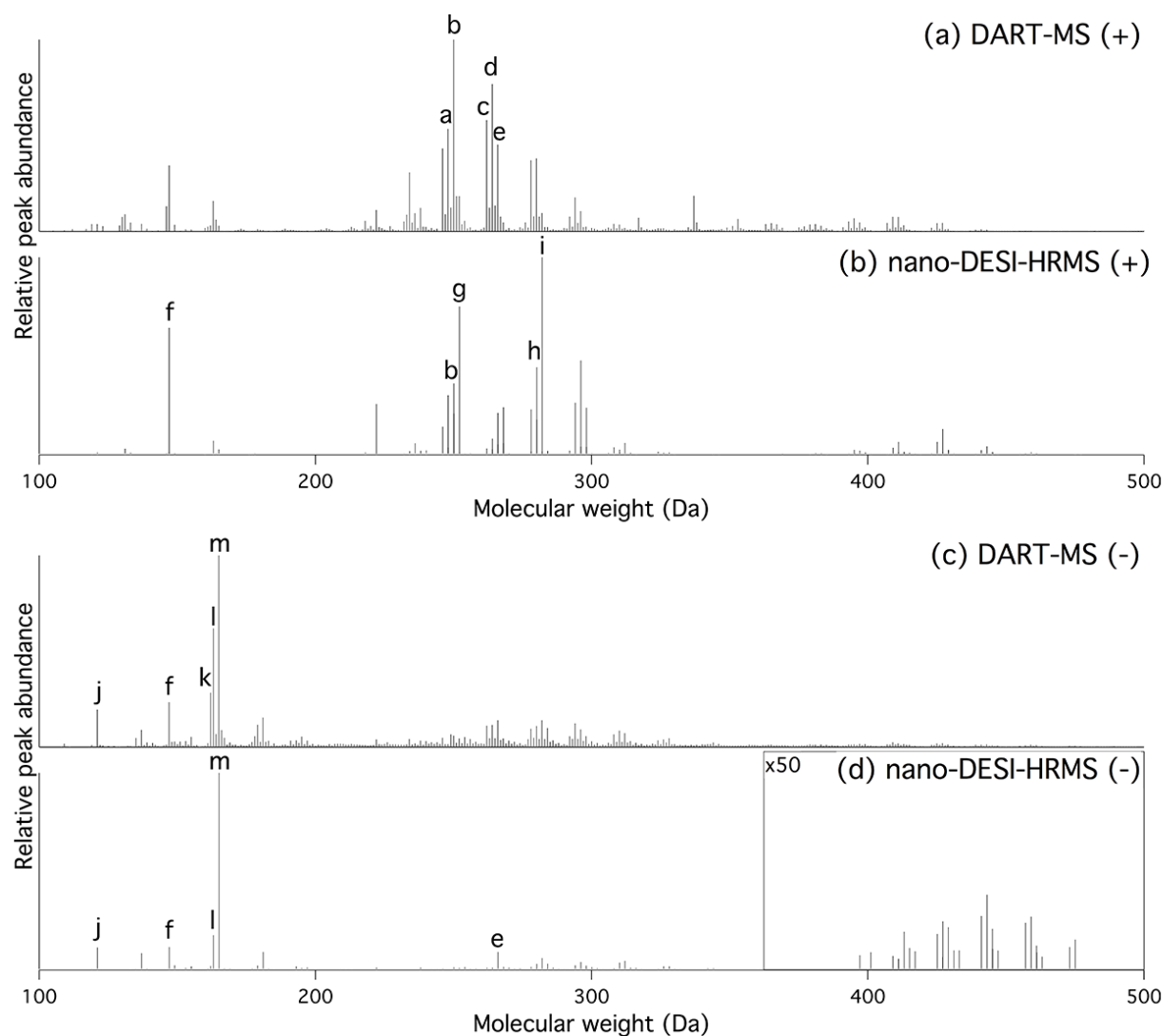


Figure 3.11. Nano-DESI and DART mass spectra of indole photooxidation SOA plotted as a function of the molecular weights of the neutral compounds. The nano-DESI mass spectra contain only peaks assignable to specific formulas, while DART mass spectra contain all observed peaks. The five most abundant peaks in each mass spectrum are indicated with letters: (a) 248Da, $C_{15}H_8O_2N_2$; (b) 250Da, $C_{15}H_{10}O_2N_2$, tryptanthrin; (c) 262 Da, $C_{16}H_{10}O_2N_2$, indirubin and/or indigo dye; (d) 264 Da, $C_{16}H_{12}O_2N_2$, dihydro indigo dye; (e) 266 Da, $C_{15}H_{10}O_3N_2$; (f) 147Da, $C_8H_5O_2N$, isatin; (g) 252Da, $C_{15}H_{12}O_2N_2$; (h) 280Da, $C_{16}H_{12}O_3N_2$; (i) 282Da, $C_{16}H_{14}O_3N_2$; (j) 121Da, C_7H_7ON , 2-formylformanilide; (k) 162 Da, $C_8H_6O_2N_2$; (l) 163 Da, $C_8H_5O_3N_2$, isatoic anhydride; (m) 165 Da, $C_8H_7O_3N$.

For a given ion mode, the DART and nano-DESI mass spectra were qualitatively similar, although nano-DESI appeared to favor larger, more oxidized compounds compared to DART.

Both DART and nano-DESI mass spectra showed a clear separation into distinct clusters of peaks corresponding to monomer, dimer, trimer, and tetramer oxidation products. For a

given ion mode, the major monomer peaks were the same in DART and nano-DESI strongly suggesting that they correspond to more abundant indole oxidation products (as opposed to minor SOA compounds that happened to have unusually high ionization efficiencies). There was also good correspondence between the major dimer peaks recorded in DART and nano-DESI. In the nano-DESI mass spectra, the peak abundances in the negative ion mode spectra were shifted towards higher molecular weights compared to the positive ion mode mass spectra. The preferential negative ion formation from more oxidized compounds was previously observed in ESI mass spectra of limonene SOA (Walser et al., 2008). Although we cannot assign formulas to the DART-MS peaks, it is evident from Figure 5 that this ionization method also favors larger, and presumably more oxidized, compounds in the negative ion mode. For example, carboxylic acids are more readily observed in the negative ion mode DART mass spectra (Nah et al., 2013).

Table 3.3 lists the most abundant peaks observed in the monomer and dimer ranges of nano-DESI-HRMS and DART-MS spectra, as well as additional smaller peaks for the specific compounds discussed in this paper. Isatin ($C_8H_5O_2N$, MW = 147 Da) was the single dominant peak in the monomer range observed in both nano-DESI(+) and DART(+); it was also detected in the negative ion mode mass spectra. Isatoic anhydride ($C_8H_5O_3N$; MW = 163 Da) was the second most abundant monomeric peak in all four mass spectra, but much lower abundance. Other abundant monomeric products included 3-oxyindole (C_8H_5ON ; MW = 131 Da) and 2-formylformanilide (C_7H_7ON ; MW = 121 Da). Of the compounds shown in Figure 1, tryptanthrin ($C_{15}H_{10}O_2N_2$; MW = 250 Da), indirubin ($C_{16}H_{10}O_2N_2$; MW = 262 Da), indigo dye ($C_{16}H_{10}O_2N_2$; MW = 262 Da), and dihydro indigo dye ($C_{16}H_{12}O_2N_2$; MW = 264 Da) were the most abundant dimer peaks. Meanwhile, indoxyl red ($C_{16}H_{10}ON_2$; MW = 246 Da) was

detected with lower but appreciable abundances in nano-DESI(-) and in both DART mass spectra. The prominent dimer compounds listed in Table 3.3 contained additional oxygen atoms compared to indoxyl red, indirubin, indigo dye, and dihydro indigo dye, and could be formed by further oxidation of these compounds.

Table 3.3. Monomer and dimer peaks with the largest peak abundance observed in DART-MS and nano-DESI-HRMS spectra for indole photooxidation SOA. Selected peaks corresponding to the compounds shown in Figure 3.1 are also included. Proposed assignments are based on the formulas from nano-DESI-HRMS. Peak abundances are normalized with respect to the most abundant peak in each spectrum.

	Nominal Mass	Formula	Ionization by H ⁺ or Na ⁺ in nano-DESI (+)	Peak Abundance nano-DESI - HRMS(+) (%)	Peak Abundance nano-DESI - HRMS(-) (%)	Peak Abundance DART-MS(+) (%)	Peak Abundance DART-MS(-) (%)	Tentative Assignment
Monomers	121	C ₇ H ₇ ON	H ⁺	0.88	11	4.0	20	2-formylformanilide
	130	-	-	-	-	7.7	0.03	
	131	C ₈ H ₅ ON	H ⁺	2.7	-	9.0	0.10	3-oxyindole
	133	C ₈ H ₇ ON	H ⁺	0.65	0.10	4.8	0.65	
	137	C ₇ H ₇ O ₂ N	-	-	8.2	4.1	9.1	anthranilic acid
	146	C ₈ H ₆ ON ₂	H ⁺	0.47	-	13	1.4	
	147	C ₈ H ₅ O ₂ N	H ⁺ , Na ⁺	0.79, 64	11	34	23	isatin
	162	C ₈ H ₆ O ₂ N ₂	-	-	1.8	3.2	28	isatoic anhydride
	163	C ₈ H ₅ O ₃ N	Na ⁺	6.7	17	16	62	
	165	C ₈ H ₇ O ₃ N	Na ⁺	2.3	100	3.1	100	
	181	C ₈ H ₇ O ₄ N	-	-	8.9	0.92	16	
Dimers	246	C ₁₆ H ₁₀ ON ₂	-	-	0.37	43	5.0	indoxyl red
	248	C ₁₅ H ₈ O ₂ N ₂	H ⁺ , Na ⁺	3.2, 30	-	53	1.6	tryptanthrin
	250	C ₁₅ H ₁₀ O ₂ N ₂	H ⁺ , Na ⁺	36, 21	1.0	100	6.1	
	252	C ₁₅ H ₁₂ O ₂ N ₂	H ⁺ , Na ⁺	75, 0.67	0.72	19	4.6	
	262	C ₁₆ H ₁₀ O ₂ N ₂	-	-	0.88	58	11	indirubin, indigo dye dihydro indigo dye
	264	C ₁₆ H ₁₂ O ₂ N ₂	H ⁺ , Na ⁺	7.8, 2.4	0.36	77	12	
	266	C ₁₅ H ₁₀ O ₃ N ₂	H ⁺ , Na ⁺	4.9, 21	8.9	45	14	
	280	C ₁₆ H ₁₂ O ₃ N ₂	H ⁺ , Na ⁺	17, 44	2.8	38	11	
	282	C ₁₅ H ₁₀ O ₄ N ₂	H ⁺ , Na ⁺	0.26, 1.3	5.7	9.7	14	
	282	C ₁₆ H ₁₄ O ₃ N ₂	H ⁺ , Na ⁺	100, 0.29	0.34			
	294	C ₁₆ H ₁₀ O ₄ N ₂	H ⁺ , Na ⁺	0.41, 26	2.1	18	12	
	296	C ₁₆ H ₁₂ O ₄ N ₂	H ⁺ , Na ⁺	3.7, 48	3.8	11	9.4	
	310	C ₁₆ H ₁₀ O ₅ N ₂	Na ⁺	2.2	3.4	3.7	8.7	
	312	C ₁₆ H ₁₂ O ₅ N ₂	H ⁺ , Na ⁺	0.18, 5.6	4.3	2.0	7.4	

Figure 3.12 shows the distribution of the number of C atoms in the indole SOA compounds, as detected by nano-DESI-HRMS (for each group of compounds with the same number of C atoms, the abundances in the positive and negative ion mode mass spectra were added together). Most of the observed compounds contained 8, 16, or 24 C atoms, corresponding to the monomer, dimer, and trimer derivatives of indole. Peaks with 7 and 15 carbon atoms were also prominent, suggesting an important role of the primary C₇ oxidation product 2-formylformanilide in the formation of low volatility species. Minor peaks containing other C-numbers were also present suggesting further fragmentation of the primary oxidation products. The average formula for all observed SOA compounds was C₁₅H₁₁O₃N₂.

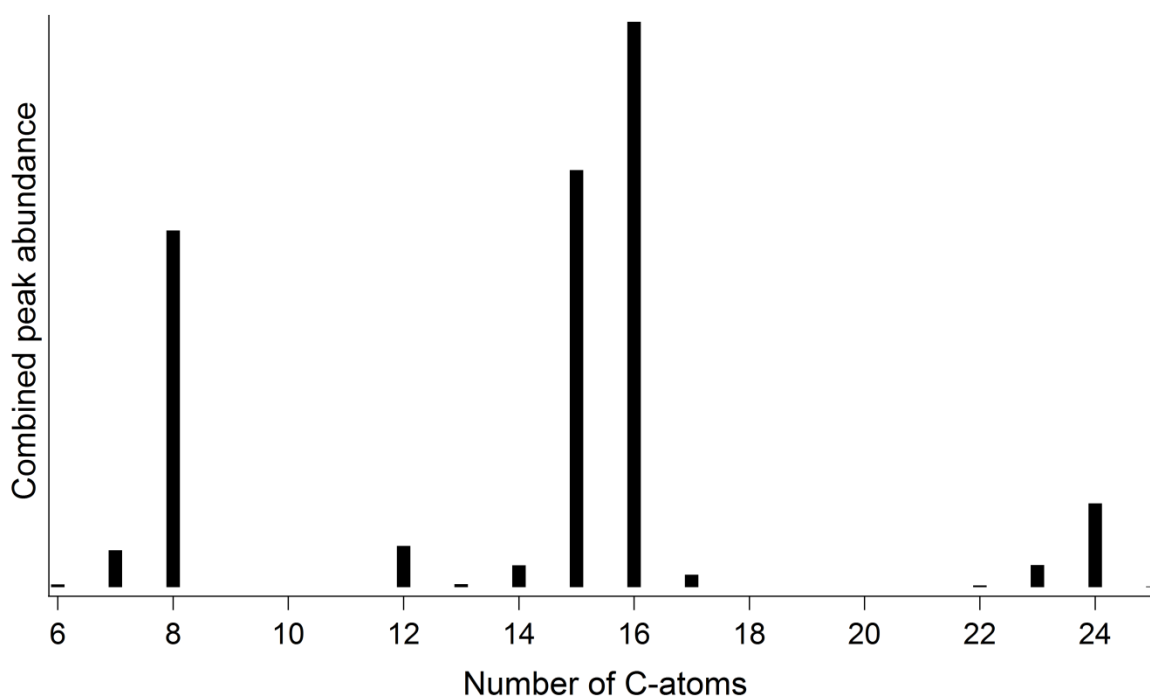


Figure 3.12. Distribution of the number of C atoms in the indole photooxidation SOA compounds detected in both positive and negative ion modes by nano-DESI-HRMS.

Figure 3.13 shows the distribution of the N/C ratios in indole SOA compounds. Many of the compounds had the same N/C ratio as indole (N/C = 1/8) indicating the oxidation and oligomerization reactions conserved both N and C atoms in many of the products. Loss and

gain of C atoms should result in a small increase and decrease in the N/C ratio, respectively. Some products had a slightly larger ratio consistent with a loss of C atoms (e.g., N/C = 1/7 and 2/15), whereas few products gained extra C atoms. One product with a relatively large abundance, $C_{12}H_{14}O_4$, had no N atoms left in it. Moreover, there were several $C_{8-9}H_hO_nN_2$ products, which gained an additional N atom. The mechanism of photooxidation is clearly complex involving a large number of secondary reactions. The full mechanism of indole photooxidation cannot be obtained from this data set. In the discussion that follows (section 3.4.6), the focus will be on the mechanism of formation of light-absorbing products.

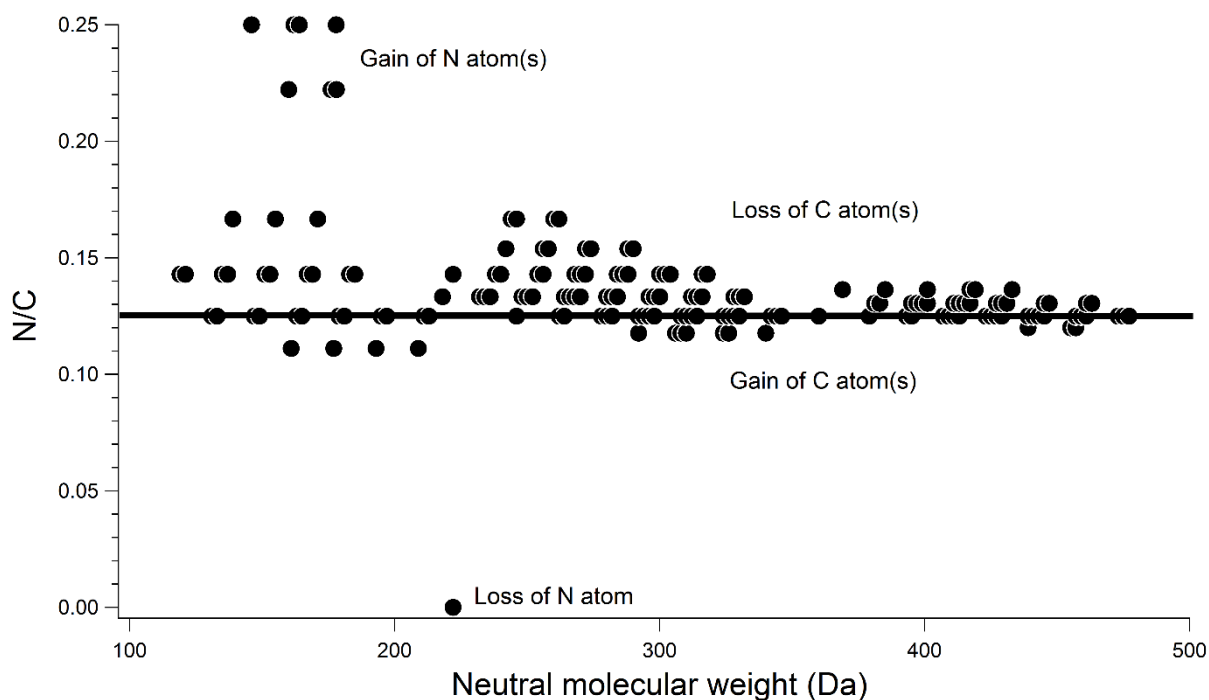


Figure 3.13: The N/C ratio of indole SOA compounds. The thick horizontal line corresponds to the N/C ratio in indole.

3.4.4 Optical properties of indole SOA

Chemical composition data showed that dimers are present in indole photooxidation SOA (Fig. 3.12). Additionally HPLC-PDA-HRMS (Table 3.4) showed that dimers contribute significantly to the absorption of indole SOA. Dimer formation may be artificially increased

by higher starting indole concentrations. To test for the possible precursor concentration effects on the absorption of SOA samples, indole+NO₃ SOA was prepared under different starting indole mixing ratios. As shown in Figure 3.14, Indole+NO₃ SOA absorption did not significantly depend on the indole mixing ratios (50-200 ppb) explored in this study, therefore 200 ppb of indole was used in the remaining experiments in order to collect sufficient mass for offline analysis. The lack of sensitivity of the spectra to the indole concentration suggests that the dimers, which are responsible for the 600 nm band, are produced by particle-phase chemistry as opposed to gas-phase chemistry.

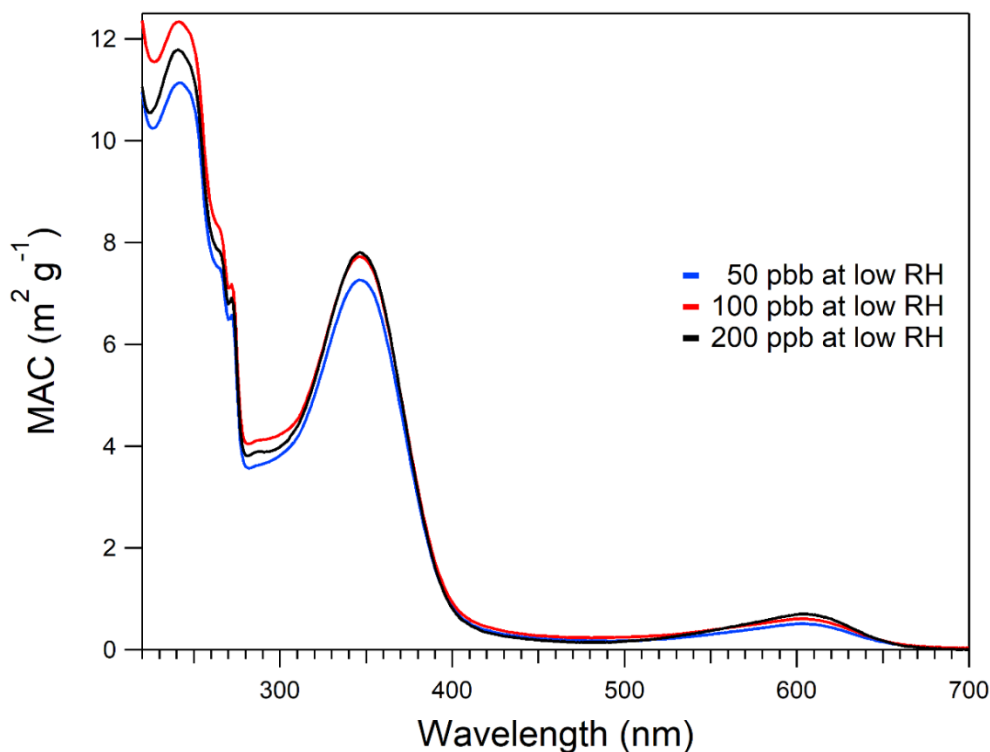


Figure 3.14. Wavelength-dependent MAC of indole + NO₃ SOA for different starting concentrations of indole.

Figure 3.15 shows the MAC values measured for an extract of indole + OH SOA in methanol. MAC values reached ~2 m²/g at λ = 300 nm. At λ = 400-700 nm, the MAC values ranged from

0.5 to 0.02 m²/g. These high MAC values are comparable to values of strongly absorbing SOA derived from naphthalene or methylpyrroles (Romonosky et al., 2015), as well as to MAC values of biomass burning organic aerosol (Sun et al., 2007). The wavelength dependence of MAC deviates from the power law commonly observed for brown carbon, e.g., see reviews of Laskin et al. (2015) and Moise et al. (2015), and has a reproducible broad band at ~350 nm, possibly due to the well-known derivatives of indole: indirubin, indigo dye, and indoxyl red, which have characteristic absorption bands at this wavelength. For the wavelength range of 300-600 nm, the absorption Angstrom exponent was ~6, comparable to the value of ~5 reported for brown carbon from biomass burning (Kirchstetter et al., 2012).

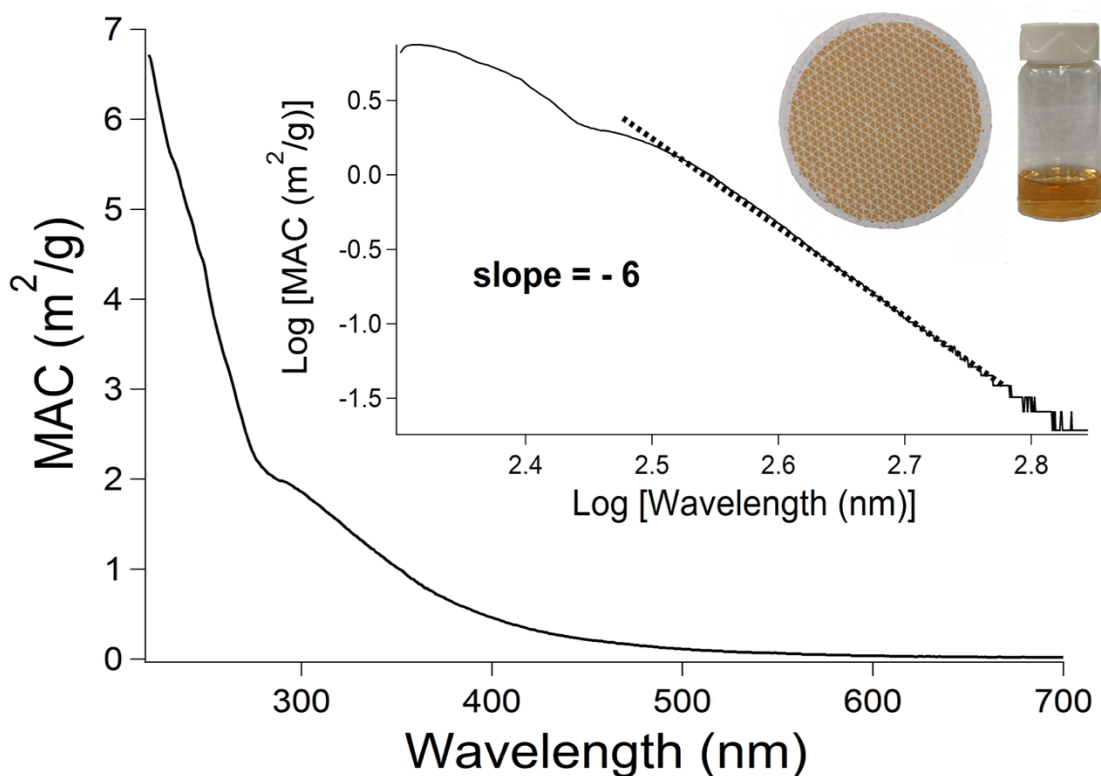


Figure 3.15. Wavelength-dependent mass absorption coefficient (MAC) of indole+OH SOA prepared under dry conditions. The inset shows the log-log version of the same data used to determine the absorption Angstrom exponent (fitted from 300 to 600 nm) and photographs of the indole SOA collected on a filter and extracted in methanol.

Figure 3.16 shows the wavelength dependent ($\lambda = 220-700$ nm) MAC of indole SOA samples prepared under the different oxidation conditions and relative humidities. The MAC spectra for indole SOA prepared under all conditions have characteristic features of brown carbon, with strong absorption in the UV and weaker absorption over the visible range. However, there are striking differences between the spectra. For example, the peak at 350 nm due to nitroindole (see Section 3.4.5) is highly prominent for the indole+NO₃ SOA. It is also observable in the indole+OH+NO_x SOA but it is missing for the indole+O₃ and indole+OH SOA systems. Another striking difference is the significant abundance of the indigo dye, recognized by its characteristic absorption band at 600 nm, in the indole + NO₃ SOA when prepared under low or 25% RH. The indigo dye peak is the largest under dry conditions but becomes much smaller at 50% RH. While much smaller, this peak at 600 nm is also observable in the indole+O₃ SOA at low RH and 25% RH traces, and also goes away at 50% RH.

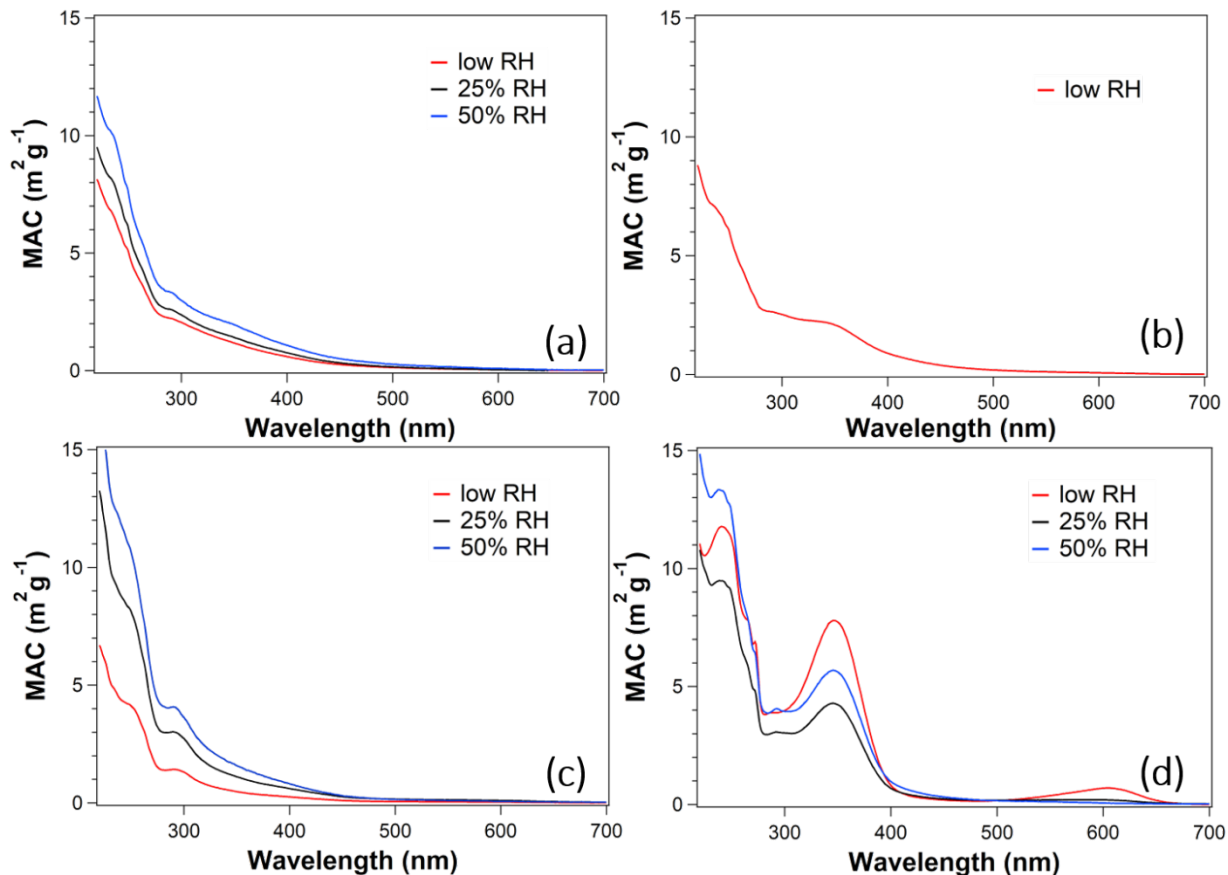


Figure 3.16. Wavelength-dependent mass absorption coefficient (MAC) of a) indole + OH SOA, b) indole + OH + NO_x SOA, c) indole + O_3 SOA, and d) indole + NO_3 SOA generated at different RH.

The MAC values (Fig. 3.16) were used to calculate the extinction coefficient, k , (Figs. 3.17-3.19 a) and were compared to the k values obtained through broadband cavity enhanced spectroscopy (BBCES) (Figs. 3.17-3.19 b). Overall, the k values obtained from the two independent methods were within the same order of magnitude suggesting good agreement between the two methods, and had the best agreement for the indole SOA prepared from photooxidation. Indole+OH SOA had higher k values at higher RH (Fig. 3.17a) and in the presence of NO_x (Fig. 3.17b). Moreover, the indole+OH+ NO_x SOA had a stronger wavelength dependence compared to the SOA prepared under low NO_x conditions. The dependence of the extinction coefficient for indole+ O_3 SOA on RH (Fig. 3.18a) had the same trend as the photooxidation samples; increasing k values with increasing RH.

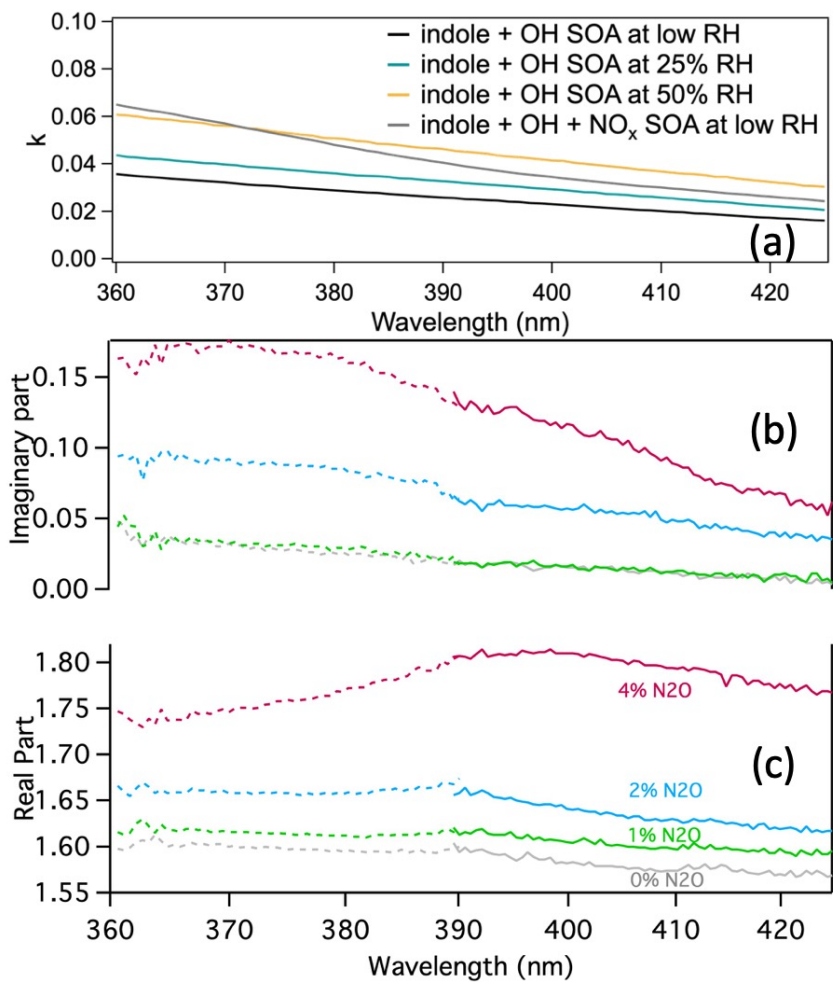


Figure 3.17. a) k values calculated from MAC of indole + OH SOA prepared in a chamber under low and high NO_x conditions. Measured b) k and c) n for indole SOA generated in an OFR under low and increasing NO_x conditions.

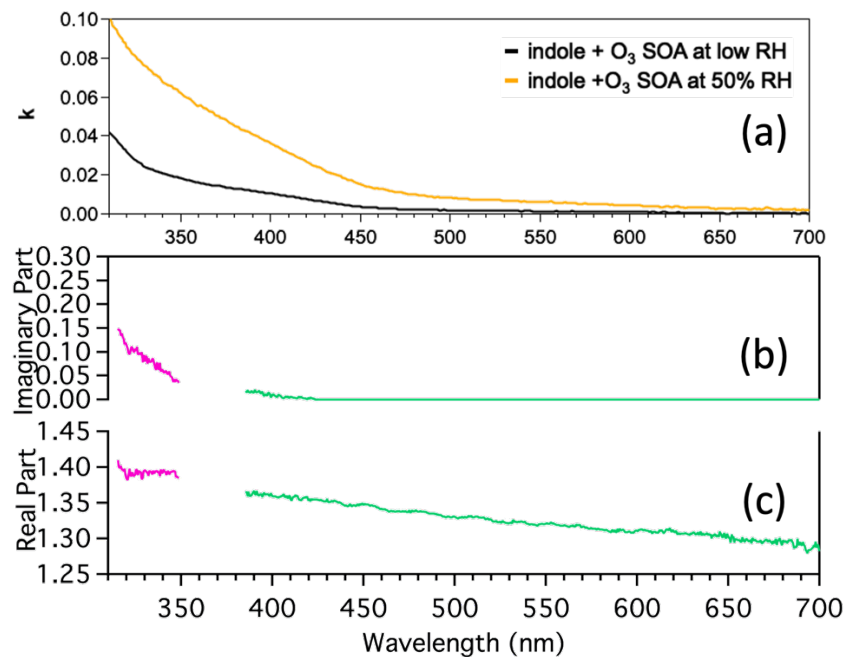


Figure 3.18. a) k values calculated from MAC of indole + O₃ SOA prepared in a chamber under different RH (<2, 25 or 50%). Measured b) k and c) n for indole + O₃ SOA generated in a glass OFR under dry conditions. The pink and green traces were collected using the BBCES in the 315-345 nm and 380-700 nm channels, respectively.

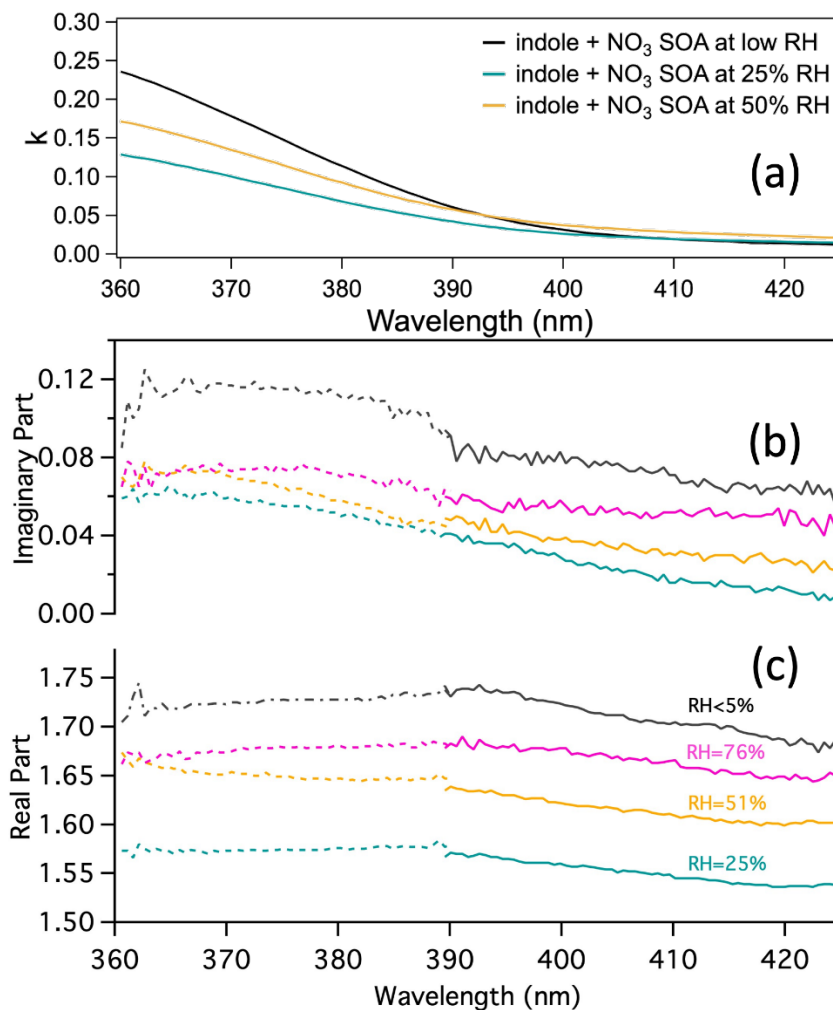


Figure 3.19. a) k values calculated from MAC of indole + NO₃ SOA prepared in a chamber under different RH (<2, 25 or 50%). Measured b) k and c) n for indole + NO₃ SOA generated in a glass OFR reactor at various RH (0, 25, 51, 76%). The dotted and solid traces were collected using the BBCES in the 360-390 nm and 385-425 nm channels, respectively.

Unlike SOA prepared by photooxidation or ozonolysis, k values for indole+NO₃ SOA did not have a monotonic dependence on RH (Figs. 3.19-3.20). Instead, the k values for indole+NO₃ SOA were highest for SOA prepared under low RH, then decreased at 25% RH, and subsequently increased at 50% RH, a trend captured by both methods (Fig. 3.19a-b).

When the k values at 400 nm reported in Fig. 3.19b were replotted as a function of RH (Fig. 3.20), we observed that going from low to 25% RH resulted in a decrease in the k value by

approximately half. Increasing the RH again by increments of ~25% led to modest increases in the k value.

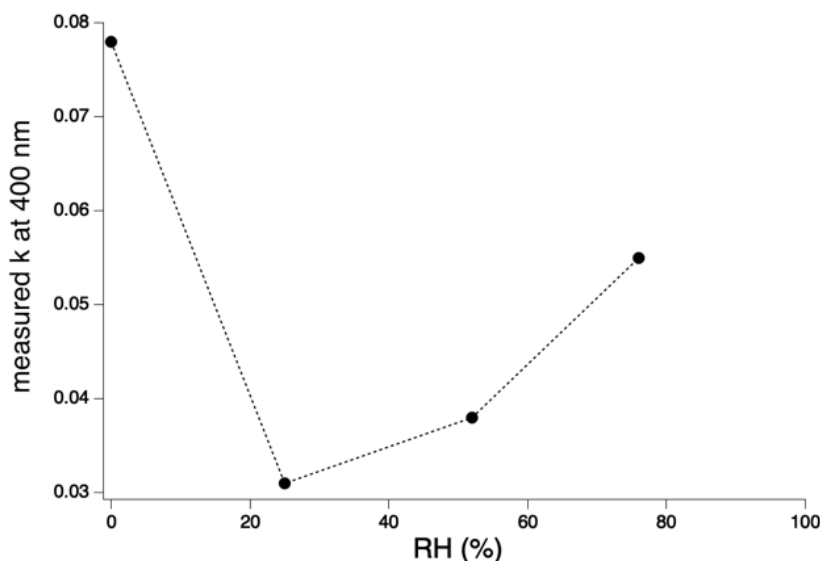


Figure 3.20. Measured k for indole + NO₃ SOA generated in a glass OFR reactor at various RH (0, 25, 51, 76%). (Same data from Fig. 3.19b)

Based on AMS data, chemical families that showed a similar RH dependence were the C_xH_yO and C_xH_yO_z families (Fig. 3.21), with the most prominent ion fragments consisting of CO⁺ and CO₂⁺ (Fig. 3.22). On the other hand, families like NO⁺ and C_xH_y⁺ followed the opposite RH dependence as the k values, with prominent ion fragment including NO⁺, NO₂⁺, and C₁-C₆ compounds (Fig. 3.23). It is possible that fragments which follow the same trend as k values do with respect to RH contribute to the absorption of the particles. However, more data are needed in order to investigate the mechanisms responsible for this absorption and the role of RH in these reactions. A future set of experiments could be done via HPLC-PDA-HRMS for indole+NO₃ SOA generated at different RH (as opposed to just one measurement at a single RH, Section 3.4.5) in order to investigate what happens to the chromophoric compounds in the SOA as a function of RH.

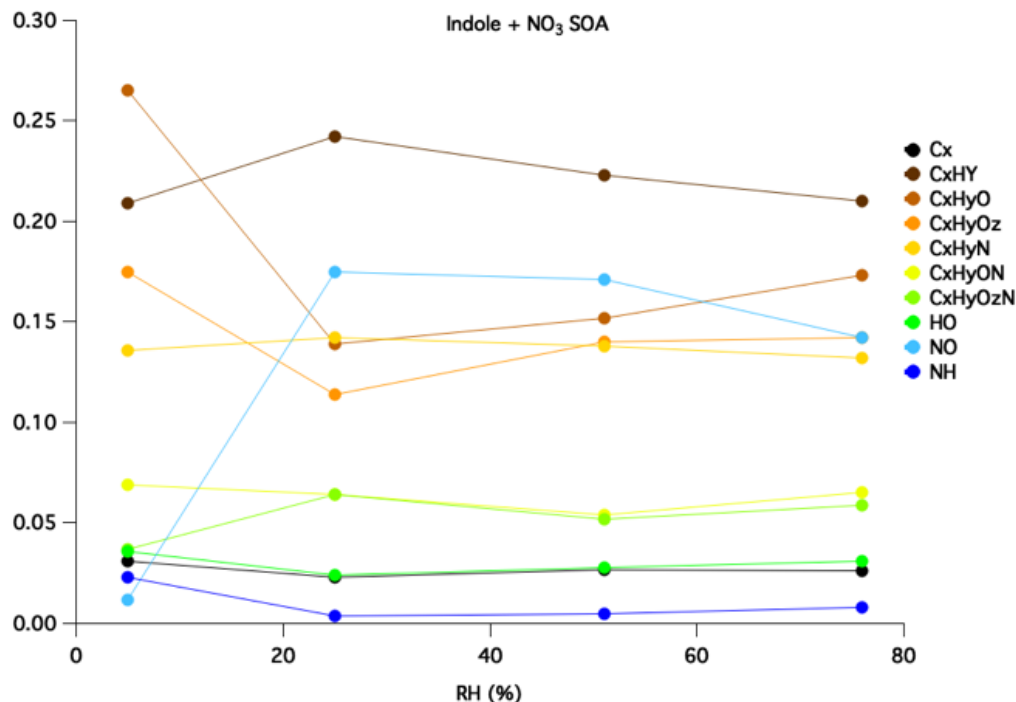


Figure 3.21. Indole + NO₃ SOA: AMS Families vs RH

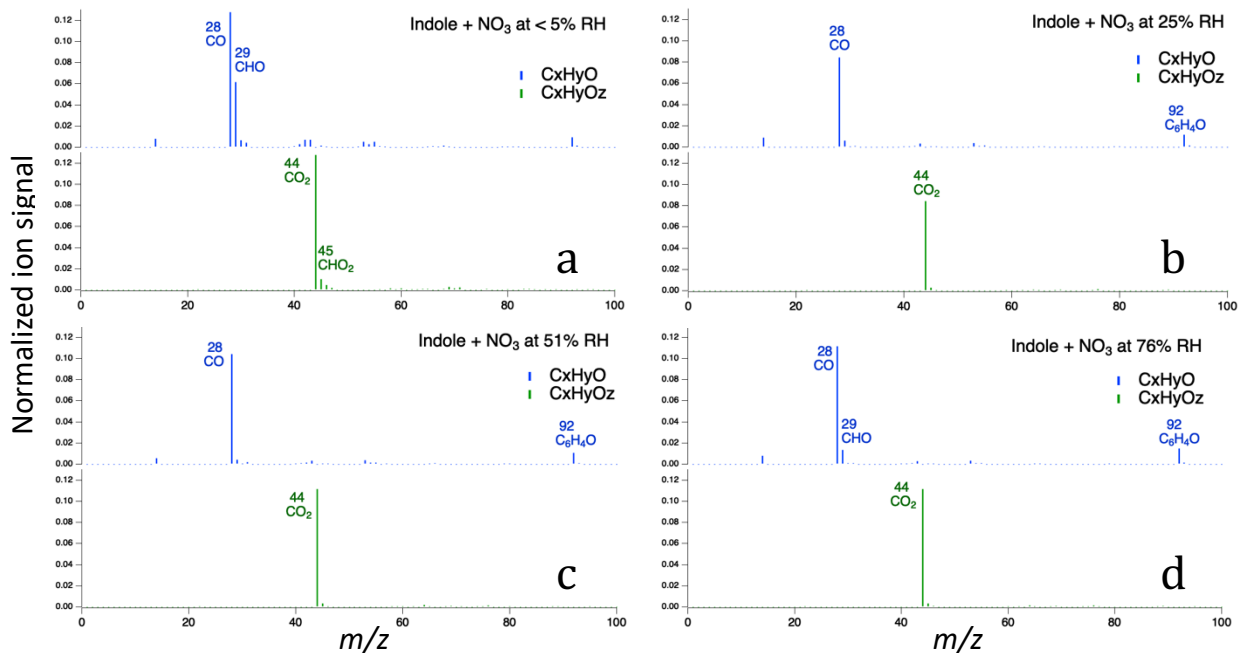


Figure 3.22. AMS families that followed the same trend with RH as k vs RH. Individual ion fragments signals are shown for indole+NO₃ SOA generated under <5% RH (a), 25% RH (b), 51% RH (c), and 76% RH (d). The ion signal has been normalized such that the total ion signal for all assigned peaks in an average mass spectrum is 1.

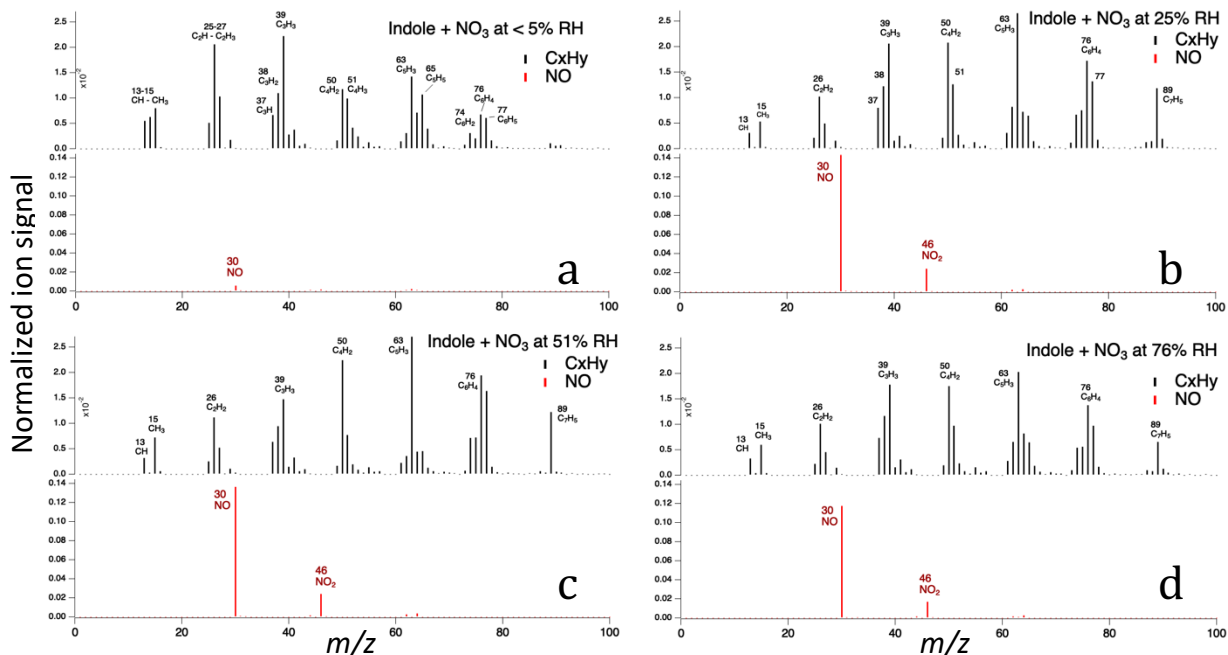


Figure 3.23. Examples of AMS families that followed opposite trend with RH to k vs RH. Individual ion fragments signals are shown for indole+NO₃ SOA generated under <5% RH (a), 25% RH (b), 51% RH (c), and 76% RH (d). The ion signal has been normalized such that the total ion signal for all assigned peaks in an average mass spectrum is 1.

3.4.5 Chromophores in indole SOA

Figure 3.24 shows the HPLC-PDA chromatogram of an indole+OH SOA sample demonstrating its components with strong light-absorbing properties near-UV and visible spectral ranges (above 300 nm). To identify specific chromophores from the HPLC-PDA-HRMS data, the methods described by Lin et al. (2015b, 2016) were followed. High-resolution mass spectra were examined to identify *m/z* values that appear at the retention times associated with the peaks in the HPLC chromatograms. The PDA absorption spectra associated with these retention times were then compared with possible candidates constrained by their molecular formula determined from the mass spectra.

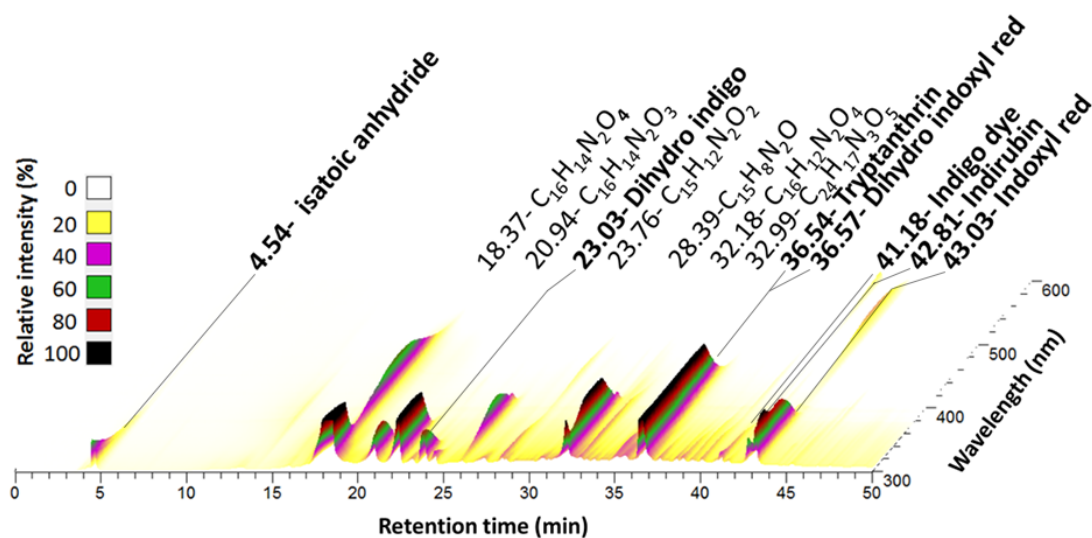


Figure 3.24. HPLC-PDA chromatogram of indole photooxidation SOA. The absorbance is plotted as a function of both retention time and wavelength. Peaks are labelled by their PDA retention time followed by their proposed assignment. Bold-faced assignments are specific isomers that are discussed further in the text. Note the reference line for dihydro indigo points to a small peak between two larger peaks that obscure it in this projection.

Figure 3.25 shows a comparison of the absorption spectra for the key peaks in the HPLC-PDA chromatogram with absorption spectra of selected compounds reported in the literature. The match is excellent in terms of the absorption peak maxima: 280, 310, 334, 392 nm for tryptanthrin; 240, 283, 335, 610 nm for indigo dye; 242, 290, 365, 540 nm for indirubin; and 217, 273, 350, 520 nm for indoxyl red. The shapes of the spectra do not match perfectly because the chromophores are not fully separated by the HPLC column (Fig. 3.24) and may co-elute with additional minor compounds. Likely, more than one chromophore contributed to the absorbance at any given retention time. However, the power of the method is clear, as illustrated, for example, by the separation of the structural isomers indigo dye and indirubin (Fig. 3.24).

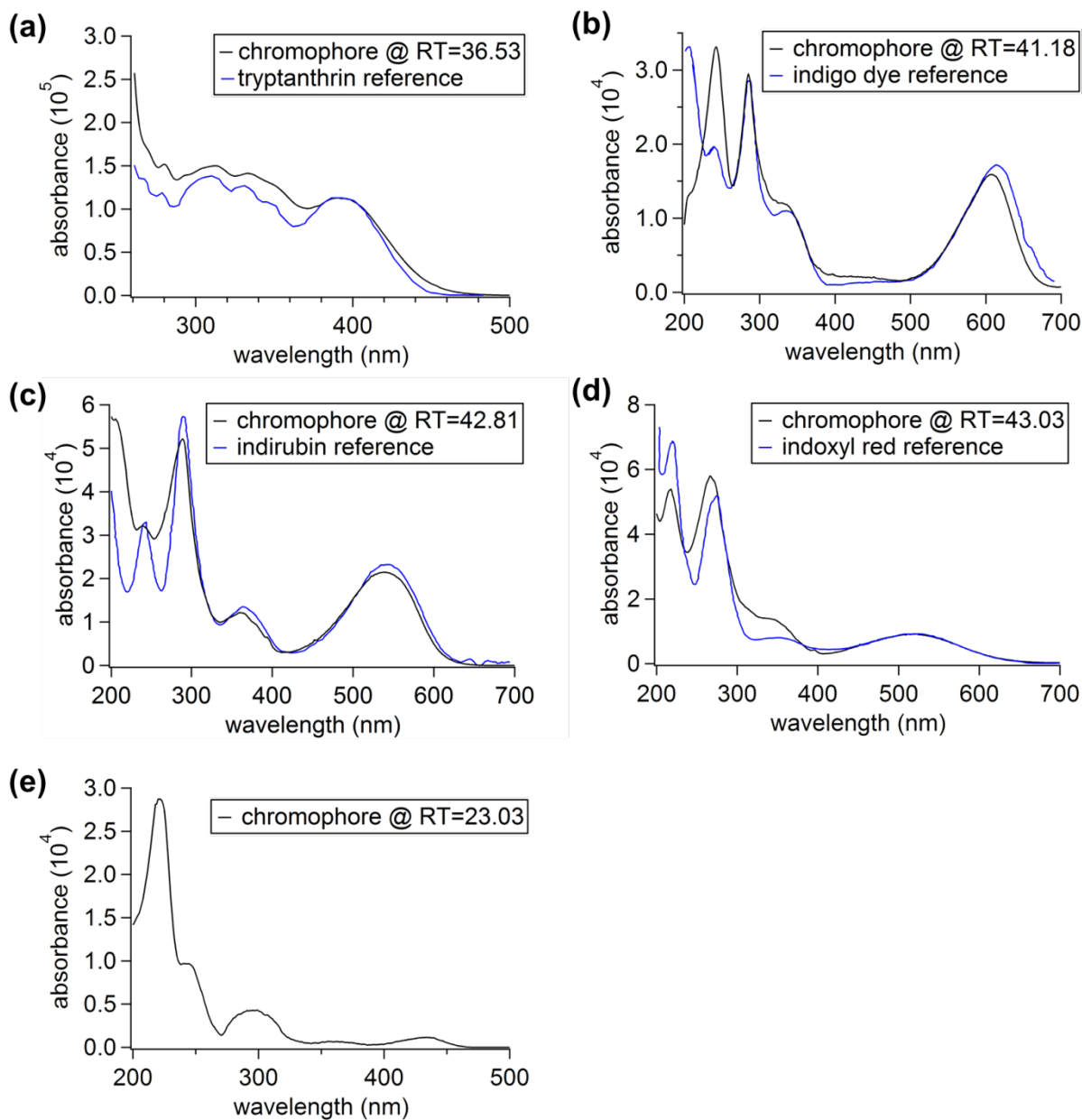


Figure 3.25. Comparison between measured PDA absorption spectra at selected retention time (RT) from an indole + OH SOA sample and reference spectra of proposed chromophores in the literature (reference spectrum is not available for dihydro indigo dye; panel e).

The HPLC-PDA chromatograph for the indole+O₃ and indole+NO₃ SOA samples is shown in Figure 3.26 and a list of the individual chromophores along with proposed structures based on elemental formulas obtained from the HRMS analysis and reference spectra from the literature are listed in Table 3.4. Altogether 28 individual compounds were identified, which included 6 monomers, 20 dimers, and 2 trimers. Monomeric compounds are especially relevant as the dimers and trimers are much less likely to form under realistic concentrations in the atmosphere. Three chromophores (tryptanthrin, indigo dye, and indirubin) were observed in all three SOA types, and an additional seven of the chromophores were shared by two SOA types. The chromophore indigo dye, while not

unique to the indole+NO₃ SOA, contributed to the prominent peak at 600 nm in the indole+NO₃ SOA absorbance spectrum.

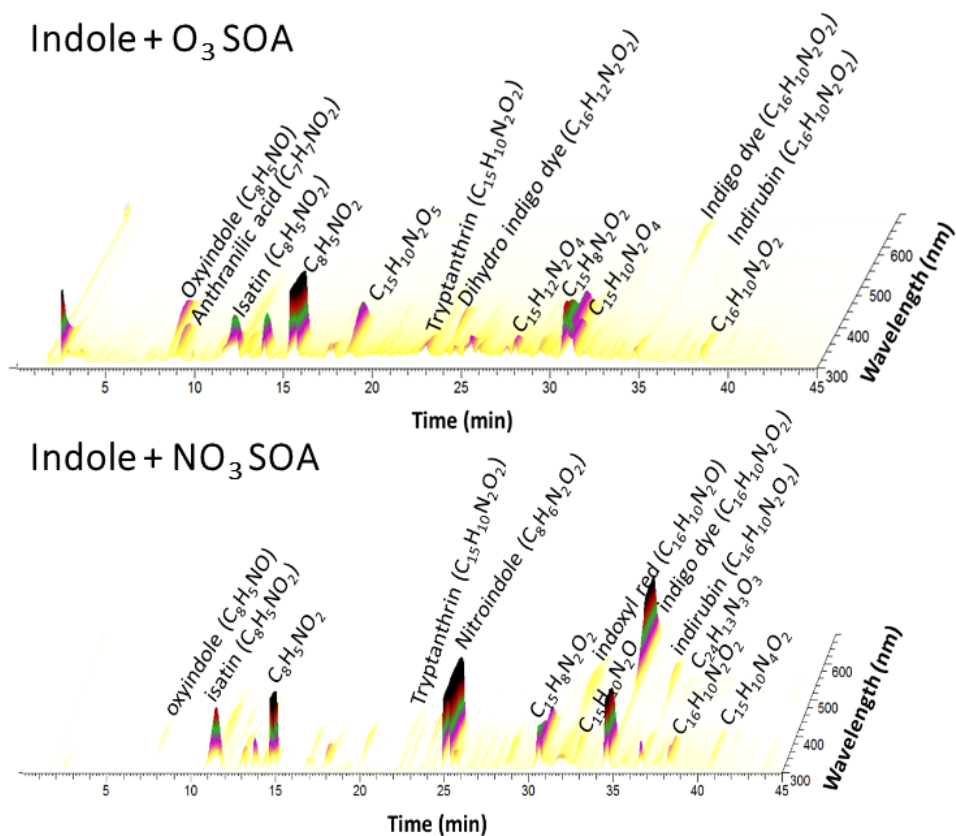
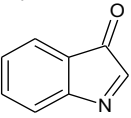
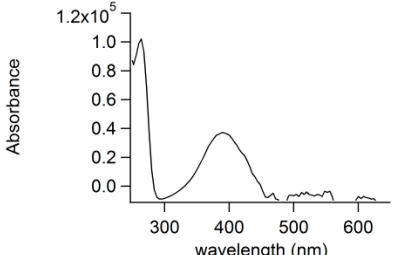
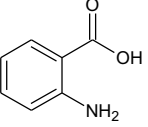
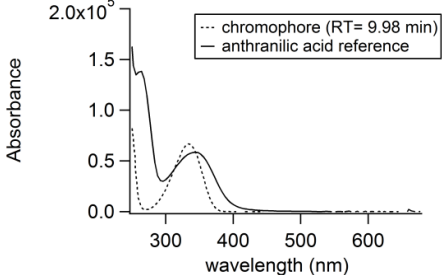
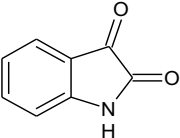
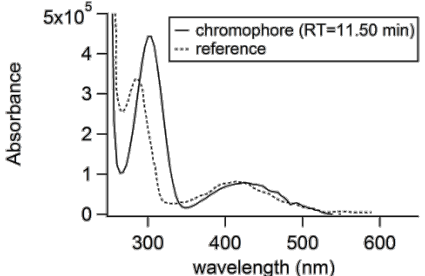
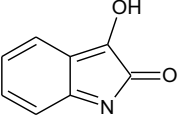
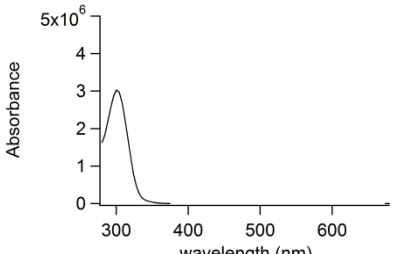
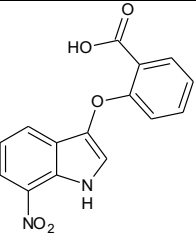
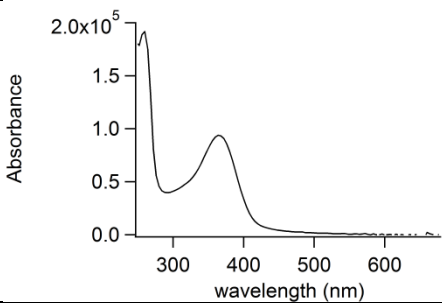
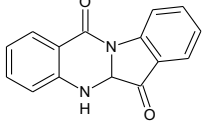
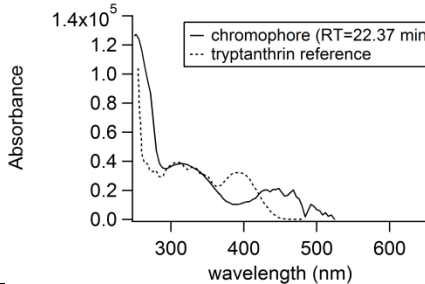
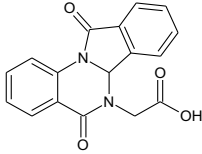
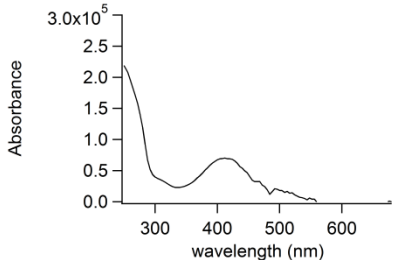
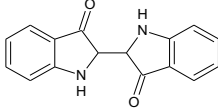
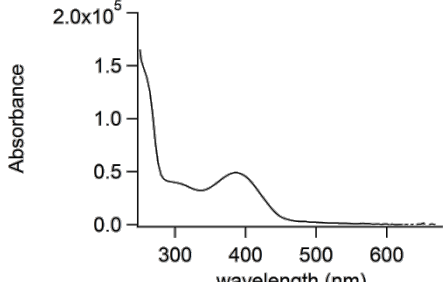
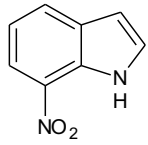
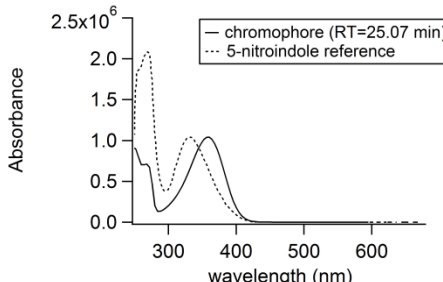
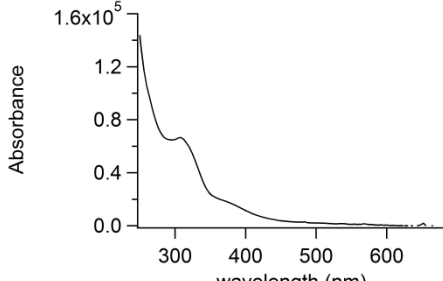


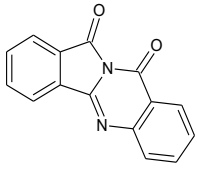
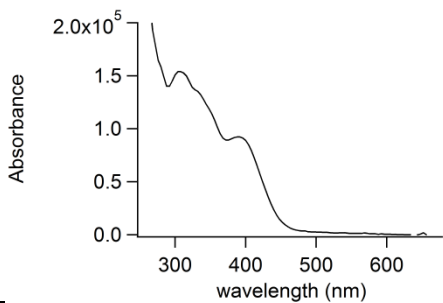
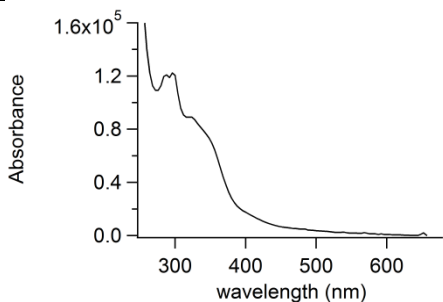
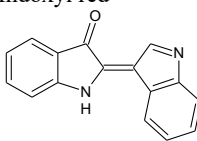
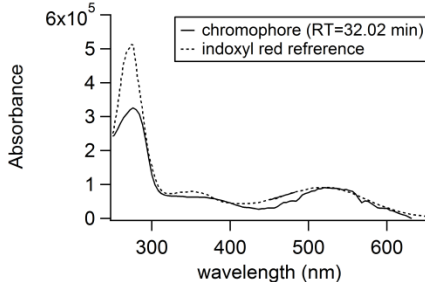
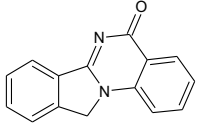
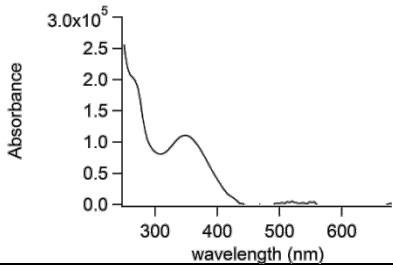
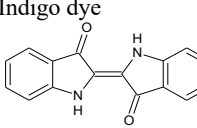
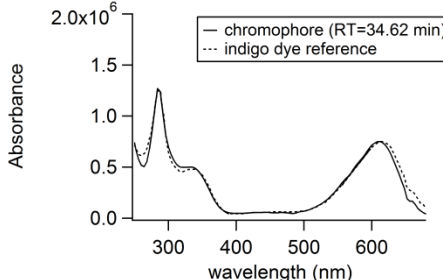
Figure 3.26. HPLC-PDA chromatogram of indole ozonolysis SOA sample (top panel) and indole + NO₃ SOA sample (bottom panel) generated at low RH. The absorbance is plotted as a function of both retention time and wavelength. Peaks are labelled by their proposed assignment. See table 3.4 for more details.

Table 3.4. Proposed chromophores from indole + NO₃ SOA, indole + O₃ SOA, and indole + OH SOA generated at low RH.

Retention time (min)	Molecular weight (amu)	Elemental formula	Tentative structure	UV-Vis Absorption spectrum	Indole + NO ₃ SOA	Indole + O ₃ SOA	Indole + OH SOA
4.54	163	C ₈ H ₅ NO ₃	Isatoic anhydride <chem>O=C1OC(=O)c2ccccc12</chem>				X

Retention time (min)	Molecular weight (amu)	Elemental formula	Tentative structure	UV-Vis Absorption spectrum	Indole + NO ₃ SOA	Indole + O ₃ SOA	Indole + OH SOA
7.69 (NO ₃) 8.4 (O ₃)	131	C ₈ H ₅ NO	Oxyindole 		X	X	
9.98	137	C ₇ H ₇ NO ₂	Anthranilic acid 			X	
11.5 (NO ₃) 12.31 (O ₃)	147	C ₈ H ₅ NO ₂	Isatin 		X	X	
14.82 (NO ₃) 15.55 (O ₃)	147	C ₈ H ₅ NO ₂			X	X	
18.37	298	C ₁₆ H ₁₄ N ₂ O ₄					X
18.61	298	C ₁₅ H ₁₀ N ₂ O ₅				X	
20.94	284	C ₁₆ H ₁₄ N ₂ O ₃					X

Retention time (min)	Molecular weight (amu)	Elemental formula	Tentative structure	UV-Vis Absorption spectrum	Indole + NO ₃ SOA	Indole + O ₃ SOA	Indole + OH SOA
22.37 (NO ₃) 22.66 (O ₃) 36.54 (OH)	250	C ₁₅ H ₁₀ N ₂ O ₂	Tryptanthrin 		X	X	X
23.69	308	C ₁₇ H ₁₂ N ₂ O ₄			X		
23.76	252	C ₁₅ H ₁₂ N ₂ O ₂					X
24.09 (O ₃) 23.03 (OH)	264	C ₁₆ H ₁₂ N ₂ O ₂	Dihydro indigo dye 			X	X
25.07	162	C ₈ H ₆ N ₂ O ₂	Nitroindole 		X		
28.02	284	C ₁₅ H ₁₂ N ₂ O ₄				X	
28.39	232	C ₁₅ H ₈ N ₂ O					X

Retention time (min)	Molecular weight (amu)	Elemental formula	Tentative structure	UV-Vis Absorption spectrum	Indole + NO ₃ SOA	Indole + O ₃ SOA	Indole + OH SOA
30.58 (NO ₃) 30.81 (O ₃)	248	C ₁₅ H ₈ N ₂ O ₂			X	X	
31.17	282	C ₁₅ H ₁₀ N ₂ O ₄				X	
32.02 (NO ₃) 43.03 (OH)	246	C ₁₆ H ₁₀ N ₂ O	Indoxyl red 		X		X
32.18	296	C ₁₆ H ₁₂ N ₂ O ₄					X
32.68	234	C ₁₅ H ₁₀ N ₂ O			X		
32.99	427	C ₂₄ H ₁₇ N ₃ O ₅					X
34.62 (NO ₃) 34.77 (O ₃) 41.18 (OH)	262	C ₁₆ H ₁₀ N ₂ O ₂	Indigo dye 		X	X	X

Retention time (min)	Molecular weight (amu)	Elemental formula	Tentative structure	UV-Vis Absorption spectrum	Indole + NO ₃ SOA	Indole + O ₃ SOA	Indole + OH SOA
35.63	324	C ₁₆ H ₁₂ N ₄ O ₄			X		
36.57	248	C ₁₆ H ₁₂ N ₂ O					X
36.66 (NO ₃) 36.84 (O ₃) 42.81 (OH)	262	C ₁₆ H ₁₀ N ₂ O ₂	Indirubin 		X	X	X
37.55	391	C ₂₄ H ₁₃ N ₃ O ₃			X		
38.3 (NO ₃) 38.45 (O ₃)	262	C ₁₆ H ₁₀ N ₂ O ₂	Isoindigo or Isoindirubin 		X	X	
40.75	278	C ₁₅ H ₁₀ N ₄ O ₂			X		

3.4.6 Proposed mechanisms for the production of chromophores in indole+OH SOA

The precursors to indoxyl red and indigo dye, dihydro indoxyl red and dihydro indigo dye, respectively, were also identified by HPLC-PDA-HRMS analysis, and were observed in nano-DESI mass spectra. This observation supports a mechanism similar to the aqueous-phase indole oxidation proposed by Iddon et al. (1971), in which indole first oxidizes to 3-oxindole, then to dihydro indigo dye or dihydro indoxyl red, then finally to indigo dye and indoxyl red (Figure 3.27a). We note that the mechanism by Iddon et al. (1971) was developed for the aqueous oxidation of indole. While our experiments were performed under dry conditions, it is conceivable that similar oligomerization processes can occur in the gas phase and/or in the organic particle phase. For example, Healy et al. (2012) observed efficient dimerization of naphthoxy radicals in the gas phase leading to rapid formation of SOA following photolysis of 1-nitronaphthalene. The dimerization of oxindole to dihydro indigo dye, as well as other oligomerization processes in indole SOA, could follow a mechanism similar to the one described by Healy et al. (2012).

Several products were assigned based on previous observations by Novotna et al. (2003), who studied photodegradation of indigo dye in dichloromethane solution. They proposed the mechanism shown in Figure 3.27b to explain the production of tryptanthrin and anthranilic acid from ambient indigo dye oxidation. In this mechanism, hydroxyl radicals attack the carbonyl carbon atoms of isatin ultimately opening the 5-membered N-heterocyclic ring to yield anthranilic acid. Although anthranilic acid does not show up in Figure 3.24 because it is not a chromophoric species, it was detected by nano-DESI-HRMS. As shown in Figure 3.27b, anthranilic acid can react with another molecule of isatin to produce tryptanthrin. This mechanism is relevant to indole photooxidation SOA, because

isatin can be produced not only from the oxidation of indigo dye but also directly from indole, through the intermediacy of 3-oxindole (Figure 3.27a). Moreover, Novotna and colleagues suggested that isatoic anhydride should also be formed from indigo dye oxidation. A compound with this formula had large abundance in both HPLC-PDA-HRMS (Figure 3.24) and nano-DESI-HRMS and DART-MS (Figure 3.11, Table 3.3). Combined with the evidence that tryptanthrin is a major secondary chromophore, this could be a significant pathway to brown carbon formation in the oxidation of indole.

We emphasize that the mechanism outlined in Figure 3.27 is *tentative* and is based on the limited information from our experiments and previous experimental data from the literature. Multiple unresolved questions remain. For example, formation of tryptanthrin was very slow in experiments by Novotna et al. (2003), and it is not clear how this compound could form in just a few hours of photooxidation in the chamber. Furthermore, it is not clear which processes occur in the gaseous phase versus the particle phase. Although indeterminate from the current experiments, at least some of the dimer formation pathways described in Figure 3.27 likely occur in the particle phase.

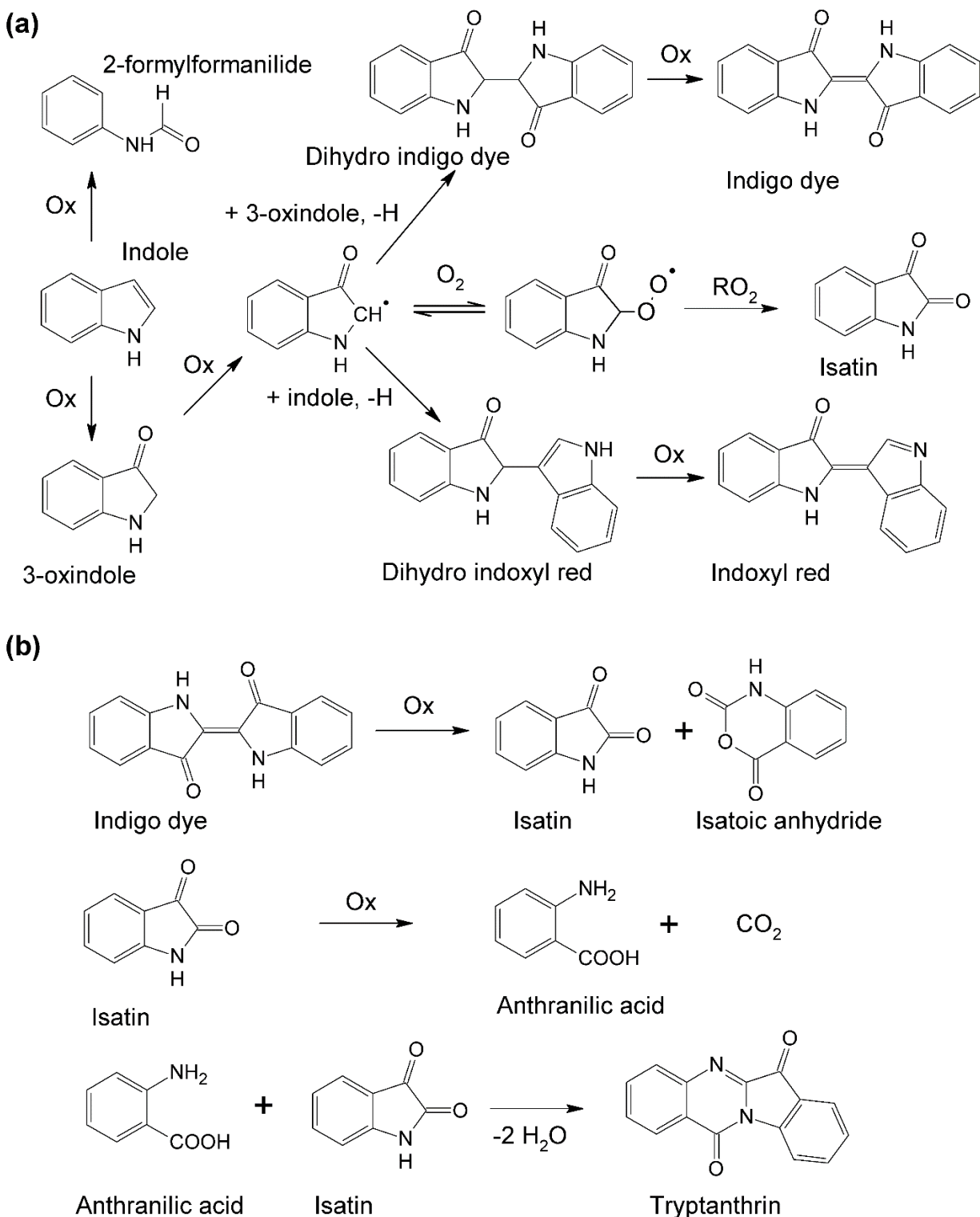


Figure 3.27. Tentative mechanism for the formation of observed chromophores in the photooxidation of indole. (a) Processes leading to indigo dye and indoxyl red based on Iddon et al. (1971). (b) Processes leading to tryptanthrin based on Novotna et al. (2003). "Ox" denotes an oxidation step.

3.5 Modeling Results

The spatiotemporal distribution of indole+OH SOA is likely controlled by a combination of: (i) the spatiotemporal distribution of gas-phase indole and its emissions sources, (ii) the availability of hydroxyl radical for gas-phase oxidation chemistry and (iii) meteorological conditions in the region, including temperature, humidity, and wind direction. Once emitted, indole reacts with hydroxyl radical to form gas-phase indigo dye. Gas phase indigo dye can then partition into the aerosol phase to form indole SOA. The presence of a sea breeze in the SoCAB results in a prevailing wind direction of north-northeast, transporting pollutants inland during the daytime hours. As a result, peak concentrations of indole+OH SOA should be located further inland than peak concentrations of gas-phase indole and occur in areas that are already burdened with poor air quality.

Figure 3.28 shows the spatial distribution of 24-hour average gas-phase indole concentrations in the SoCAB for the low, medium, and high emissions scenarios considered in this study. The amount of indole+OH SOA formed in the model, and thus the impact of indole on the total predicted SOA concentrations, depends strongly on the emissions of gas-phase indole. In the high emissions scenario, hourly gas-phase indole concentrations peaked at 0.3 ppbv, with the highest concentrations occurring in the early morning hours before sunrise (Fig. 3.31). For comparison, during a field measurement campaign in the San Joaquin Valley of California, Gentner et al. (2014) reported gas-phase indole concentrations of about 1-3 ppbv in ambient air during a springtime flowering event. Measured concentrations of indole were slightly higher during the late night and early morning hours than during the daytime, consistent with the model results obtained in this study. Gentner et al. (2014) also

showed that flowering was a major biogenic emissions event, causing emissions of many compounds to increase by several factors to over an order of magnitude. Therefore, episodic emissions of indole in rural areas are likely to be significantly greater than the emissions used in this study. Based on the high SOA yield from gas-phase indole found in the indole+OH SOA experiments, we propose that biogenic emissions events such as springtime flowering may degrade local air quality.

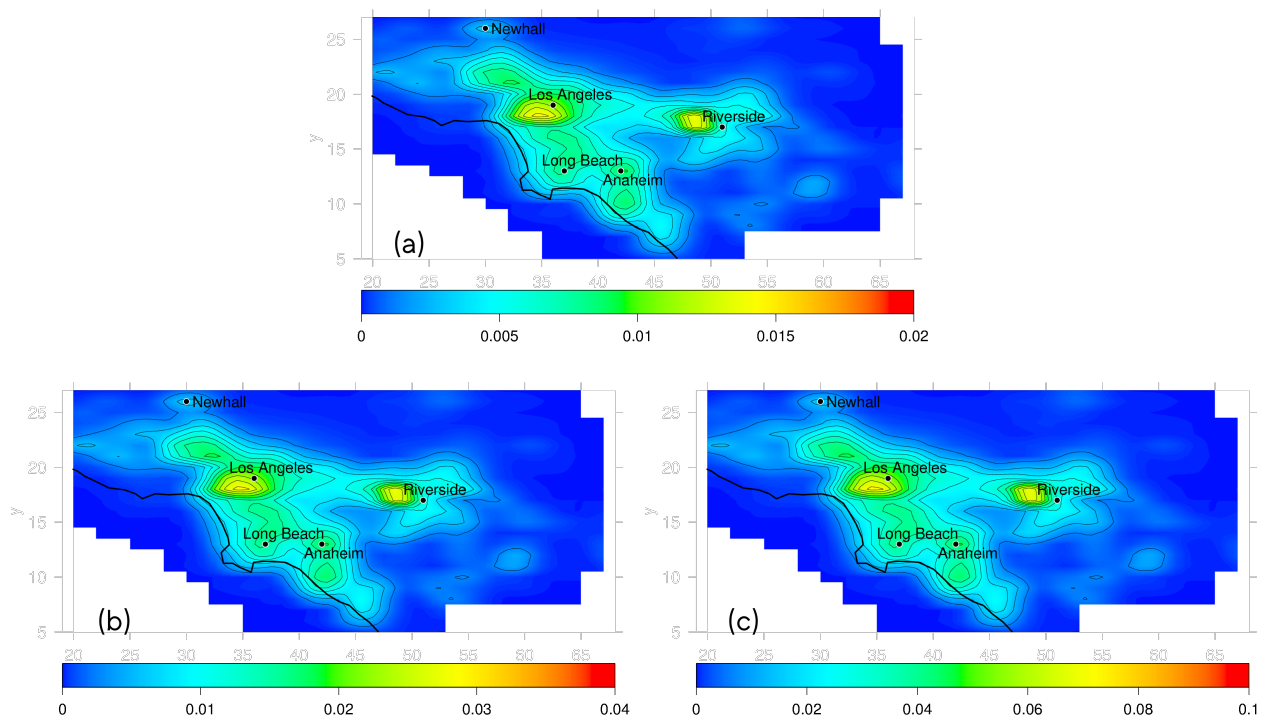


Figure 3.28. The 24-hour average gas-phase indole concentrations. The indole mixing ratios in ppbv are shown in the low emission scenario (a), medium emissions scenario (b), and high emission scenario (c).

Figure 3.29 a shows 24-hour average SOA concentrations in the base case model simulation, and Figures 3.29 b-d show the additional SOA resulting from indole photooxidation in the three emissions scenarios. The highest SOA concentrations occurred directly east of Riverside where a combination of biogenic and anthropogenic precursors accumulated during days one and two and into day three. The 24-hour average indole+OH SOA

concentrations peaked at about $0.13 \mu\text{g}/\text{m}^3$ in the high emissions scenario (Figure 3.29d). The highest concentrations of indole+OH SOA occurred north of Los Angeles and Riverside. To put this number in perspective, aerosol with mass concentration of $0.1 \mu\text{g}/\text{m}^3$ and MAC of $0.5 \text{ m}^2/\text{g}$ will have an absorption coefficient of 0.05 Mm^{-1} (we neglect the particle size effects in this estimation). Thompson et al. (2012) reported an absorption coefficient of 4 Mm^{-1} at 532 nm during the 2010 CalNex campaign in Pasadena, California, with the absorption being dominated by black carbon. The average absorption coefficients reported for “average urban USA” and “average remote USA” by Horvath et al. (1993) were 22 Mm^{-1} and 0.7 Mm^{-1} , respectively. While the absorption by indole+OH SOA is unlikely to compete with that by black carbon in urban areas, it may contribute to the aerosol absorption in more remote areas, where the black carbon concentrations are smaller.

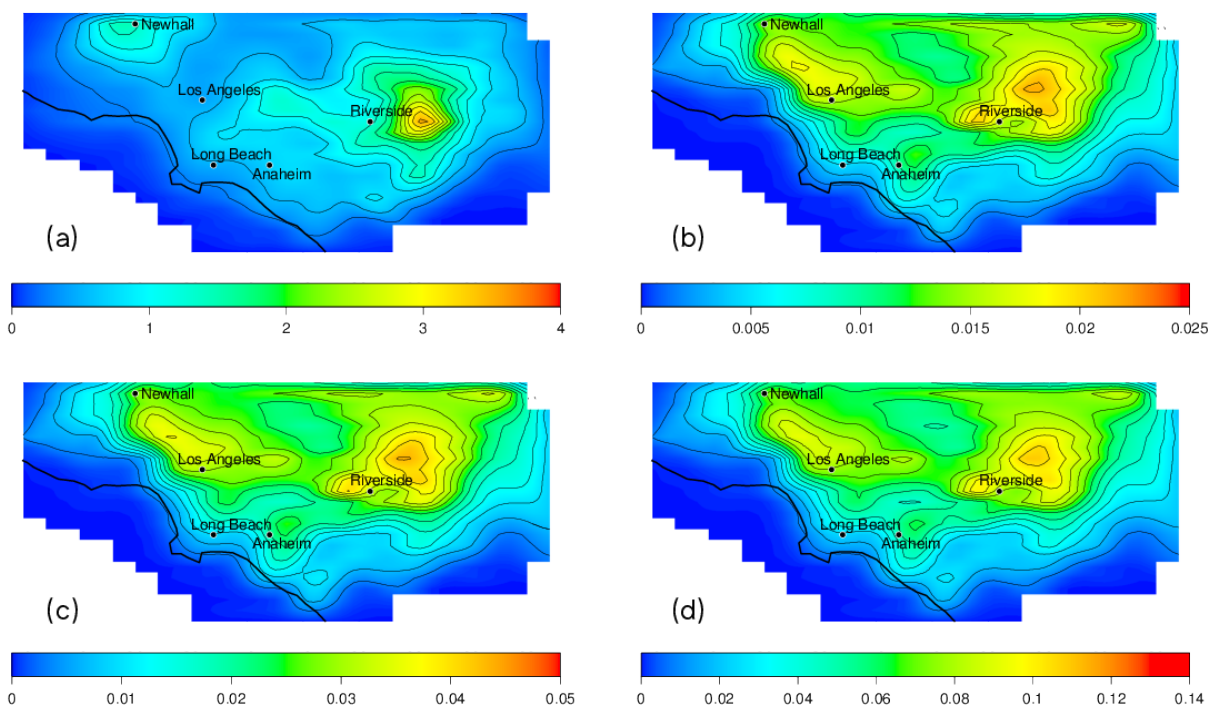


Figure 3.29. Twenty-four-hour average concentrations ($\mu\text{g m}^{-3}$) of (a) total SOA in the base case and additional SOA resulting from indole photooxidation in (b) the low emission scenario, (c) the medium emission scenario, and (d) the high emission scenario.

SOA concentrations averaged over the entire domain are shown in Figure 3.30 for the first four modeled scenarios. The averaged SOA concentrations were computed by averaging the concentration of total SOA in all computation cells in the domain. Therefore, changes in the averaged SOA concentrations are representative of the overall impact on total SOA concentrations for the entire basin. In the high emissions scenario, the averaged SOA concentrations increased by about 4-13%, indicating that indole+OH SOA can contribute significantly to total organic aerosol concentrations. While base case SOA concentrations peaked during the early morning and late-night hours when meteorological conditions were favorable, the largest *changes* in SOA concentrations occurred during the late morning and afternoon hours. The formation of gas-phase indigo dye and indole+OH SOA depends on the availability of the hydroxyl radical, which reaches peak concentrations during daylight hours when photochemistry is active. Therefore, increased production of hydroxyl radical during the daytime accelerates the oxidation of gas-phase indole, ultimately resulting in increased formation of indole+OH SOA. Increases in total SOA are due mostly to the formation of indole+OH SOA, with only small changes in the concentration of other SOA species.

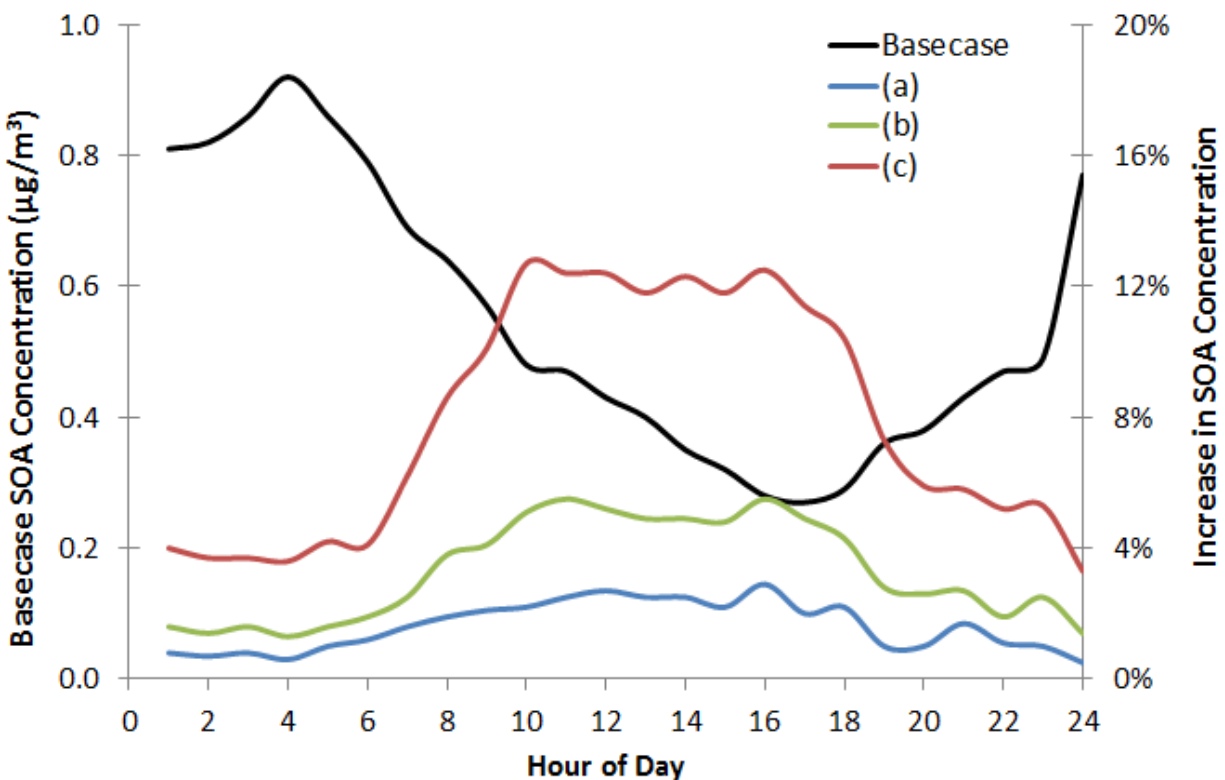


Figure 3.30. Domain-wide average SOA concentrations in the base case (black line, left axis) and the relative increase in domain-wide average SOA concentrations (right axis) driven by the oxidation of indole by OH in the (a) low emission scenario, (b) medium emission scenario, and (c) high emission scenario. Figure 3.32 additionally shows the effect of inclusion of the indole + NO₃ reaction on the model.

Figures 3.31 and 3.32 suggest that the oxidation of indole via reaction with NO₃ may also be an important pathway to indole SOA formation during the late night and early morning hours when photochemistry is inactive. When the oxidation of indole via reaction with NO₃ is included in the fifth modeled scenario, gas-phase indole concentrations are lower (Fig. 3.31) and indole SOA concentrations are higher (Fig. 3.32) than in the fourth scenario. The differences are most pronounced during the late night and early morning hours due to the different diurnal profiles of OH and NO₃; OH concentrations peak during the daytime hours when photochemistry is active, whereas NO₃ concentrations peak at night. Thus, the relative increase in total SOA concentrations due to indole SOA shows less temporal variability

throughout the day when the reaction of gas-phase indole with NO_3 is included in the model, but peak indole SOA concentrations remain essentially unchanged.

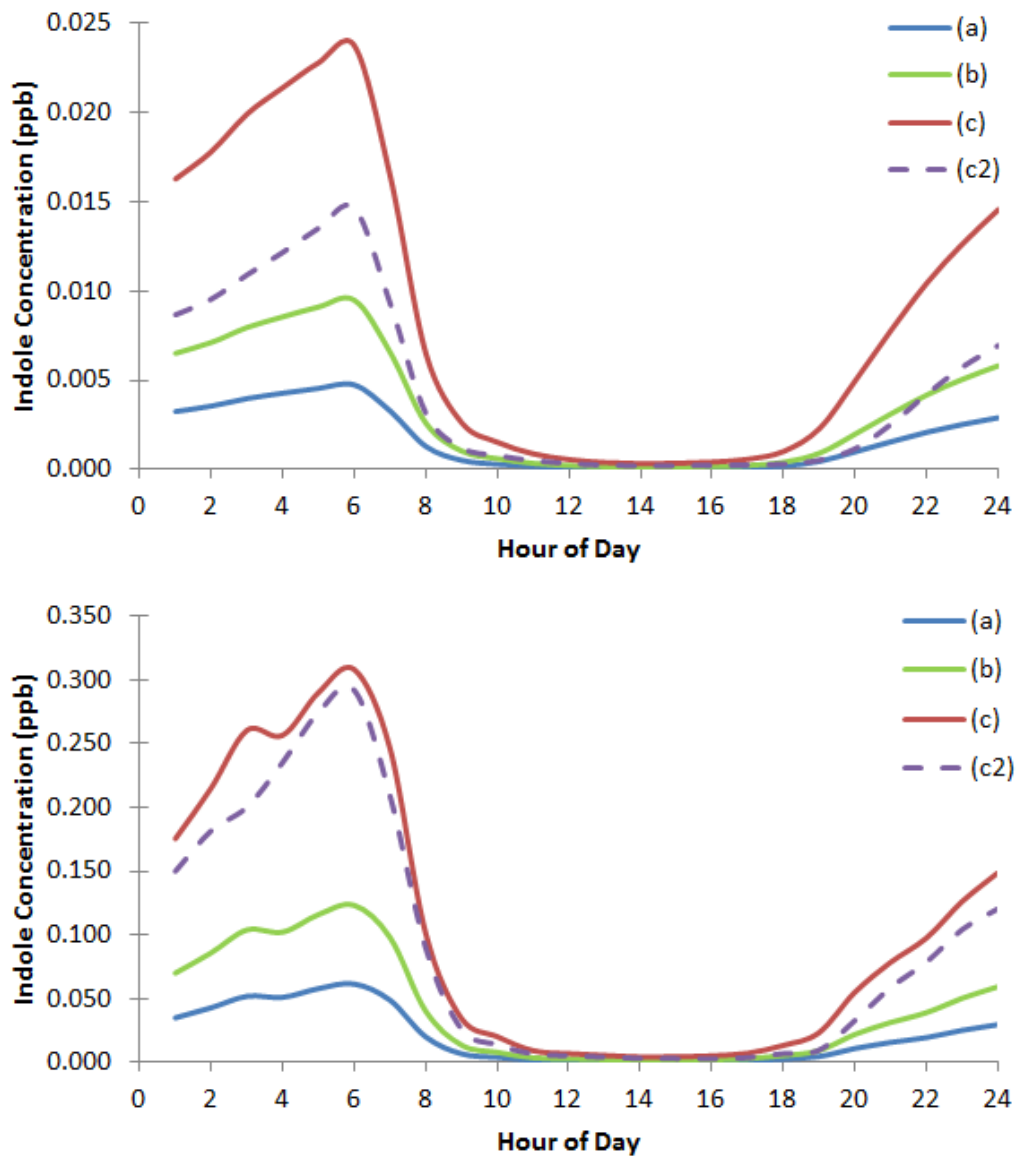


Figure 3.31. Gas-phase indole concentrations. The indole mixing ratios in ppbv are shown for the low emissions scenario (a), medium emissions scenario (b), and high emissions scenario (c). In addition, trace (c2) shows mixing ratios in the high emissions scenario with indole oxidation via reaction with NO_3 included in the model. Domain wide average concentrations are shown in the top panel and domain maximum concentrations are shown in the bottom panel.

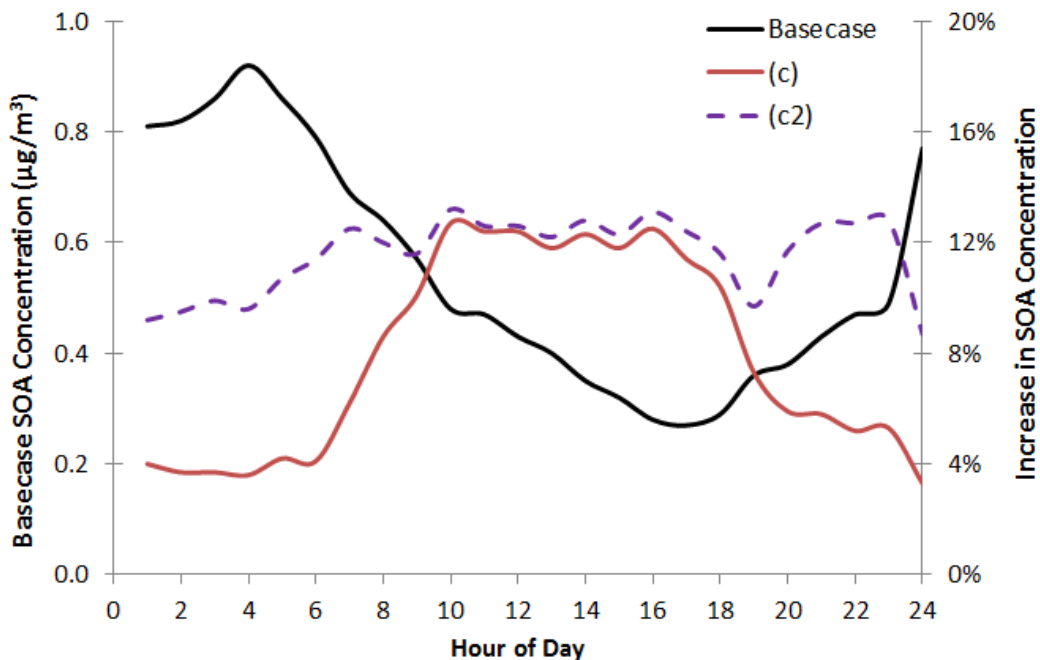


Figure 3.32. Domain wide average SOA concentrations. The base case mass concentration of SOA is shown in black line referenced to the left axis. Also shown is the percent increase in the domain wide average SOA concentrations (right axis) due to indole SOA in the high emissions scenario (c), and high emissions scenario with indole oxidation via reaction with NO_3 included in the model (c2). The daytime concentrations are not significantly affected by NO_3 but the nighttime concentrations increase.

The amount of indole SOA formed in each scenario was found to be directly proportional to the emissions of gas-phase indole. In the low emissions scenario, gas-phase indole and indole SOA concentrations were about factor of five lower than those seen in the high emissions scenario, with 24-hour average indole SOA concentrations peaking at about $0.025 \mu\text{g}/\text{m}^3$. Similarly, relative increases in the averaged SOA concentrations ranged from 1-3% in the low emissions scenario. In the medium emissions scenario, 24-hour average indole SOA concentrations reached about $0.05 \mu\text{g}/\text{m}^3$, causing total SOA concentrations to increase by 2-6%. In all three emissions scenarios, the spatial distribution of indole SOA remained essentially the same, with peak concentrations occurring in the northeast portion of the basin, an area already burdened with poor air quality.

3.6 Conclusions

This work demonstrates that indole is an effective precursor to SOA. At the concentrations used in this chamber study, the majority of indole photooxidation products ended up in the particle phase, with an effective SOA yield of $\sim 1.3 \pm 0.3$. SOA generated from either OH, O₃, or NO₃ oxidation was found to be strongly light-absorbing, with MAC values ranging from ~ 1 to $0.02 \text{ m}^2/\text{g}$ across the visible spectrum and approaching those of strongly-absorbing brown carbon from biomass burning. The high MAC values were due to various products of indole oxidation, including well-known chromophoric compounds such as isatin, tryptanthrin, indirubin, indoxyl red, and indigo dye which were identified by their molecular formulas and characteristic peaks in their absorption spectra. These observations suggest that N-heterocyclic compounds may be important contributors to secondary brown carbon. Moreover UV-Vis experiments of bulk indole SOA samples and BBCES experiments of indole SOA particles both showed that the absorption properties of indole SOA are sensitive to relative humidity. More experiments are necessary to better understand the role of water in indole oxidation reactions in order to better inform modelers of the absorptive properties of indole SOA in various RH environments.

Contribution of indole to SOA formation can potentially result in reduced visibility, particularly in regions where plants are exposed to biotic and abiotic stresses. When combining the experimental MAC values with peak SOA concentrations predicted in the model, the estimated maximum absorption coefficient is 0.05 Mm^{-1} due to indole+OH SOA. This is smaller than the values typically reported for SoCAB but comparable to values reported in more remote areas. Thus, despite its large MAC, indole+OH SOA is not likely to contribute to particle absorption in urban areas, where anthropogenic black carbon

dominates the aerosol absorption. However, the situation could be different in remote areas, where black carbon does not contribute to aerosol absorption, and indole emissions are higher.

The UCI-CIT regional airshed model showed significant potential for indole SOA formation driven by the oxidation of indole by OH. Simulations indicate that the oxidation of indole via reaction with NO_3 may also be an important SOA formation pathway during the late night and early morning hours when photochemistry is inactive. While the mass loading of indole SOA in the SoCAB was relatively low in all scenarios, it represents a previously unconsidered source of SOA in air quality models, which have been improved in recent years, but still tend to disagree with measured SOA concentrations (Couvidat et al., 2013; Heald et al., 2005; Hodzic et al., 2010; Jiang et al., 2012; Volkamer et al., 2006). Indole SOA can interact with other aerosol-phase species, causing indirect changes in the concentration of total SOA. Such interactions were not considered in this study because an activity coefficient of unity was used for indole SOA in the model simulations. Rural or agricultural regions with significant biomass burning or a high density of plant life likely have much higher emissions of gas-phase indole than the SoCAB. For example, field measurement studies (Gentner et al., 2014) reported ambient indole concentrations up to an order of magnitude greater than the peak modeled concentrations employed in this study, indicating a significant potential for indole SOA formation in rural areas. Furthermore, future climate change is likely to increase gas-phase indole emissions through environmental and physical stress factors such as drought, elevated temperatures, increased CO_2 and O_3 concentrations, and enhanced herbivore feeding (Yuan et al., 2009). Therefore, indole represents a potentially important source of biogenic SOA that should be included in regional and global models.

CHAPTER 4

Ammonia Uptake by Secondary Organic Aerosol

Portions of this chapter were reproduced under the Creative Commons Attribution 4.0 License and with permission from the American Chemical Society from:

Horne, J.R.; Zhu, S.; Montoya-Aguilera, J.; Hinks, M.L.; Wingen, L.M.; Nizkorodov, S.A.; Dabdub, D., Reactive uptake of ammonia by secondary organic aerosols: Implications for air quality, *Atmospheric Environment*, **189** (2018) 1-8.

Montoya-Aguilera, J.; Hinks, M.L.; Aiona, P.K.; Wingen, L.M.; Horne, J.R.; Zhu, S., Dabdub, D.; Laskin, A.; Laskin, J.; Lin, P.; Nizkorodov, S.A., Reactive uptake of ammonia by biogenic and anthropogenic organic aerosols, *ACS Symposium Series*, Volume 1299, Chapter 7, pp 127-147 in "Multiphase Environmental Chemistry in the Atmosphere", Hunt S., Laskin A., Nizkorodov S.A. Eds., 2018; ISBN13: 9780841233638. Copyright © 2018, American Chemical Society

Zhu, S.; Horne, J.R.; Montoya-Aguilera, J.; Hinks, M.L.; Nizkorodov, S.A.; Dabdub, D., Modeling reactive ammonia uptake by secondary organic aerosol in CMAQ: application to the continental US, *Atmospheric Chemistry and Physics*, **18** (2018) 3641-3657.

4.1 Background

As the most abundant basic gas in the atmosphere (Behera et al., 2013), gaseous ammonia (NH_3) has long been considered responsible for controlling the eutrophication and acidification of ecosystems (Erisman et al., 2008; Sheppard et al., 2011; Sutton et al., 1993). More recently, studies also demonstrated the importance of NH_3 in the formation of airborne fine particulate matter ($\text{PM}_{2.5}$) (Vayenas et al., 2005; Wang et al., 2013; West et al., 1999). Through reactions with acidic species, NH_3 is converted into ammonium salts, such as ammonium nitrate and ammonium sulfate, which constitute an important fraction of total $\text{PM}_{2.5}$ mass (Behera and Sharma, 2010). Fine particulate matter consists of approximately 25–50% inorganic compounds and 40–65% organic compounds on a mass basis (Gray et al., 1986; Zhang et al., 2000). Gaseous NH_3 is a precursor to inorganic aerosols and can be the limiting reactant in their formation (Wang et al., 2013; Lelieveld et al., 2015). These aerosols

have been proven to affect human health (Lelieveld et al., 2015; Pope III et al., 2002), visibility (Ye et al., 2011), and the atmospheric radiative balance (Park et al., 2014; Xu and Penner, 2012).

In the South Coast Air Basin of California (SoCAB), a large fraction of total $PM_{2.5}$ mass is comprised of ammonium sulfate (NH_4HSO_4 and $(NH_4)_2SO_4$) and ammonium nitrate (NH_4NO_3) (Kim et al., 2010), produced by the reaction of NH_3 with sulfuric acid (H_2SO_4) and nitric acid (HNO_3), respectively. In the SoCAB, the largest NH_3 emission sources are agricultural activities (e.g., dairy facilities) and automobiles (Nowak et al., 2012), whereas HNO_3 and H_2SO_4 come from the oxidation of NO_x and SO_2 from various combustion sources. The total automobile and agricultural NH_3 emissions are estimated as similar in magnitude (Nowak et al., 2012). However, the spatial concentration and high emissions of dairy facilities cause downwind NH_3 mixing ratios to be about an order of magnitude greater than those from vehicle emission sources (Nowak et al., 2012). These concentrated NH_3 plumes can be transported from their source region and react with inorganic acids to form ammonium salts. The high concentration of NH_3 in these plumes drives all of the H_2SO_4 and most of the HNO_3 into the particle phase, causing high concentrations of inorganic $PM_{2.5}$ in the eastern part of the SoCAB (Hughes et al., 2002; Neuman et al., 2003; Nowak et al., 2012).

In the US, the largest NH_3 emission source is agricultural activity (~ 85 % of total US NH_3 emissions) (Pinder et al., 2004, 2006), largely from animal waste and commercial fertilizer application, such as the intensive farming in California's Central Valley (Jovan and McCune, 2005) and industrialized hog farms in central North Carolina (Aneja et al., 2000; McCulloch et al., 1998). Ammonia-rich plumes from those areas drive most of the nitric acid into the particle phase, resulting in high $PM_{2.5}$ concentrations in those regions (Baek and Aneja, 2004;

Neuman et al., 2003). The equilibrium of this reaction is sensitive to relative humidity and temperature, with lower temperatures and higher humidity favoring the formation of the particle phase (Stelson et al., 1979; Stelson and Seinfeld 1982).

Over the past two decades atmospheric NH_3 has increased and is expected to continue increasing as a result of global warming, increasing agricultural activity, and intensifying fertilizer use due to a growing population (Amann et al., 2013; Galloway et al., 2008; Warner et al., 2017).

The conversion of inorganic gases into ammonium, nitrate, and sulfate particles is well understood (Seinfeld and Pandis, 2016). However, significant uncertainty remains regarding reactions between gaseous NH_3 and organic compounds found in secondary organic aerosols (SOA). Ammonia has been shown to react with certain carbonyl compounds found in SOA (Hawkins et al., 2016; Laskin et al., 2015). These reactions convert NH_3 into heterocyclic nitrogen-containing organic compounds (NOC) that remain in particles. The neglect of this process may result in an incorrect prediction of the distribution of organics in PM, and at the same time, over-prediction of gas-phase NH_3 , and therefore inorganic PM concentrations, in models. NOC have also been observed in ambient particles in California (O'Brien et al., 2013a, 2013b) and in China (Wang et al., 2010), with evidence for NH_3 playing a key role in their formation. For example, O'Brien et al. (2013b) analyzed the molecular composition of aerosol samples collected during CalNex 2010 in Bakersfield, California and concluded that NOC, which accounted for more than 40% of the observed organic compounds, were produced via reactions between NH_3 and carbonyl groups converting them into imines. Similarly, O'Brien et al. (2013a) compared the composition of field-collected and laboratory-generated SOA and found that some of the NOC observed in Bakersfield were likely formed

through reactions of products of oxidation of diesel fuel emissions with gas-phase NH_3 , potentially driven by high concentrations of gaseous NH_3 in the area. Their conclusions were supported by photochemical chamber experiments, where the addition of gaseous NH_3 to SOA generated from diesel fuel oxidation was necessary to produce many of the compounds observed in Bakersfield, and improved overlap between laboratory-generated and observed compounds. It is likely that similar reactions occur in the Los Angeles basin, particularly in areas downwind of strong NH_3 emissions sources with high NH_3 concentrations. In addition, a browning effect on SOA under NH_3 exposure was observed by Updyke et al. (2012), indicating the production of light-absorbing products. These processes are not included in current air quality models, which could lead to overestimation of gaseous NH_3 concentrations and thus inorganic aerosol concentration. Additionally, the neglect of these processes may also result in underestimation of organics aerosol, especially species related to acid-catalyzed reactions (Lin et al., 2013), and an incorrect prediction of aerosol particle acidity.

In 2015, Liu et al. reported for the first time chemical uptake coefficients for NH_3 onto SOA particles measured by direct observation of NOC by an aerosol mass spectrometer. The initial reactive uptake coefficients were on the order of 10^{-2} to 10^{-3} , dropping to 10^{-5} after six hours of reaction. Several other studies demonstrated chemical reactions between NH_3 and various types of SOA but have not quantified the uptake coefficients, rate constants, or equilibrium constants that could be used in models (Bones et al., 2010; Laskin et al., 2010; Updyke et al., 2012). The maximal yield of NOC in reactions between NH_3 and SOA has not been quantified, but there are indications that the yield is modest, on the order of a few percent (Laskin et al., 2014).

In this study, experiments were performed to explore the effect of NH_3 on SOA mass loading and composition in order to better constrain the maximal possible fraction of NOC in SOA after long-term exposure to NH_3 . Moreover, a surface reaction between NH_3 and SOA particles was implemented into the University of California, Irvine – California Institute of Technology (UCI-CIT) model based on the NH_3 uptake coefficients onto SOA reported by Liu et al. (2015) to estimate the impact of this process on NH_3 and $\text{PM}_{2.5}$ concentrations in the SoCAB region. Similarly, a first-order loss rate for NH_3 onto SOA was implemented into the Community Multiscale Air Quality (CMAQ) model in order to explore the impact of this uptake on air quality in the continental United States. In order to also investigate the seasonal impact on this process for the continental US, simulations were conducted for both winter and summer. Air quality simulations for both the SoCAB and continental US regions were conducted using a range of uptake coefficients to determine the sensitivity of NH_3 removal to the magnitude of the uptake coefficient. This study represents the first attempt to quantify the potential importance of including NH_3 + SOA chemistry in air quality models and presents the initial findings of implementing a simplified uptake mechanism into a high-resolution air quality model. Although there are limitations to the simplified mechanism implemented into the model, it provides a modeling framework and methodology that can be refined and applied in future studies to better characterize and simulate interactions between NH_3 and organic particles.

4.2 Experimental Methods

In order to confirm NOC formation in SOA + NH_3 reactions and establish an upper limit on the fraction of SOA compounds that can be converted to NOC, we performed several smog chamber experiments. A biogenic (limonene) or an anthropogenic (toluene, n-hexadecane)

VOC was oxidized in a 5 m³ Teflon chamber to generate SOA under low-NO_x conditions. We deliberately used low-NO_x conditions (even for anthropogenic VOCs) to avoid interference between NOC formed during the oxidation and NOC resulting from the reactive uptake of NH₃ onto SOA particles. No inorganic seed aerosol was used to avoid interference with mass-spectrometric analysis of SOA. Relative humidity (RH) in the chamber was achieved by flowing purified air through a Nafion humidifier. The relative humidity ($\pm 2\%$ RH) and temperature ($\pm 1^\circ\text{C}$) were monitored with a Vaisala HMT330 probe. The RH was $< 2\%$ for most experiments. However, in addition to generating toluene SOA at low RH, a set of experiments were also performed at $\sim 50\%$ RH due to the known high viscosity of toluene SOA at low RH. Limonene (97%, Sigma Aldrich) was introduced to the chamber to reach a mixing ratio of 500 ppb. Subsequently, 1 part per million by volume (ppm) of O₃ was introduced into the chamber, and gases in the chamber were mixed with a fan for 10 minutes. The fan was turned off after that to slow down particle wall loss. Anthropogenic SOA was produced from photooxidation of 1 ppm toluene (99.8%, Fisher Scientific) or 500 ppb n-hexadecane (99%, Sigma-Aldrich). In these photooxidation experiments, evaporated aqueous hydrogen peroxide (30 wt %, Fisher Scientific) was injected into the chamber by evaporation into a flow of clean air to achieve an initial mixing ratio of 2 ppm. After mixing with a fan for 10 minutes, UV-B lamps were turned on to initiate the photooxidation. After the particle mass concentration of SOA reached a peak value, a measured volume of gas mixture containing NH₃ (1000 ppm NH₃ in N₂, Airgas) was introduced into the chamber. The target mixing ratio of NH₃ in the chamber was supposed to be 500 ppb, however, due to losses in the inlet lines and chamber walls the actual mixing ratio of NH₃ was around 200 ppb as verified with an Ecotech 9842 NH₃/NO_x analyzer (which uses an external converter

to convert NH_3 to NO and then measures NO via chemiluminescence). Particle volume concentration was monitored with a scanning mobility particle sizer (SMPS; TSI 3936) equipped with a condensed particle counter (CPC; TSI 3775). The chemical composition of SOA particles was probed online with a Time-of-Flight Aerosol Mass Spectrometer (ToF-AMS). The ToF-AMS data were analyzed using PIKA 1.16I with SQUIRREL 1.57I software.

The polydispersed particles were collected on a Teflon filter (47 mm diameter, Millipore FGLP04700) at 20 L min^{-1} for 3 hours and prepared for composition analysis via direct analysis in real time mass spectrometry (DART-MS). The sample was extracted by placing the filter face down in a petri dish containing 3 mL of acetonitrile (LC-MS grade, 99.9% purity, Honeywell) and placed in a shaker for 5 minutes. Aliquots from the acetonitrile SOA extracts were transferred onto a clean stainless-steel mesh, dried in air and manually inserted between the DART ion source and mass spectrometer inlet. The DART-MS consisted of a Xevo TQS quadrupole mass spectrometer (Waters) equipped with a commercial DART ion source (Ion-Sense, DART SVP with Vapur® Interface). It was operated with the following settings: -350 V grid electron voltage, 3.1 L/min He gas flow, 350°C He gas temperature, and 70°C source temperature. The samples were analyzed with DART-MS in both positive and negative ion modes. Background spectra from the pure solvent were also collected and subtracted from the DART mass spectra.

Additional experiments were performed in which SOA particles were collected and then exposed to NH_3 vapor. The Teflon filter containing the collected particles was cut in half. Each filter half was placed in a small petri dish and was allowed to float on the surface of a liquid in a larger petri dish. One of the larger petri dishes contained nanopure water and another contained a 0.1 M ammonium sulfate (>99%, EMD) solution. Each larger petri dish

was covered separately and stored in the dark. The filter was never in direct contact with liquid, but it was exposed to the vapors above the liquid. The estimated mixing ratio of gaseous ammonia above 0.1 M ammonium sulfate solution is about 300 ppb according to AIM-II model [Clegg *et al.*, 1998]. In the case of limonene SOA, the filter that was aged over the ammonium sulfate solution became visibly brown, in agreement with previous experiments conducted in our group [Laskin *et al.*, 2010]. After two days of aging, the samples were extracted in acetonitrile and analyzed with DART-MS as described above.

In a typical DART ionization, a proton is either added (positive mode) or subtracted (negative mode) leading to largely unfragmented molecular ions of with an m/z of $[M+H]^+$ or $[M-H]^-$ ions, respectively. We expected the SOA compounds which were not exposed to NH_3 to consist of only C, H, and O atoms (CHO compounds). The CHO compounds have even nominal molecular weights and appear in the DART mass spectra at odd nominal m/z values. After the exposure, we expected some of the CHO compounds to be converted into molecules having one nitrogen atom. The resulting CHON compounds would have odd nominal molecular weights and appear at even m/z values. Our (crude) way of testing for the occurrence of the $CHO + NH_3 \rightarrow CHON$ reaction was to compare the combined abundances of all even peaks and odd peaks before and after the exposure to ammonia. Specifically, the average nitrogen fraction (f_N) of nitrogen-containing organic compounds (NOC) in the SOA sample exposed to NH_3 was estimated with the following equations:

$$f_N = \frac{1}{\sigma} (Ratio_{NH_3} - Ratio_{control}) \quad (4.1)$$

$$Ratio = \frac{\sum_{even} I_i}{\sum_{odd} I_i} \quad (4.2)$$

The variable “ σ ” accounts for the different ionization probability of CHON compounds (typically higher in the positive ion mode mass spectra) relative to that of CHO compounds. In the absence of better information, the average detection sensitivity for CHO and CHON was assumed to be equal ($\sigma = 1$). We note that this is a highly approximate treatment, and therefore, the fractional amount of nitrogen obtained from these equations should be treated as an order-of- magnitude estimate.

4.3 Modeling Methods

4.3.1 Modeling Methods for the South Coast Air Basin of California (SoCAB)

Modeling was performed to assess the potential impact of this chemistry on the formation of particulate matter at the regional and continental scales. All of the modeling simulations reported in this chapter were carried out by Professor Donald Dabdub, Dr. Jeremy Horne, and Dr. Shupeng Zhu. The UCI-CIT regional airshed model was used for the air quality simulations. The modeling domain covered the SoCAB, which contains Orange County and portions of Riverside, Los Angeles, San Bernardino, and Ventura counties. It utilized 994 computational cells, each with an area of 5 km \times 5 km. The unique modeling domain encompassed a variety of landscapes, including seaside communities, urban and suburban areas, and agricultural activity centered around Chino. Numerous studies have used the UCI-CIT model to simulate air quality in the SoCAB (Nguyen and Dabdub, 2002; Carreras-Sospedra et al., 2006, 2010; Chang et al., 2010; Horne and Dabdub, 2017; Montoya-Aguilera et al., 2017). The model's chemical mechanism is based on the Caltech Atmospheric Chemical Mechanism (CACM) (Griffin et al., 2002a, 2002b, 2005), expanded to include additional SOA precursors (Dawson and Griffin, 2016). The 3-day episode August 27–29 was chosen for the

air quality simulations, using meteorological conditions that typically occur in the region during the summertime and for which the model has been previously evaluated (Nguyen and Dabdub, 2002; Carreras-Sospedra et al., 2006, 2010; Chang et al., 2010), with 2008 emissions. The model's spatially and temporally resolved emissions were derived from the South Coast Air Quality Management District's 2012 Air Quality Management Plan (SCAQMD, 2013). A previous study conducted with the UCI-CIT model indicated that model-predicted NH₃ concentrations were similar to those measured in Chino during a field study (Perraud et al., 2015), supporting the accurate representation of NH₃ emissions in the model. Initial conditions and boundary conditions were based on values typical to the region. All results presented in this study were from the final simulation day using the emissions described above.

To explore the potential impact of the heterogeneous uptake of NH₃ by SOA on air quality, a parameterization of the removal of gaseous NH₃ by SOA compounds was implemented into the UCI-CIT model as follows. First, the total concentration of SOA in each of the eight size bins (C_{mass_1} , C_{mass_2} , ..., C_{mass_8}) was calculated. Next, assuming spherical particles with a density of 1.2 g/cm³, the area of SOA particles per volume of air was computed for each size bin (C_{area_1} , C_{area_2} , ..., C_{area_8}) from the mass concentration of SOA in each bin (C_{mass_1} , C_{mass_2} , ..., C_{mass_8}) and the representative (average) diameter of particles in that bin (dp_1 , dp_2 , ..., dp_8).

$$C_{area_i} = \frac{C_{mass_i}}{\rho} \times \frac{6}{dp_i} \quad (4.3)$$

The total available area of SOA particles per volume of air was then determined by summing the combined area of SOA particles in each of the eight size bins.

$$C_{area} = \sum_{i=1}^8 area_i \quad (4.4)$$

The area calculated by this approach is an approximation for the surface area presented by the SOA compounds because the actual particles contain inorganic species and have complex non-spherical morphologies. Finally, using an average speed of NH₃ molecules of 6.1×10^2 m/s (v_{NH_3}) at 298 K, the first-order loss rate constant, k , was calculated as

$$k = \gamma \times \frac{v_{NH_3} \times C_{area}}{4} \quad (4.5)$$

where γ is the reactive uptake coefficient for NH₃. The above calculations were performed separately for each model grid cell at every time step to determine the effective first order rate constant in that cell at that time. The loss rate for NH₃ was then determined from the first-order rate constant and the gas-phase NH₃ concentration in that cell at that time, with one limitation. The loss rate for NH₃ was limited by the yield of NOC observed in previous studies (Laskin et al., 2014) and estimated in this work. Specifically, we assumed that the yield of NOC from reactions between NH₃ and SOA compounds cannot exceed 10%. Therefore, the maximum amount of NH₃ that could be taken up by SOA in each model grid cell at each time step was 0.1 mole of NH₃ per mole of SOA compounds.

Ammonia uptake coefficients (γ values) were obtained from Liu et al. (2015), who studied particulate NOC formation after SOA formed from OH oxidation of m-xylene and ozonolysis of α -pinene were exposed to NH₃. They showed that NOC compounds can be formed reasonably quickly via the uptake of NH₃ by SOA and reported uptake coefficients for NH₃

onto SOA ranging from 10^{-5} to 10^{-2} , with an average value of 4.0×10^{-3} . Here, simulations were performed with a variety of γ values as reported by Liu et al. (2015) to determine the sensitivity of NH_3 removal to changes in the uptake coefficient. Figure 4.1 illustrates our modeling approach in which NH_3 (g) is in equilibrium with inorganic salts in $\text{PM}_{2.5}$ but may now also be irreversibly uptaken by organic aerosols and converted to NOC.

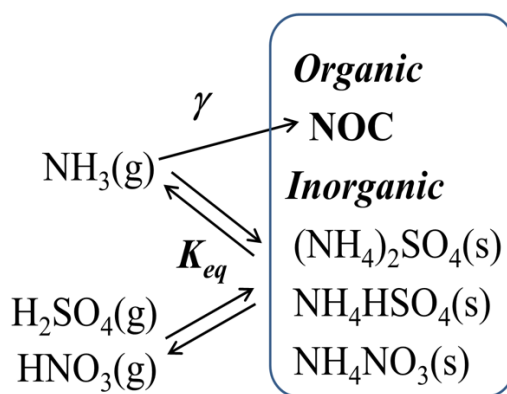


Figure 4.1. The modeling approach for the reactive uptake of ammonia by secondary organic aerosol. In addition to the equilibrium between ammonia and inorganic aerosol, the irreversible conversion of ammonia into NOC was added to the model, with its rate controlled by reactive uptake coefficient, γ . Since NOC is less basic than ammonia, formation of NOC reduces the amount of inorganic salts, as well as affects the particle pH.

In total, five scenarios were considered: (a) reference case with no NH_3 uptake, (b) NH_3 uptake with $\gamma = 10^{-2}$, (c) NH_3 uptake with $\gamma = 10^{-3}$, (d) NH_3 uptake with $\gamma = 10^{-4}$, and (e) NH_3 uptake with $\gamma = 10^{-5}$. Results for (b), (c), (d), and (e) were compared to the reference case model simulations in (a), where the removal of NH_3 by SOA was not included, to determine the impact on NH_3 and $\text{PM}_{2.5}$ concentrations. This study assumed that γ remained constant in each scenario (i.e., no saturation effects) and therefore each scenario represented an upper limit to the amount of NH_3 removed by SOA with the selected uptake coefficient. However, the uptake was programmed to stop once the molar fraction of NOC in SOA

particles reached 0.1, as mentioned above. A sensitivity analysis was performed to determine the influence of this assumption on simulation results. Additional model runs conducted assuming a maximum NOC molar fraction of 0.05 or 0.20 changed domain-averaged NH_3 and $\text{PM}_{2.5}$ concentrations by $< 1\%$ in all scenarios except (b) when the largest uptake coefficient (10^{-2}) was utilized. Although the impact on gas-phase NH_3 concentrations in this scenario was reduced and increased by about 5% when changing the assumed molar fraction of NOC from 0.10 to 0.05 and from 0.10 to 0.20, respectively, the impact on $\text{PM}_{2.5}$ concentrations remained essentially unchanged in both cases. All other model inputs (emissions, meteorology, etc.) were held constant between each scenario. Results presented here were for the final simulation day to provide adequate time for NH_3 uptake processes to occur and minimize the influence of initial conditions.

This study assumed that the NOC products of reactions between NH_3 and particulate organics remain in the particles and do not cause a significant increase in the mass concentration of particulate organics. In these reactions, carbonyl groups are first converted into primary imines, and further reactions lead to more stable secondary imines and heterocyclic compounds (Laskin et al., 2015). The uptake of NH_3 is accompanied by loss of one or several water molecules, and the molecular weight and volatility of the NOC product should not be too different from those of the starting SOA compound. Indeed, experiments by Liu et al. (2015) as well as our experiments show that there is no significant change in the particle mass concentration after exposure of SOA particles to NH_3 . Furthermore, although reactions between NH_3 and organic acids/carbonyls can potentially lead to condensable NOC (Duporté et al., 2017), we assumed that the contribution of these reactions to particle-phase NOC is negligible based on the results of Liu et al. (2015). In Liu et al. (2015), gas-phase

reactions leading to particulate NOC were assumed to be negligible based on (1) the observed anti-correlation between the calculated reactive uptake coefficient and NH_3 concentration, and (2) the exceedingly slow rate of the termolecular reaction between NH_3 , acid, and carbonyls required in the gas phase to form particle-phase NOC. Therefore, the chemical uptake of gas-phase NH_3 in the model was assumed to occur only via the surface reaction with SOA particles.

This study also assumed that NOC are less effective than NH_3 in neutralizing inorganic acids. In other words, the formation of nitrates and sulfates of protonated NOC (salts containing an organic cation and inorganic anion) was neglected. If the basicity of NOC were as high as that of NH_3 , the conversion of NH_3 into NOC would cause little to no change in PM concentrations. However, NH_3 is a stronger base compared to the stable NOC products it forms: the $\text{pK}_b = 4.8$ of NH_3 is smaller than pK_b of secondary imines ($\text{pK}_b \sim 10$) and nitrogen containing aromatic compounds (e.g., pyrrole $\text{pK}_b = 13.6$, pyridine $\text{pK}_b = 8.8$). Therefore, neglect of NOC salts is a reasonable approximation.

4.3.2 Modeling Methods for the Continental United States

The CMAQ modeling system (Byun and Schere, 2006) is a widely used state-of-the-art chemical transport model. In the United States, it is among the most commonly used air quality models in attainment demonstrations for National Ambient Air Quality Standards for ozone and $\text{PM}_{2.5}$ (US EPA, 2007). In our study, eight simulations were conducted using the 2017 release of CMAQ (version 5.2), including one base case simulation for the winter (Jan. 1 - Feb. 27, 2011), one base case simulation for the summer (1 July–30 August 2011), and

three different NH₃ uptake scenarios for each period. The carbon bond version 6 (CB6) mechanism (Yarwood et al., 2010) was used for the gas-phase chemistry, which includes 127 species as detailed on the website (Adams, 2017), and the AERO6 module was used for aerosol dynamics, which includes 21 inorganic species and 34 organic species (28 SOA and 6 primary organic species) as detailed on the CMASWIKI website (Pye, 2016). The modeling domain used in this study covers the contiguous US using a 12 km × 12 km horizontal-grid resolution (resulting in 396 (x) × 246 (y) = 97 416 grid cells) and a 29-layer logarithmic vertical structure (set on a terrain following sigma coordinate, from the surface to 50 hPa) with the depth of the first layer around 26 m. Only the simulation results from the first layer, representative of ground level, were used for the analysis in this study.

The meteorological fields were derived from NCEP FNL (Final) Operational Global Analysis data (NCEP, 2000) using the Weather Research and Forecasting Model (WRF, version 3.7) (Skamarock et al., 2008), with the MODIS land use database (Friedl et al., 2010) and the Yonsei University (YSU) parametrization (Hong et al., 2006) for the planetary boundary layer. The WSM3 scheme (Hong et al., 2004) was used for the microphysics option of WRF, and the Kain–Fritsch convective parametrization (Kain, 2004) was used for cumulus physics. These fields were then processed using version 4.3 of Meteorology–Chemistry Interface Processor (MCIP) (Otte and Pleim, 2010). The initial and boundary conditions were obtained from the Model for Ozone and Related Chemical Tracers (MOZART v2.0) (Horowitz et al., 2003). Emissions were generated based on the 2014 National Emissions Inventory (NEI) (US EPA, 2017a) and processed by the Sparse Matrix Operator Kernel Emission (SMOKE, version 4.5) processor (US EPA, 2017b). Biogenic emissions were obtained from the Biogenic

Emission Inventory System (BEIS) (Pierce and Waldruff, 1991), and emissions from cars, trucks, and motorcycles were calculated with MOBILE6 (US EPA, 2003).

In this study, the AERO6 module in CMAQ was updated to simulate the heterogeneous uptake of NH₃ by SOA. AERO6 used the modal representation to simulate aerosol dynamics (Binkowski and Roselle, 2003). The size distribution of the aerosol particles was represented by three log-normal modes: the Aitken mode (size up to approximately 0.1 μm), the accumulation mode (size between 0.1 to 2.5 μm), and the coarse mode (size between 2.5 to 10 μm). The particles were assumed to be internally mixed within each mode. In the AERO6 modal approach, three integral properties of the size distribution were followed for mode *j*: the total particle number concentration *N_j*, the total wet surface area concentration *S_j*, and the total mass concentration *m_{ij}* of each individual chemical component *i*. In order to calculate the total uptake of NH₃ by SOA, one must know the representative wet surface area concentration of SOA (*S_{SOA}*) (SOA hygroscopic growth is not considered in the model), which can be calculated as follows (assuming a uniform density across different chemical components):

$$S_{SOA} = \sum_{j=1}^x \left(S_j \times \frac{\sum_{i=1}^y m_{ij}}{\sum_{k=1}^z m_{kj}} \right) \quad (4.6)$$

where *y* is the total number of SOA species in mode *j*, *z* is the total number of aerosol species in mode *j*, and *x* is the total number of modes that contain SOA species. Here, *x* = 2 since SOAs only exist in the Aitken mode and the accumulation mode. From *S_{SOA}* the first-order rate of NH₃ uptake was calculated the same as in the UC-CIT model

$$k = \gamma \times \frac{v_{NH3} \times S_{SOA}}{4} \quad (4.7)$$

where γ is the reactive uptake coefficient for ammonia and v_{NH_3} is the average speed of NH_3 molecules. The above calculations were performed separately for each grid cell at every time step to obtain the effective first-order rate constant for each individual cell at each time step. The first-order rate constant of NH_3 uptake was then multiplied by the gas-phase NH_3 concentration to determine the loss rate of NH_3 in each cell at each time step.

As in the UCI-CIT modeling approach for the SoCAB region, we assumed that all NH_3 taken up by SOA carbonyls led to the formation of NOCs (Laskin et al., 2015). These reactions are expected to lead to the loss of one or more water molecules; because the difference in the molecular weights of water and ammonia is small, we neglected the mass loss of particulate organics directly due to the NH_3 uptake in these simulations.

Although, the NH_3 uptake process does not directly impact the mass of SOA, the conversion of NH_3 into NOCs can affect the SOA mass indirectly due to particle acidity changes. The particle acidity is altered because strongly basic NH_3 , which is converted into weakly basic NOCs, is no longer available to form inorganic salts of NH_4^+ . Therefore, as the extent of neutralization of inorganic acids with NH_3 is reduced, the particle acidity may increase.

A range of uptake coefficients (γ) based on the work of Liu et al., (2015) was selected and applied to all SOA species Liu et al. (2015) reported a range of possible uptake coefficients from 10^{-5} to 10^{-2} . However, some of our initial modeling tests showed that the use of a 10^{-2} uptake coefficient value would lead to an unrealistic amount of NH_3 taken up by SOA, where within a single time step the number of moles of NH_3 taken up exceeded 10 % of the total moles of SOA in one grid cell, a limit derived from the mass spectrometry experiments in our work. Based on this limit, an uptake coefficient of 10^{-3} was considered a more reasonable

upper limit value for the continental US simulations instead of the 10^{-2} upper limit applied in the SoCAB simulations. Therefore for the continental US, four simulations were performed for each period to investigate the sensitivity of NH_3 removal to changes in the uptake coefficient: (a) base case with no NH_3 uptake, (b) NH_3 uptake with $\gamma = 10^{-3}$, (c) NH_3 uptake with $\gamma = 10^{-4}$, and (d) NH_3 uptake with $\gamma = 10^{-5}$.

Results from each simulation were evaluated by comparing with observations from multiple monitoring networks. Then simulation results for scenario (b)–(d) are compared to the base case results in (a) to determine the impact of different uptake coefficients on different gas- and particle-phase species. The value of γ was assumed to remain constant in each scenario (i.e., no saturation or aging effects), which means each scenario represents an upper limit for the amount of NH_3 that would be taken up by SOA with the chosen value of the uptake coefficient. No further changes were made to the model or its inputs between each scenario. Results of the first 7 days of each simulations were discarded as a model spin-up period to minimize the effect of initial conditions and allow sufficient time for the NH_3 removal process to occur.

4.4 Experimental Results

After exposure of SOA to a pulse of NH_3 in the chamber, there was no change in the particle mass concentration for any of the three SOA systems (Fig. 4.2). After the experiments, we were able to get an NH_3 analyzer, which upon being connected to the chamber showed that most of the injected NH_3 was actually quickly removed by the chamber walls making it difficult to quantify the uptake coefficient from the ToF-AMS data. Despite the NH_3 wall loss, slow chemical uptake of NH_3 was observable in some ToF-AMS data. Specifically, when

limonene/O₃ SOA was exposed to NH₃, there was a slow increase in the N:C ratio (Fig. 4.3). However, we observed no uptake of NH₃ on toluene/OH SOA (Fig. 4.3), despite the fact that efficient uptake was observed by Liu et al. (2015) for related xylene/OH SOA. It is possible that the difference is due to the presence of NO_x in Liu et al. (2015) experiments and absence of NO_x in our experiments; the presence of nitric acid produced by photooxidation of NO_x is likely to promote uptake of NH₃ and subsequent acid-catalyzed conversion of NH₃ to NOC.

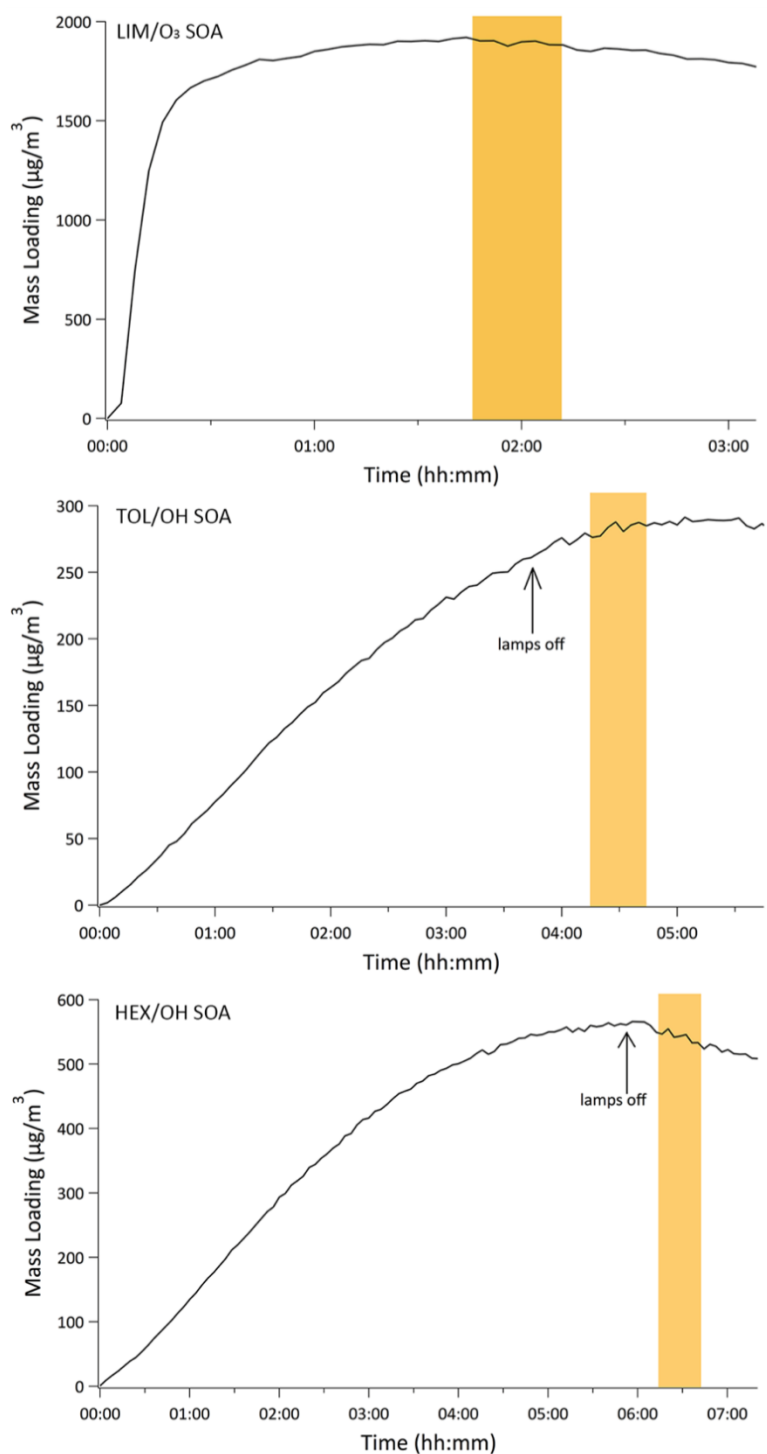


Figure 4.2. Plots showing the particle mass concentration over time under low RH conditions. The time during which NH₃ was injected in the chamber is shown by the shaded region. For all three SOA tested: limonene/O₃ SOA (top), toluene/OH SOA (middle), and n-hexadecane/OH SOA (bottom) the injection of ammonia did not have an effect on the total particle mass loading.

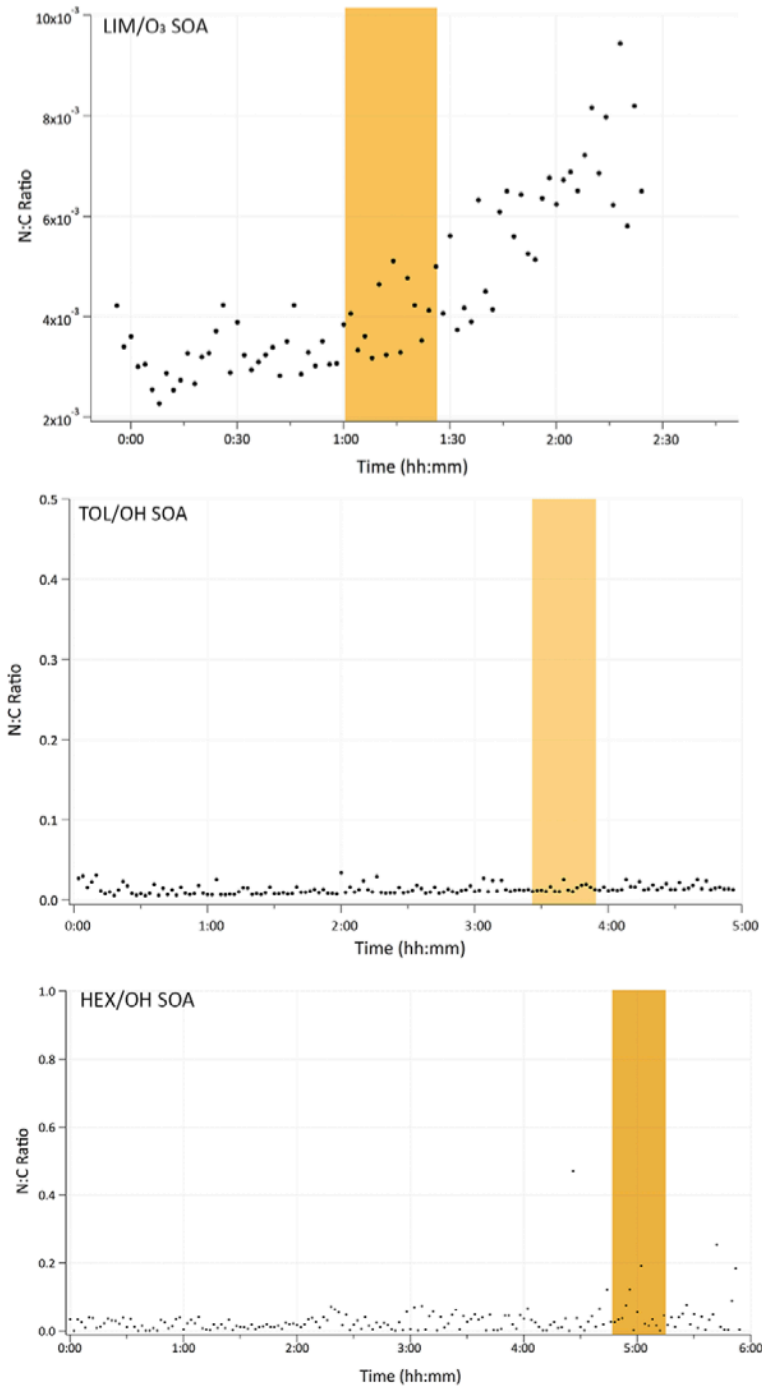


Figure 4.3. Plots showing the N:C ratio of the particle composition over time for limonene/ O_3 SOA and n-hexadecane/OH SOA generated under low RH and toluene/OH SOA generated under 54% RH in the chamber. Ammonia exposure (shaded region) caused a small increase in the N:C ratio in the limonene/ O_3 SOA (top). In contrast, after NH_3 exposure, no clear changes in N:C ratio were observed in the toluene/OH SOA (middle) nor n-hexadecane/OH SOA (bottom). Given the known higher viscosity of toluene/OH particles at low RH, toluene/OH was also generated at higher RH (54%) shown here. The H:C and O:C ratios (not shown) remained approximately constant in all three SOA systems over time.

There was an increase in the abundance of even m/z peaks in the DART mass spectra of the limonene/ O_3 SOA particles that were exposed to NH_3 in the chamber (Fig. 4.4). The fraction of NOC ($f_N = 20\%$) was estimated from the increases in the relative abundance of the even m/z peaks in the DART mass spectra based on the procedure described in the methodology section. Liu et al. (2015) reported comparable conversion efficiencies for SOA particles, with 9% of α -pinene/ O_3 SOA compounds and 32% of m-xylene SOA compounds (by mass) being converted to NOC. Prolonged exposure of bulk SOA filter samples to NH_3 led to browning of limonene/ O_3 SOA material, as observed in previous experiments (Updyke et al., 2012). The limonene/ O_3 bulk SOA sample exposed to NH_3 on a filter had an f_N value of 11%, lower than that resulting from an exposure of SOA particles to NH_3 in the chamber. These results suggest that NH_3 reacts with SOA more efficiently with suspended particles compared to the bulk SOA sample. It may also be that NH_3 is incorporated more effectively into the SOA as the SOA is forming. The f_N values for the toluene/OH and hexadecane/OH bulk SOA samples exposed to NH_3 were a factor of two smaller than for limonene/ O_3 SOA, with an f_N of 5% for both samples. This suggests that different types of SOA exhibit different reactivity towards NH_3 . The low values of f_N observed in this work are similar to the results of Laskin et al. (2014), who estimated from IR spectra that less than 5% of SOA carbonyls in SOA filter samples are converted in NOC.

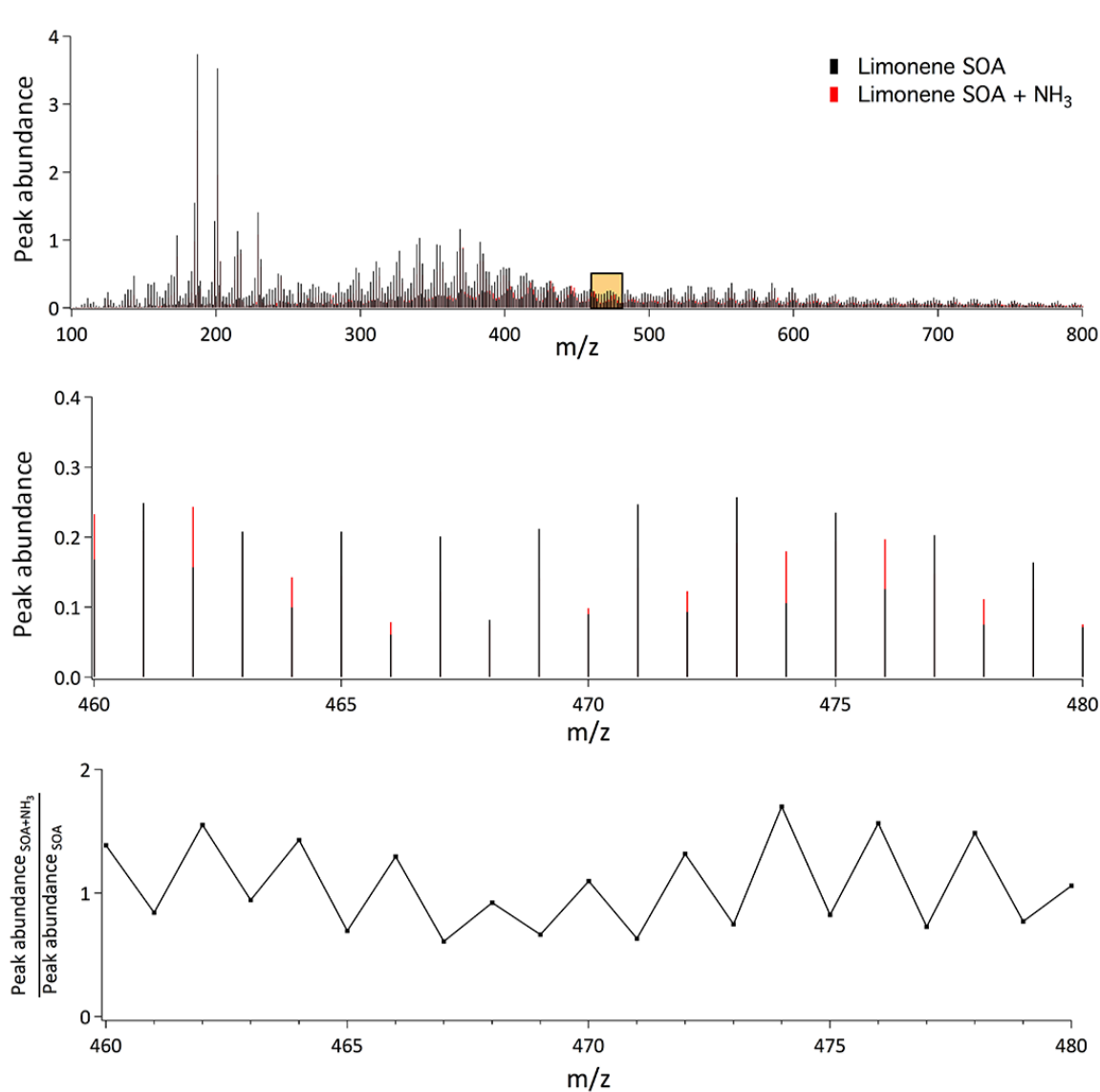


Figure 4.4. DART mass spectra of limonene/O₃ SOA samples generated under low RH conditions in the chamber in the absence of NH₃ (black) and in the presence of NH₃ (red). The shaded box in the top panel is magnified in the middle panel. In the bottom panel, the ratio of the peak abundance of the SOA exposed to NH₃ over the peak abundance of SOA not exposed to NH₃ is plotted as a function of m/z . The bottom plot illustrates how presence of NH₃ generally leads to an increase in the abundance of even m/z peaks in the limonene SOA system. The peak abundance at each m/z has been normalized with respect to the sum of total peak abundances in each mass spectrum.

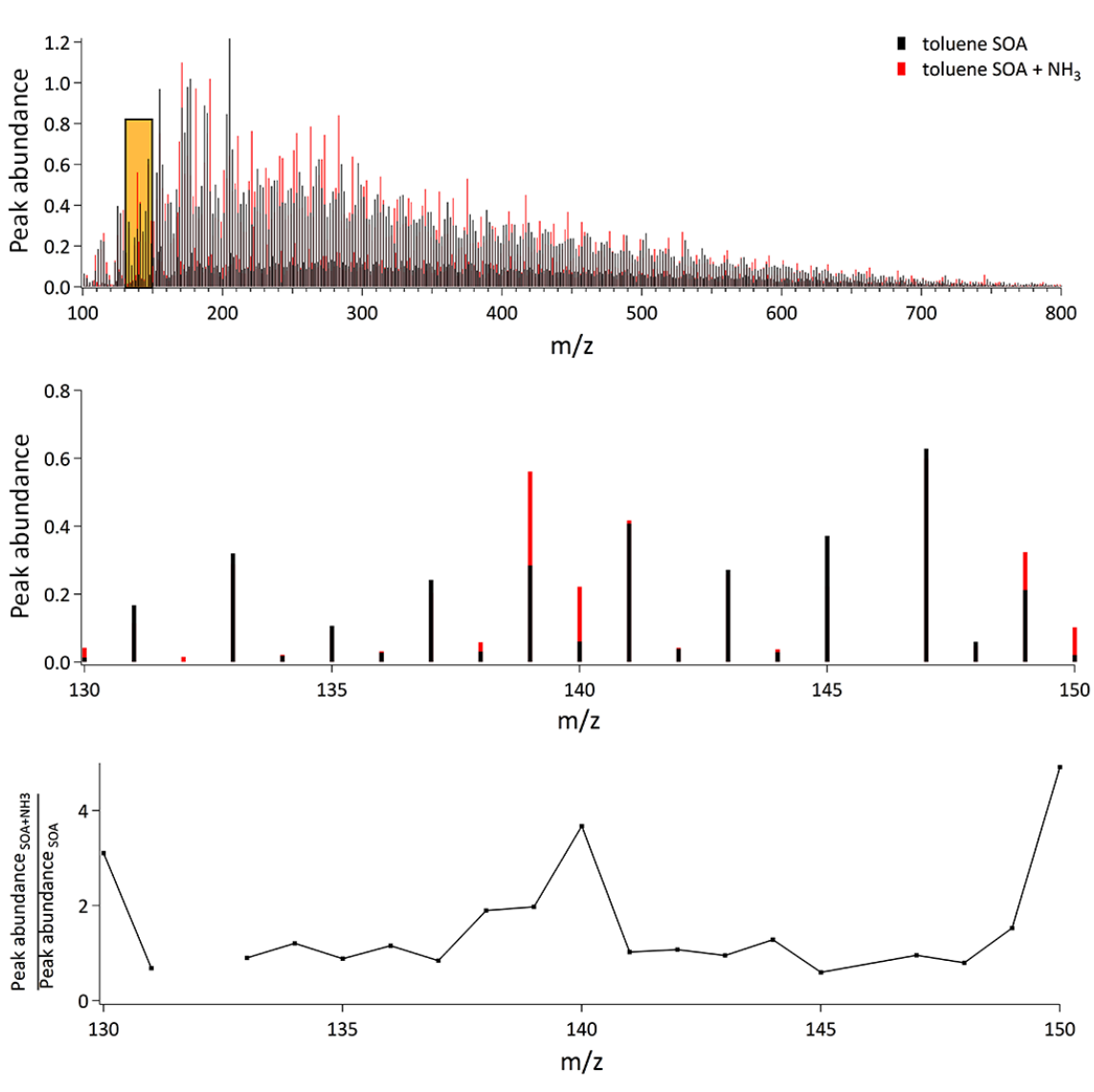


Figure 4.5. DART mass spectra of toluene/OH SOA samples generated under low RH conditions in the chamber in the absence of NH_3 (black) and in the presence of NH_3 (red). The boxed region in the top panel is magnified in the middle panel. In the bottom panel, the ratio of the peak abundance of the SOA exposed to NH_3 over the peak abundance of SOA not exposed to NH_3 was plotted as a function of m/z . The bottom plot illustrates how NH_3 exposure generally leads to an increase in even m/z peaks in toluene SOA products. The peak abundance at each m/z has been normalized with respect to the sum of total peak abundances in each mass spectrum.

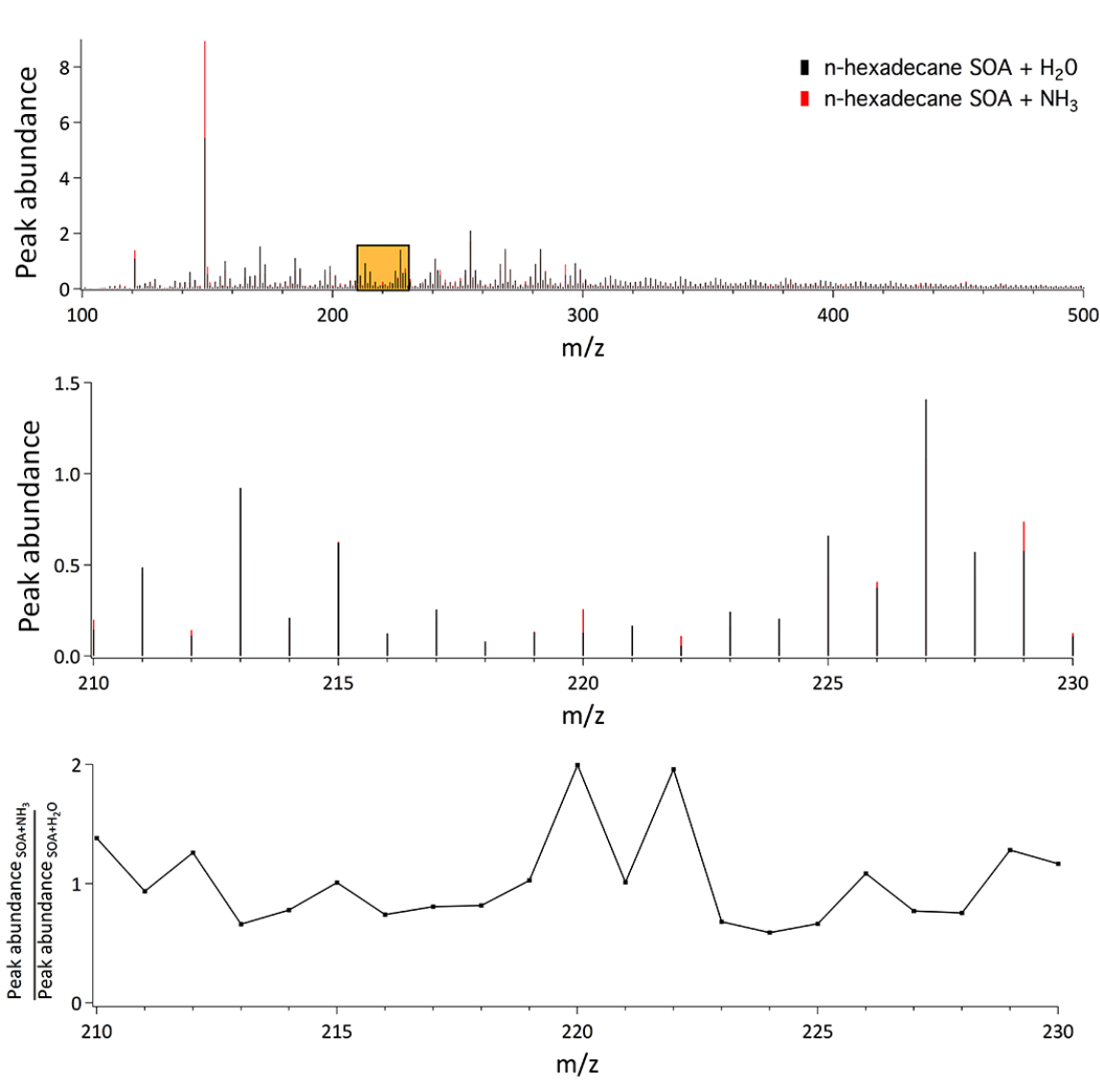


Figure 4.6. DART mass spectra of n-hexadecane/OH SOA samples generated under low RH conditions in the chamber, collected onto filters, and then aged in the presence of H₂O (black) and NH₃ (red). The shaded box in the top panel is magnified in the middle panel. In the bottom panel, the ratio of the peak abundance of the SOA exposed to NH₃ over the peak abundance of SOA exposed to H₂O was plotted as a function of m/z . The bottom plot illustrates how NH₃ exposure generally leads to an increase in even m/z peaks in the n-hexadecane SOA system. The peak abundance at each m/z has been normalized with respect to the sum of total peak abundances in each mass spectrum.

In summary, the experiments described here generally support the assumptions made in the model, specifically, the assumption that on the order of 10% of SOA compounds can be converted to NOC. However, they do not provide additional information on the uptake coefficients relative to the previous study by Liu et al. (2015).

4.5 Model Predictions for the SoCAB

The air quality impacts of including the uptake of NH_3 by SOA vary greatly between scenarios depending on the magnitude of the uptake coefficient. Table 4.1 and Fig. 4.7 show the impact of the $\text{NH}_3 + \text{SOA}$ reactions on the domain-averaged hourly NH_3 and $\text{PM}_{2.5}$ concentrations. When using $\gamma = 10^{-2}$, domain wide average NH_3 concentrations decrease by 15–40%, with the greatest percentage decreases (30–40%) occurring between 08:00 h and 17:00 h local time. Because domain wide averages are computed by averaging all cells in the model domain, this indicates that more than one third of all gas-phase NH_3 in the basin is removed in this scenario during these times. However, the decrease in NH_3 concentrations is highly spatially dependent. In certain areas, such as those with a high concentration of SOA and relatively low (<40 ppb) gas-phase NH_3 concentrations in the reference case, hourly NH_3 concentrations decrease by over 60%. On the other hand, areas near the coast experience little change in NH_3 concentration due to low levels of both gaseous NH_3 and SOA in the reference case (see Fig. 4.8 for map of SOA concentrations in the reference case).

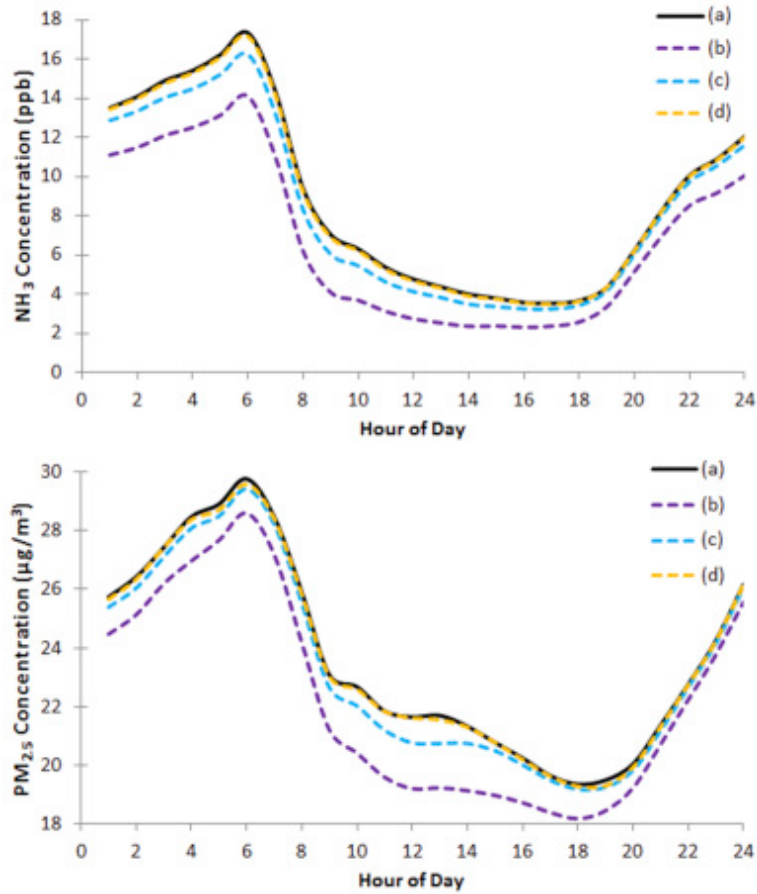


Figure 4.7. Domain wide average concentrations of ammonia (NH₃, top panel) and PM_{2.5} (bottom panel) in the (a) base case, (b) $\gamma = 10^{-2}$ scenario, (c) $\gamma = 10^{-3}$ scenario, and (d) $\gamma = 10^{-4}$ scenario. Ammonia and PM_{2.5} concentrations change by less than 1% at all hours of the day in the $\gamma = 10^{-5}$ scenario (not shown).

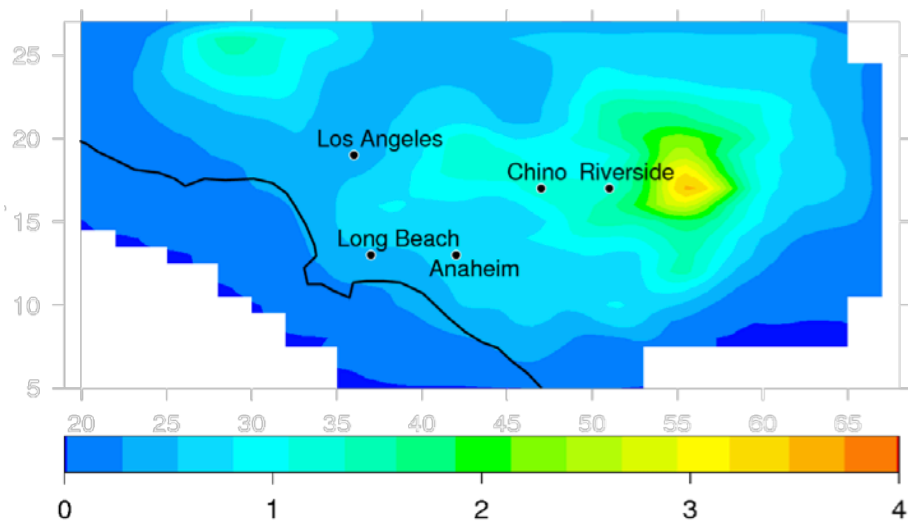


Figure 4.8. 24-hour average concentrations of SOA (µg/m³) in the reference case.

Table 4.1. Domain-averaged (left columns) ammonia concentrations (NH₃, ppb) and (right columns) PM_{2.5} mass concentrations (µg/m³) in the reference case shown in (a). Absolute and percent change in concentration versus the reference case shown in (b), (c), and (d) when using (b) $\gamma=10^{-2}$, (c) $\gamma=10^{-3}$, and (d) $\gamma=10^{-4}$. Decreases relative to the reference case are indicated by negative values. Changes in concentration less than the number of significant digits shown are indicated by a double dash (--). Both NH₃ and PM_{2.5} concentrations change by less than 1% when using (e) $\gamma=10^{-5}$ (not shown).

NH ₃				Hour	PM _{2.5}			
a	b	c	d		a	b	c	d
13.5	-2.4, 17.8%	-0.6, - 4.7%	-0.1, - 0.5%	1	25.7	-1.3, - 4.9%	-0.4, -1.4%	-0.1, -0.3%
14.1	-2.6,- 18.5%	-0.8, - 5.3%	-0.1, - 0.8%	2	26.4	-1.3, -4.9%	-0.4, -1.5%	-0.1, -0.3%
14.9	-2.8,- 18.8%	-0.9, - 5.8%	-0.1, - 0.9%	3	27.4	-1.2, -4.5%	-0.3, -1.2%	--
15.4	-2.9,- 18.8%	-0.9, - 6.0%	-0.1, - 0.8%	4	28.4	-1.5, -5.2%	-0.4, -1.4%	-0.1, -0.3%
16.2	-3.1,- 19.0%	-1.0, - 6.2%	-0.1, - 0.9%	5	28.8	-1.2, -4.3%	-0.4, -1.4%	-0.2, -0.7%
17.4	-3.2,- 18.7%	-1.1, - 6.3%	-0.2, - 1.0%	6	29.7	-1.2, - 3.9%	-0.4, -1.2%	-0.2, -0.6%
14.3	-3.3,- 23.3%	-1.1, - 7.9%	-0.2, - 1.1%	7	28.5	-1.3, -4.5%	-0.3, -0.9%	-0.1, -0.2%
9.4	-3.2,- 34.0%	-1.1,- 11.5%	-0.2, - 1.7%	8	25.9	-1.7, -6.6%	-0.4, -1.5%	-0.1, -0.3%
7.1	-3.0,- 41.8%	-1.0,- 14.3%	-0.1, - 1.9%	9	23	-1.9, -8.1%	-0.4, -1.8%	-0.1, -0.2%
6.4	-2.6,- 41.5%	-0.9,- 13.6%	-0.1, - 1.7%	10	22.5	-2.3,- 10.0%	-0.7, -2.9%	-0.1, -0.4%
5.3	-2.2,- 41.8%	-0.7,- 13.8%	-0.1, - 2.0%	11	21.9	-2.2,- 10.3%	-0.7, -3.0%	--
4.8	-2.2,- 41.8%	-0.6,- 13.2%	-0.1, - 1.9%	12	21.6	-2.4,- 11.3%	-0.9, -4.1%	--
4.4	-1.8,- 41.9%	-0.5,- 12.4%	-0.1, - 1.3%	13	21.7	-2.5,- 11.3%	-0.9, -4.3%	-0.2, -0.7%
4	-1.6,- 40.6%	-0.5,- 12.4%	-0.1, - 2.1%	14	21.4	-2.2,- 10.3%	-0.6, -2.7%	--
3.8	-1.4,- 37.2%	-0.4,- 11.1%	--	15	20.8	-1.8, -8.7%	-0.3, -1.4%	--

3.6	-1.3,- 35.3%	-0.3, - 9.1%	--	16	20.3	-1.5, - 7.5%	-0.2, -1.1%	-0.1, -0.2%
3.5	-1.2,- 32.9%	-0.3, - 7.8%	--	17	19.7	-1.3, - 6.4%	-0.2, -0.7%	--
3.7	-1.1,- 29.7%	-0.2, - 6.4%	--	18	19.4	-1.2, - 6.0%	-0.2, -0.9%	-0.1, -0.4%
4.4	-1.0,- 22.6%	-0.2, - 3.9%	--	19	19.4	-1.0, - 5.3%	-0.2, -1.2%	-0.2, -0.9%
6.2	-1.1,- 17.3%	-0.2, - 3.1%	--	20	19.9	-0.8, - 4.1%	-0.2, -1.1%	-0.1, -0.6%
8.3	-1.3,- 15.7%	-0.2, - 2.9%	--	21	21.3	-0.7, - 3.0%	-0.2, -0.8%	-0.1, -0.2%
10.1	-1.5,- 15.2%	-0.3, - 3.0%	--	22	22.7	-0.5, - 2.3%	-0.1, -0.4%	--
10.9	-1.7,- 15.8%	-0.3, - 3.1%	-0.1, - 0.5%	23	24.2	-0.5, - 2.0%	-0.1, -0.4%	--
12.1	-2.0,- 16.6%	-0.5, - 3.7%	-0.1, - 0.5%	24	26.1	-0.6, - 2.3%	-0.1, -0.4%	--

Fig. 4.9 shows the spatially resolved 24-h average NH_3 concentrations in the reference case and the changes induced by the reactive uptake of NH_3 . The greatest decreases occur near and downwind of areas with agricultural activity and large quantities of NH_3 emissions. 24-hour average NH_3 concentrations near Chino peak at 250 ppb in the reference case and are reduced by up to 15 ppb in the same area when using $\gamma = 10^{-2}$ (Fig. 4.9b, left column). Although the greatest decreases occur near the strongest emissions sources, NH_3 continues to be removed by SOA as it is transported further inland. As a result, hourly and 24-h average NH_3 concentrations decrease by 15–20 ppb and 5–10 ppb, respectively, for many areas in the northeast portion of the basin. Changes in the concentration of gas-phase NH_3 can affect the formation of inorganic PM due to its rapid reaction with different acids (e.g., nitric acid and

sulfuric acid) to form corresponding salts, which contribute to secondary particle formation and particle growth (Schiferl et al., 2014).

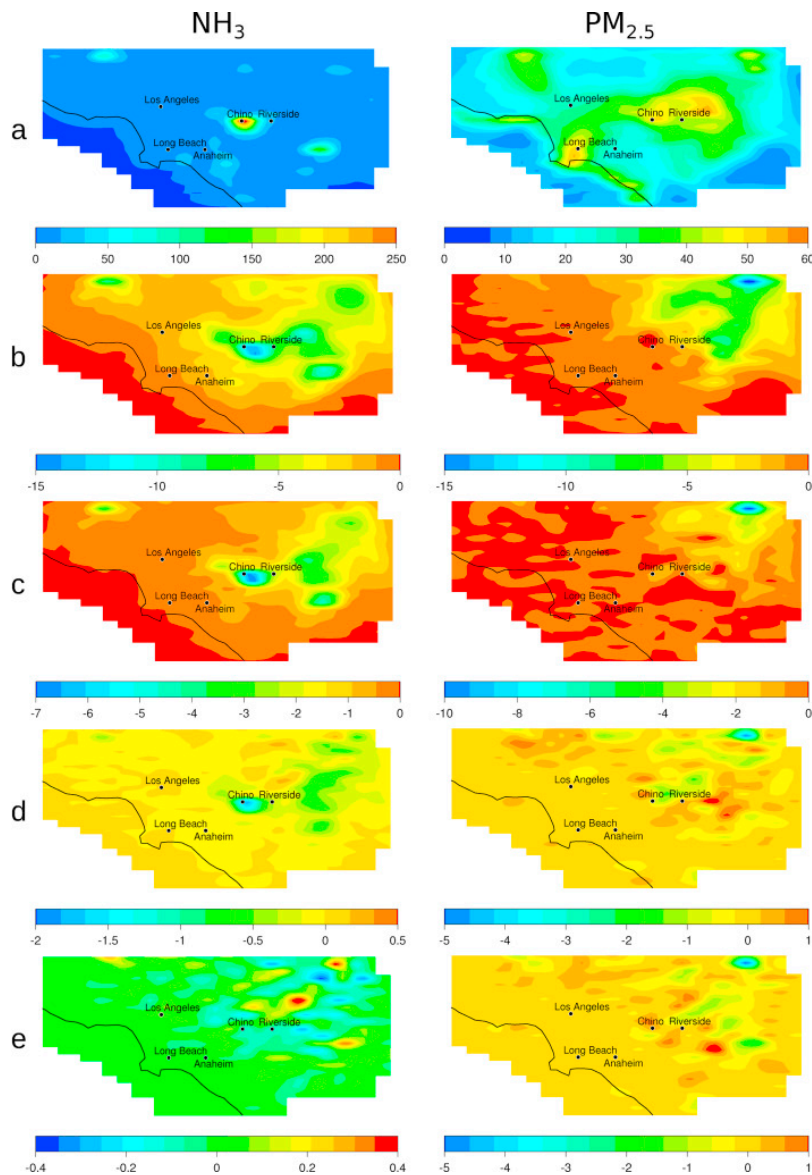


Figure 4.9. 24-hour average concentrations of NH_3 (ppb) and $\text{PM}_{2.5}$ ($\mu\text{g}/\text{m}^3$) in the reference case shown in (a). Difference in concentration versus the reference case shown in rows (b), (c), (d), and (e) when using (b) $\gamma = 10^{-2}$, (c) $\gamma = 10^{-3}$, (d) $\gamma = 10^{-4}$, and (e) $\gamma = 10^{-5}$. Concentration decreases relative to the reference case are indicated by negative values.

Table 4.1 shows domain-averaged concentrations of $\text{PM}_{2.5}$ in the reference case, as well as the absolute and percent change in concentration for scenarios (b), (c), and (d) versus the

reference case, (a). With the uptake coefficient of 10^{-2} used in this scenario, decreases in domain wide average concentrations range from 2% late at night to 11% during midday (Fig. 4.7). In some locations, the impact on hourly $PM_{2.5}$ concentrations is far greater, with decreases up to $35 \mu\text{g}/\text{m}^3$ (60%) in areas northeast of Riverside. A combination of meteorological and geographical features in the SoCAB cause the buildup of pollutants in the downwind (northeastern) portion of the basin. A sea breeze during the daytime hours causes predominantly southwesterly winds while the northern edge of the domain is bounded by mountainous terrain in the Angeles and San Bernardino National Forests, preventing pollutants from being transported further inland. Thus, NH_3 continues to be taken up by SOA as it is transported inland, causing the largest impacts on PM to occur in the downwind areas of the basin where a variety of anthropogenic and biogenic precursors accumulate, rather than near NH_3 emissions sources.

Fig. 4.9 shows that the greatest impacts on 24-h average $PM_{2.5}$ concentrations occur in the northeastern area of the basin. Here, reference case levels range from 40 to $55 \mu\text{g}/\text{m}^3$ (Fig. 4.9) and decrease by up to $15 \mu\text{g}/\text{m}^3$ in this scenario (Fig. 4.9b, right column). Previous studies showed that concentrated NH_3 plumes from agricultural activity shift the NH_4NO_3 equilibrium towards the particle phase, leading to coincident formation of NO_3^- and NH_4^+ particles and depletion of gas-phase HNO_3 in downwind areas of the basin (Hughes et al., 2002; Neuman et al., 2003; Nowak et al., 2012). Additionally, these studies suggested that NH_4NO_3 particle formation in the SoCAB could be best controlled by reducing the highly concentrated NH_3 emissions from agricultural activity, rather than emissions from automobiles, which are well distributed throughout the domain. Here we show that decreases in NH_3 concentration due to uptake by SOA reduce the availability of gas-phase

NH_3 to react with HNO_3 and H_2SO_4 to form NH_3 nitrate and ammonium sulfate particles, and that the largest impacts occur directly downwind of strong NH_3 emissions sources. Changes in the concentration of gas-phase HNO_3 and H_2SO_4 , shown in Fig. 4.10, are consistent with this result. Because gas-phase HNO_3 and H_2SO_4 concentrations are inversely correlated with gas-phase NH_3 concentrations, HNO_3 and H_2SO_4 concentrations are generally higher in scenarios (b), (c), (d) and (e) than in the reference case. In particular, areas that show decreases in ammonium nitrate particle concentrations typically show increases in gas-phase nitric acid concentrations. This confirms that reductions in gas-phase NH_3 concentrations cause the equilibrium between $\text{NH}_3(\text{g})$ and $\text{NH}_4\text{NO}_3(\text{s})$ to shift toward the gas phase.

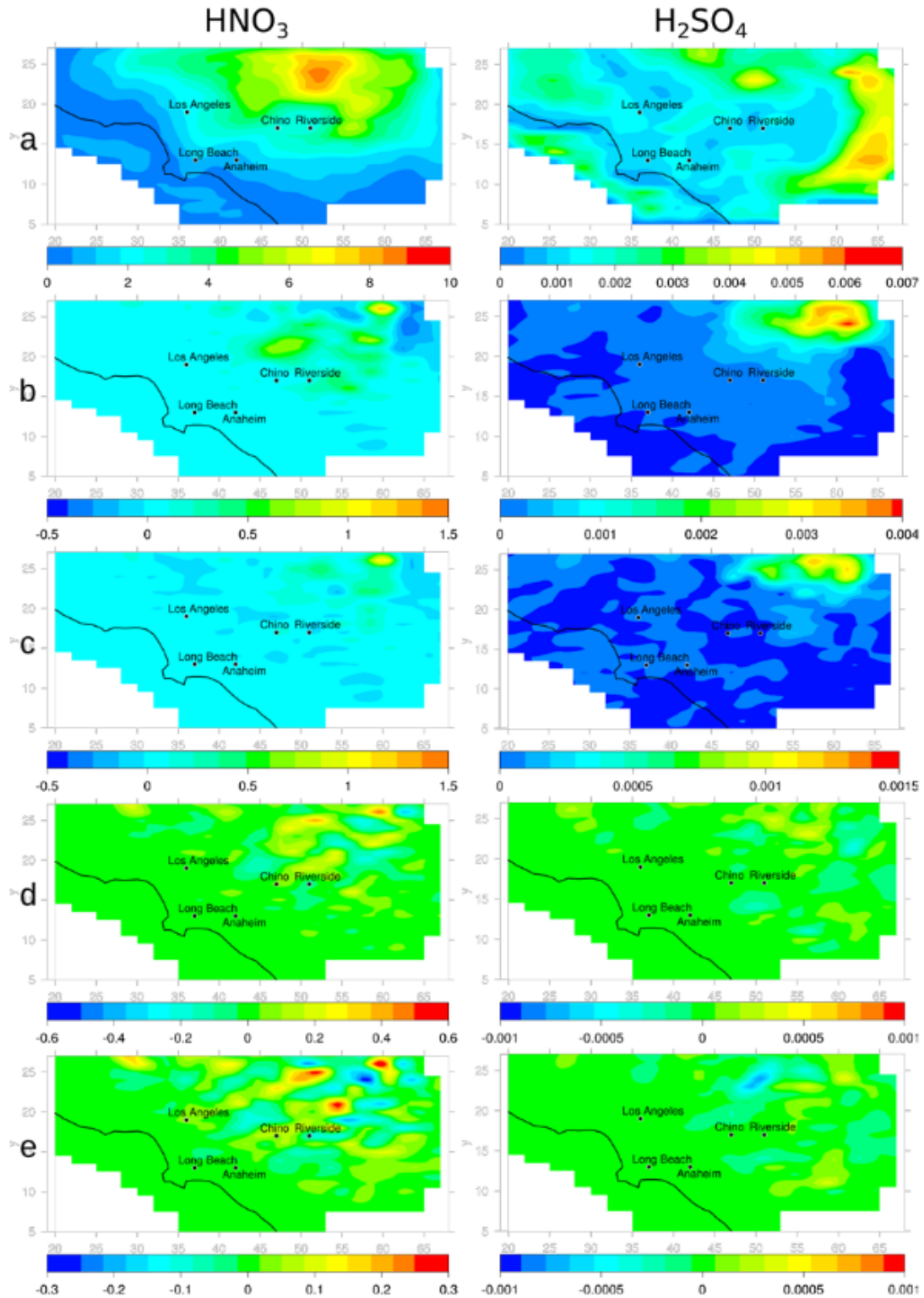


Figure 4.10. 24-hour average concentrations of nitric acid (HNO_3 , ppb) and sulfuric acid (H_2SO_4 , ppb) in the base case shown in (a). Difference in concentration versus the base case shown in rows (b), (c), (d) and (e) when using (b) $\gamma=10^{-2}$, (c) $\gamma=10^{-3}$, (d) $\gamma=10^{-4}$ and (e) $\gamma=10^{-5}$. Negative values represent decreases in concentration with respect to the base case.

Fig. 4.11 shows reference case levels and the change in 24-h nitrate (NO_3^-), ammonium (NH_4^+), and sulfate (SO_4^{2-}) particle concentrations for scenarios (b), (c), (d) and (e) versus the reference case, (a). These figures show that although the spatial distribution of these species differs in the reference case (because of the different patterns of SO_2 and NO_x emissions), the largest changes in 24-h average concentrations for all three particulate species generally occur in the same geographical area northeast of Riverside. Together, decreases in nitrate, ammonium, and sulfate particle concentrations account for essentially all of the decrease in total $\text{PM}_{2.5}$ concentrations shown in Fig. 4.9. The spatial distribution and magnitude of model-predicted nitrate particle concentrations in the reference case (Fig. 4.11a, left column) agree with those measured by Neuman et al. (2003), who reported a peak concentration of $12.7 \mu\text{g}/\text{m}^3$ near Rubidoux.

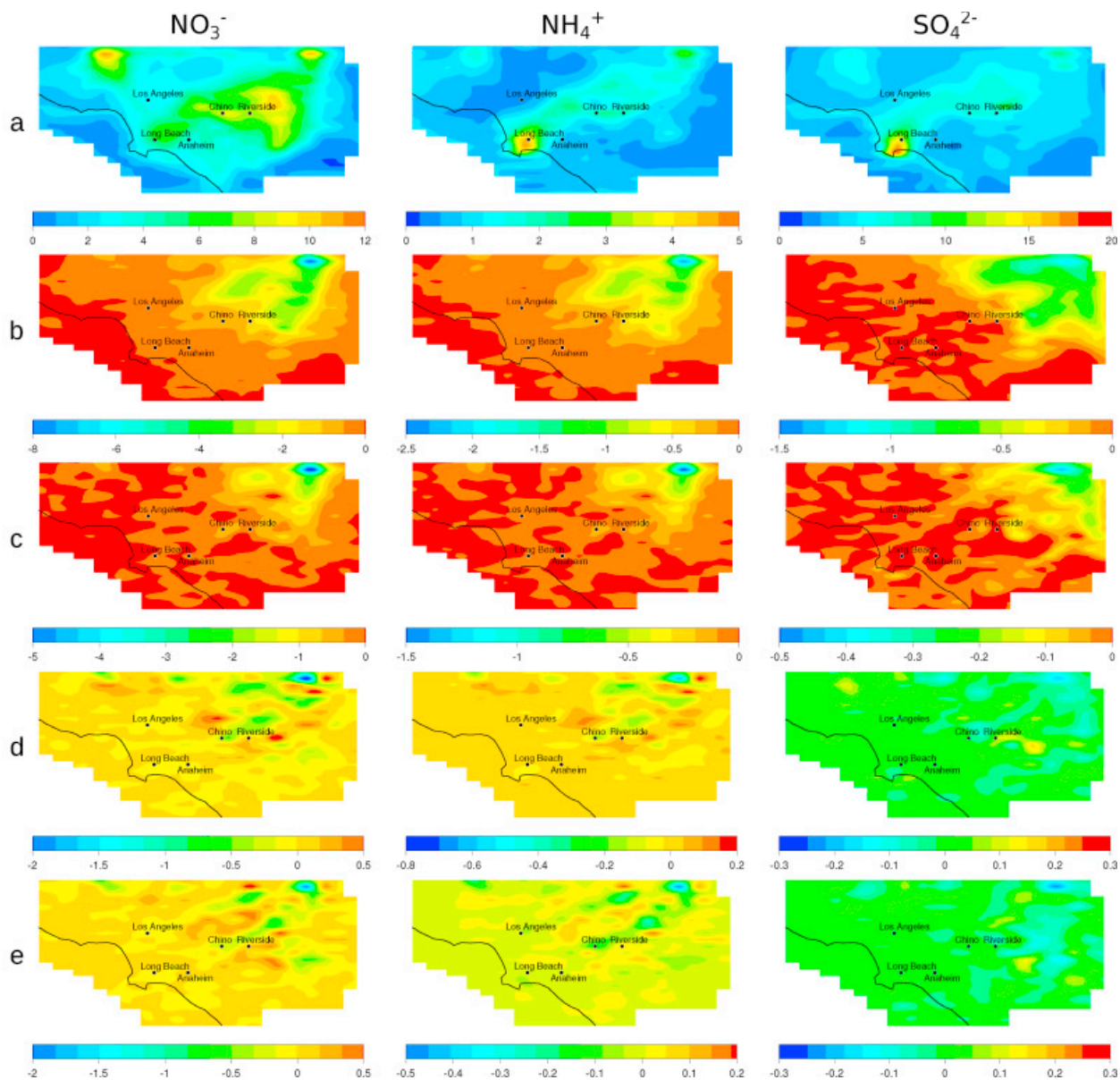


Figure 4.11. 24-h average concentrations of particulate nitrate (NO_3^- , $\mu\text{g}/\text{m}^3$), ammonium (NH_4^+ , $\mu\text{g}/\text{m}^3$) and sulfate (SO_4^{2-} , $\mu\text{g}/\text{m}^3$) in the base case shown in (a). Difference in concentration versus the base case shown in rows (b), (c), (d) and (e) when using (b) $\gamma = 10^{-2}$, (c) $\gamma = 10^{-3}$, (d) $\gamma = 10^{-4}$ and (e) $\gamma = 10^{-5}$. Concentration decreases relative to the reference case are indicated by negative values.

In scenario (c), when the uptake coefficient is set to 10^{-3} , the magnitude of the impact on NH_3 and $\text{PM}_{2.5}$ concentrations is lower than in scenario (b), although the spatial distribution of changes remains similar. In this case, hourly domain wide average NH_3 concentrations decrease by 3–14% (Table 4.1), with some locations experiencing decreases of over 25%

compared to reference case levels. Fig. 4.9c (left column) shows that the largest impacts on gas-phase NH_3 occur in the same areas as in scenario (b), with decreases in 24-h average concentrations of about 7 ppb near Chino where the strongest NH_3 emissions sources in the basin are located. Although 24-h average NH_3 concentrations decrease by only 2–4 ppb in areas downwind of Riverside, the spatial distribution of changes in total $\text{PM}_{2.5}$ (Fig. 4.9, right column), as well as in nitrate, ammonium, and sulfate particle concentrations (Fig. 4.11) is similar in scenarios (b) and (c). In both scenarios, the largest reductions in 24-h average particle concentrations occur northeast of Riverside. Comparing parts (b) and (c) of Fig. 4.9, Fig. 4.11 illustrates this result. Although the impact is lower than in scenario (b) due to the uptake coefficient being reduced by an order of magnitude, significant reductions in $\text{PM}_{2.5}$ concentrations still occur in this scenario. Decreases in 24-h average concentrations of 2–4 $\mu\text{g}/\text{m}^3$ cover large areas in the northeast portion of the basin, with peak decreases reaching 10 $\mu\text{g}/\text{m}^3$. Given that the national standard for 24-h average $\text{PM}_{2.5}$ concentrations is 35 $\mu\text{g}/\text{m}^3$, decreases of this magnitude have important implications for reaching attainment of national ambient air quality standards for fine particulate matter. Reducing 24-h average gas-phase NH_3 concentrations by only a few ppb significantly reduces the formation of ammonium nitrate and ammonium sulfate particles. Similar to scenario (b), the impact on hourly $\text{PM}_{2.5}$ concentrations is even greater, with decreases exceeding 20 $\mu\text{g}/\text{m}^3$ (33%) in downwind areas of the basin during the afternoon hours. Coastal areas and locations upwind of NH_3 emissions sources again experience little to no change in NH_3 or $\text{PM}_{2.5}$ concentrations. In scenario (d) with $\gamma = 10^{-4}$, domain wide average NH_3 concentrations decrease by only a few percent at all hours of the day (Table 4.1). Although isolated locations in the basin experience larger decreases, the overall impact on NH_3 concentrations is small when an

uptake coefficient of 10^{-4} is used. Decreases in 24-h average NH_3 concentrations peak at 2 ppb and show a similar spatial distribution to those seen in scenario (c) (Fig. 4.9, left column). Areas downwind of strong emissions sources show decreases of 0.5–1 ppb, causing 24-h average $\text{PM}_{2.5}$ concentrations to decrease by $1\text{--}5\ \mu\text{g}/\text{m}^3$. This indicates that the formation of ammonium nitrate and ammonium sulfate particles in the SoCAB is highly sensitive to changes in gas-phase NH_3 concentrations, consistent with Schiferl et al. (2014). The largest decreases in $\text{PM}_{2.5}$ concentrations again occur in the far northeast portion of the basin where pollutants accumulate. Peak decreases in hourly $\text{PM}_{2.5}$ concentrations reach $12\ \mu\text{g}/\text{m}^3$ (20%) in some locations, although decreases of this magnitude are localized to highly impacted areas and only occur at certain times of the day. Overall, the impact on 24-h average NH_3 and $\text{PM}_{2.5}$ concentrations is around a factor of 2–3 lower in this scenario than scenario (c).

In the final scenario (e), an uptake coefficient of 10^{-5} is utilized. Although this uptake coefficient is three orders of magnitude lower than that used in scenario (b), peak decreases in $\text{PM}_{2.5}$ concentrations are only a factor of three lower. However, decreases of this magnitude are isolated to only a small area in the northeast corner of the basin. There are only small changes in NH_3 concentrations in this scenario. Hourly domain wide average NH_3 concentrations change by less than 1%, and most individual locations show decreases of only a few percent. Changes in 24-h average NH_3 concentrations are less than 0.5 ppb, as shown in Fig. 4.9e (left column). In contrast to scenarios (b) and (c), the increases and decreases in NH_3 concentrations are similar in magnitude in this scenario. Additionally, changes in NH_3 concentrations in this scenario are less localized and occur throughout the inland portion of the basin. Reducing the magnitude of the uptake coefficient increases the lifetime of NH_3 ,

causing the spatial distribution of impacts to be more dependent on the meteorological conditions in the basin during the first two days and into day three. Fig. 4.9 (right column) shows that the spatial distribution of changes in $PM_{2.5}$ concentrations is also different in this scenario than in scenarios (b) and (c). Here, changes in 24-h average $PM_{2.5}$ levels of $\pm 1 \mu\text{g}/\text{m}^3$ occur at various locations, with decreases of $1\text{--}2 \mu\text{g}/\text{m}^3$ occurring in downwind areas of the basin. However, domain wide average $PM_{2.5}$ concentrations decrease by less than 1% at all hours of the day, indicating that the overall impact on fine particle concentrations is small. As in the previous scenarios, changes in the concentration of ammonium and nitrate particles cause nearly all of the change in total $PM_{2.5}$ concentrations. Overall, the impact on both gas-phase and particulate species is of variable sign when the lowest uptake coefficient of 10^{-5} is utilized.

4.6 Model Predictions for the Continental US

Results from the CMAQ model validation comparing simulated mixing ratios for various atmospheric species (i.e., O_3 , NH_3 , NH_4^+ , NO_3^- , and $PM_{2.5}$) against observations obtained by the Ammonia Monitoring Network (AMoN), the US Environmental Protection Agency's (EPA's) Air Quality System (AQS), and US EPA's Chemical Speciation Network (CSN) showed an overall good model performance for most of the criteria. Details of the model validation can be found in Zhu et al., 2018.

4.6.1 Impact on gas-phase NH_3 and HNO_3 concentrations

Figure 4.12 shows the time series of daily domain-averaged (averaged over 24 h and the simulation domain) NH_3 for both the winter and summer, for different uptake coefficient values.

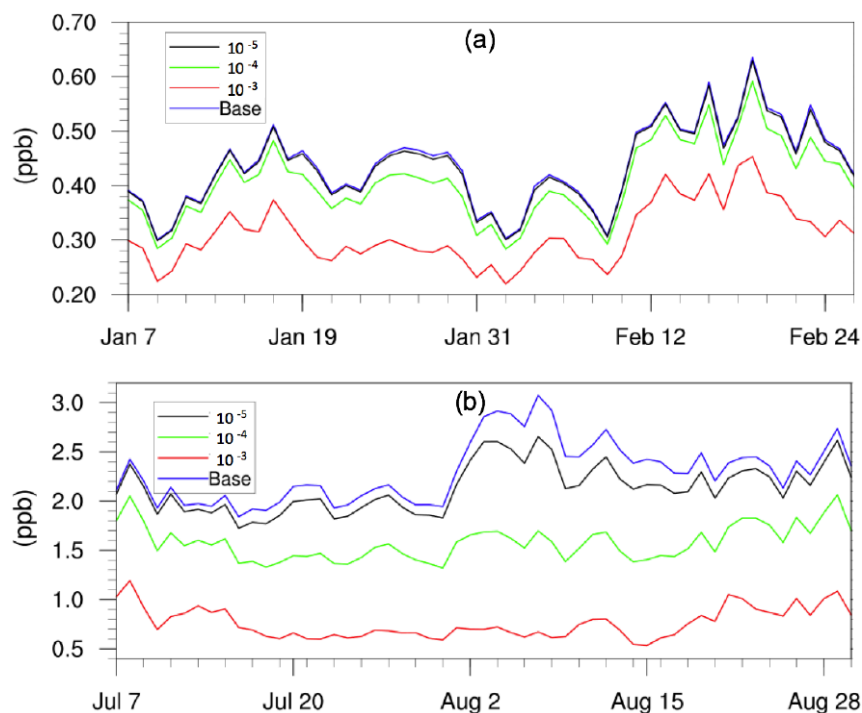


Figure 4.12. Daily, spatially-averaged NH₃ concentrations for different uptake coefficient scenarios for the (a) winter period and (b) summer period.

In general, the NH₃ concentration is reduced after the introduction of the NH₃ uptake process, and the magnitude of the reduction is increased as the uptake coefficient increases. For the winter, the spatiotemporally averaged (averaged over entire period and the simulation domain) NH₃ concentration for the base case is 0.44 ppb, while the value decreases to 0.43 ppb (-2.3 %) for the $\gamma = 10^{-5}$ case, 0.41 ppb (-6.8 %) for the $\gamma = 10^{-4}$ case, and 0.31 ppb (-29.5 %) for the $\gamma = 10^{-3}$ case. These results indicate that an uptake of 10^{-5} is not significant. For the summer, the spatiotemporally averaged NH₃ concentration for the base case is 2.30 ppb, while the value decreases to 2.10 ppb (-8.7 %) for the $\gamma = 10^{-5}$ case, 1.58 ppb (-31.3 %) for the $\gamma = 10^{-4}$ case, and 0.76 ppb (-67.0 %) for the $\gamma = 10^{-3}$ case. The impact of the uptake process is higher for the summer due to larger SOA concentrations during the summer (spatiotemporally averaged $9.25 \mu\text{g m}^{-3}$ for the base case) than the winter (spatiotemporally averaged $2.72 \mu\text{g m}^{-3}$ for the base case).

The spatial distribution of the impact over the simulated domain is also investigated. Figure 4.13a and c show the time-averaged spatial distribution of NH_3 for the winter and summer base cases, while the differences between the $\gamma = 10^{-3}$ case and the base case are shown in Fig. 4.13b and d. For both periods, the Central Valley of California is a hotspot for NH_3 emissions, and the region exhibits the most significant impact due to the introduction of the new NH_3 uptake mechanism. This is due to the intensive agricultural activities in this region including the heavy application of fertilizers (Krauter et al., 2002) and the year-round farming pattern supported by California's relatively warm climate. The hog farm industry is largely responsible for the high NH_3 concentration in North Carolina and north Iowa in the summer, where significant NH_3 loss can also be spotted in the $\gamma = 10^{-3}$ case. Agriculture and wildfires also produce some hotspots of ammonia concentration in other areas, such as southern Florida in the winter and several locations in northern California and Washington states, where NH_3 concentrations also decreased significantly in the $\gamma = 10^{-3}$ case. The spatial distribution of differences between the base case and the $\gamma = 10^{-4}$ and $\gamma = 10^{-5}$ cases is similar to the $\gamma = 10^{-3}$ only with different scales.

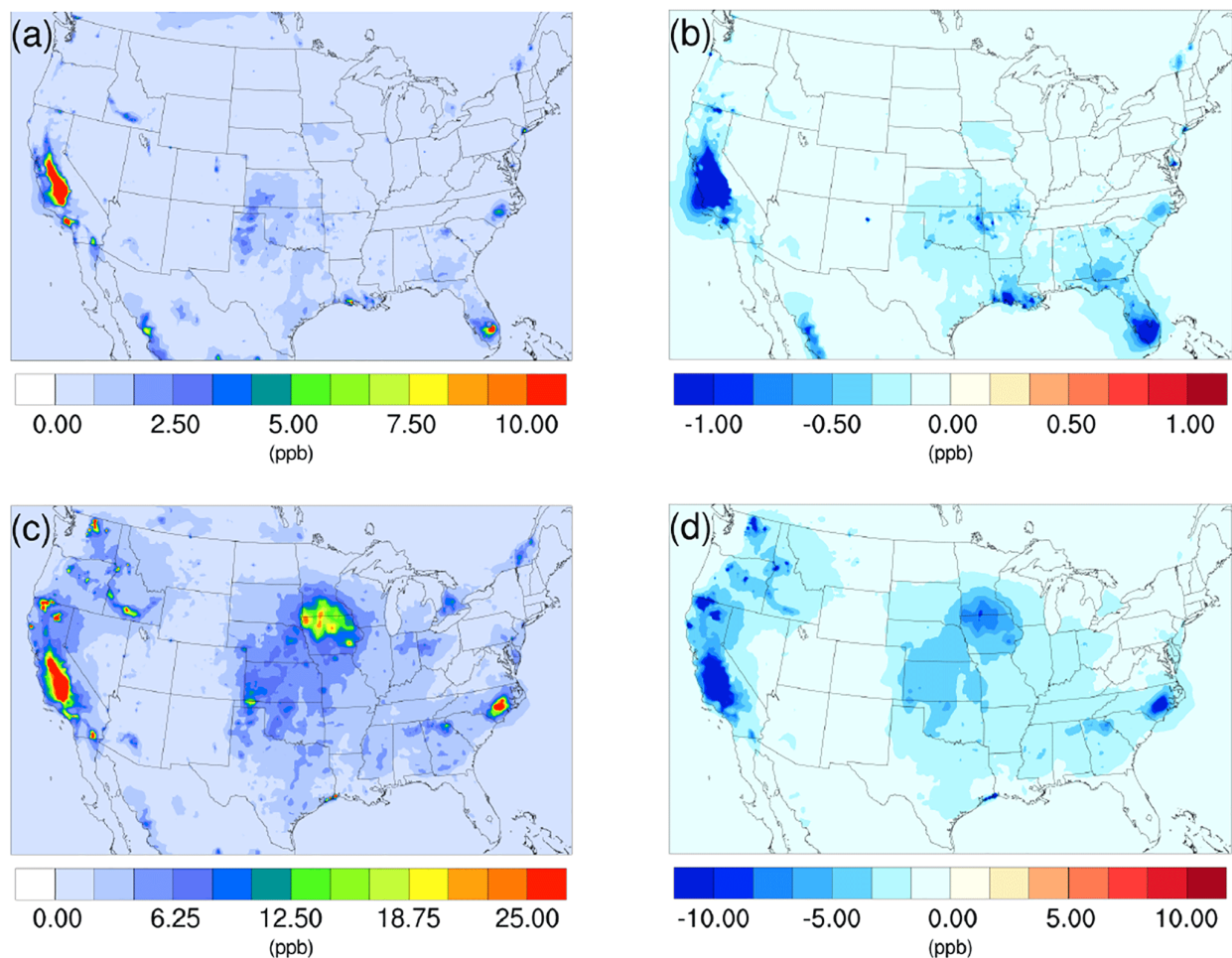


Figure 4.13. Spatial distribution of time-averaged NH_3 concentrations in the base case for (a) winter and (c) summer. Spatial distribution of the difference in time-averaged NH_3 concentrations between the $\gamma = 10^{-3}$ and the base case for (b) winter and (d) summer. Negative values represent decreases in concentration with respect to the base case.

As the condensation of HNO_3 into the particle phase is directly associated with NH_3 concentration, it is reasonable to infer that the introduction of the NH_3 uptake mechanism could also impact the concentration of HNO_3 . In contrast to NH_3 , the integration of the NH_3 uptake mechanism leads to an increase in HNO_3 concentration, and the scale of magnitude of the increase rises as the uptake coefficient is increased, although the extent of variation is smaller than that of NH_3 . For the winter, the difference between the base case and the $\gamma = 10^{-5}$ case is very small ($< 0.2\%$) and remains insignificant for the $\gamma = 10^{-4}$ case ($\sim 1.2\%$). Only the

$\gamma=10^{-3}$ case shows a significant increase in HNO_3 as concentrations increase by 8.5 % (the spatiotemporally averaged concentration is 0.27 ppb for the base case and 0.30 ppb for the $\gamma = 10^{-3}$ case). Similar to the NH_3 variation, the impact becomes larger for the summer, where the spatiotemporally averaged HNO_3 concentration for the base case is 0.51 ppb, while the value increases by 2.0 % (0.52 ppb) for the $\gamma = 10^{-5}$ case, 7.8 % (0.55 ppb) for the $\gamma = 10^{-4}$, case, and 19.6 % (0.61 ppb) for the $\gamma = 10^{-3}$ case. These increase in HNO_3 concentrations is due to the reduction in NH_3 caused by the conversion of NH_3 into NOCs, making less NH_3 available for reaction with HNO_3 to form the particle-phase NH_4NO_3 .

The time-averaged spatial distributions of HNO_3 for both the winter and summer base cases are presented in Fig. 4.14a and c. The northeast region exhibits relatively high HNO_3 concentration for both periods, largely due to the high NO_x ($\text{NO} + \text{NO}_2$) emissions from transportation activities. The addition of the NH_3 uptake process does not cause an obvious impact in this region for the winter, as the reduction of NH_3 is very small (Fig. 4.13b) due to low SOA and NH_3 concentrations in the base case. In contrast, the increase in HNO_3 becomes much more significant for this region in the summer, as the loss of NH_3 becomes greater due to larger NH_3 and SOA concentrations in the base case.

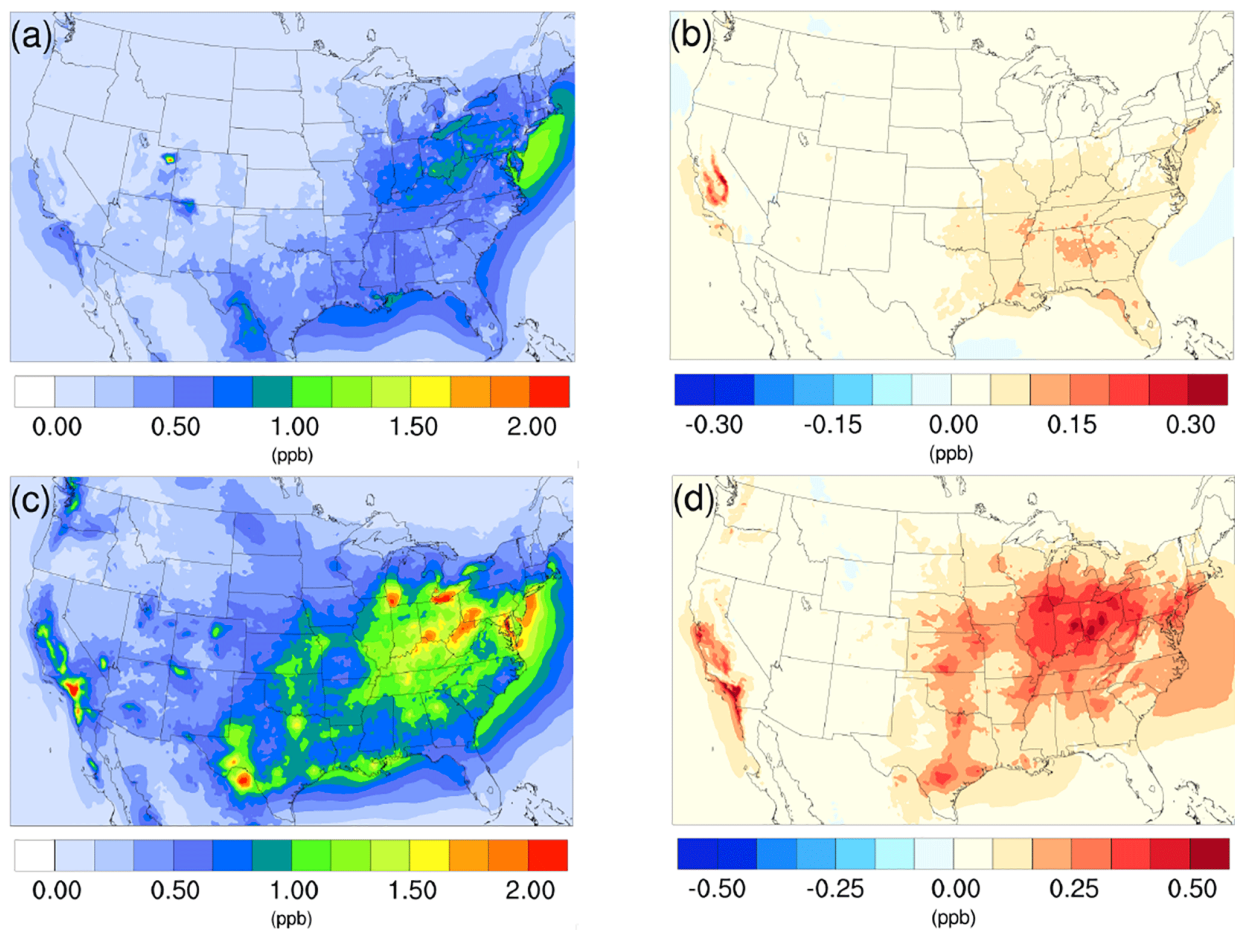


Figure 4.14. Spatial distribution of time-averaged HNO₃ concentrations in the base case for **(a)** winter and **(c)** summer. Spatial distribution of the difference in time-averaged HNO₃ concentrations between the $\gamma = 10^{-3}$ case and the base case for **(b)** winter and **(d)** summer. Positive values represent increases in concentration with respect to the base case.

The winter hotspot around northeastern Utah (Uintah Basin) could be caused by the stagnant atmospheric conditions during the winter in the valley (Lee et al., 2014), which traps NO_x emitted from local and remote sources located on the east side of the valley. The resulting NO_x undergoes a nighttime reaction with O₃, forming N₂O₅ (high N₂O₅ concentration is spotted in the model at the same place). Additionally, the lack of NH₃ also favors the HNO₃ accumulation, as a result, the addition of NH₃ does not have much impact on this spot. The largest increase in HNO₃ concentrations in winter is found over the Central

Valley of California, which also corresponds to the largest NH_3 reduction (Fig. 4.13b). For the summer, the largest impact occurs over the hotspot of southern California, where strong traffic emissions of NO_x and active photochemistry provide a strong HNO_3 source. The significant reduction of NH_3 concentration from the south Central Valley could reduce the potential sink of HNO_3 into the particle phase and leave more HNO_3 in the gas phase. The spatial distribution of differences between the base case and the $\gamma = 10^{-4}$ and $\gamma = 10^{-5}$ cases is similar to the $\gamma = 10^{-3}$ only with smaller scales. The increase in time-averaged HNO_3 between the base case and the $\gamma = 10^{-4}$ case was on the scale of 0.03 ppb and 0.20 ppb in the winter and summer, respectively. The increase in time-averaged HNO_3 between the base case and the $\gamma = 10^{-5}$ case was on the scale of 0.007 ppb and 0.05 ppb in the winter and summer, respectively.

4.6.2 Impact on Inorganic PM

One of the effects of the gas-phase NH_3 reduction due to the inclusion of the NH_3 uptake was the decrease in the particle phase NH_4^+ concentration, as all NH_4^+ originates from gas-phase NH_3 . In general, the addition of NH_3 uptake in the model causes a decrease in particle-phase NH_4^+ concentration, and the impact is more significant for the summer than the winter. For the summer case, the average decrease in NH_4^+ is 1.8 % for $\gamma = 10^{-5}$, 10.7 % for $\gamma = 10^{-4}$, and 28.2 % for $\gamma = 10^{-3}$; for the winter case, the average decrease is 0.2 % for $\gamma = 10^{-5}$, 2.3 % for $\gamma = 10^{-4}$, and 13.2 % for $\gamma = 10^{-3}$. Such behavior corresponds well to the level of NH_3 reduction in Fig. 4.12 caused by the higher SOA concentrations during the summer.

The time-averaged spatial distributions of the NH_4^+ concentration for both the winter and summer base case are shown on Fig. 4.15a and c. Most of the NH_4^+ is concentrated over the

eastern part of the US, as a result of high NH_3 concentrations (see Fig. 4.13) in this region combined with the abundance of NH_3 neutralizers (e.g., HNO_3 and H_2SO_4). Another hotspot is the Central Valley of California and the South Coast Air Basin of California (Nowak et al., 2012), resulting from high NH_3 emissions from the intensive agriculture (Fig. 4.13).

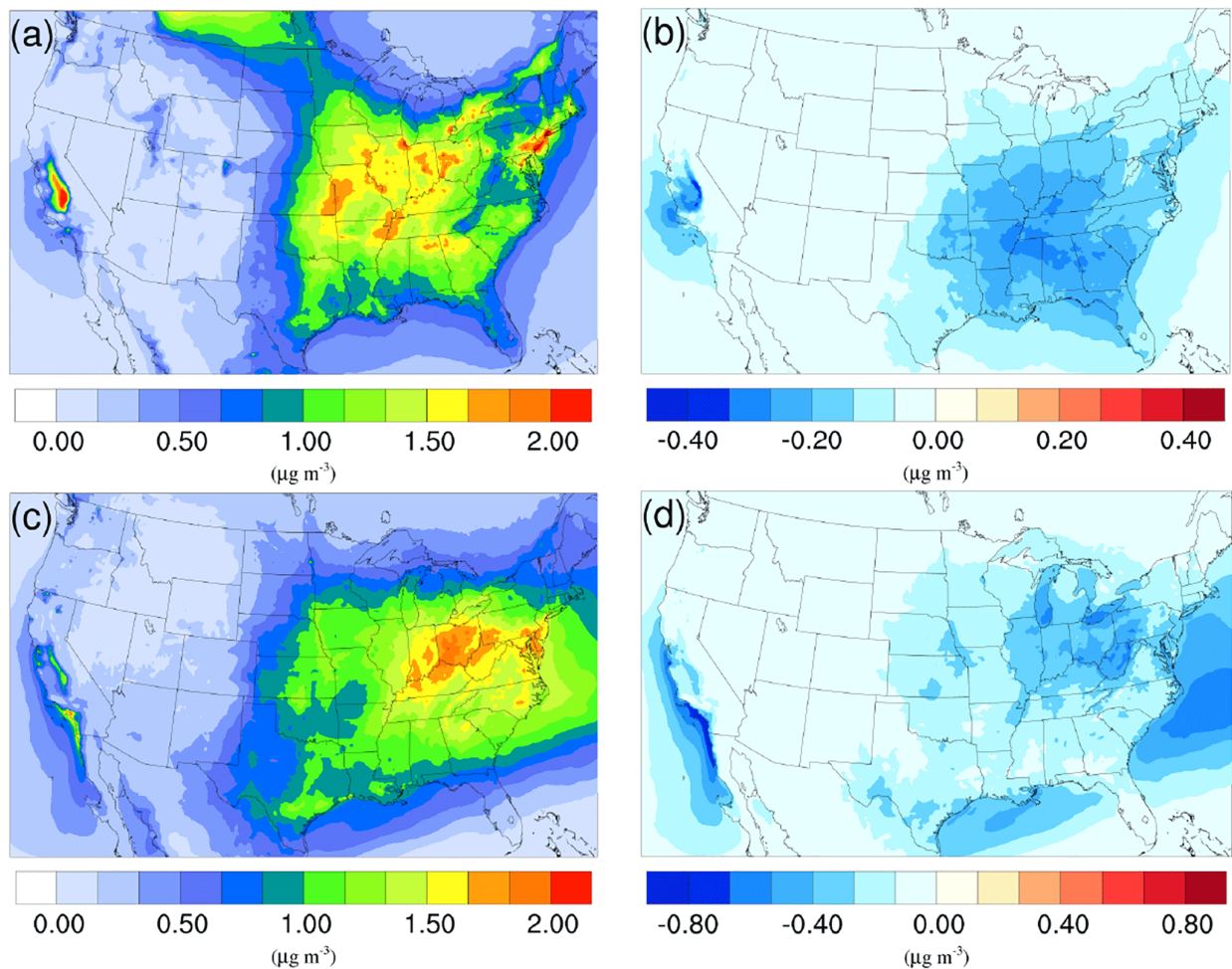


Figure 4.15. Spatial distribution of time-averaged NH_4^+ concentrations in the base case for **(a)** winter and **(c)** summer. Spatial distribution of the difference in time-averaged NH_4^+ concentrations between the $\gamma = 10^{-3}$ case and the base case for **(b)** winter and **(d)** summer. Negative values represent decreases in concentration with respect to the base case.

In the presence of both HNO_3 and H_2SO_4 , NH_3 is first neutralized by H_2SO_4 to form either $(\text{NH}_4)_2\text{SO}_4$ or NH_4HSO_4 in the particle phase, while the rest of the NH_3 reacts with HNO_3 and

forms particle-phase NH_4NO_3 . The percentage of NH_4^+ associated with NO_3^- , SO_4^{2-} , and HSO_4^- could be investigated by comparing the spatial distribution of the NO_3^- concentration for the corresponding period in Fig. 4.16a and c and the SO_4^{2-} in Fig. 4.17a and b. In the West Coast and Central Valley of California, the enriched NH_4^+ mostly exists in the form of NH_4NO_3 , as the sulfate concentration is low in this region for both periods (Fig. 4.17). Figure 4.15b and d presents the spatial distribution of the difference in NH_4^+ concentration between the $\gamma = 10^{-3}$ case and the base case, which is highly correlated with the NH_3 variation map (Fig. 4.13). The reduction in NH_3 due to the SOA uptake directly impacts the available NH_3 that could be condensed into the particle phase and reduces the NH_4^+ concentration consequently. The spatial distribution of differences between the base case and the $\gamma = 10^{-4}$ and $\gamma = 10^{-5}$ cases is similar to the $\gamma = 10^{-3}$ only with different scales. In mid-east region during the winter, the H_2SO_4 concentration is insufficient to neutralize all the NH_3 , so more NO_3^- is involved in the NH_3 neutralization, and there are more nitrate particles than sulfate particles. For the summer, as the sulfate concentration nearly doubles over the mid-east US compared to the winter, most of the NH_3 is neutralized by H_2SO_4 . This causes an absence of NO_3^- above this region and only appears on the surrounding region where sulfate concentration is low.

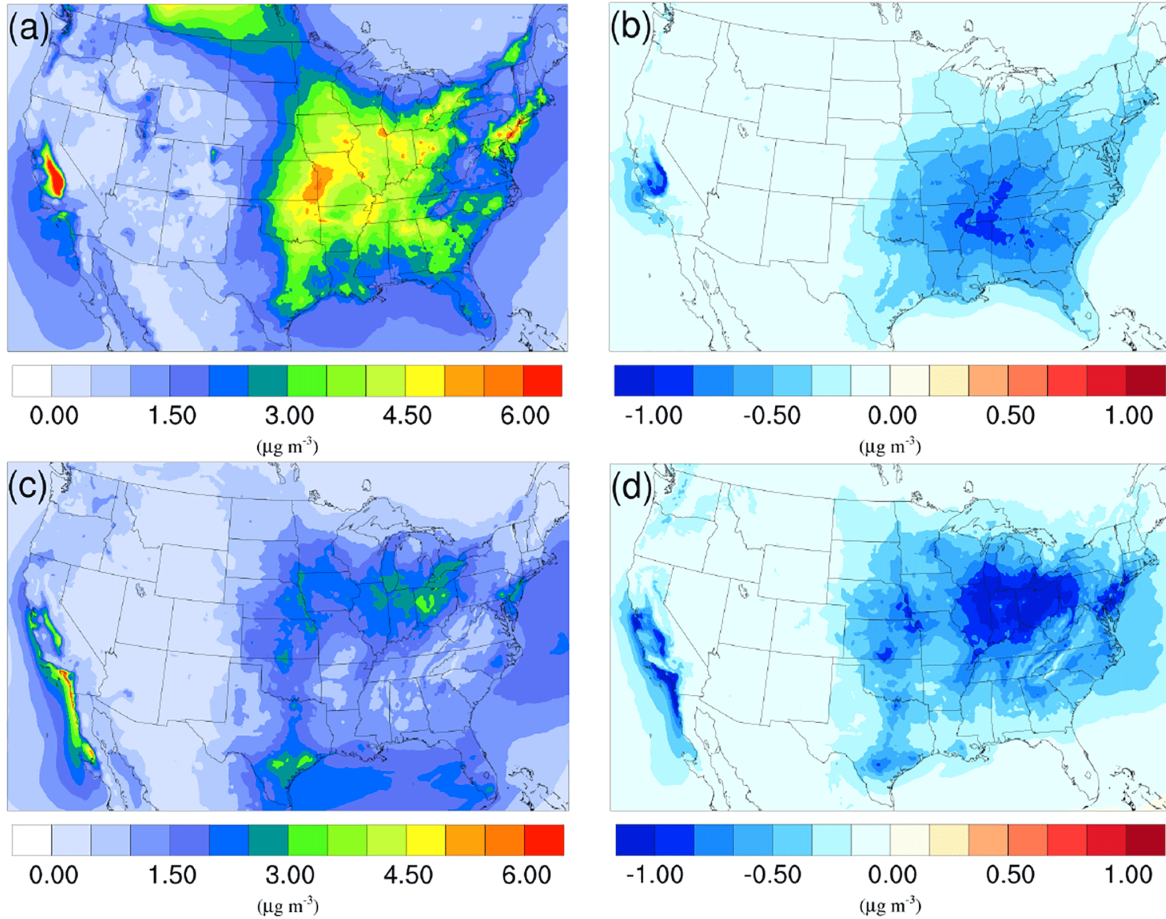


Figure 4.16. Spatial distribution of time-averaged NO_3^- concentrations in the base case for (a) winter and (c) summer. Spatial distribution of the difference in time-averaged NO_3^- concentrations between the $\gamma=10^{-3}$ case and the base case for (b) winter and (d) summer. Negative values represent decreases in concentration with respect to the base case.

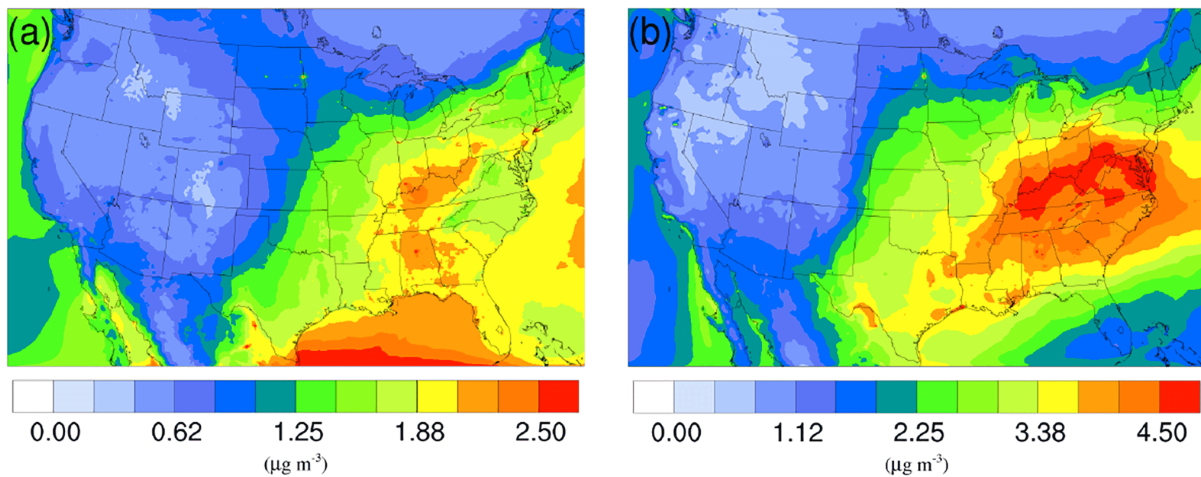


Figure 4.17. Spatial distribution of time-averaged SO_4^{2-} concentrations in the base case for (a) winter and (b) summer. The difference due to NH_3 conversion into NOCs is not shown because it is very small.

The concentration of NO_3^- changes as a result of adding the NH_3 conversion into NOCs, namely, adding the NH_3 uptake mechanism leads to a decrease in NO_3^- concentrations for both periods. The spatial distributions of the NO_3^- variation due to the addition of the NH_3 uptake mechanism ($\gamma = 10^{-3}$) are presented in Fig. 4.16b and d for the winter and summer. By comparing with the base cases (see Fig. 4.16a and c), it is clear that most of the NO_3^- reduction occurs over regions with high NO_3^- concentration, such as the Central Valley of California, the South Coast Air Basin of California, and vast regions over the mid-east US. One exception is the high NO_3^- region over Canada on the north edge of Montana and North Dakota during the winter. Neither NH_4^+ concentration nor NO_3^- concentration changes much, mostly because the SOA concentration is extremely low for that region (see Fig. 4.18a), so almost no NH_3 is lost due to the SOA uptake. The same occurs in south Florida during the summer.

Overall, similar to NH_4^+ , the impact on NO_3^- is more significant for the summer than the winter. The average reductions for the winter are 0.2 % for $\gamma = 10^{-5}$, 1.9 % for $\gamma = 10^{-4}$, and 10.9 % for $\gamma = 10^{-3}$. For the summer, the average reductions are 1.9 % for $\gamma = 10^{-5}$, 10.6 % for $\gamma = 10^{-4}$, and 24.3 % for $\gamma = 10^{-3}$. Moreover, the magnitude of the difference is also close to the difference in NH_4^+ , indicating that almost all the NH_4^+ reduction is from NH_4NO_3 .

4.6.3 Impact on Organic PM

Figure 4.18a and c show the time-averaged spatial distribution of SOA for the winter and summer base cases, respectively. For both seasons, high SOA concentrations are found over the southeastern US due to high vegetation coverage in this region, while hotspots in the

northwestern region are caused by widespread fire events. The averaged SOA concentration in the base case is more than 3 times higher in the summer ($9.25 \mu\text{g m}^{-3}$) than in the winter ($2.72 \mu\text{g m}^{-3}$), largely due to the higher biogenic SOA (BIOSOA) concentrations (summer vs. $0.22 \mu\text{g m}^{-3}$ winter) resulting from elevated biogenic emissions in the warm season.

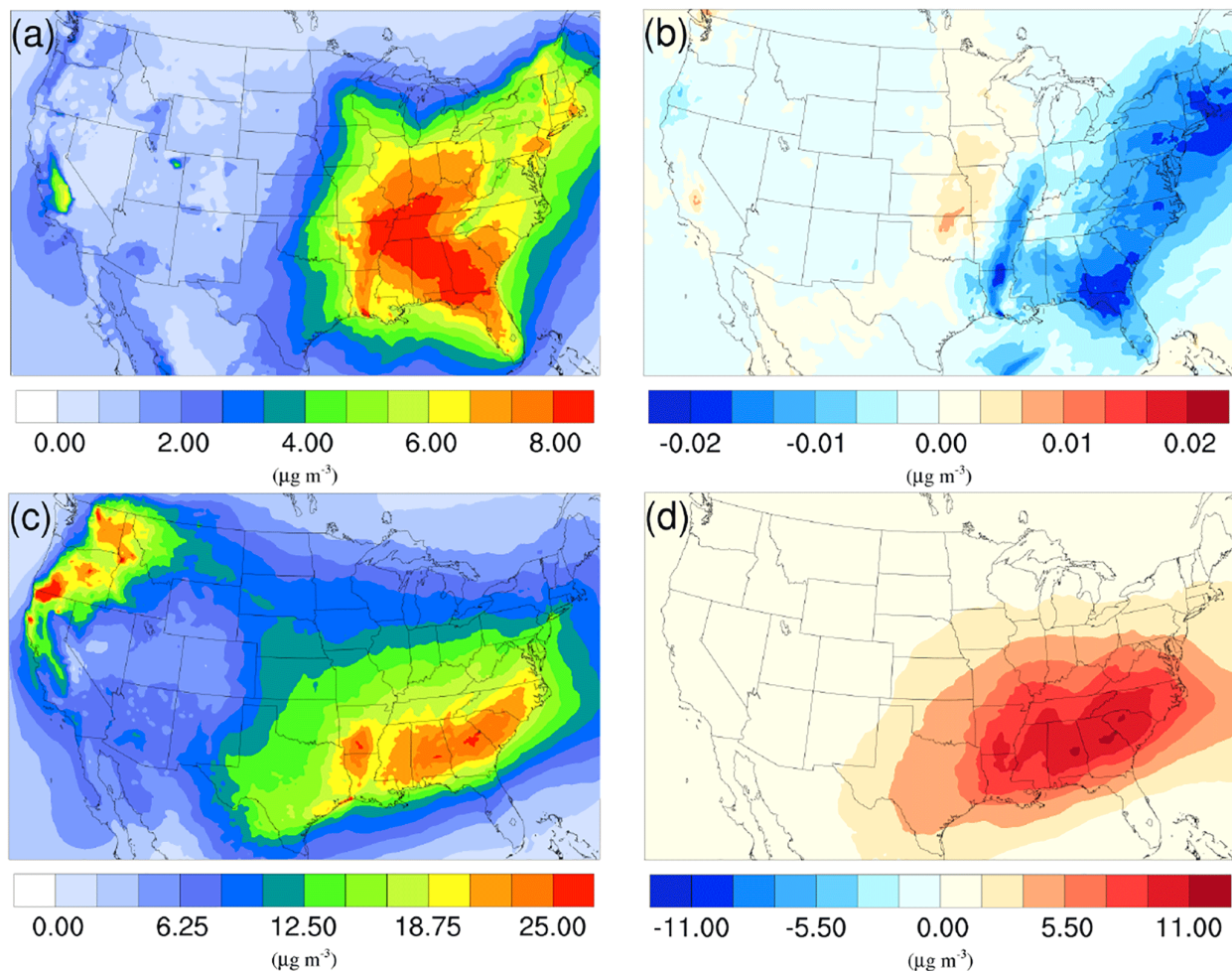


Figure 4.18. Spatial distribution of time-averaged SOA concentrations in the base case for **(a)** winter and **(c)** summer. Spatial distribution of the difference in time-averaged SOA concentrations between the $\gamma = 10^{-3}$ case and the base case for **(b)** winter and **(d)** summer. Positive values represent increases in concentration with respect to the base case, and negative values represent decreases in concentration with respect to the base case.

As mentioned in the modeling methods (Sect. 4.3.2), the NH_3 uptake parametrization added to the CMAQ model does not directly add mass to SOA because the original SOA carbonyl and

the NOCs they convert into have similar molecular weights. However, significant changes in SOA mass concentration are observed after implementing the NH_3 uptake mechanism and is indirectly caused by the changes in particle acidity. As demonstrated in Fig. 4.18b and d, implementing the NH_3 uptake mechanism has a stronger impact on SOA concentrations during the summer than in the winter. Almost the entire increase in SOA concentrations in the summer is due to the mass change in biogenic SOA (see Figs. 4.19a and 4.18d). Further investigation reveals that the majority of the increase ($\sim 80\%$) is caused by the nonvolatile AISO3 species (Fig. 4.19b), which is the isoprene epoxydiols (IEPOX)-derived SOA through the acid-catalyzed ring-opening reactions (Pye et al., 2013). This increase in AISO3 is caused by the increase in aerosol aqueous-phase acidity due to the reduction in NH_4^+ after adding the NH_3 conversion into NOCs. This increase in particle acidity corresponds well with the sensitivity study between NH_3 , SO_4^{2-} , and particle pH presented in Fig. 2 of Weber et al. (2016), where particle pH is found to be more sensitive to NH_3 concentrations than to SO_4^{2-} concentrations. Figure 4.19c shows a large drop in pH value (~ 0.9 – 2.3) in the southeast region where the increase in the AISO3 is most significant and there is a simultaneous decrease in IEPOX concentrations (Fig. 4.19d). The largest pH variation appears over the northwest region. However, there is no observable impact on SOA concentrations due to the extremely low concentration of both isoprene and IEPOX (see Fig. 4.19e and f) in this area. Moreover, the reduction in NH_4^+ concentrations also increases the ratio of $\text{SO}_4^{2-}/\text{HSO}_4^-$, where SO_4^{2-} can act as a nucleophile and promote the IEPOX uptake process. This also contributes to the increase in AISO3.

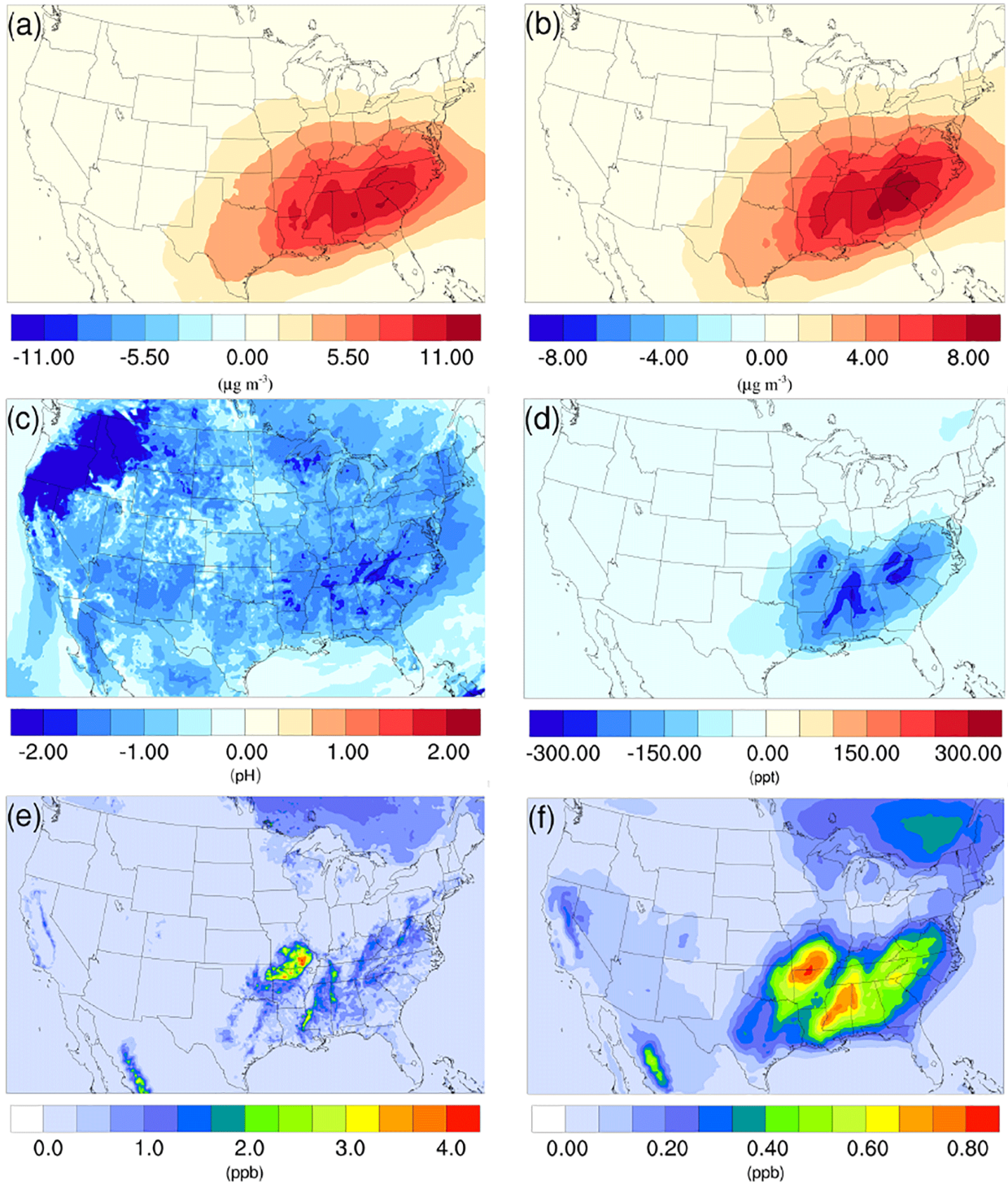


Figure 4.19. Spatial distribution of the difference in time-averaged **(a)** biogenic SOA concentrations, **(b)** isoprene epoxydiols (IEPOX)-derived SOA concentrations, **(c)** particle acidity (pH), and **(d)** isoprene epoxydiols concentrations between the $\gamma = 10^{-3}$ case and the base case during the summer. Spatial distribution of time-averaged **(e)** isoprene, and **(f)** isoprene epoxydiols concentration in the base case during the summer.

Figure 4.20 shows the time evolution of daily–spatially averaged H^+ , IEPOX, and AISO3 for both the winter and summer. Although the average H^+ concentration in the base case is similar between two periods, the variation between the NH_3 uptake scenarios and the base case is much smaller for the winter largely due to the lower SO_4^{2-} concentrations in the winter which restrain the acidity variation level. Additionally, lower SOA concentrations in winter also reduce the magnitude of NH_4^+ variation. As a result, addition of the NH_3 uptake mechanism does not have a large impact on the AISO3 concentration for most of the simulation (except for the last several days). On the contrary, the summer shows a significant increase in H^+ concentrations as the NH_3 uptake coefficient increases, while the concentration of IEPOX decreases. And the increase in AISO3 concentration is remarkable, with more than 10 times the growth on average between the $\gamma = 10^{-3}$ case (1875 ng m^{-3}) and the base case (182 ng m^{-3}). The amount of growth on AISO3 seems linear with different values of the NH_3 uptake coefficient ($\gamma = 10^{-5}$: 16 %; $\gamma = 10^{-4}$: 172 %; $\gamma = 10^{-3}$: 932 %).

In addition to the isoprene epoxydiols pathway, other biogenic SOA species contribute the rest of the SOA changes ($\sim 20 \%$), including other SOA species derived from isoprene (AISO1 and AISO2), from monoterpenes (ATRP1 and ATRP2), from sesquiterpenes (ASQT), and AOLGB, which represents the aged nonvolatile SOA origin from AISO1, AISO2, ATRP1, ATRP2, and ASQT. The common point with those SOAs (AISO1, AISO2, ATRP1, ATRP2, and ASQT) is that they all have a pathway to be formed through the oxidation between gas-phase NO_3 radicals and their gas precursors. One possible explanation could be that the addition of NH_3 uptake leads to an increase in gas-phase HNO_3 , which could shift the reaction balances between NO_3 and HNO_3 and leave more NO_3 available for SOA oxidation.

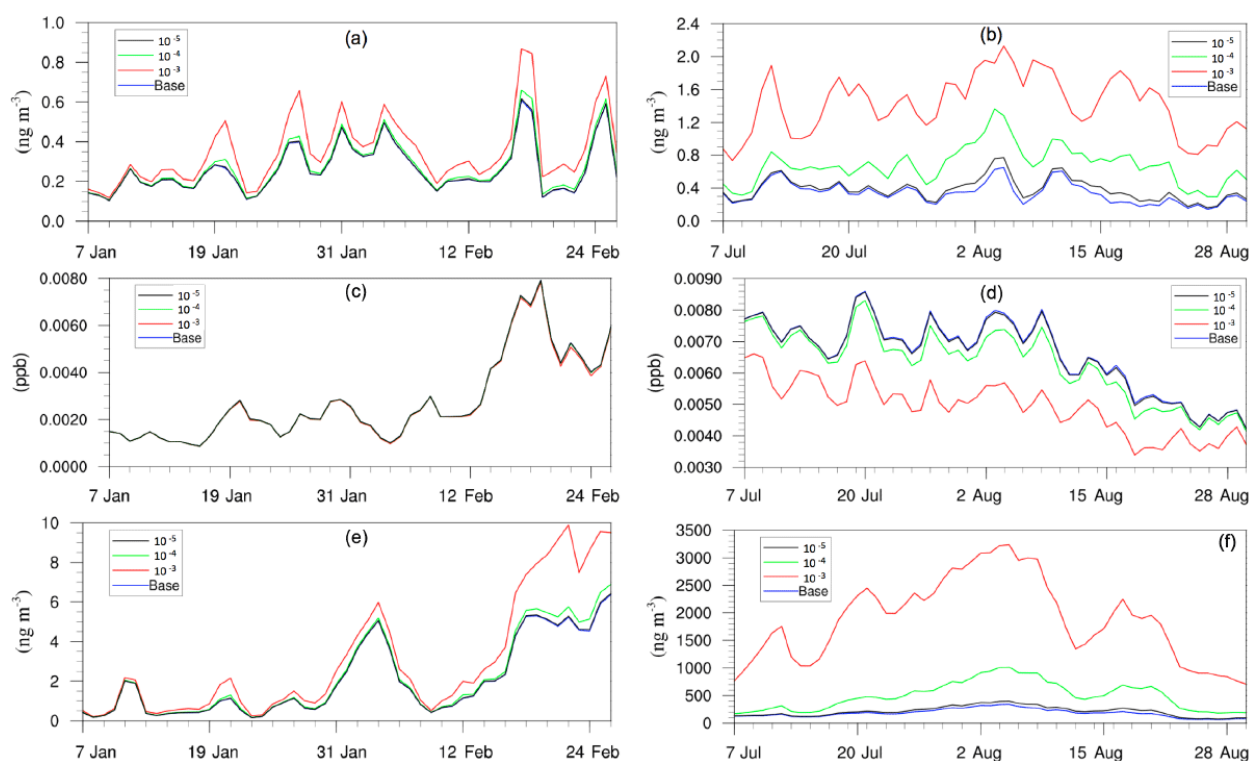


Figure 4.20. Daily, spatially averaged concentrations of (a) particle-phase H^+ in winter, (b) particle-phase H^+ in summer, (c) isoprene epoxydiols in winter, (d) isoprene epoxydiols in summer, (e) isoprene-epoxydiol-derived SOA in winter, and (f) isoprene-epoxydiol-derived SOA in summer.

4.6.4 Impact on Total PM

Figure 4.21 presents the time evolution of daily-averaged concentrations of $PM_{2.5}$ and PM_{10} in different scenarios during both periods. First, both the pattern and level of impact caused by the NH_3 uptake mechanism is similar for $PM_{2.5}$ and PM_{10} , which indicates that most of the mass change due to this process occurs on fine particles. Secondly, the level of impact on both $PM_{2.5}$ and PM_{10} is much more significant over the summer than the winter, which is consistent with previous analysis of individual species. Third, opposite impact patterns are found between the winter and summer. The inclusion of the NH_3 uptake mechanism leads to a decrease in the total PM mass for the winter, which is caused by the reduction of inorganic NH_4^+ and NO_3^- due to the decrease in the NH_3 concentration. On the contrary, PM

concentrations during the summer increase after adding the NH_3 uptake mechanism. Although the concentration of inorganic species still decreases during the summer, the increase in biogenic SOA concentration, as detailed in Sect. 4.6.3, outpaces the decrease caused by inorganic species and leads to an overall increase in total PM mass for the summer. For the winter, the average $\text{PM}_{2.5}$ concentration reduction is 0.07 % for the $\gamma = 10^{-5}$ case, 0.59 % for the $\gamma = 10^{-4}$ case, and 3.39 % for the $\gamma = 10^{-3}$ case. For the summer, the average $\text{PM}_{2.5}$ concentration increase is 0.14 % for the $\gamma = 10^{-5}$ case, 2.05 % for the $\gamma = 10^{-4}$ case, and 12.38 % for the $\gamma = 10^{-3}$ case.

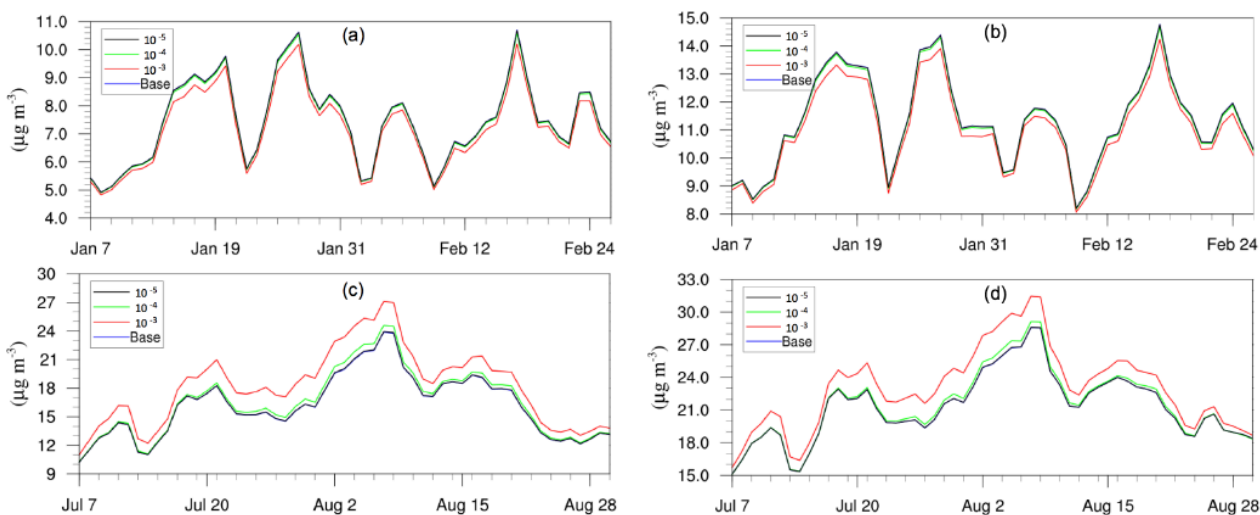


Figure 4.21. Daily, spatially-averaged concentrations of different scenarios for (a) $\text{PM}_{2.5}$ in the winter (b) PM_{10} in the winter (c) $\text{PM}_{2.5}$ in the summer, and (d) PM_{10} in the summer

The spatial distribution of time-averaged $\text{PM}_{2.5}$ concentration for the winter and summer is presented in Fig. 4.22a and c, respectively. Most of the high $\text{PM}_{2.5}$ concentration happens over the mid-east US during the winter, with additional hotspots over the Central Valley of California, resulting in an overall average of $7.5 \mu\text{g m}^{-3}$. $\text{PM}_{2.5}$ concentrations are highly correlated with the population density map of the US, indicating a dominant anthropogenic origin. The relatively low fraction of biogenic SOA in winter also supports this point (Fig.

4.23a). The model predicts a much higher $PM_{2.5}$ concentration for the summer, with an average concentration of $16 \mu\text{g m}^{-3}$. The hotspots observed over the northwest of the country and coastal area over southeast Texas are due to wildfire events. In general, high $PM_{2.5}$ concentrations are predicted over the southeast of the US, where high fractions of biogenic SOA are present (Fig. 4.23b). This could be a result of both high average temperatures during the summer and high vegetation density in that region. Figure 4.22b shows the variation in $PM_{2.5}$ concentrations between the $\gamma = 10^{-3}$ case and the base case for the winter. An overall reduction can be observed from the map, with the highest reduction around the Central Valley of California and a smaller reduction over the vast mid-east region. This is mostly caused by the decrease in NH_4NO_3 due to the reduction of gas-phase NH_3 concentrations as discussed earlier. During the summer, although the decrease still appears over the northwest of the country, the prominent feature becomes a significant increase in $PM_{2.5}$ concentrations over the southeast region. This is due to the increase in biogenic SOA resulting from the enhanced acid-catalyzed uptake reactions.

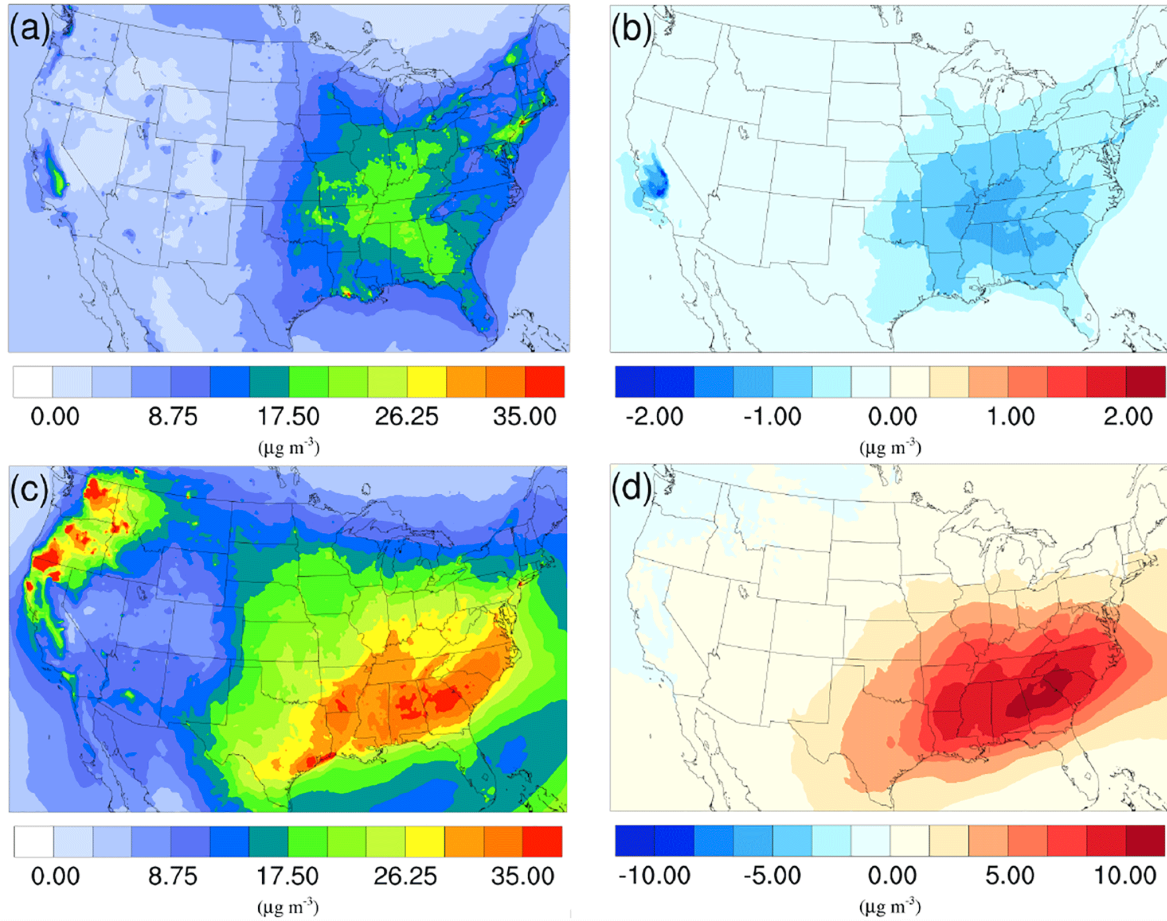


Figure 4.22. Spatial distribution of time-averaged PM_{2.5} concentrations in the base case for (a) winter and (c) summer. Spatial distribution of the difference in time-averaged PM_{2.5} concentrations between the $\gamma = 10^{-3}$ case and the base case for (b) winter and (d) summer. Positive values represent increases in concentration with respect to the base case, and negative values represent decreases in concentration with respect to the base case.

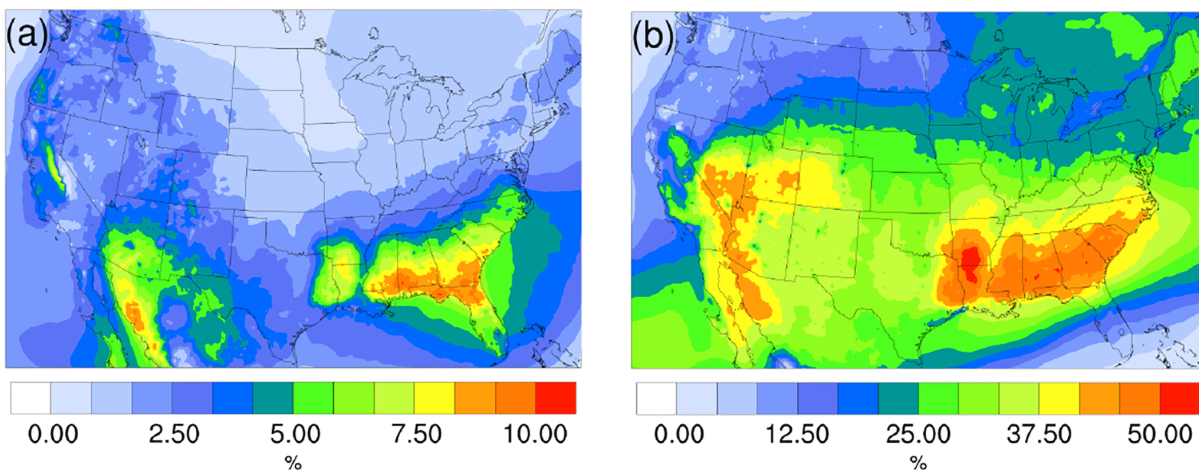


Figure 4.23. Spatial distribution of time-averaged biogenic SOA fraction of total PM_{2.5} for (a) the winter and (b) summer.

4.7 Conclusions

This study presents the initial findings of including this previously unaccounted for process in air quality models. Our results indicate the chemical uptake of NH_3 by SOA can reduce the concentration of gas-phase NH_3 , thereby reducing the potential to form ammonium nitrate and ammonium sulfate in the particle phase. The main chemical mechanism for this is the conversion of NH_3 in SOA particles to less basic nitrogen-containing organic compounds that are less efficient in neutralizing inorganic acids than NH_3 is. We show that the inclusion of this previously unaccounted for sink for gas-phase NH_3 into an urban airshed model for the SoCAB region reduces 24-h average $\text{PM}_{2.5}$ concentrations by up to $15 \mu\text{g}/\text{m}^3$ in highly impacted areas. However, this result should be seen as an upper limit as it reflects the use of the largest plausible uptake coefficient (10^{-2}) without any consideration of possible reaction saturation effects. It is more likely that the changes in $\text{PM}_{2.5}$ concentrations caused by the uptake of NH_3 by SOA are in the $1\text{--}5 \mu\text{g}/\text{m}^3$ range, as projected in scenarios $\gamma = 10^{-4}$ (d) and $\gamma = 10^{-5}$ (e). Results also indicate that the formation of inorganic $\text{PM}_{2.5}$ is highly sensitive to changes in the concentration of gas-phase NH_3 , as reductions in 24-h average NH_3 concentrations of $0.5\text{--}2$ ppb cause 24-h average $\text{PM}_{2.5}$ concentrations to decrease by $1\text{--}5 \mu\text{g}/\text{m}^3$ in downwind areas (see Fig. 4.9d). Previous studies have shown that ammonium nitrate particles form when concentrated NH_3 plumes are mixed into areas of active urban photochemistry, such as the northeast portion of the SoCAB (Nowak et al., 2012; Schiferl et al., 2014). Both primary and secondary pollutants accumulate in the northeast portion of the basin, which is photochemically active and where high temperatures are observed during the summer months. Thus, while the largest decreases in gas-phase NH_3 concentrations occur near the strongest emissions sources, the largest decreases in $\text{PM}_{2.5}$ concentrations

occur in downwind areas, particularly northeast of Riverside. Together, changes in the concentration of nitrate, ammonium, and sulfate particles account for essentially all of the decrease in total PM_{2.5} concentrations.

Simulations over the continental US were performed for the winter and summer seasons of 2011 with a range of NH₃ uptake coefficients ($\gamma = 10^{-3} - 10^{-5}$). The inclusion of the SOA-based NH₃ conversion into NOCs had a significant impact on the concentrations of NH₃, NH₄⁺, and NO₃⁻, but did not affect O₃ and SO₄²⁻. The overestimation of NH₃ and NH₄⁺ for the summer was reduced by this new mechanism. Moreover, the prediction of NO₃⁻ was improved by this mechanism, given that the overestimation of NO₃⁻ concentration gradually subsides as the uptake coefficient increases.

The comparison between different uptake coefficient scenarios and the base case allowed a more detailed understanding of the impact of this mechanism on both gas-phase and particle-phase species. Simulations indicated a significant reduction in gas-phase NH₃ due to conversion of NH₃ into NOCs. The highest spatially averaged reduction in gas-phase NH₃ is 31.3 % in the winter and 67.0 % in the summer when the largest uptake is used ($\gamma = 10^{-3}$). The actual value for each individual SOA may be lower or higher than the uniform uptake coefficient used in this study, regardless the magnitude of the impact indicates the importance of including this process in air quality models. The seasonal differences are obvious as the impact is much more significant in the summer than in the winter, due to the higher NH₃ and SOA concentrations in the summer. The concentration of gas-phase HNO₃ was also impacted by this new mechanism. As the NH₃ concentration drops because it is being converted into NOCs, less HNO₃ is neutralized by NH₃, resulting in an overall increase in HNO₃ concentration. Geographically, the biggest reduction in NH₃ happens in the Central

Valley of California during both seasons, the same location as the biggest increase in HNO_3 in the winter. While for the summer, HNO_3 increases more dramatically over the South Coast Air Basin of California and the northeast region of the country.

PM concentrations were found to decrease during the winter period, largely due to the reduction in ammonium nitrate formation caused by the decrease in gas-phase ammonia. The largest uptake scenario ($\gamma = 10^{-3}$) led to a 13.2 % reduction of NH_4^+ , 10.6 % reduction of NO_3^- , and 3.4 % reduction of $\text{PM}_{2.5}$ in the winter, and the largest reduction in $\text{PM}_{2.5}$ occurred over the Central Valley region of California. In contrast, PM concentrations increased during the summer due to an increase in biogenic SOA production resulting primarily from the enhanced acid-catalyzed uptake of IEPOX. Although the reduction in ammonium nitrate was even larger in magnitude during the summer than in the winter, the dramatic increase in biogenic SOA outpaced the decrease caused by ammonium nitrate to result in an overall increase in total $\text{PM}_{2.5}$. The largest increase of biogenic SOA occurred over the southeast region of the US, where high vegetation density is located.

Results from the SoCAB and continental US simulations revealed that the chemical uptake of NH_3 by SOA can have a significant impact on the model-predicted concentrations of important atmospheric pollutants, including NH_3 , HNO_3 , NH_4^+ , NO_3^- , SOA, and PM. Furthermore, while the inclusion of ammonia uptake led to a decrease in inorganic PM concentrations, the effect on total PM concentrations (increase/decrease) was dependent on seasonality. Because inorganic particles (comprised of ammonium, sulfate and nitrate) represent a large portion of total fine particulate matter mass in the SoCAB (Kim et al., 2010; Schiferl et al., 2014), continental US, and many other locations around the world, accurate modeling of gas-phase NH_3 concentrations is essential for predicting future air quality.

Although we focus on the SoCAB and US, results shown here have important global implications as NH_3 emissions have shown increasing trends over the last few decades and are expected to increase even more in the future (Amann et al., 2013; Warner et al., 2017). It is especially important to account for the uptake of NH_3 by SOA in models used to simulate air quality in agricultural areas with strong NH_3 emissions sources. Additionally, models used in the development of air quality management strategies should account for changes in the concentration of NH_3 due to its uptake by SOA to ensure accurate prediction of $\text{PM}_{2.5}$ concentrations. Because significant uncertainty remains regarding the mechanism, rate and extent of reactions between gaseous NH_3 and organic compounds found in SOA, additional studies are needed to better constrain and quantify uptake coefficients for a variety of SOA compounds. Furthermore, better knowledge about basicity of NOCs is needed to verify whether they can neutralize inorganic acids. For example, single particle measurements conducted by Neuman et al. (2003) showed that organic aerosols also contributed to increases in fine-particle mass in regions with high NH_3 emissions rates, suggesting that NH_3 uptake can increase organic aerosol mass concentrations directly. Current air quality models only include one pathway for the acid-catalyzed SOA generation (based on the high NO_x case in the study of Pye et al., 2013), and a more detailed representation of other acid-catalyzed pathways could lead to an even larger impact on the SOA concentration.

CHAPTER 5

Effect of Humidity on Ammonia and Amine Uptake by Secondary Organic Aerosol

5.1 Background

In addition to ammonia, amines provide a source of atmospheric reactive N and are therefore important to consider when investigating potential atmospheric sources of N in particulate matter. Anthropogenic sources of amines include animal husbandry, industrial operations, automobiles, cooking, composting, and sewage (Ge et al., 2011). Examples of natural sources of amines include the ocean, vegetation, biomass burning, and geologic sources, such as volcanic eruptions (Ge et al., 2011). The most common atmospheric amines contain one to six carbons (C_1 - C_6), such as methylamine, dimethylamine, trimethylamine, ethylamine, diethylamine, triethylamine, 1-propanamine, and 1-butanamine (Ge et al., 2011).

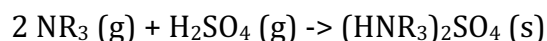
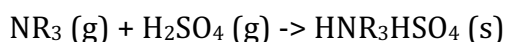
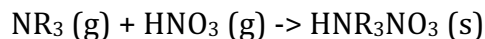
The mixing ratios of amines in the atmosphere vary widely by location; they can range from ppt to ppm levels near their sources and decrease rapidly with distance due to their high reactivity. Trimethylamine, often associated with the putrid smell of fish, has been detected near fish markets and fish processing plants with peak mixing ratios ranging from 0.59 ppb to 10 ppm (Namiesnik et al., 2003; Kamiya and Ose, 1984; Okita, 1970). When measured at these same locations, peak mixing ratios of methylamine and dimethylamine were of the same order of magnitude as trimethylamine. Near industrial sites, peak mixing ratios of methylamine, C_2 amines (dimethylamine, ethylamine), and C_3 amines (trimethylamine, N-methylethaneamine, propanamine) ranged from 0.03-120 ppb, 0.04-130 ppb, and 0.01-120

ppb, respectively (Fuselli et al., 1982; Audunsson and Mathiasson, 1983; Zheng et al., 2015). Aniline, an aromatic amine widely used as raw material in the polymer, rubber, agricultural, and dye industries, has been detected in industrial workplaces at even higher mixing ratios of up to 240 ppb (Patil and Lonkar, 1994). Near animal husbandry operations, peak mixing ratios of methylamine and trimethylamine ranged from 4.2-12.4 ppb and 1.6-69.7 ppb, respectively (Hutchinson et al., 1982; Kuwata et al., 1983; Fujii and Kitai, 1987; Kallinger and Niessner, 1999). Other locations where mixing ratios of small aliphatic amines have been measured in the tens of ppb or higher include food waste composting plants and landfills (Tsai et al., 2008; Rampfl et al., 2008).

When concentrations of ammonia and amines are measured simultaneously, emissions of individual amines are typically 2-3 orders of magnitude smaller than those of ammonia (Hutchinson et al., 1982; Schade and Crutzen, 1995; Chang et al., 2003; Tsai et al., 2008; Zheng et al., 2015). Moreover, Schade and Crutzen (1995) relied on animal husbandry emissions to estimate that the combined annual global emissions of methylamines were approximately 2 orders of magnitude smaller than NH_3 emissions (145 Gg N/yr from amines versus 23.3 Tg N/yr from NH_3). When emissions from marine and biomass were also considered, the estimated global NH_3 emissions remained about 2 orders of magnitude larger than those from methylamines (Ge et al., 2011; Yu and Luo, 2014). It is worth noting that while the concentrations of amines are expected to be two to three orders of magnitude smaller relative to ammonia in the gas phase, particulate concentrations can be much more similar in magnitude (Makela et al., 2001; Sorooshian et al., 2008).

Ammonia, as discussed in the previous chapter can contribute to PM mass and aging. In addition to ammonia, which remains an important atmospheric basic gas due to its

abundance, amine derivatives of ammonia may contribute to PM in similar ways. For instance, amines may also neutralize atmospheric acids and therefore lead to new particle formation (Murphy et al., 2007; Kumar et al., 2018).



Theoretical studies indicate that amines are more effective than ammonia at stabilizing sulfuric acid – amine clusters (Kurten et al., 2008; Kupiainen et al., 2012; Paasonen et al., 2012) that lead to new particle formation. A theoretical study comparing the relative efficiencies of methylamines to stabilize sulfuric acid, found the stabilizing strength of ammonia and amines to increase in the following way: ammonia < monomethylamine < trimethylamine ≤ dimethylamine (Olenius et al., 2017). Evidence for particle formation from DMA–H₂SO₄–H₂O clusters was observed in the megacity of Shanghai, China (Yao et al., 2018).

Other pathways explored in laboratory experiments by which amines may contribute to aerosol mass include the gas phase oxidation of amines by O₃, OH, and NO₃ (Atkinson et al., 1987; Murphy et al., 2007; Tang et al., 2013; Tuazon et al., 1984; Tuazon et al., 1994), gas phase oxidation of a known SOA precursor in the presence of dimethylamine (Duporte et al., 2017), and reactions between amines and carbonyl species carried out in the gas, surface, and bulk phase (De Haan et al., 2011; Galloway et al., 2014; Duporte et al., 2016; Kampf et al., 2016; De Haan et al., 2017; De Haan et al., 2019). This latter pathway may contribute to aerosol aging, for instance by leading to the formation of light absorbing species when pre-existing aerosol is exposed to amines (De Haan et al., 2019), akin to the browning of lab-generated SOA when exposed to ammonia (Bones et al., 2010; Updyke et al., 2012).

The change in the optical properties of aerosol exposed to NH_3 or amines is one clear piece of evidence that reactions occur between species in the aerosol and ammonia or amines. In this study, we focused on the incorporation of organic N into aerosol particles for evidence of ammonia and dimethylamine reactions with SOA and also considered the effects of relative humidity on this process. Liu et al. (2018) explored the NH_3 uptake by toluene SOA and found that when the relative humidity was increased from 20-60%, the uptake of NH_3 also increased. The explanation offered for this trend was that due to the high viscosity of toluene SOA, the reactive uptake and diffusivity of NH_3 is kinetically inhibited at $\text{RH} < 20\%$ where toluene SOA can be classified as a glassy material. Then the transition from diffusion-limited to saturated uptake occurred across 20-60% RH, which suggested that toluene secondary organic material (SOM) is semi-solid across this RH range. Above 60% RH, reactive uptake of NH_3 no longer increased with RH and this was attributed to the toluene SOM behaving as a viscous liquid at this RH range. On the other hand, for less viscous SOA, increasing the RH may theoretically suppress reactive uptake of NH_3 due the fact that this reaction follows a condensation mechanism accompanied by a loss of water. Previous studies investigating the browning of SOA after NH_3 exposure have proposed reaction pathways for browning in which carbonyl groups in the SOA react with NH_3 and water is a byproduct (Bones et al., 2010, Updyke et al., 2012; Lin et al., 2015; Laskin et al., 2015). Therefore, increasing RH can favor the reverse reaction and suppress NH_3 uptake by SOA.

Studies exploring the effect of relative humidity on amine uptake by SOA are lacking, however if amine uptake is similar to that of ammonia, we would expect to see the same trends. Specifically, our working hypothesis for this study is that as RH increases, amine

uptake by highly viscous SOA will also increase, but amine uptake by less viscous SOA will be suppressed.

5.2 Experimental Methods

Smog chamber experiments were performed in order to explore the reactive uptake of ammonia and dimethylamine by SOA particles, as well as the dependence of this process on relative humidity.

A biogenic (d-limonene or α -cedrene) or an anthropogenic (toluene) VOC was oxidized in a 5 m³ Teflon chamber to generate SOA under low-NO_x conditions. In these low-NO_x experiments, no NO was added to the chamber; background concentrations of NO as measured by an NO/NO_y analyzer (Thermo Scientific, Model 42i) were typically below 1 ppb. Organic seed aerosol containing nitrogen was used to serve as an internal standard of nitrogen in the particles when analyzing particle composition data. The seed solution was made by dissolving nicotinic acid (99.5%, Sigma Aldrich) in deionized water (1 g/L). Relative humidity (RH) in the chamber was achieved by flowing purified air through a Nafion humidifier. The relative humidity ($\pm 2\%$ RH) and temperature ($\pm 1^\circ\text{C}$) were monitored with a Vaisala HMT330 probe. The RH was varied between <2-50% to investigate the effect of relative humidity on the uptake of ammonia or dimethylamine by SOA. D-Limonene (97%, Sigma) or α -cedrene (98%, Sigma-Aldrich) was introduced to the chamber to reach a mixing ratio of 50 ppb and was subsequently oxidized via ozonolysis (500 ppb O₃) or photooxidation (1 ppm H₂O₂). Anthropogenic SOA consisted of injecting 1 ppm toluene (99.8%, Fisher Scientific) and 2 ppm of aqueous H₂O₂ (30% wt, Fisher Scientific). The mixing ratio used for toluene was higher than that of the biogenic VOCs due to the lower SOA mass yield of toluene

SOA than d-limonene and α -cedrene SOA, as well as the suppression of the SOA mass yield for toluene SOA at higher relative humidity under low-NO_x conditions (see Chapter 2). In the photooxidation experiments, aqueous hydrogen peroxide was introduced into the chamber by evaporation into a flow of clean air, and then UV-B lamps were turned on to initiate the photooxidation. In all experiments, prior to oxidation, gases in the chamber were mixed with a fan for 10 minutes and a PTRMS was used to confirm that the VOC was well mixed before initiating oxidation. The fan was turned off after that to slow down particle wall loss. After the particle mass concentration of SOA reached a peak value, a gas mixture containing NH₃ (1000 ppm NH₃ in N₂, Airgas), aqueous NH₃ (NH₄OH, 28 wt %, Fisher Scientific), or aqueous DMA (C₂H₇N, 40 wt %) was introduced into the chamber. The target mixing ratio of NH₃ or DMA in the chamber was supposed to be 500 ppb, however, due to losses in the inlet lines and chamber walls the actual mixing ratio was around 200 ppb as verified with an Ecotech 9842 NH₃/NO_x analyzer. Particle volume concentration was monitored with a scanning mobility particle sizer (SMPS; TSI 3936) equipped with a condensed particle counter (CPC; TSI 3775). The chemical composition of SOA particles was probed online with a Time-of-Flight Aerosol Mass Spectrometer (ToF-AMS). The ToF-AMS data were analyzed using PIKA 1.22A with SQUIRREL 1.62A software.

Calculating uptake coefficients for NH₃ and DMA from NH₃ monitor data

The uptake coefficients for NH₃ and DMA were calculated from NH₃ monitor data. The monitor can detect NH₃, small amines, and other simple nitrogen containing organic compounds by converting them to NO on a Pt-based catalyst and then detecting NO by chemiluminescence. The loss of NH₃ or DMA mixing ratios as captured by the NH₃ analyzer was fitted to a first order decay rate equation in order to obtain the first-order loss rate

constant, k (s^{-1}) The rate constant was used in the following equation to determine the uptake coefficient, γ .

$$\gamma = \frac{4 \times k}{v_{NH_3} \times C_{area}} \quad (5.1)$$

At room temperature, the average speed of NH_3 molecules, v_{NH_3} ($m\ s^{-1}$), and DMA molecules is $6.1 \times 10^2\ m\ s^{-1}$ and $3.7 \times 10^2\ m\ s^{-1}$, respectively. The concentration of surface area of the particles, C_{area} ($m^2\ m^{-3}$), was calculated by averaging the total surface area of the particles (obtained from the SMPS) from the time of NH_3 or DMA injection through the end of the experiment. This time segment matched the period of time for which the first-order loss rate constant was calculated.

Note, that this method cannot distinguish uptake due to wall loss or the formation organic nitrogen compounds in particle due to neutralization of acids and physical dissolution of ammonia or amine in the particle material. Therefore, it measures the total uptake coefficient. Given that the elemental ratios in the particles as determined with the AMS should be less sensitive to wall loss effects, AMS data was used to obtain a normalized uptake coefficient.

$$normalized\ \gamma_{NH_3} = \gamma_{NH_3} \times \frac{n_N^{added}\ (AMS)}{n_N^{added}\ (NH_3\ monitor)} \quad (5.2)$$

The moles of nitrogen, n_N^{added} , added to the particles are described below.

Calculating moles of nitrogen added from NH₃ monitor and AMS data

The moles of nitrogen added to the particles, n_N^{added} (mol), is equal to the loss in the moles of NH₃ or DMA after injection. For simplicity, NH₃ is used in the following equations, but note that these equations can be used in the same manner for DMA.

$$n_N^{added} = ([NH_3]_0 - [NH_3]_t) \times V_{chamber} \quad (5.3)$$

The starting concentration of NH₃, $[NH_3]_0$, is equivalent to the amount we inject (e.g., 200 ppb as determined by the NH₃ analyzer). The concentration of NH₃ at some later time t , $[NH_3]_t$, can be obtained from the first order decay fit of the NH₃ loss. The concentration of NH₃ is multiplied by the chamber volume, $V_{chamber}$, to convert to moles of NH₃. Equation 5.3 above can be expressed as:

$$n_N^{added} = [NH_3]_0 \times (1 - e^{-k \times \Delta t}) \times V_{chamber} \quad (5.4)$$

The first-order loss rate constant, k , is the same one used earlier in the uptake coefficient calculations.

For an independent and potentially more accurate measurement of the amount of N inserted to the particles, we relied on AMS data. AMS can sensitively detect presence of nitrogen in particles, and furthermore, it can separately measure organic and inorganic nitrogen. Prior to NH₃ or DMA injection, nicotinic acid was the only source of N in the particles and was responsible for the initial average total N:C ratio of the particles. While nicotinic acid could react with the oxidant, we would expect this to be minimal given that nicotinic acid is in the condensed phase when introduced into the chamber and is expected to be less reactive than the other precursors used in this study (Atkinson et al., 1986; Atkinson, 1988; Atkinson,

1990; Tully et al., 1981). After the injection of NH₃ or DMA, the increase in the N:C ratio of the particles was used to calculate the moles of N added into the particles. The following equation was used to calculate the moles of N added to particles from the AMS data.

$$n_N^{added} = n_N^0 \times \left(\frac{N:C \text{ after } NH_3 \text{ injection}}{N:C \text{ before } NH_3 \text{ injection}} - 1 \right) \quad (5.5)$$

The initial moles of nitrogen in the particles, n_N^0 , were calculated from the concentration of nicotinic acid seeds present in the chamber before organic aerosol formation and before NH₃ or DMA injection. This equation assumes that the amount of organic carbon in particles is not affected by the reaction of SOA with ammonia or amine. It also assumes that AMS is equally sensitive to the nicotinic acid and to the organic nitrogen compounds formed in the reaction.

5.3 Results

When toluene SOA was exposed to dimethylamine in the chamber, there was no observed change in particle number and mass concentrations, as was the case when SOA was exposed to NH₃ (Fig. 4.2). Figure 5.1 is an example of SMPS-recorded data for a typical NH₃ or DMA uptake in a toluene SOA experiment. The experiment began with the injection of nicotinic acid seeds (light blue region), which led to an initial rapid increase in particle number concentration (blue trace); subsequently the number concentration decreased as seed particles coalesced and some partitioned to the walls. As the SOA was generated through photooxidation (yellow region), the particle number concentration (blue trace) did not change significantly while the particle mass concentration (red trace) rose significantly suggesting that most of the new SOA particles formed on the pre-existing seeds.

After photooxidation was stopped, the SOA was exposed to dimethylamine (green region) and the particle number and mass concentrations remained unaffected. This is fully consistent with our expectation that the chemical uptake of ammonia/amine should not significantly change the mass of the reacting SOA compound (ammonia/amine are taken up but water molecules are released as products).

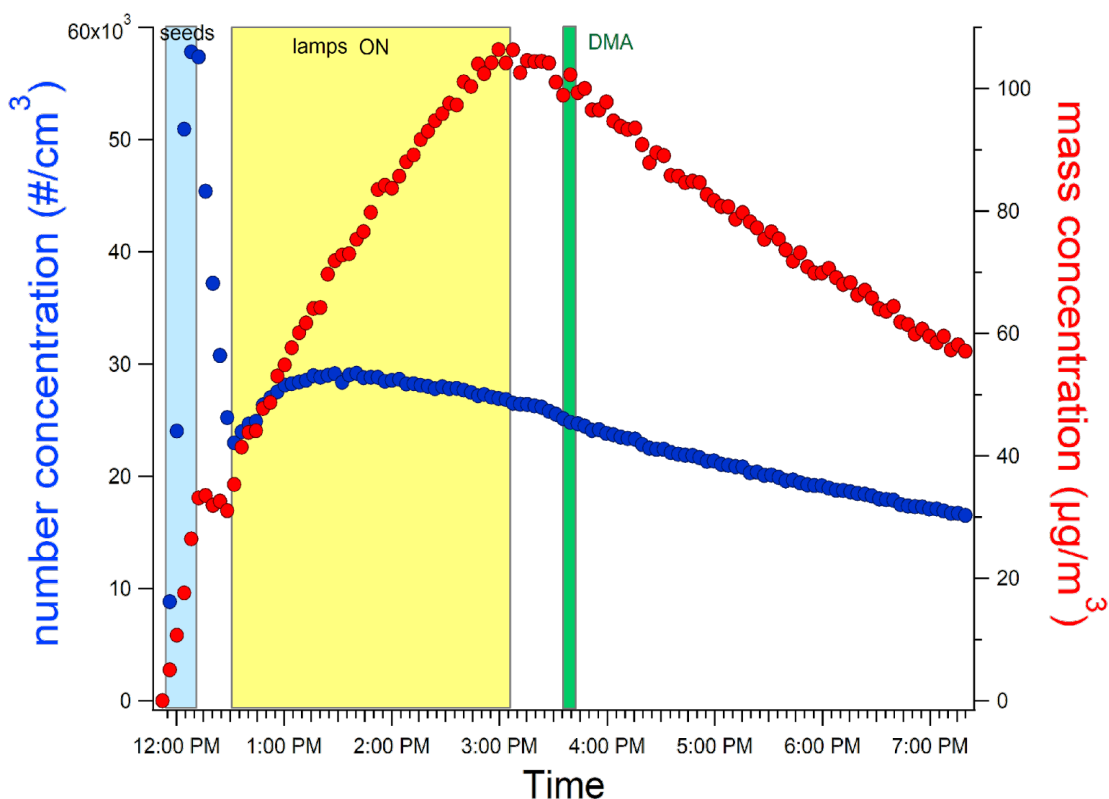


Figure 5.1. Particle number concentration (blue trace) and particle mass concentration (red trace) for toluene/OH SOA at low relative humidity exposed to dimethylamine (green region), showing that dimethylamine amine exposure did not affect these parameters.

SMPS data for d-limonene or α -cedrene SOA exposed to NH_3 or dimethylamine in the chamber was very similar to that from toluene SOA. Again, as shown in Figure 5.2, there was no significant change in particle number and mass concentrations after exposure of the SOA to DMA. One distinction between the SOA made from the biogenic VOCs (d-limonene, α -cedrene) versus toluene was that the d-limonene and α -cedrene oxidation formed particles

much more rapidly. This can be seen in Figure 5.2, where upon the addition of O₃ in the chamber, there is a sudden increase in the particle number concentration (blue trace), suggesting that upon oxidation new particles formed instead of solely growing onto the pre-existing seed particles.

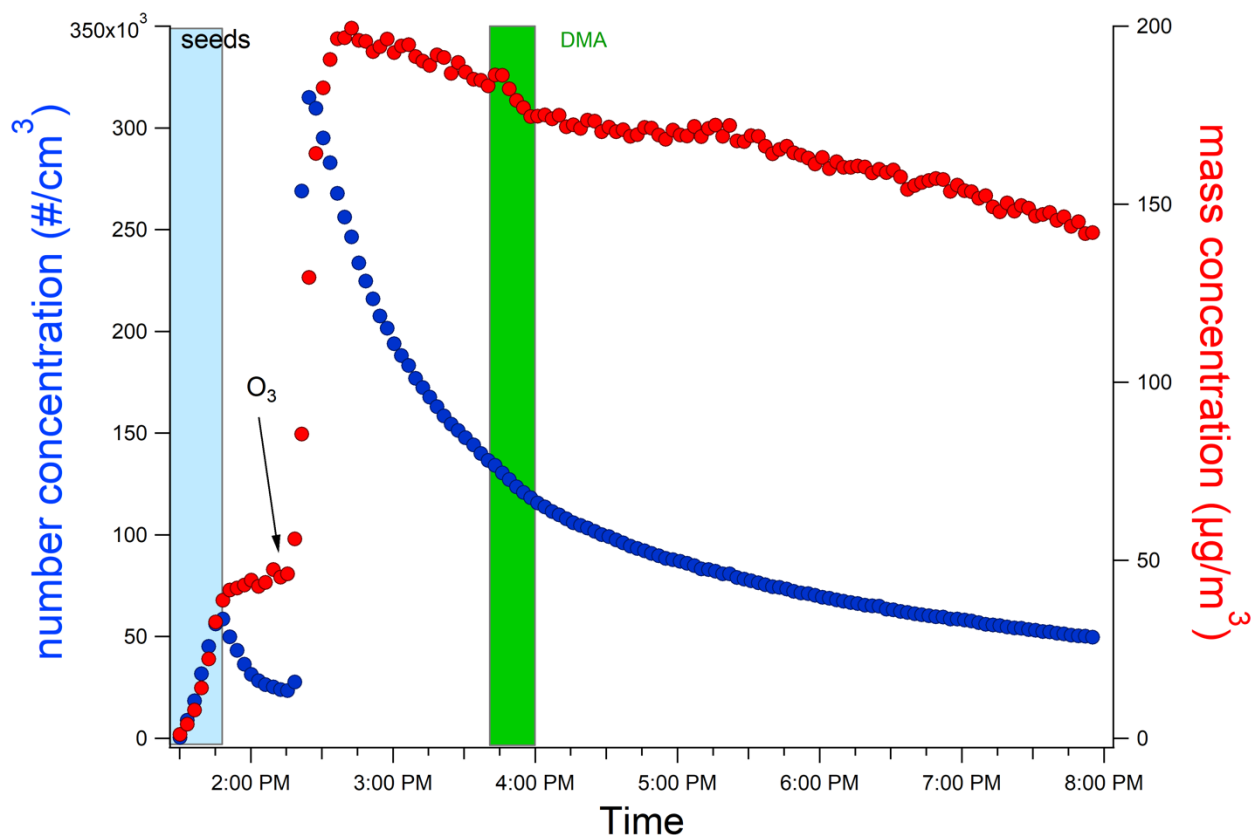


Figure 5.2. Particle number concentration (blue trace) and particle mass concentration (red trace) for d-limonene/O₃ SOA at low relative humidity exposed to dimethylamine (green region), showing that dimethylamine amine exposure did not significantly affect these parameters.

Figure 5.3 compares the reactive uptake of NH₃ to that of DMA by d-limonene SOA particles under low RH. We focus on d-limonene SOA for this comparison because d-limonene SOA showed the strongest interaction with NH₃ in comparison to toluene SOA and n-hexadecane SOA (discussed in Chapter 4). When exposed to the same mixing ratios of NH₃ and DMA (200 ppb), d-limonene SOA reacted more efficiently with DMA as evidenced by the faster and larger increase in the N:C ratio in the particles. More specifically, when exposed to NH₃, the

N:C ratios of the d-limonene SOA particles increased by 0.005 after nearly 2 h (Fig. 5.3 left panel); however, the increase in the N:C ratios was an order of magnitude greater after 2 h when exposed to DMA (Fig. 5.3 right panel). It is likely that the lower volatility of DMA (vapor pressure = 1520 mm Hg at 25°C; Daubert and Danner, 1989) than NH₃ (vapor pressure = 7500 mm Hg at 25°C; Daubert and Danner, 1999) contributes to the observed higher uptake by d-limonene SOA.

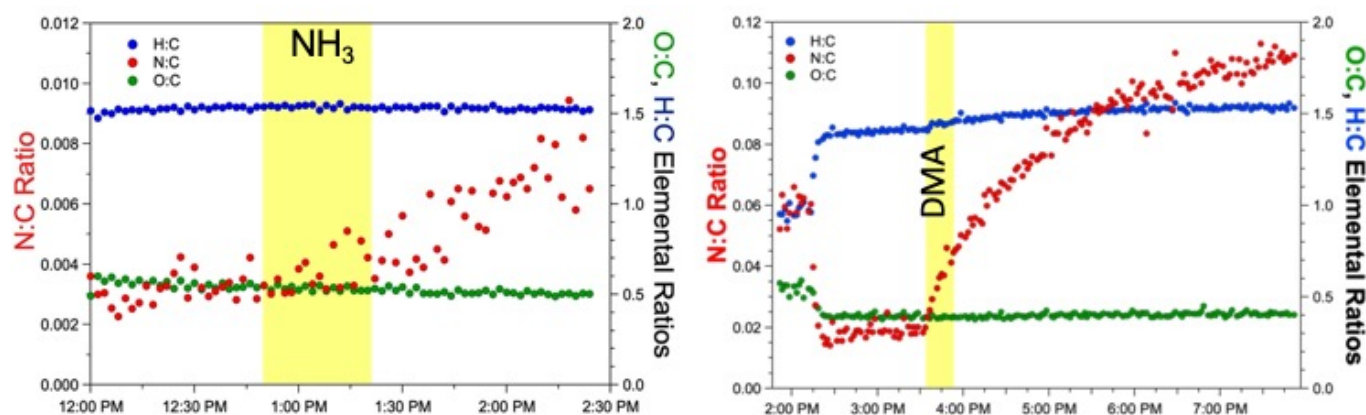


Figure 5.3. Elemental ratios of d-limonene ozonolysis SOA particles when exposed to NH₃ (left panel) and DMA (right panel), showing how N:C ratios increases more significantly from DMA uptake than NH₃ uptake. Note that the left y-axis is an order of magnitude larger in the right panel than in the left.

Figure 5.4 shows d-limonene ozonolysis SOA exposed to DMA at varying RH. After exposure of d-limonene SOA to DMA (yellow region) under low RH (a), we see a significant increase in the N:C ratio of the particles (red trace). As the RH was increased from <2% to 20% (b) and then to 50% (c), the increase in the N:C ratios for the particles after DMA exposure was suppressed. These observations agree with the hypothesis that the uptake of amines leads to condensations reactions where one or more water molecules are produced, therefore as RH increases and the reverse reaction is favored, the uptake of DMA is suppressed.

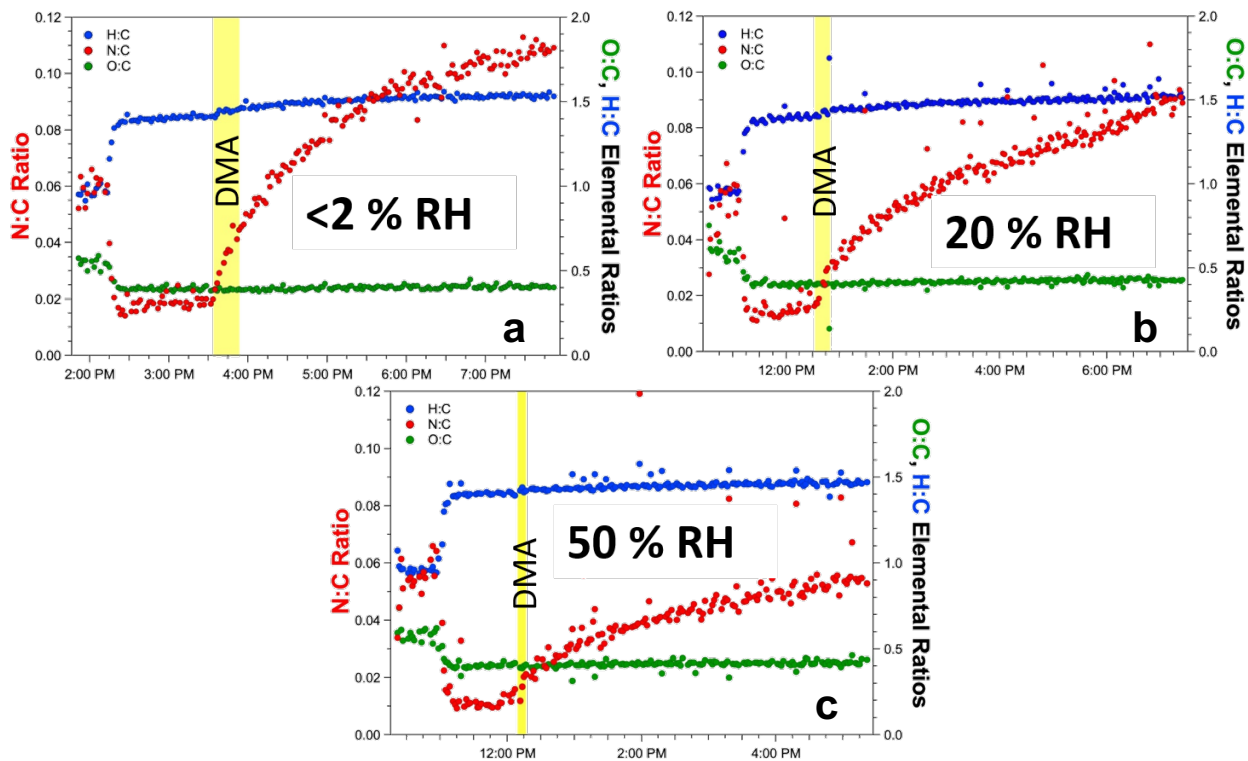


Figure 5.4. d-Limonene ozonolysis SOA exposed to DMA at varying RH. As the RH humidity was increased from <math><2\%</math> (a) to 20% (b) to 50% (c), the increase in the N:C ratio (red trace) after DMA exposure (yellow region) became smaller indicating that an increase in RH suppresses DMA uptake.

Figure 5.5 shows α -cedrene ozonolysis SOA exposed to DMA at varying RH. Similar to the trend observed in the d-limonene SOA data, as the RH was increased from <math><2\%</math> (a) to 20% (b) to 50% (c), the increase in the N:C ratios for the particles was suppressed. Again, these observations agree with the proposed mechanism that the uptake of amines leads to condensations reactions, and therefore as RH increases, the uptake of DMA is suppressed.

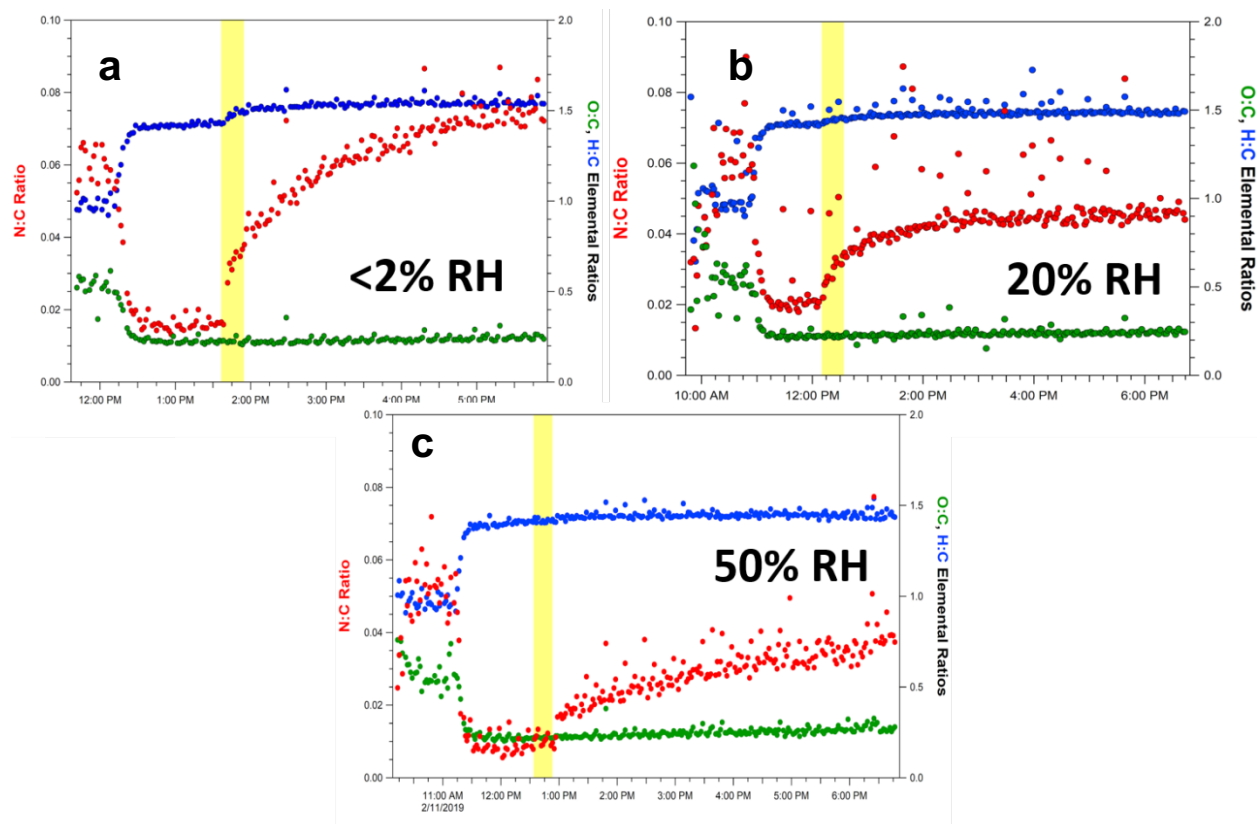


Figure 5.5. Plots showing the H:C (blue trace), O:C (green trace), and N:C (red trace) ratios as a function of time for α -cedrene ozonolysis SOA particles exposed to DMA at varying RH. As the RH humidity was increased from <2% (a) to 20% (b) to 50% (c), the increase in the N:C ratio (red trace) after DMA exposure (yellow region) became smaller indicating that an increase in RH suppresses DMA uptake.

Figure 5.6 shows toluene photooxidation SOA exposed to DMA at low and 20% RH. Note that experiments performed at 50% RH need to be repeated because insufficient time was given for photooxidation and the growth in particle mass concentration was small and therefore is not discussed here. Unlike in the NH_3 uptake experiments (Chapter 4), exposure of toluene SOA to DMA (yellow region) resulted in a noticeable increase in the particles N:C ratio (red trace), again suggesting that uptake of DMA is more efficient than that of NH_3 .

At <2% RH (left panel) after DMA exposure (yellow region), the N:C ratio (red trace) of the particles increased from approximately 0.08 to 0.12 ($\Delta = 0.04$) after 2.5 h. At 20% RH (right panel) after DMA exposure (yellow region), the N:C ratio (red trace) of the particles

increased from about 0.06 to 0.10 ($\Delta = 0.04$) after 2.5 h. Given the similar change in the N:C ratios, more experiments at higher RH are necessary to establish a trend. Within this range of RH (0-20%), Liu et al. (2018) reported no significant change in NH_3 uptake by toluene SOM. In that same publication, they report an increase in NH_3 uptake by toluene SOM with an increase in RH when the RH was between 20% and 60%, explaining that the limitations in mass transfer rate for uptake due to the high viscosity of toluene SOM at low RH disappear at $\text{RH} > 20\%$ (Liu et al., 2018).

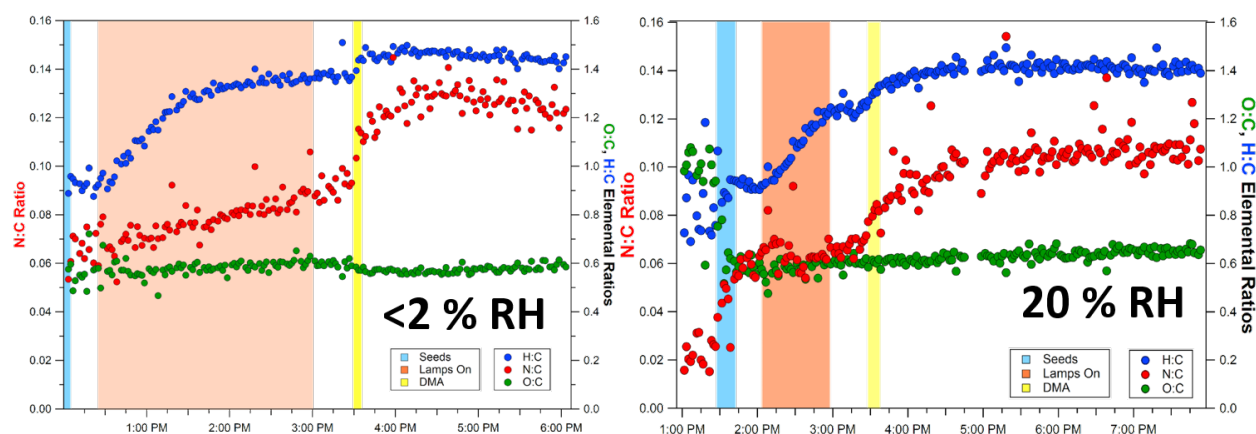


Figure 5.6. Toluene photooxidation SOA exposed to DMA at varying RH. As the RH humidity was increased from $< 2\%$ (left) to 20% (right), the increase in the N:C ratio (red trace) after DMA exposure (yellow region) was similar (~ 0.04).

When looking at the N-containing families, the largest increase after DMA exposure was in the CHN family, shown in Fig. 5.7 (purple trace), indicating that DMA uptake predominantly led to an increase in organic nitrogen in the particles. Individual N-containing fragments that led to an increase in organic nitrogen in the particles. Individual N-containing fragments that had a strong signal after DMA exposure are listed in Table 5.1. These fragments were taken from mass spectra representing the particle composition averaged from the time beginning with DMA injection through the end of the experiment.

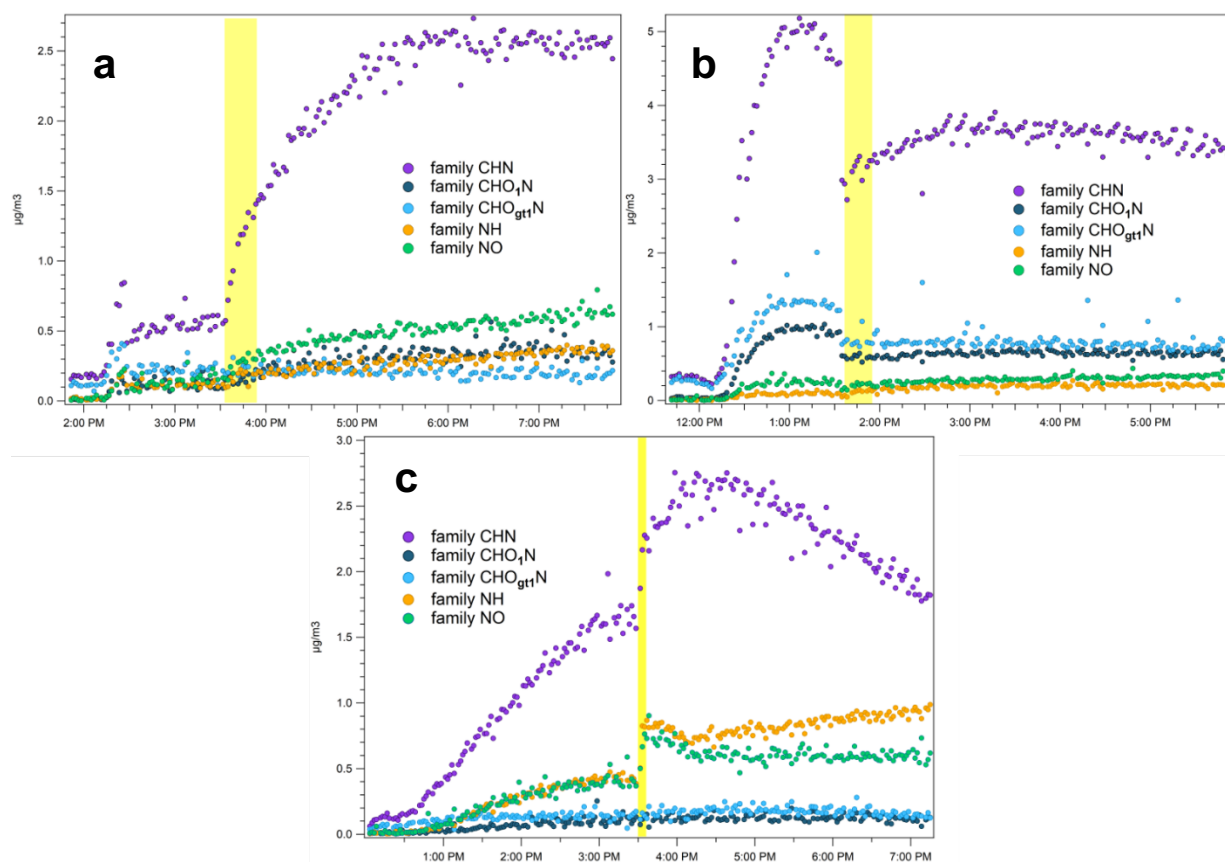


Figure 5.7. Nitrogen-containing families plotted versus time for LIM/O₃ SOA (a), CED/O₃ SOA (b), and TOL/OH SOA (c) exposed to DMA (yellow region) under low RH. The initial decrease seen in the N-containing families for the LIM/O₃ SOA particles (~2:30 pm) and the CED/O₃ SOA particles (~1:30 pm) prior to DMA injection were caused by diluting the particle flow to the AMS, not by a change in particle composition. This data show that the largest increase after DMA exposure was in the CHN family (purple trace) for the three SOA systems.

Table 5.1. Table listing the 15 most prominent N-containing peaks and their families for LIM/O₃ SOA, CED/O₃ SOA, and TOL/OH SOA after exposure to DMA under low RH. Peaks are listed in descending order with respect to their signal.

	LIM/O ₃ SOA, low RH		CED/O ₃ SOA, low RH		TOL/OH SOA, low RH	
	family	<i>m/z</i> , fragment	family	<i>m/z</i> , fragment	family	<i>m/z</i> , fragment
1	CHN	42.034, C ₂ H ₄ N	CHN	44.050, C ₂ H ₆ N	CHN	44.050, C ₂ H ₆ N
2	CHN	27.011, CHN	CHN	42.034, C ₂ H ₄ N	NO	29.998, NO
3	NO	29.998, NO	CHN	79.042, C ₅ H ₅ N	NH	17.027, NH ₃
4	CHN	44.050, C ₂ H ₆ N	NO	29.998, NO	NH	16.019, NH ₂
5	CHN	30.034, CH ₄ N	CHN	55.042, C ₃ H ₅ N	CHN	45.058, C ₂ H ₇ N (DMA)
6	CHN	41.027, C ₂ H ₃ N	CHN	53.027, C ₃ H ₃ N	CHN	42.034, C ₂ H ₄ N
7	NO	45.993, NO ₂	CHN	51.011, C ₃ HN	CHN	27.011, CHN
8	CHN	43.042, C ₂ H ₅ N	CHN	27.011, CHN	CHN	28.019, CH ₂ N
9	CHN	28.019, CH ₂ N	NH	18.034, NH ₄	NH	18.034, NH ₄
10	CHN	29.027, CH ₃ N	CHO ₁ N	55.006, C ₂ HON	CHN	43.042, C ₂ H ₅ N
11	CHN	58.066, C ₃ H ₈ N	CHN	30.034, CH ₄ N	CHN	30.034, CH ₄ N
12	NH	17.027, NH ₃	CHN	43.042, C ₂ H ₅ N	NO	45.993, NO ₂
13	CHN	45.058, C ₂ H ₇ N (DMA)	CHN	95.074, C ₆ H ₉ N	CHN	41.027, C ₂ H ₃ N
14	CHN	40.019, C ₂ H ₂ N	CHN	50.003, C ₃ N	CHN	40.019, C ₂ H ₂ N
15	CHO _{>1} N	123.032, C ₆ H ₅ O ₂ N (nicotinic acid)	CHN	41.027, C ₂ H ₃ N	CHO _{>1} N	123.032, C ₆ H ₅ O ₂ N (nicotinic acid)

The presence of DMA in the particles at *m/z* 45.058 (Table 5.1) suggests that a portion of DMA uptake may lead to non-reactive uptake within the time of the experiment. It is also possible that this C₂H₇N fragment may be a fragment of something larger. Figure 5.8 shows that removing the DMA peak from the data (solid black squares) does not affect the change in N:C trends (solid red circles) observed after DMA exposure (yellow region). Therefore, while some DMA may remain in the particles, most of the change in N:C results from reactive uptake of DMA.

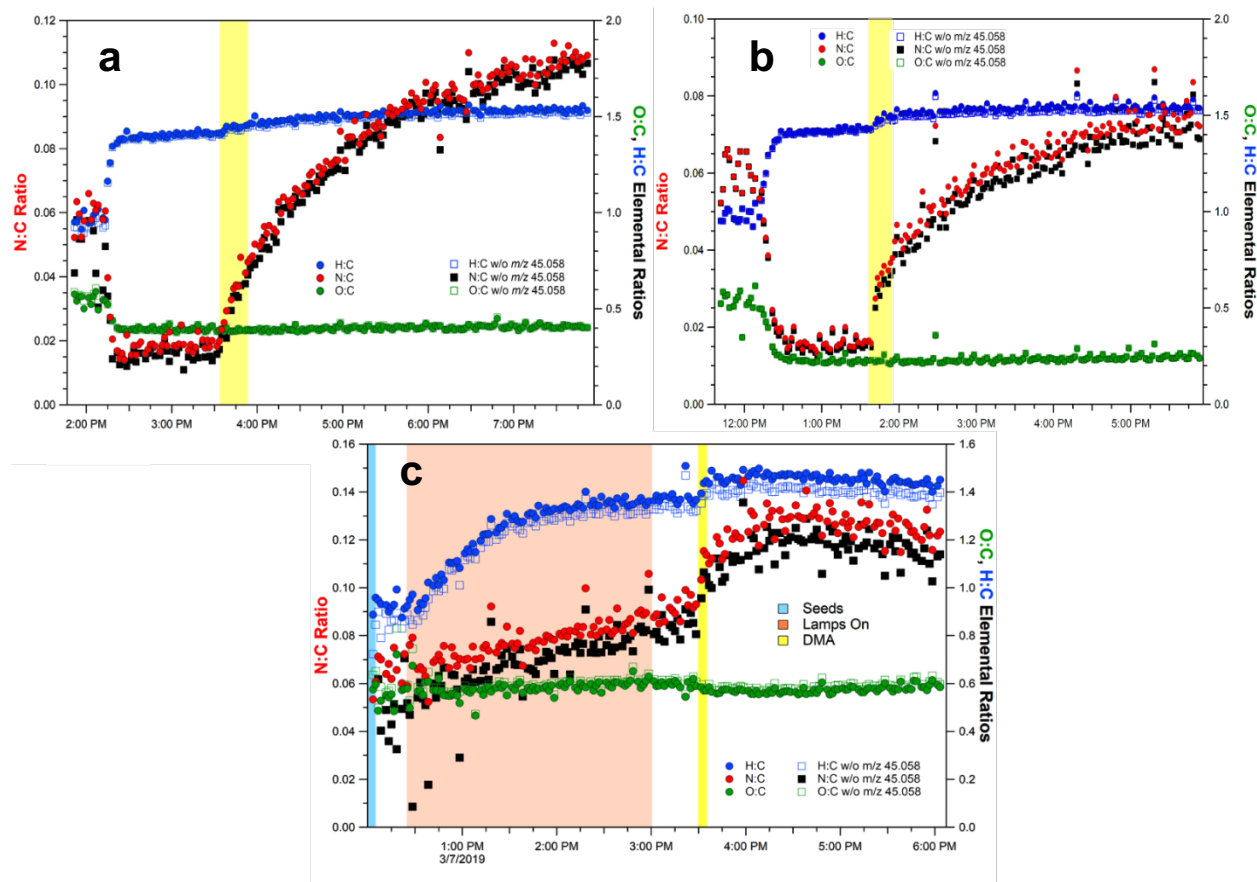


Figure 5.8. Elemental ratios plotted versus time for LIM/O₃ SOA (a), CED/O₃ SOA (b), and TOL/OH SOA (c) exposed to DMA (yellow region) under low RH. The elemental ratios for each SOA system are plotted to compare how including the DMA peak (circle traces) versus removing the DMA peak (square traces) affects the elemental ratios. Removing the DMA peak leads to a small overall decrease in the N:C ratios but does not affect how the N:C ratio changes after DMA exposure.

Table 5.2 lists the uptake coefficients obtained from NH₃ monitor data for NH₃ (left) by LIM/OH and LIM/O₃ SOA under different RH conditions. Uptake coefficients for DMA (right) by LIM/O₃, CED/O₃, and TOL/OH SOA under varying RH conditions are also listed. The normalized uptake coefficients for NH₃ were on the order of 10⁻⁵, which falls within the lower end of the range of NH₃ uptake coefficients previously reported for α -pinene ozonolysis SOA and m-xylene SOA (Liu et al., 2015). The DMA uptake coefficients ranged from 10⁻⁵ to 10⁻⁴.

The moles of nitrogen per cubic meter of air incorporated into the particles was calculated by using NH₃ monitor and AMS data. The values calculated from the NH₃ monitor were

consistently higher than those calculated from the AMS data. One possibility for this discrepancy is that when using NH_3 monitor data, we assume that all NH_3 loss is due to uptake by the particles; this may be an overestimation as some NH_3 can partition to the chamber walls. Since the uptake coefficients calculated using the NH_3 analyzer data reflects total NH_3 or DMA uptake in the chamber (rather than solely that from the SOA), normalized uptake coefficients were calculated using AMS data in order to obtain more realistic values. These normalized coefficients resulted in values approximately one order of magnitude smaller and were comparable to the lower NH_3 uptake coefficient values previously reported for α -pinene ozonolysis SOA and m-xylene SOA (Liu et al., 2015). Furthermore, while the normalized uptake coefficients are likely to be more realistic than the un-normalized coefficients reported in Table 5.2, it is evident that these normalized uptake coefficients still do not capture the RH dependence that the AMS data does. Future control experiments performed at various RH, which are necessary to estimate the contribution to the uptake coefficient from wall loss, may allow us to better capture the RH dependence with the NH_3 analyzer.

Table 5.2. NH₃ uptake coefficients and increase in moles of N in the particles after exposure to NH₃ (left). DMA uptake coefficients and increase in moles of N in the particles after DMA exposure (right).

VOC / Oxidant	RH (%)	Y _{NH3}	normalized Y _{NH3}	NH ₃ monitor	AMS
				n _{N added} (mol)	n _{N added} (mol)
LIM/OH	50	3.9E-4	9.7E-6	1.7E-5	4.2E-7
LIM/OH	50	4.9E-4	1.5E-5	1.9E-5	6.0E-7
LIM/OH	50	2.9E-4	4.7E-6	1.3E-5	2.1E-7
LIM/OH	20	9.0E-4	1.5E-5	3.2E-5	5.5E-7
LIM/OH	<2	8.3E-4	2.7E-5	4.0E-5	1.3E-6
LIM/OH	<2	8.2E-4	3.3E-5	9.0E-6	3.6E-7
LIM/O ₃	50	2.0E-4	2.5E-6	2.6E-5	3.3E-7
LIM/O ₃	50	6.4E-4	2.5E-5	2.5E-5	9.8E-7
LIM/O ₃	50	5.0E-4	3.2E-5	1.7E-5	1.1E-6
LIM/O ₃	20	2.1E-4	1.7E-5	2.0E-5	1.6E-6
LIM/O ₃	<2	2.0E-4	1.2E-5	1.3E-5	8.0E-7

VOC / Oxidant	RH (%)	Y _{DMA}	normalized Y _{DMA}	DMA (from NH ₃ monitor)	AMS
				n _{N added} (mol)	n _{N added} (mol)
LIM/O ₃	50	2.2E-4	2.8E-5	3.2E-5	4.1E-6
LIM/O ₃	20	1.8E-4	3.0E-5	2.9E-5	4.8E-6
LIM/O ₃	<2	3.4E-4	8.0E-5	3.6E-5	8.5E-6
CED/O ₃	50	3.3E-4	1.5E-5	3.1E-5	1.4E-6
CED/O ₃	20	2.0E-4	1.2E-5	3.6E-5	2.1E-6
CED/O ₃	<2	2.1E-4	3.2E-5	3.2E-5	4.8E-6
TOL/OH	20	3.5E-3	1.0E-4	4.0E-5	1.2E-6
TOL/OH	20	2.5E-3	7.6E-5	3.6E-5	1.1E-6
TOL/OH	<2	2.2E-3	3.4E-5	3.9E-5	6.0E-7

5.4 Conclusions

This study illustrates that under the conditions explored in this study, dimethylamine uptake is more efficient than that of ammonia by secondary organic aerosol. These findings suggest that while ammonia is more abundant in the atmosphere, amine uptake may still be a potential source of organic nitrogen in particulate matter. This idea is indirectly supported by field studies in which amine concentrations are much more similar to ammonia concentrations in the particulate phase than in the gas phase (Makela et al., 2001; Sorooshian et al., 2008). Emission inventories for amines are not as robust as those of NH₃, making air

quality simulations (such as those described in the previous chapter for NH_3 uptake) difficult. However, these experiments suggest that the uptake of amines may be an important source of organic N in particulate matter. Here, we chose to focus on DMA, a C_2 amine, but other common atmospheric C_1 - C_6 amines remain to be explored and those with even lower volatilities than DMA may lead to more efficient uptake by SOA.

Moreover, when relative humidity was increased, the reactive uptake of dimethylamine by d-limonene and α -cedrene SOA was suppressed, as indicated by AMS data. These observations are consistent with previous studies suggesting that reaction of ammonia with carbonyls in the SOA resulting in the loss of water is an important pathway in the uptake of ammonia of SOA. We propose here that amine reactions undergo similar dehydration reactions and therefore as relative humidity was increased, the reverse reaction was favored resulting in the observed suppression of amine uptake.

CHAPTER 6

Summary

6.1 Research Goals

Secondary organic aerosols (SOA) constitute a significant fraction of fine particulate matter ($PM_{2.5}$) and because SOA is not well-understood, it remains a large source of uncertainty in models that aim to predict global climate. SOA are formed in the atmosphere through the oxidation of volatile organic compounds (VOCs). VOCs are emitted from various anthropogenic (e.g., incomplete combustion, industrial processes) and natural (e.g., vegetation) processes. Biogenic terpenes, such as isoprene, d-limonene, and α -pinene, as well as anthropogenic compounds such as saturated hydrocarbons, toluene and xylenes, and condensed aromatics are some of the most commonly studied SOA precursors. A motivation for studying these hydrocarbon compounds is their prevalence in the environment. Beyond various types of hydrocarbons, scant research exists on SOA made from VOCs containing other common elements such as O, N, and S, thereby potentially missing others sources of SOA. One of the goals of my research was to investigate the formation of SOA from VOCs containing nitrogen atoms.

In addition to studying previously unaccounted sources of SOA, other ways in which laboratory studies can continue to improve our understanding of SOA behavior in the environment is to generate SOA under more realistic conditions. Examples of how experiment designs have improved over time in order to generate SOA under more environmentally relevant conditions include using lower VOC concentrations, using VOC mixtures instead of single VOC precursors, and varying the temperature and relative

humidity (RH) at which SOA is generated. A second goal of my research was to investigate the effect of RH on the formation of SOA.

Once SOA is generated, a myriad of critical questions can be asked about its subsequent chemical transformations or 'aging' in the environment. Many pathways of SOA aging exist that can lead to SOA mass gain or loss, changes in chemical composition (e.g., increasing oxidation), and changes in light-absorption properties, among others. In particular, I was interested in how the presence of nitrogen-containing organic compounds (NOC) in SOA can alter its light-absorption properties. Therefore, the third goal of my research was to investigate the introduction of NOC in SOA by aging SOA in the presence of ammonia (NH_3) and dimethylamine (DMA), two reduced nitrogen species common in the atmosphere.

6.2 Goal 1: Studying the effect of RH on SOA particle formation

Chapter 2 described the study where SOA made from toluene, an anthropogenic VOC was generated under a range of RH, and the RH was found to affect both the amount of toluene SOA formed (mass yield) and its chemical composition.

SOA was produced in a smog chamber from the photooxidation of toluene at <2-90% RH, collected on filters, and analyzed with high-resolution mass spectrometry (HRMS) to look for changes in chemical composition. A scanning mobility particle sizer (SMPS) was employed to look at the RH dependence of particle mass concentration. SMPS data showed that the particle mass loading decreased by nearly an order of magnitude when RH increased from < 2 to 75–90% for low- NO_x toluene SOA. HRMS measurements revealed a significant reduction in the fraction of oligomers present in the SOA generated at 75 % RH compared to SOA generated under dry conditions. The volatility distributions of the SOA compounds,

estimated from their molecular formulas using the “molecular corridor” approach, confirmed that low-NO_x toluene SOA became more volatile on average under high-RH conditions. In contrast, the effect of RH on SOA mass loading was found to be much smaller for high-NO_x toluene SOA. The observed increase in the oligomer fraction and particle mass loading under dry conditions were attributed to the enhancement of condensation reactions, which produce water and oligomers from smaller compounds in low-NO_x toluene SOA. The reduction in the fraction of oligomeric compounds under humid conditions may partly counteract the previously observed enhancement in the toluene SOA yield driven by the aerosol liquid water chemistry in deliquesced inorganic seed particles.

6.3 Goal 2: Investigate the formation of SOA from a N-containing VOC

Chapter 3 described how highly light-absorbing SOA was efficiently generated from the oxidation of indole, a N-containing heterocyclic compound emitted from plants and animal waste.

SOA was generated in a smog chamber from the oxidation of indole by OH, O₃, and NO₃ in order to explore the formation, optical properties, and chemical composition of indole SOA. Indole photooxidation resulted in a high SOA mass yield (1.3 ± 0.3), suggesting that most oxidized indole products eventually end up in the particle phase. Moreover, indole SOA generated by reactions with any of the three oxidants studied all resulted in SOA that was highly absorbing in the UV-Vis spectrum. The optical properties of indole SOA were probed with two independent methods: UV-Vis spectrophotometry was used to study the bulk SOA, and broadband cavity enhanced spectroscopy was used to measure the light-absorption/scattering of SOA particles. When RH was increased from <2 to 25 to 50%,

indole/OH SOA and indole/O₃ SOA had a higher light-absorption. However, the absorption properties of indole/NO₃ SOA showed a non-linear dependence with RH. These trends were captured by both methods. High-performance liquid chromatography coupled to photodiode array spectrophotometry and high-resolution mass spectrometry (HPLC-PDA-HRMS) was used to identify chromophoric compounds that are responsible for the color of indole SOA. Indole derivatives containing one or two N atoms, such as tryptanthrin, indirubin, indigo dye, indoxyl red, and nitroindole were found to contribute significantly to the visible absorption spectrum of indole SOA. These observations suggest that NOC produced from indole oxidation may be important contributors to the pool of organic species that absorb radiation strongly in the near-UV and visible spectral ranges (aka brown carbon) in the atmosphere and that the light-absorption properties of indole SOA will vary depending on the ambient RH.

The potential effect of indole/OH SOA on the total SOA mass concentration and on the light-absorbing properties of SOA in the South Coast Air Basin of California (SoCAB) was explored with an airshed model. The model projected elevated concentrations of indole SOA during the afternoon hours, which contributed considerably to the total organic aerosol under selected scenarios. Despite its high light-absorption, indole/OH SOA is unlikely to contribute significantly to decreased visibility in an urban area such as the SoCAB where absorbance by black carbon dominates. However, the impact on visibility may be greater in more remote environments, especially under plant-stressed conditions or during flowering events when emissions of indole are elevated.

This study illustrated how indole oxidation can effectively lead to the formation of SOA. However, several questions remain including: 'What role does RH play in the oxidation

reactions of indole that lead to the production of chromophoric species?’ and ‘How photostable are the NOC chromophores produced from indole oxidation?’ Furthermore, indole is one of many N-containing VOCs present in the atmosphere that could potentially contribute to the formation of SOA in the environment.

6.4 Goal 3: Investigate NOC formation in SOA particles via SOA uptake of ammonia (NH₃) and dimethylamine (DMA)

Chapter 4 described how the reactive uptake of NH₃ by SOA leads to the formation of NOC in the SOA particles and how the efficiency of this uptake varies depending on the SOA precursor. Chapter 5 compared the reactive uptake of NH₃ to that of DMA by SOA and explored the RH dependence of this uptake.

Anthropogenic (toluene, n-hexadecane) and biogenic (d-limonene, α -cedrene) VOCs were oxidized in a smog chamber at various RH (<2-50%) resulting in SOA. After the initial SOA formation, a pulse of NH₃ or DMA was introduced into the chamber. An NH₃ monitor was used to track the decay of NH₃ and DMA in order to calculate their uptake coefficients, i.e., the probability that a molecule of NH₃ or DMA will react with an SOA particle upon contact. The normalized measured uptake coefficients ranged from 10⁻⁶ to 10⁻⁴. More careful experiments are necessary in order to distinguish the loss of NH₃ and DMA to the particles versus to the chamber walls and to determine the extent of RH dependence of the wall loss. Offline mass spectrometry was used to estimate the percentage of N-containing compounds in the SOA samples after exposure to NH₃, which resulted in approximately 20% for limonene SOA, 5% for toluene SOA, and 5% for n-hexadecane SOA. Based on these results, modeling of NH₃ uptake by SOA was given an upper limit of a 10% conversion of NOC

formation in the SOA. Online mass spectrometry was used to characterize chemical composition of the SOA particles. The appearance of NOC in the SOA particles after DMA exposure was larger and faster compared to after NH₃ exposure. These results suggest that in addition to NH₃ uptake contributing to NOC formation in SOA, amines while present in lower mixing ratios, may also be an important source of NOC in SOA due to their more efficient uptake by SOA. Moreover, when RH was increased from <2 to 50%, less NOC was incorporated into the SOA particles after exposure to DMA, indicating that water suppresses the uptake of DMA by SOA. This suggests that DMA reactions with SOA species likely follow similar condensation reactions shown to produce NOC from NH₃ reactions with carbonyl species in SOA, which are accompanied by a loss of water.

Air quality simulations for the SoCAB and continental US were conducted using a range of uptake coefficients (10^{-5} to 10^{-2}) to explore the sensitivity of changes in NH₃ and PM_{2.5} concentrations to the magnitude of the uptake coefficient. Results indicate that introducing this chemical uptake of NH₃ by SOA depletes gaseous NH₃ concentrations, causing indirect reductions in the amount of ammonium nitrate and ammonium sulfate in PM_{2.5}, and decreases particle pH. The magnitude of the impact on NH₃ and PM_{2.5} concentrations exhibited a strong but non-linear dependence on the value of the uptake coefficient. Furthermore, simulations over the continental US showed that the mass concentration of PM_{2.5} is significantly affected, with a distinct spatial pattern over different seasons. For example, PM_{2.5} concentrations decreased during the winter, largely due to the reduction in ammonium nitrate concentrations. On the other hand, PM_{2.5} concentrations increased during the summer especially in the southeastern U.S. due to increased biogenic SOA production resulting from enhanced acid-catalyzed uptake of isoprene-derived epoxides. It is important

to understand and capture processes that can significantly impact PM mass given that enforceable parameters used to protect air quality, such as the US National Ambient Air Quality Standards (NAAQS), focus on regulating PM mass concentrations.

This study showed experimentally that reactive uptake of NH_3 can occur in SOA, and that the extent of the uptake varies depending on the SOA precursor. The precursor dictates the resulting SOA composition and therefore its properties, such as viscosity. Previous studies have shown that toluene SOA has a high viscosity, and therefore its higher viscosity relative to limonene SOA likely contributed to the lower uptake of NH_3 . Examples of other parameters that can be explored in future experiments to further probe the relationship between viscosity and uptake include varying the temperature at which experiments are conducted and generating SOA from VOC mixtures. This set of experiments also demonstrated that DMA uptake was considerably more efficient than NH_3 uptake by SOA. Other common amines that may potentially contribute to NOC formation in SOA include monomethylamine, trimethylamine, ethylamine, diethylamine, triethylamine, 1-propanamine, and 1-butanamine. Provided more robust inventories for amines are available in the future, these findings could help improve projections of NOC in PM by air quality models.

6.5 Conclusions

Overall, this body of work highlights the novel chemistry and important properties of NOC in the atmospheric environment and illustrates the importance of considering the dependence of SOA properties on RH, which can vary widely in the ambient atmosphere. As mentioned above, SOA constitutes a significant fraction of $\text{PM}_{2.5}$, and because SOA is not well-understood, it remains a large source of uncertainty in models that aim to predict air quality

and global climate. Laboratory experiments like the ones discussed here are a critical tool that, in conjunction with field studies, contributes to our scientific understanding of SOA in the environment, allowing us to use more realistic parameterizations of atmospheric processes and reduce uncertainties in the models. Addressing uncertainties in regional and global models is imperative given that model projections are often shared with policymakers who have the authority to make the decisions that ultimately impact our air quality.

REFERENCES

- Abbatt, J.P.D., Benz, S., Cziczo, D.J., Kanji, Z., Lohmann, U., Mohler, O.: Solid ammonium sulphate aerosols as ice nuclei: a pathway for cirrus cloud formation. *Science* 313, 1770. <http://dx.doi.org/10.1126/science1129726>, 2006.
- Adams, L.: Mechanism for cb6r3_ae6_aq uses the following species, [https://github.com/USEPA/CMAQ/blob/5.2/DOCS/User Manual/Appendix A/cb6r3 ae6 aq/CB6 species table.md](https://github.com/USEPA/CMAQ/blob/5.2/DOCS/User%20Manual/Appendix%20A/cb6r3_ae6_aq/CB6_species_table.md), last access: 15 December 2017.
- Adams, P.J., Seinfeld, J.H., Koch, D., Mickley, L., Jacob, D.: General circulation model assessment of direct radiative forcing by the sulfate–nitrate–ammonium–water inorganic aerosol system. *J. Geophys. Res.* 106, 1097–1111. <http://dx.doi.org/10.1029/2000JD900512>, 2001.
- Aiona, P. K., Lee, H. J., Lin, P., Heller, F., Laskin, A., Laskin, J., and Nizkorodov, S. A.: A role for 2-methyl pyrrole in the browning of 4-oxopentanal and limonene secondary organic aerosol., *Environ. Sci. Technol.*, 51, 11048-11056, <http://dx.doi.org/10.1021/acs.est.7b02293>, 2017.
- Amann, M., Klimont, Z., and Wagner, F.: Regional and global emissions of air pollutants: recent trends and future scenarios, *Ann. Rev. Environ. Resour.*, 38, 31–55, 2013.
- Andreae, M. O. and Gelencsér, A.: Black carbon or brown carbon? The nature of light-absorbing carbonaceous aerosols, *Atmos. Chem. Phys.*, 6, 3131–3148, <https://doi.org/10.5194/acp-6-3131-2006>, 2006.
- Aneja, V. P., Chauhan, J., and Walker, J.: Characterization of atmospheric ammonia emissions from swine waste storage and treatment lagoons, *J. Geophys. Res.-Atmos.*, 105, 11535–11545, 2000.
- Appel, K. W., Bhave, P. V., Gilliland, A. B., Sarwar, G., and Roselle, S. J.: Evaluation of the community multiscale air quality (CMAQ) model version 4.5: sensitivities impacting model performance; part II – particulate matter, *Atmos. Environ.*, 42, 6057–6066, 2008.
- Atkinson, R.: Estimation of gas-phase hydroxyl radical rate constants for organic chemicals, *Environmental Toxicology and Chemistry: An International Journal*, 7(6), 435-442, 1988.
- Atkinson, R.: Gas-phase tropospheric chemistry of organic compounds: a review, *Atmospheric Environment. Part A. General Topics*, 24(1), 1-41, 1990.
- Atkinson, R., Aschmann, S.M. and Pitts, J.N., Jr.: Rate constants for the gas-phase reactions of the OH radical with a series of monoterpenes at 294 ± 1 K, *International Journal of Chemical Kinetics*, 18(3), 287-299, 1986.
- Atkinson, R., Tuazon, E. C., Arey, J., and Aschmann, S. M.: Atmospheric and indoor chemistry of gas-phase indole, quinoline, and isoquinoline, *Atmos. Environ.*, 29, 3423–3432, [https://doi.org/10.1016/1352-2310\(95\)00103-6](https://doi.org/10.1016/1352-2310(95)00103-6), 1995.
- Atkinson, R., Tuazon, E.C., Wallington, T.J., Aschmann, S.M., Arey, J., Winer, A.M. and Pitts, J.N.: Atmospheric chemistry of aniline, N, N-dimethylaniline, pyridine, 1,3,5-triazine, and nitrobenzene, *Environmental science & technology*, 21(1), 64-72, 1987.
- Audunsson, G., and Mathiasson, L.: Simultaneous determination of amines and isocyanates in working atmospheres by gas-liquid chromatography, *Journal of Chromatography*, 261, 253-264, 1983.

- Baek, B. H. and Aneja, V. P.: Measurement and analysis of the relationship between ammonia, acid gases, and fine particles in Eastern North Carolina, *J. Air Waste Manage. Assoc.*, 54, 623–633, 2004.
- Baluja, S., Bhalodia, R., Bhatt, M., Vekariya, N., and Gajera, R.: Solubility of a pharmacological intermediate drug isatin in different solvents at various temperatures, *Int. Lett. Chem. Phys. Astron.*, 17, 36–46, <https://doi.org/10.18052/www.scipress.com/ILCPA.17.36>, 2013.
- Bateman, A. P., Nizkorodov, S. A., Laskin, J., and Laskin, A.: Photolytic processing of secondary organic aerosols dissolved in cloud droplets, *Phys. Chem. Chem. Phys.*, 13, 12199–12212, <https://doi.org/10.1039/c1cp20526a>, 2011.
- Bateman, A. P., Laskin, J., Laskin, A., and Nizkorodov, S. A.: Applications of high-resolution electrospray ionization mass spectrometry to measurements of average oxygen to carbon ratios in secondary organic aerosols, *Environ. Sci. Technol.*, 46, 8315–8324, <https://doi.org/10.1021/es3017254>, 2012.
- Behera, S. N. and Sharma, M.: Investigating the potential role of ammonia in ion chemistry of fine particulate matter formation for an urban environment, *Sci. Total Environ.*, 408, 3569–3575, 2010.
- Behera, S. N., Sharma, M., Aneja, V. P., and Balasubramanian, R.: Ammonia in the atmosphere: a review on emission sources, atmospheric chemistry and deposition on terrestrial bodies, *Environ. Sci. Pollut. Res.*, 20, 8092–8131, 2013.
- Bellouin, N., Quaas, J., Gryspeerdt, E., Kinne, S., Stier, P., Watson-Parris, D., Boucher, O., Carslaw, K.S., Christensen, M., Daniau, A.-L., Dufresne, J.-L., Feingold, G., Fiedler, S., Forster, P., Gettelman, A., Haywood, J.M., Lohmann, U., Malavelle, F., Mauritsen, T., McCoy, D.T., Myhre, G., Mülmenstädt, J., Neubauer, D., Possner, A., Rugenstein, M., Sato, Y., Schulz, M., Schwartz, S.E., Sourdeval, O., Storelvmo, T., Toll, V., Winker, D., and Stevens, B.: Bounding global aerosol radiative forcing of climate change, *Reviews of Geophysics*, 58, e2019RG000660, <https://doi.org/10.1029/2019RG000660>, 2020.
- Binkowski, F. S. and Roselle, S. J.: Models-3 Community Multiscale Air Quality (CMAQ) model aerosol component 1. Model description, *J. Geophys. Res.-Atmos.*, 108, 4183, <https://doi.org/10.1029/2001JD001409>, 2003.
- Bloss, C., Wagner, V., Jenkin, M. E., Volkamer, R., Bloss, W. J., Lee, J. D., Heard, D. E., Wirtz, K., Martin-Reviejo, M., Rea, G., Wenger, J. C., and Pilling, M. J.: Development of a detailed chemical mechanism (MCMv3.1) for the atmospheric oxidation of aromatic hydrocarbons, *Atmos. Chem. Phys.*, 5, 641–664, <https://doi.org/10.5194/acp-5-641-2005>, 2005.
- Bones, D.L., Henricksen, D.K., Mang, S.A., Gonsior, M., Bateman, A.P., Nguyen, T.B., Cooper, W.J., Nizkorodov, S.A.: Appearance of strong absorbers and fluorophores in limonene-O₃ secondary organic aerosol due to NH₄⁺-mediated chemical aging over long time scales. *J. Geophys. Res.: Atmosphere* 115 (D5), 2010.
- Bongiorno, D., Camarda, L., Ceraulo, L., and Ferrugia, M.: Mass spectrometry of simple indoles. Part 2: Fourier transform mass spectrometry, fast atom bombardment, laser desorption and electrospray ionisation, *Targets Heterocycl. Syst.*, 8, 398–427, 2004.
- Boylan, J. W. and Russell, A.G.: PM and light extinction model performance metrics, goals, and criteria for three-dimensional air quality models, *Atmos. Environ.*, 40, 4946–4959, 2006.

- Byun, D. and Schere, K. L.: Review of the governing equations, computational algorithms, and other components of the Models-3 Community Multiscale Air Quality (CMAQ) modeling system, *Appl. Mech. Rev.*, 59, 51–77, 2006.
- Cai, L., A. Koziel, J., Zhang, S., J. Heber, A., L. Cortus, E., B. Parker, D., J. Hoff, S., Sun, G., Y. Heathcote, K., D. Jacobson, L., Akdeniz, N., P. Hetchler, B., D. Bereznicki, S., A. Caraway, E., and T. Lim, T.: Odor and Odorous Chemical Emissions from Animal Buildings: Part 3. Chemical Emissions, *Transactions of the ASABE*, 58, 1333-1347, <https://doi.org/10.13031/trans.58.11199>, 2015.
- Cao, G. and Jang, M.: An SOA model for toluene oxidation in the presence of inorganic aerosols, *Environ. Sci. Technol.*, 44, 727–733, <https://doi.org/10.1021/es901682r>, 2010.
- Cardoza, Y. J., Lait, C. G., Schmelz, E. A., Huang, J., and Tumlinson, J. H.: Fungus-induced biochemical changes in peanut plants and their effect on development of beet armyworm, *Spodoptera exigua* Hübner (Lepidoptera: Noctuidae) larvae, *Environ. Entomol.*, 32, 220–228, <https://doi.org/10.1603/0046-225X-32.1.220>, 2003.
- Carreras-Sospedra, M., Griffin, R. J., and Dabdub, D.: Calculations of incremental secondary organic aerosol reactivity, *Environ. Sci. Technol.*, 39, 1724–1730, <https://doi.org/10.1021/es0495359>, 2005.
- Carreras-Sospedra, M., Dabdub, D., Rodriguez, M., and Brouwer, J.: Air quality modeling in the south coast air basin of California: What do the numbers really mean?, *J. Air Waste Manage.*, 56, 1184–1195, <https://doi.org/10.1080/10473289.2006.10464530>, 2006.
- Carreras-Sospedra, M., Vutukuru, S., Brouwer, J., and Dabdub, D.: Central power generation versus distributed generation—an air quality assessment in the South Coast Air Basin of California, *Atmos. Environ.*, 44, 3215–3223, <https://doi.org/10.1016/j.atmosenv.2010.05.017>, 2010.
- Chan, A. W. H., Kautzman, K. E., Chhabra, P. S., Surratt, J. D., Chan, M. N., Crouse, J. D., Kürten, A., Wennberg, P. O., Flagan, R. C., and Seinfeld, J. H.: Secondary organic aerosol formation from photooxidation of naphthalene and alkyl naphthalenes: implications for oxidation of intermediate volatility organic compounds (IVOCs), *Atmos. Chem. Phys.*, 9, 3049–3060, <https://doi.org/10.5194/acp-9-3049-2009>, 2009.
- Chang, I.H., Lee, C.G., and Lee, D.S.: Development of an automated method for simultaneous determination of low molecular weight aliphatic amines and ammonia in ambient air by diffusion scrubber coupled to ion chromatography, *Anal. Chem.*, 75, 6141-6146, 2003.
- Chang, W. L., Griffin, R. J., and Dabdub, D.: Partitioning phase preference for secondary organic aerosol in an urban atmosphere, *P. Natl. Acad. Sci. USA*, 107, 6705–6710, <https://doi.org/10.1073/pnas.0911244107>, 2010.
- Chen, C., Kacarab, M., Tang, P., and Cocker, D. R.: SOA formation from naphthalene, 1-methylnaphthalene, and 2-methylnaphthalene photooxidation, *Atmos. Environ.*, 131, 424–433, <https://doi.org/10.1016/j.atmosenv.2016.02.007>, 2016.
- Cocker III, D. R., Clegg, S. L., Flagan, R. C., and Seinfeld, J. H.: The effect of water on gas–particle partitioning of secondary organic aerosol. Part I: α -pinene/ozone system, *Atmos. Environ.*, 35, 6049–6072, [https://doi.org/10.1016/S1352-2310\(01\)00404-6](https://doi.org/10.1016/S1352-2310(01)00404-6), 2001.
- Cohan, A., Eiguren-Fernandez, A., Miguel, A. H., and Dabdub, D.: Secondary organic aerosol formation from naphthalene roadway emissions in the South Coast Air Basin of

- California, *Int. J. Environ. Pollut.*, 52, 206–224, <https://doi.org/10.1504/IJEP.2013.058461>, 2013.
- Couvidat, F., Kim, Y., Sartelet, K., Seigneur, C., Marchand, N., and Sciare, J.: Modeling secondary organic aerosol in an urban area: application to Paris, France, *Atmos. Chem. Phys.*, 13, 983–996, <https://doi.org/10.5194/acp-13-983-2013>, 2013.
- Das, A., Frenkel, M., Gadalla, N. A. M., Kudchadker, S., Marsh, K. N., Rodgers, A. S., and Wilhoit, R. C.: Thermodynamic and thermophysical properties of organic nitrogen compounds: Part II. 1- and 2-butanamine, 2-methyl-1-propanamine, 2-methyl-2-propanamine, pyrrole, 1-, 2-, 3-methylpyrrole, pyridine, 2-, 3-, and 4-methylpyridine, pyrrolidine, piperidine, indole, quinolone, isoquinoline, acridine, carbazole, phenanthridine, 1- and 2-naphthalenamine, and 9-methylcarbazole, *J. Phys. Chem. Ref. Data*, 22, 659–782, <https://doi.org/10.1063/1.555925>, 1993.
- Daubert, T.E., R.P. Danner. *Physical and Thermodynamic Properties of Pure Chemicals Data Compilation*. Washington, D.C.: Taylor and Francis, 1989.
- Daubert TE, Danner RP; *Physical and Thermodynamic Properties of Pure Chemicals: Data Compilation*. Design Institute for Physical Property Data, American Institute of Chemical Engineers. New York, NY: Hemisphere Pub Corp, 1999.
- Dawson, M. L., Xu, J., Griffin, R. J., and Dabdub, D.: Development of aroC/ACM/MPMPO 1.0: a model to simulate secondary organic aerosol from aromatic precursors in regional models, *Geosci. Model Dev.*, 9, 2143–2151, <https://doi.org/10.5194/gmd-9-2143-2016>, 2016.
- De Boer, J. G., Posthumus, M. A., and Dicke, M.: Identification of volatiles that are used in discrimination between plants infested with prey or nonprey herbivores by a predatory mite, *J. Chem. Ecol.*, 30, 2215–2230, <https://doi.org/10.1023/B:JOEC.0000048784.79031.5e>, 2004.
- De Haan, D. O., Hawkins, L. N., Kononenko, J. A., Turley, J. J., Corrigan, A. L., Tolbert, M. A., and Jimenez, J. L.: Formation of nitrogen-containing oligomers by methylglyoxal and amines in simulated evaporating cloud droplets, *Environ. Sci. Technol.*, 45(3), 984–991, 2011.
- De Haan, D. O., Hawkins, L. N., Welsh, H. G., Pednekar, R., Casar, J. R., Pennington, E. A., de Loera, A., Jimenez, N. G., Symons, M. A., Zauscher, M., Pajunoja, A., Caponi, L., Cazaunau, M., Formenti, P., Gratien, A., Pangui, E., and Doussin, J. F.: Brown carbon production in ammonium- or amine-containing aerosol particles by reactive uptake of methylglyoxal and photolytic cloud cycling, *Environ. Sci. Technol.*, 51 (13), 7458–7466, 2017.
- De Haan, D.O., Pajunoja, A., Hawkins, L.N., Welsh, H.G., Jimenez, N.G., De Loera, A., Zauscher, M., Andretta, A.D., Joyce, B.W., De Haan, A.C. and Riva, M.: Methylamine’s Effects on Methylglyoxal-Containing Aerosol: Chemical, Physical, and Optical Changes, *ACS Earth and Space Chemistry*, 3(9), 1706–1716, 2019.
- Dockery, D.W., Pope, C.A., Xu, X., Spengler, J.D., Ware, J.H., Fay, M.E., Ferris, B.G., and Speizer F.E.: An association between air pollution and mortality in six U.S. cities, *N. Engl. J. Med.*, 329, 1753–1759, <https://doi.org/10.1056/NEJM199312093292401>, 1993.
- Donahue, N. M., Robinson, A. L., Stanier, C. O., and Pandis, S. N.: Coupled partitioning, dilution, and chemical aging of semivolatile organics, *Environ. Sci. Technol.*, 40, 2635–2643, <https://doi.org/10.1021/es052297c>, 2006.

- Duporté, G., Riva, M., Parshintsev, J., Heikkinen, E., Barreira, L.M., Myllys, N., Heikkinen, L., Hartonen, K., Kulmala, M., Ehn, M. and Riekkola, M.L.: Chemical Characterization of Gas-and Particle-Phase Products from the Ozonolysis of α -pinene in the Presence of Dimethylamine, *Environ. Sci. Technol.*, 51(10), 5602-5610, 2017.
- Duporté, G., Parshintsev, J., Barreira, L.M., Hartonen, K., Kulmala, M. and Riekkola, M.L.: Nitrogen-containing low volatile compounds from pinonaldehyde-dimethylamine reaction in the atmosphere: A laboratory and field study. *Environ. Sci. Technol.*, 50(9), 4693-4700, 2016.
- Eder, B. and Yu, S.: A performance evaluation of the 2004 release of Models-3 CMAQ, *Atmos. Environ.*, 40, 4811-4824, 2006.
- Edney, E. O., Driscoll, D. J., Speer, R. E., Weathers, W. S., Kleindienst, T. E., Li, W., and Smith, D. F.: Impact of aerosol liquid water on secondary organic aerosol yields of irradiated toluene/propylene/ NO_x / $(\text{NH}_4)_2\text{SO}_4$ /air mixtures, *Atmos. Environ.*, 34, 3907-3919, [https://doi.org/10.1016/S1352-2310\(00\)00174-6](https://doi.org/10.1016/S1352-2310(00)00174-6), 2000.
- Erb, M., Veyrat, N., Robert, C. A. M., Xu, H., Frey, M., Ton, J., and Turlings, T. C. J.: Indole is an essential herbivore-induced volatile primal signal in maize, *Nature Communications*, 6, 6273, <https://doi.org/10.1038/ncomms7273>, 2015.
- Erisman, J. W., Sutton, M. A., Galloway, J., Klimont, Z., and Winiwarter, W.: How a century of ammonia synthesis changed the world, *Nat. Geosci.*, 1, 636-639, 2008.
- Ervens, B., Turpin, B. J., and Weber, R. J.: Secondary organic aerosol formation in cloud droplets and aqueous particles (aqSOA): a review of laboratory, field and model studies, *Atmos. Chem. Phys.*, 11, 11069-11102, <https://doi.org/10.5194/acp-11-11069-2011>, 2011.
- Faust, J. A., Wong, J. P. S., Lee, A. K. Y., and Abbatt, J. P. D.: Role of aerosol liquid water in secondary organic aerosol formation from volatile organic compounds, *Environ. Sci. Technol.*, 51, 1405-1413, <https://doi.org/10.1021/acs.est.6b04700>, 2017.
- Feilberg, A., Liu, D., Adamsen, A. P. S., Hansen, M. J., and Jonassen, K. E. N.: Odorant emissions from intensive pig production measured by online proton-transfer-reaction mass spectrometry, *Environ. Sci. Technol.*, 44, 5894-5900, <https://doi.org/10.1021/es100483s>, 2010.
- Finlayson-Pitts, B.J., and Pitts J.N.: *Chemistry of the Upper and Lower Atmosphere*, San Diego: Academic Press, 2000.
- Forstner, H. J. L., Flagan, R. C., and Seinfeld, J. H.: Secondary organic aerosol from the photooxidation of aromatic hydrocarbons: molecular composition, *Environ. Sci. Technol.*, 31, 1345-1358, <https://doi.org/10.1021/es9605376>, 1997.
- Frey, M., Spitteller, D., Boland, W., and Gierl, A.: Transcriptional activation of Igl, the gene for indole formation in Zea mays: a structure-activity study with elicitor-active N-acyl glutamines from insects, *Phytochemistry*, 65, 1047-1055, <https://doi.org/10.1016/j.phytochem.2003.11.021>, 2004.
- Friedl, M. A., Sulla-Menashe, D., Tan, B., Schneider, A., Ramankutty, N., Sibley, A., and Huang, X.: MODIS Collection 5 global land cover: Algorithm refinements and characterization of new datasets, *Remote Sens. Environ.*, 114, 168-182, 2010.
- Fujii, T., and Kitai, T.: Determination of trace levels of trimethylamine in air by gas chromatography/surface ionization organic mass spectrometry. *Anal. Chem.*, 59, 379-382, 1987.

- Fuselli, S., Bebedetti, G., and Mastrangeli, R.: Determination of methylamines in air using activated charcoal traps and gas chromatographic analysis with an alkali flame detector (AFD), *Atmos. Environ.*, 16, 2943-2946, 1982.
- Galloway, J. N., Townsend, A. R., Erisman, J. W., Bekunda, M., Cai, Z., Freney, J. R., Martinelli, L. A., Seitzinger, S. P., and Sutton, M. A.: Transformation of the nitrogen cycle: recent trends, questions, and potential solutions, *Science*, 320, 889–892, 2008.
- Galloway, M.M., Powelson, M.H., Sedehi, N., Wood, S.E., Millage, K.D., Kononenko, J.A., Rynaski, A.D. and De Haan, D.O.: 2014. Secondary organic aerosol formation during evaporation of droplets containing atmospheric aldehydes, amines, and ammonium sulfate, *Environ. Sci. Technol.*, 48(24), 14417-14425, 2014.
- Ge, X., Wexler, A.S., and Clegg, S.L.: Atmospheric amines – Part I. A review, *Atmos. Environ.*, 45 (3), 524-546, <https://doi.org/10.1016/j.atmosenv.2010.10.012>, 2011.
- Gentner, D. R., Ormeño, E., Fares, S., Ford, T. B., Weber, R., Park, J.-H., Brioude, J., Angevine, W. M., Karlik, J. F., and Goldstein, A. H.: Emissions of terpenoids, benzenoids, and other biogenic gas-phase organic compounds from agricultural crops and their potential implications for air quality, *Atmos. Chem. Phys.*, 14, 5393–5413, <https://doi.org/10.5194/acp-14-5393-2014>, 2014.
- Gols, R., Posthumus, M. A., and Dicke, M.: Jasmonic acid induces the production of gerbera volatiles that attract the biological control agent *Phytoseiulus persimilis*, *Entomol. Exp. Appl.*, 93, 77–86, <https://doi.org/10.1046/j.1570-7458.1999.00564.x>, 1999.
- Gray, H.A., Cass, G.R., Huntzicker, J.J., Heyerdahl, E.K., Rau, J.A.: Characteristics of atmospheric organic and elemental carbon particle concentrations in Los Angeles. *Environ. Sci. Technol.* 20 (6), 580–589, 1986.
- Griffin, R. J., Dabdub, D., and Seinfeld, J. H.: Secondary organic aerosol 1. Atmospheric chemical mechanism for production of molecular constituents, *J. Geophys. Res.*, 107, 4332, <https://doi.org/10.1029/2001JD000541>, 2002a.
- Griffin, R. J., Dabdub, D., Kleeman, M. J., Fraser, M. P., Cass, G. R., and Seinfeld, J. H.: Secondary organic aerosol 3. Urban/regional scale model of size- and composition- resolved aerosols, *J. Geo-phys. Res.*, 107, 4334, <https://doi.org/10.1029/2001JD000544>, 2002b.
- Griffin, R. J., Nguyen, K., Dabdub, D., and Seinfeld, J. H.: A coupled hydrophobic-hydrophilic model for predicting secondary organic aerosol formation, *J. Atmos. Chem.*, 44, 171–190, <https://doi.org/10.1023/A:1022436813699>, 2003.
- Griffin, R. J., Dabdub, D., and Seinfeld, J. H.: Development and initial evaluation of a dynamic species-resolved model for gas phase chemistry and size-resolved gas/particle partitioning associated with secondary organic aerosol formation, *J. Geophys. Res.*, 110, D05304, <https://doi.org/10.1029/2004JD005219>, 2005.
- Hansen, H. K., Rasmussen, P., Fredenslund, A., Schiller, M., and Gmehling, J.: Vapor–liquid equilibria by UNIFAC group contribution. 5. Revision and extension, *Ind. Eng. Chem. Res.*, 30, 2352–2355, <https://doi.org/10.1021/ie00058a017>, 1991.
- Harvey, R. M., Bateman, A. P., Jain, S., Li, Y. J., Martin, S., and Petrucci, G. A.: Optical properties of secondary organic aerosol from cis-3-hexenol and cis-3-hexenyl acetate: effect of chemical composition, humidity, and phase, *Environ. Sci. Technol.*, 50, 4997–5006, <https://doi.org/10.1021/acs.est.6b00625>, 2016.
- Hawkins, L. N.; Lemire, A. N.; Galloway, M. M.; Corrigan, A. L.; Turley, J. J.; Espelien, B. M.; De Haan, D. O., Maillard Chemistry in Clouds and Aqueous Aerosol As a Source of

- Atmospheric Humic-Like Substances. *Environ. Sci. Technol.* 2016, 50, (14), 7443-7452.
- Heald, C. L., Jacob, D. J., Park, R. J., Russell, L. M., Huebert, B. J., Seinfeld, J. H., Liao, H., and Weber, R. J.: A large organic aerosol source in the free troposphere missing from current models, *Geophys. Res. Lett.*, 32, L18809, <https://doi.org/10.1029/2005GL023831>, 2005.
- Healy, R. M., Chen, Y., Kourtev, I., Kalberer, M., O'Shea, D., and Wenger, J. C.: Rapid formation of secondary organic aerosol from the photolysis of 1-nitronaphthalene: role of naphthoxy radical self-reaction, *Environ. Sci. Technol.*, 46, 11813–11820, <https://doi.org/10.1021/es302841j>, 2012.
- Henze, D.K., Shindell, D.T., Akhtar, F., Spurr, R.J.D., Pinder, R.W., Loughlin, D., Kopacz, M., Sing, K., Shim, C., 2012. Spatially refined aerosol direct radiative forcing efficiencies. *Environ. Sci. Technol.* 46 (17), 9511–9518. <http://dx.doi.org/10.1021/es301993s>.
- Herrmann, H., Schaefer, T., Tilgner, A., Styler, S. A., Weller, C., Teich, M., and Otto, T.: Tropospheric aqueous-phase chemistry: kinetics, mechanisms, and its coupling to a changing gas phase, *Chem. Rev.*, 115, 4259–4334, <https://doi.org/10.1021/cr500447k>, 2015.
- Hildebrandt, L., Donahue, N. M., and Pandis, S. N.: High formation of secondary organic aerosol from the photo-oxidation of toluene, *Atmos. Chem. Phys.*, 9, 2973–2986, <https://doi.org/10.5194/acp-9-2973-2009>, 2009.
- Hinks, M.L.; Montoya-Aguilera, J.; Ellison, L.; Lin, P.; Laskin, A.; Laskin, J.; Shiraiwa, M.; Dabdub, D.; Nizkorodov, S.A., Effect of relative humidity on the composition of secondary organic aerosol from the oxidation of toluene, *Atmospheric Chemistry and Physics*, 18, 1643-1652. [DOI:10.5194/acp-18-1643-2018](https://doi.org/10.5194/acp-18-1643-2018), 2018.
- Hobbs, P., Webb, J., Mottram, T., Grant, B., and Misselbrook, T.: Emissions of volatile organic compounds originating from UK livestock agriculture, *J. Sci. Food Agr.*, 84, 1414–1420, <https://doi.org/10.1002/jsfa.1810>, 2004.
- Hodzic, A., Jimenez, J. L., Madronich, S., Canagaratna, M. R., De-Carlo, P. F., Kleinman, L., and Fast, J.: Modeling organic aerosols in a megacity: potential contribution of semi-volatile and intermediate volatility primary organic compounds to secondary organic aerosol formation, *Atmos. Chem. Phys.*, 10, 5491–5514, <https://doi.org/10.5194/acp-10-5491-2010>, 2010.
- Hong, S.-Y., Dudhia, J., and Chen, S.-H.: A revised approach to ice microphysical processes for the bulk parameterization of clouds and precipitation, *Mon. Weather Rev.*, 132, 103–120, 2004.
- Hong, S.-Y., Noh, Y., and Dudhia, J.: A new vertical diffusion package with an explicit treatment of entrainment processes, *Mon. Weather Rev.*, 134, 2318–2341, 2006.
- Horne, J.R., and Dabdub, D.: Impact of global climate change on ozone, particulate matter, and secondary organic aerosol concentrations in California: a model perturbation analysis. *Atmos. Environ.* 153, 1–17, 2017.
- Horne, J.R.; Zhu, S.; Montoya-Aguilera, J.; Hinks, M.L.; Wingen, L.M.; Nizkorodov, S.A.; Dabdub, D., Reactive uptake of ammonia by secondary organic aerosols: Implications for air quality, *Atmospheric Environment*, 189, 1-8, 2018.
- Horowitz, L. W., Walters, S., Mauzerall, D. L., Emmons, L. K., Rasch, P. J., Granier, C., Tie, X., Lamarque, J. F., Schultz, M. G., Tyndall, G. S., Orlando, J. J., and Brasseur, G. P.: A global simulation of tropospheric ozone and related tracers: Description and evaluation of

- MOZART, version 2, J. Geophys. Res.-Atmos., 108, 4784, <https://doi.org/10.1029/2002JD002853>, 2003.
- Horvath, H.: Atmospheric light-absorption – a review, *Atmos. Environ.*, 27, 293–317, [https://doi.org/10.1016/0960-1686\(93\)90104-7](https://doi.org/10.1016/0960-1686(93)90104-7), 1993.
- Huang, Y., Zhao, R., Charan, S.M., Kenseth, C.M., Zhang, X. and Seinfeld, J.H.: Unified Theory of Vapor–Wall Mass Transport in Teflon-Walled Environmental Chambers, *Environmental science & technology*, 52(4), 2134-2142, 2018.
- Hughes, L.S., Allen, J.O., Salmon, L.G., Mayo, P.R., Johnson, R.J., and Cass, G.R.: Evolution of nitrogen species air pollutants along trajectories crossing the Los Angeles area. *Environ. Sci. Technol.* 36 (18), 3928–3935, 2002.
- Hutchinson, G.L., Mosier, A.R., and Andre, C.E.: Ammonia and amine emissions from a large cattle feedlot. *Journal of Environmental Quality*, 11, 288-292, 1982.
- Iddon, B., Phillips, G. O., Robbins, K. E., and Davies, J. V.: Radiation chemistry of aqueous solutions of indole and its derivatives, *J. Chem. Soc. B.*, 1887–1892, <https://doi.org/10.1039/J29710001887>, 1971.
- IPCC (2013), IPCC, 2013: Climate Change 2013: The Physical Science Basis. Contribution of Working Group I to the Fifth Assessment Report of the Intergovernmental Panel on Climate Change Rep., 1535 pp, Cambridge, United Kingdom and New York, NY, USA.
- Jang, M., Czoschke, N. M., Lee, S., and Kamens, R. M.: Heterogeneous atmospheric aerosol production by acid-catalyzed particle-phase reactions, *Science*, 298, 814–817, <https://doi.org/10.1126/science.1075798>, 2002.
- Jia, L. and Xu, Y.: Different roles of water in secondary organic aerosol formation from toluene and isoprene, *Atmos. Chem. Phys. Discuss.*, <https://doi.org/10.5194/acp-2017-1064>, in review, 2017.
- Jiang, F., Liu, Q., Huang, X., Wang, T., Zhuang, B., and Xie, M.: Regional modeling of secondary organic aerosol over China using WRF/Chem, *J. Aerosol Sci.*, 43, 57–73, <https://doi.org/10.1016/j.jaerosci.2011.09.003>, 2012.
- Jo, S.-H., Kim, K.-H., Jeon, B.-H., Lee, M.-H., Kim, Y.-H., Kim, B.-W., Cho, S.-B., Hwang, O.-H., and Bhattacharya, S. S.: Odor characterization from barns and slurry treatment facilities at a commercial swine facility in South Korea, *Atmospheric Environment*, 119, 339–347, <https://doi.org/10.1016/j.atmosenv.2015.08.064>, 2015.
- Jovan, S. and McCune, B.: Air-quality bioindication in the greater central valley of california, with epiphytic macrolichen communities, *Ecol. Appl.*, 15, 1712–1726, 2005.
- Kain, J. S.: The Kain–Fritsch convective parameterization: an update, *J. Appl. Meteorol.*, 43, 170–181, 2004.
- Kallinger, G., and Niessner, R.: Laboratory investigation of annular denuders as sampling system for the determination of aliphatic primary and secondary amines in stack gas. *Mikrochimica Acta*, 130, 309-316, 1999.
- Kamens, R. M., Zhang, H., Chen, E. H., Zhou, Y., Parikh, H. M., Wilson, R. L., Galloway, K. E., and Rosen, E. P.: Secondary organic aerosol formation from toluene in an atmospheric hydrocarbon mixture: water and particle seed effects, *Atmos. Environ.*, 45, 2324–2334, <https://doi.org/10.1016/j.atmosenv.2010.11.007>, 2011.
- Kamiya, A., and Ose, Y.: Study of odorous compounds produced by putrefaction of foods. *Journal of Chromatography*, 292, 383-391, 1984.
- Kampf, C. J., Filippi, A., Zuth, C., Hoffmann, T., and Opatz, T.: Secondary brown carbon formation via the dicarbonyl imine pathway: nitrogen heterocycle formation and

- synergistic effects, *Phys. Chem. Chem. Phys.*, 18, 18353-18364, <https://doi.org/10.1039/C6CP03029G>, 2016.
- Kim, E., Turkiewicz, K., Zulawnick, S.A., Magliano, K.L.: Sources of fine particles in the South Coast area, California. *Atmos. Environ.* 44 (26), 3095–3100, 2010.
- Kind, T. and Fiehn, O.: Seven Golden Rules for heuristic filtering of molecular formulas obtained by accurate mass spectrometry, *BMC Bioinformatics*, 8, 105, <https://doi.org/10.1186/1471-2105-8-105>, 2007.
- Kirchstetter, T. W. and Thatcher, T. L.: Contribution of organic carbon to wood smoke particulate matter absorption of solar radiation, *Atmos. Chem. Phys.*, 12, 6067–6072, <https://doi.org/10.5194/acp-12-6067-2012>, 2012.
- Kourtchev, I., Doussin, J.-F., Giorio, C., Mahon, B., Wilson, E. M., Maurin, N., Pangu, E., Venables, D. S., Wenger, J. C., and Kalberer, M.: Molecular composition of fresh and aged secondary organic aerosol from a mixture of biogenic volatile compounds: a high-resolution mass spectrometry study, *Atmos. Chem. Phys.*, 15, 5683–5695, <https://doi.org/10.5194/acp-15-5683-2015>, 2015.
- Krapf, M., El Haddad, I., Bruns, E. A., Molteni, U., Daellenbach, K. R., Prevot, A. S. H., Baltensperger, U., and Dommen, J.: Labile peroxides in secondary organic aerosol, *Chemistry*, 1, 603–616, <https://doi.org/10.1016/j.chempr.2016.09.007>, 2016.
- Krauter, C., Goorahoo, D., Potter, C., and Klooster, S.: Ammonia emissions and fertilizer applications in California's Central Valley, *Emission Inventories – Partnering for the Future*, 11, 15–18, 2002.
- Kroll, J. H., Chan, A. W. H., Ng, N. L., Flagan, R. C., and Seinfeld, J. H.: Reactions of semivolatile organics and their effects on secondary organic aerosol formation, *Environ. Sci. Technol.*, 41, 3545–3550, <https://doi.org/10.1021/es062059x>, 2007.
- Kumar, M., Li, H., Zhang, X., Zeng, X.C., and Francisco, J.S.: Nitric acid – amine chemistry in the gas phase and at the air-water interface, *J. Am. Chem. Soc.*, 140 (20), 6456-6466, 2018.
- Kurtén, T., Loukonen, V., Vehkamäki, H., and Kulmala, M.: Amines are likely to enhance neutral and ion-induced sulfuric acid-water nucleation in the atmosphere more effectively than ammonia, *Atmos. Chem. Phys.*, 8, 4095–4103, 2008.
- Kupiainen, O., Ortega, I. K., Kurtén, T., and Vehkamäki, H.: Amine substitution into sulfuric acid – ammonia clusters, *Atmos. Chem. Phys.*, 12, 3591–3599, <https://doi.org/10.5194/acp-12-3591-2012>, 2012.
- Kuwata, K., Akiyama, E., Yamazaki, Y., Yamasaki, H., Kuge, Y., and Kisa, Y.: Trace determination of low molecular weight aliphatic amines in air by gas chromatography, *Anal. Chem.*, 55, 2199-2201, 1983.
- Lambe, A. T., Massoli, P., Zhang, X., Canagaratna, M., Nowak, J., Yan, C., Nie, W., Onasch, T., Jayne, J., Kolb, C., Davidovits, P., Worsnop, D., and Brune, W.: Controlled nitric oxide production via O(1D) + N₂O reactions for use in oxidation flow reactor studies, *Atmos. Meas. Tech.*, 10, 2283-2298, 2017.
- Lang-Yona, N., Rudich, Y., Segre, E., Dinar, E., and Abo-Riziq, A.: Complex Refractive Indices of Aerosols Retrieved by Continuous Wave-Cavity Ring Down Aerosol Spectrometer, *Ana. Chem.*, 81, 1762-1769, 2009.
- Laskin, A., Laskin, J., and Nizkorodov, S. A.: Chemistry of atmospheric brown carbon, *Chem. Rev.*, 115, 4335–4382, <https://doi.org/10.1021/cr5006167>, 2015.

- Laskin, A., Smith, J. S., and Laskin, J.: Molecular characterization of nitrogen-containing organic compounds in biomass burning aerosols using high-resolution mass spectrometry, *Environ. Sci. Technol.*, 43, 3764–3771, <https://doi.org/10.1021/es803456n>, 2009.
- Laskin, J., Laskin, A., Roach, P.J., Slysz, G.W., Anderson, G.A., Nizkorodov, S.A., Bones, D.L., Nguyen, L.Q.: High-resolution desorption electrospray ionization mass spectrometry for chemical characterization of organic aerosols. *Anal. Chem.* 82 (5), 2048–2058, 2010.
- Laskin, J., Laskin, A., Nizkorodov, S.A., Roach, P., Eckert, P., Gilles, M.K., Wang, B., Lee, H.J., Hu, Q., Molecular selectivity of brown carbon chromophores. *Environ. Sci. Technol.* 48 (20), 12047–12055, 2014.
- Le, P. D., Aarnink, A. J. A., Ogink, N. W. M., Becker, P. M., and Versteegen, M. W. A.: Odour from animal production facilities: its relationship to diet, *Nutrition Research Reviews*, 18, 3-30, 10.1079/NRR200592, 2005.
- Lee, L., Wooldridge, P. J., Gilman, J. B., Warneke, C., de Gouw, J., and Cohen, R. C.: Low temperatures enhance organic nitrate formation: evidence from observations in the 2012 Uintah Basin Winter Ozone Study, *Atmos. Chem. Phys.*, 14, 12441–12454, <https://doi.org/10.5194/acp-14-12441-2014>, 2014.
- Lelieveld, J., Evans, J., Fnais, M., Giannadaki, D., and Pozzer, A.: The contribution of outdoor air pollution sources to premature mortality on a global scale, *Nature*, 525, 367–371, 2015.
- Li, Y., Pöschl, U., and Shiraiwa, M.: Molecular corridors and parameterizations of volatility in the chemical evolution of organic aerosols, *Atmos. Chem. Phys.*, 16, 3327–3344, <https://doi.org/10.5194/acp-16-3327-2016>, 2016.
- Lin, P., Laskin, J., Nizkorodov, S. A., and Laskin, A.: Revealing brown carbon chromophores produced in reaction of methylglyoxal with ammonium sulfate, *Environ. Sci. Technol.*, 49, 14257–14266, <https://doi.org/10.1021/acs.est.5b03608>, 2015a.
- Lin, P., Liu, J., Shilling, J. E., Kathmann, S. M., Laskin, J., and Laskin, A.: Molecular characterization of brown carbon (BrC) chromophores in secondary organic aerosol generated from photo-oxidation of toluene, *Phys. Chem. Chem. Phys.*, 17, 23312, <https://doi.org/10.1039/C5CP02563J>, 2015b.
- Lin, P., Aiona, P. K., Li, Y., Shiraiwa, M., Laskin, J., Nizkorodov, S. A., and Laskin, A.: Molecular characterization of brown carbon in biomass burning aerosol particles, *Environ. Sci. Technol.*, 50, 11815–11824, <https://doi.org/10.1021/acs.est.6b03024>, 2016.
- Lin, Y.-H., Knipping, E. M., Edgerton, E. S., Shaw, S. L., and Surratt, J. D.: Investigating the influences of SO₂ and NH₃ levels on isoprene-derived secondary organic aerosol formation using conditional sampling approaches, *Atmos. Chem. Phys.*, 13, 8457–8470, <https://doi.org/10.5194/acp-13-8457-2013>, 2013.
- Liu, J. Q., Chen, S. Y., and Ji, B.: Solubility and thermodynamic functions of isatin in pure solvents, *J. Chem. Eng. Data*, 59, 3407–3414, <https://doi.org/10.1021/je500396b>, 2014.
- Liu, P., Li, Y.J., Wang, Y., Bateman, A.P., Zhang, Y., Gong, Z., Bertram, A.K. and Martin, S.T.: Highly viscous states affect the browning of atmospheric organic particulate matter, *ACS Central Science*, 4(2), 207-215, 2018.
- Liu, T., Huang, D. D., Li, Z., Liu, Q., Chan, M., and Chan, C. K.: Comparison of secondary organic aerosol formation from toluene on initially wet and dry ammonium sulfate

- particles, *Atmos. Chem. Phys. Discuss.*, <https://doi.org/10.5194/acp-2017-1008>, in review, 2017.
- Liu, Y., Liggió, J., Staebler, R., and Li, S.-M.: Reactive uptake of ammonia to secondary organic aerosols: kinetics of organonitrogen formation, *Atmos. Chem. Phys.*, 15, 13569–13584, <https://doi.org/10.5194/acp-15-13569-2015>, 2015.
- Makela, J.M., Yli-Koivisto, S., Hiltunen, V., Seidl, W., Swietlicki, E., Teinila, K., Sillanpaa, M., Koponen, I.K., Paatero, J., Rosman, K. and Hameri, K.: Chemical composition of aerosol during particle formation events in boreal forest, *Tellus*, 53B, 380–393, <https://doi.org/10.1034/j.1600-0889.2001.530405.x>, 2001.
- Malm, W. C., Schichtel, B. A., Pitchford, M. L., Ashbaugh, L. L., and Eldred, R. A.: Spatial and monthly trends in speciated fine particle concentration in the United States, *J. Geophys. Res.-Atmos.*, 109, D03306, <https://doi.org/10.1029/2003JD003739>, 2004.
- Mang, S. A., Henricksen, D. K., Bateman, A. P., Andersen, M. P. S., Blake, D. R., and Nizkorodov, S. A.: Contribution of carbonyl photochemistry to aging of atmospheric secondary organic aerosol, *J. Phys. Chem. A*, 112, 8337–8344, <http://dx.doi.org/10.1021/jp804376c>, 2008.
- Martin, S.T., Hung, H.M., Park, R.J., Jacob, D.J., Spurr, R.J.D., Chance, K.V., Chin, M.: Effects of the physical state of tropospheric ammonium-sulfate-nitrate particles on global aerosol direct radiative forcing. *Atmos. Chem. Phys.* 4 (1), 183–214. <http://dx.doi.org/10.5194/acp-4-183-2004>, 2004.
- McCall, P. J., Turlings, T. C., Lewis, W. J., and Tumlinson, J. H.: Role of plant volatiles in host location by the specialist parasitoid *Microplitis croceipes* Cresson (Braconidae: Hymenoptera), *J. Insect Behav.*, 6, 625–639, <https://doi.org/10.1007/BF01048128>, 1993.
- McCulloch, R. B., Few, G. S., Murray, G. C., and Aneja, V. P.: Analysis of ammonia, ammonium aerosols and acid gases in the atmosphere at a commercial hog farm in eastern North Carolina, USA, *Environ. Pollut.*, 102, 263–268, 1998.
- Misztal, P. K., Hewitt, C. N., Wildt, J., Blande, J. D., Eller, A. S. D., Fares, S., Gentner, D. R., Gilman, J. B., Graus, M., Greenberg, J., Guenther, A. B., Hansel, A., Harley, P., Huang, M., Jardine, K., Karl, T., Kaser, L., Keutsch, F. N., Kiendler-Scharr, A., Kleist, E., Lerner, B. M., Li, T., Mak, J., Nolscher, A. C., Schnitzhofer, R., Sinha, V., Thornton, B., Warneke, C., Wegener, F., Werner, C., Williams, J., Worton, D. R., Yassaa, N., and Goldstein, A. H.: Atmospheric benzenoid emissions from plants rival those from fossil fuels, *Sci. Rep.-UK*, 5, 12064, <https://doi.org/10.1038/srep12064>, 2015.
- Moise, T., Flores, J.M, and Rudich, Y.: Optical properties of secondary organic aerosols and their changes by chemical processes, *Chem. Rev.*, 115, 4400–4439, <https://doi.org/10.1021/cr5005259>, 2015.
- Montoya-Aguilera, J.; Hinks, M.L.; Aiona, P.K.; Wingen, L.M.; Horne, J.R.; Zhu, S., Dabdub, D.; Laskin, A.; Laskin, J.; Lin, P.; Nizkorodov, S.A., Reactive uptake of ammonia by biogenic and anthropogenic organic aerosols, *ACS Symposium Series*, Volume 1299, Chapter 7, pp 127-147 in "Multiphase Environmental Chemistry in the Atmosphere", Hunt S., Laskin A., Nizkorodov S.A. Eds., ISBN13: 9780841233638, 2018.
- Montoya-Aguilera, J., Horne, J.R., Hinks, M.L., Fleming, L.T., Perraud, V., Lin, P., Laskin, A., Laskin, J., Dabdub, D., Nizkorodov, S.A.: Secondary organic aerosol from atmospheric photooxidation of indole. *Atmos. Chem. Phys.* 17, 11605–11621. <https://doi.org/10.5194/acp-17-11605-2017>, 2017.

- Murphy, S.M., Sorooshian, A., Kroll, J.H., Ng, N.L., Chhabra, P., Tong, C., Surratt, J.D., Knipping, E., Flagan, R.C., and Seinfeld, J.H.: Secondary aerosol formation from atmospheric reactions of aliphatic amines. *Atmos. Chem. Phys.*, 7, 2313-2337, 2007.
- Na, K., Song, C., Switzer, C., and Cocker, D. R.: Effect of ammonia on secondary organic aerosol formation from α -pinene ozonolysis in dry and humid conditions, *Environ. Sci. Technol.*, 41, 6096–6102, 2007.
- NADP: Ambient Ammonia Monitoring Network (AMoN), <http://nadp.sws.uiuc.edu/AMoN/AMoNFactSheet.pdf> (last access: 25 September 2017), 2014.
- Nah, T., Chan, M., Leone, S. R., and Wilson, K. R.: Real time in situ chemical characterization of submicrometer organic particles using direct analysis in real time-mass spectrometry, *Anal. Chem.*, 85, 2087–2095, <https://doi.org/10.1021/ac302560c>, 2013.
- Namiesnik, J., Jastrzebska, A., Zygmunt, B.: Determination of volatile aliphatic amines in air by solid-phase microextraction coupled with gas chromatography with flame ionization detection, *Journal of Chromatography A* 1016, 1-9, 2003.
- NCEP: National Weather Service, NCEP FNL, Operational Model Global Tropospheric Analyses, NOAA, US Department of Commerce, continuing from July 1999, Research Data Archive at the National Center for Atmospheric Research, Computational and Information Systems Laboratory, <https://doi.org/10.5065/D6M043C6>, 2000.
- Neuman, J. A., Nowak, J. B., Brock, C. A., Trainer, M., Fehsenfeld, F. C., Holloway, J. S., Hübler, G., Hudson, P. K., Murphy, D. M., Nicks, D. K., and Orsini, D.: Variability in ammonium nitrate formation and nitric acid depletion with altitude and location over California, *J. Geophys. Res.-Atmos.*, 108, 4557, <https://doi.org/10.1029/2003JD003616>, 2003.
- Ng, N. L., Kroll, J. H., Chan, A. W. H., Chhabra, P. S., Flagan, R. C., and Seinfeld, J. H.: Secondary organic aerosol formation from m-xylene, toluene, and benzene, *Atmos. Chem. Phys.*, 7, 3909–3922, <https://doi.org/10.5194/acp-7-3909-2007>, 2007.
- Nguyen, K. and Dabdub, D.: NO_x and VOC control and its effects on the formation of aerosols, *Aerosol Sci. Tech.*, 36, 560–572, <https://doi.org/10.1080/02786820252883801>, 2002.
- Nguyen, T. B., Roach, P. J., Laskin, J., Laskin, A., and Nizkorodov, S. A.: Effect of humidity on the composition of isoprene photooxidation secondary organic aerosol, *Atmos. Chem. Phys.*, 11, 6931–6944, <https://doi.org/10.5194/acp-11-6931-2011>, 2011.
- Nguyen, T. B., Lee, P. B., Updyke, K. M., Bones, D. L., Laskin, J., Laskin, A., and Nizkorodov, S. A.: Formation of nitrogen- and sulfur-containing light-absorbing compounds accelerated by evaporation of water from secondary organic aerosols, *J. Geophys. Res.*, 117, D01207, <https://doi.org/10.1029/2011JD016944>, 2012.
- Nguyen, T. B., Laskin, A., Laskin, J., and Nizkorodov, S. A.: Brown carbon formation from ketoaldehydes of biogenic monoterpenes, *Faraday Discuss.*, 165, 473–494, <https://doi.org/10.1039/c3fd00036b>, 2013.
- Niinemets, U., Kannaste, A., and Copolovici, L.: Quantitative patterns between plant volatile emissions induced by biotic stresses and the degree of damage, *Front. Plant. Sci.*, 4, 1–15, <https://doi.org/10.3389/fpls.2013.00262>, 2013.
- Novotna, P., Boon, J. J., Horst, J., and Pacakova, V.: Photodegradation of indigo in dichloromethane solution, *Color. Technol.*, 119, 121–127, <https://doi.org/10.1111/j.1478-4408.2003.tb00161.x>, 2003.

- Nowak, J., Neuman, J., Bahreini, R., Middlebrook, A., Holloway, J., McKeen, S., Parrish, D., Ryerson, T., and Trainer, M.: Ammonia sources in the California South Coast Air Basin and their impact on ammonium nitrate formation, *Geophys. Res. Lett.*, 39, L07804, <https://doi.org/10.1029/2012GL051197>, 2012.
- O'Brien, R.E., Nguyen, T.B., Laskin, A., Laskin, J., Hayes, P.L., Liu, S., Jimenez, J.L., Russell, L.M., Nizkorodov, S.A., and Goldstein, A.H.: Probing molecular associations of field-collected and laboratory-generated SOA with nano-DESI high-resolution mass spectrometry. *J. Geophys. Res.: Atmos.* 118 (2), 1042–1051, 2013a.
- O'Brien, R.E., Laskin, A., Laskin, J., Liu, S., Weber, R., Russell, L.M., and Goldstein, A.H.: Molecular characterization of organic aerosol using nanospray desorption/electrospray ionization mass spectrometry: CalNex 2010 field study. *Atmos. Environ.* 68, 265–272, 2013b.
- Okita, T.: Filter method for the determination of trace quantities of amines, mercaptans, and organic sulphides in the atmosphere, *Atmos. Environ.*, 4, 93-102, 1970.
- Olenius, T., Halonen, R., Kurtén, T., Henschel, H., Kupiainen-Määttä, O., Ortega, I. K., Jen, C. N., Vehkamäki, H., and Riipinen, I.: New particle formation from sulfuric acid and amines: Comparison of monomethylamine, dimethylamine, and trimethylamine, *J. Geophys. Res. Atmos.*, 122, 7103– 7118, doi:10.1002/2017JD026501, 2017.
- Osaka, N., Miyazaki, A., and Tanaka, N.: Emissions of Volatile Organic compounds from a swine shed, *Asian Journal of Atmospheric Environment*, 12, 178-191, 2018.
- Otte, T. L. and Pleim, J. E.: The Meteorology-Chemistry Interface Processor (MCIP) for the CMAQ modeling system: updates through MCIPv3.4.1, *Geosci. Model Dev.*, 3, 243–256, <https://doi.org/10.5194/gmd-3-243-2010>, 2010.
- Paasonen, P., Olenius, T., Kupiainen, O., Kurtén, T., Petäjä, T., Birmili, W., Hamed, A., Hu, M., Huey, L. G., Plass-Duelmer, C., Smith, J. N., Wiedensohler, A., Loukonen, V., McGrath, M. J., Ortega, I. K., Laaksonen, A., Vehkamäki, H., Kerminen, V.-M., and Kulmala, M.: On the formation of sulphuric acid – amine clusters in varying atmospheric conditions and its influence on atmospheric new particle formation, *Atmos. Chem. Phys.*, 12, 9113–9133, <https://doi.org/10.5194/acp-12-9113-2012>, 2012.
- Pankow, J. F.: An absorption model of gas/particle partitioning of organic compounds in the atmosphere, *Atmos. Environ.*, 28, 185–188, [https://doi.org/10.1016/1352-2310\(94\)90093-0](https://doi.org/10.1016/1352-2310(94)90093-0), 1994.
- Pankow, J. F. and Asher, W. E.: SIMPOL.1: a simple group contribution method for predicting vapor pressures and enthalpies of vaporization of multifunctional organic compounds, *Atmos. Chem. Phys.*, 8, 2773–2796, <https://doi.org/10.5194/acp-8-2773-2008>, 2008.
- Park, R. S., Lee, S., Shin, S.-K., and Song, C. H.: Contribution of ammonium nitrate to aerosol optical depth and direct radiative forcing by aerosols over East Asia, *Atmos. Chem. Phys.*, 14, 2185–2201, <https://doi.org/10.5194/acp-14-2185-2014>, 2014.
- Parker, D.: Reduction of odor and VOC emissions from a dairy lagoon, *Applied engineering in agriculture*, 24, 647-655, 2008.
- Parker, D. B., Gilley, J., Woodbury, B., Kim, K.-H., Galvin, G., Bartelt-Hunt, S. L., Li, X., and Snow, D. D.: Odorous VOC emission following land application of swine manure slurry, *Atmospheric Environment*, 66, 91-100, 2013.

- Patil, S.F. and Lonkar, S.T.: Determination of benzene, aniline and nitrobenzene in workplace air: a comparison of active and passive sampling. *Journal of Chromatography A*, 688, 189-199, 1994.
- Perraud, V., Bruns, E. A., Ezell, M. J., Johnson, S. N., Yu, Y., Alexander, M. L., Zelenyuk, A., Imre, D., Chang, W. L., Dabdub, D., Pankow, J. F., and Finlayson-Pitts, B. J.: Nonequilibrium atmospheric secondary organic aerosol formation and growth, *P. Natl. Acad. Sci. USA*, 109, 2836–2841, <https://doi.org/10.1073/pnas.1119909109>, 2012.
- Perraud, V., Horne, J.R., Martinez, A.S., Kalinowski, J., Meinardi, S., Dawson, M.L., Wingen, L.M., Dabdub, D., Blake, D.R., Gerber, R.B., and Finlayson-Pitts, B.J.: The future of airborne sulfur-containing particles in the absence of fossil fuel sulfur dioxide emissions. *Proc. Natl. Acad. Sci. Unit. States Am.* 112 (44), 13514–13519. <http://dx.doi.org/10.1073/pnas.1510743112>, 2015.
- Pierce, J. R., Engelhart, G. J., Hildebrandt, L., Weitkamp, E. A., Pathak, R. K., Donahue, N. M., Robinson, A. L., Adams, P. J., and Pandis, S. N.: Constraining particle evolution from wall losses, coagulation, and condensation-evaporation in smog-chamber experiments: optimal estimation based on size distribution measurements, *Aerosol Sci. Tech.*, 42, 1001–1015, <https://doi.org/10.1080/02786820802389251>, 2008.
- Pierce, T. E. and Waldruff, P. S.: PC-BEIS: a personal computer version of the biogenic emissions inventory system, *J. Air Waste Manage. Assoc.*, 41, 937–941, 1991.
- Pilinis, C. and Seinfeld, J.H.: Continued development of a general equilibrium model for inorganic multicomponent atmospheric aerosols, *Atmos. Environ.*, 21 (11), 2453-2466, [https://doi.org/10.1016/0004-6981\(87\)90380-5](https://doi.org/10.1016/0004-6981(87)90380-5), 1987.
- Pinder, R. W., Strader, R., Davidson, C. I., and Adams, P. J.: A temporally and spatially resolved ammonia emission inventory for dairy cows in the United States, *Atmos. Environ.*, 38, 3747–3756, 2004.
- Pinder, R. W., Adams, P. J., Pandis, S. N., and Gilliland, A. B.: Temporally resolved ammonia emission inventories: Current estimates, evaluation tools, and measurement needs, *J. Geophys. Res.-Atmos.*, 111, D16310, <https://doi.org/10.1029/2005JD006603>, 2006.
- Pope III, C. A., Burnett, R. T., Thun, M. J., Calle, E. E., Krewski, D., Ito, K., and Thurston, G. D.: Lung cancer, cardiopulmonary mortality, and long-term exposure to fine particulate air pollution, *J. Am. Med. Assoc.*, 287, 1132–1141, 2002.
- Pöschl, U. and Shiraiwa, M.: Multiphase Chemistry at the Atmosphere–Biosphere Interface Influencing Climate and Public Health in the Anthropocene, *Chemical Reviews*, 115 (10), 4440-4475, <https://doi.org/10.1021/cr500487s>, 2015.
- Price, D. J., Clark, C. H., Tang, X. C., Cocker, D. R., Purvis-Roberts, K. L., and Silva, P. J.: Proposed chemical mechanisms leading to secondary organic aerosol in the reactions of aliphatic amines with hydroxyl and nitrate radicals, *Atmos. Environ.*, 96, 135–144, <https://doi.org/10.1016/j.atmosenv.2014.07.035>, 2014.
- Pye, H. O., Pinder, R. W., Piletic, I. R., Xie, Y., Capps, S. L., Lin, Y. H., Surratt, J. D., Zhang, Z., Gold, A., Luecken, D. J., and Hutzell, W. T. : Epoxide pathways improve model predictions of isoprene markers and reveal key role of acidity in aerosol formation, *Environ. Sci. Technol.*, 47, 11056–11064, 2013.
- Pye, H. O.: CMAQv5.1 SOA Update, https://www.airqualitymodeling.org/index.php/CMAQv5.1_SOA_Update (last access: 25 September 2017), 2016.

- Rampfl, M., Mair, S., Mayer, F., Sedlbauer, K., Breuer, K., and Niessner, R.: Determination of primary, secondary, and tertiary amines in air by direct or diffusion sampling followed by determination with liquid chromatography and tandem mass spectrometry. *Environ. Sci. Technol.*, 42, 5217-5222, 2008.
- Ravishankara, A.R., Rudich, Y., and Wuebbles, D.J.: Physical Chemistry of Climate Metrics, *Chemical Reviews*, 115 (10), 3682-3703, <https://doi.org/10.1021/acs.chemrev.5b00010>, 2015.
- Renbaum-Wolff, L., Grayson, J. W., Bateman, A. P., Kuwata, M., Sellier, M., Murray, B. J., Shilling, J. E., Martin, S. T., and Bertram, A. K.: Viscosity of α -pinene secondary organic material and implications for particle growth and reactivity, *P. Natl. Acad. Sci. USA*, 110, 8014–8019, <https://doi.org/10.1073/pnas.1219548110>, 2013.
- Riva, M., Budisulistiorini, S. H., Chen, Y., Zhang, Z., D'Ambro, E. L., Zhang, X., Gold, A., Turpin, B. J., Thornton, J. A., Canagaratna, M. R., and Surratt, J. D.: Chemical characterization of secondary organic aerosol from oxidation of isoprene hydroxyhydroperoxides, *Environ. Sci. Technol.*, 50, 9889–9899, <https://doi.org/10.1021/acs.est.6b02511>, 2016.
- Riziq, A. A., Erlick, C., Dinar, E., and Rudich, Y.: Optical properties of absorbing and non-absorbing aerosols retrieved by cavity ring down (CRD) spectroscopy, *Atmos. Chem. Phys.*, 7, 1523-1536, 2007.
- Roach, P. J., Laskin, J., and Laskin, A.: Molecular characterization of organic aerosols using nanospray-desorption/electrospray ionization-mass spectrometry, *Anal. Chem.*, 82, 7979–7986, <https://doi.org/10.1021/ac101449p>, 2010a.
- Roach, P. J., Laskin, J., and Laskin, A.: Nanospray desorption electrospray ionization: an ambient method for liquid-extraction surface sampling in mass spectrometry, *Analyst*, 135, 2233–2236, <https://doi.org/10.1039/C0AN00312C>, 2010b.
- Romonosky, D. E., Ali, N. N., Saiduddin, M. N., Wu, M., Lee, H. J., Aiona, P. K., and Nizkorodov, S. A.: Effective absorption cross sections and photolysis rates of anthropogenic and biogenic secondary organic aerosols, *Atmos. Environ.*, 130, 172–179, <https://doi.org/10.1016/j.atmosenv.2015.10.019>, 2015a.
- Romonosky, D. E.; Laskin, A.; Laskin, J.; and Nizkorodov, S. A.: High-resolution mass spectrometry and molecular characterization of aqueous photochemistry products of common types of secondary organic aerosols, *J. Phys. Chem. A*, 119, 2594–2606, <https://doi.org/10.1021/jp509476r>, 2015b.
- Romonosky, D. E., Li, Y., Shiraiwa, M., Laskin, A., Laskin, J., and Nizkorodov, S. A.: Aqueous photochemistry of secondary organic aerosol of α -pinene and α -humulene oxidized with ozone, hydroxyl radical, and nitrate radical, *J. Phys. Chem. A*, 121, 1298–1309, <https://doi.org/10.1021/acs.jpca.6b10900>, 2017.
- Russell, A. and Dennis, R.: NARSTO critical review of photochemical models and modeling, *Atmos. Environ.*, 34, 2283–2324, 2000.
- Sato, K., Hatakeyama, S., and Imamura, T.: Secondary organic aerosol formation during the photooxidation of toluene: NO_x dependence of chemical composition, *J. Phys. Chem. A*, 111, 9796–9808, <https://doi.org/10.1021/jp071419f>, 2007.
- SCAQMD: Final 2012 Air Quality Management Plan, Tech. rep., South Coast Air Quality Management District, Diamond Bar, California, available at: <http://www.aqmd.gov/home/library/clean-air-plans/air-quality-mgt-plan/final-2012-air-quality-management-plan>, last access: 15 January 2015.

- Schade, G.W. and Crutzen, P.J.: Emission of aliphatic amines from animal husbandry and their reactions: potential source of N₂O and HCN, *J. Atmos. Chem.*, 22, 319-346, 1995.
- Schneidmesser, E., Monks, P.S., Allan, J.D., Bruhwiler, L., Forster, P., Fowler, D., Lauer, A., Morgan, W.T., Paasonen, P., Righi, M., Sindelarova, K., and Sutton, M.A.: Chemistry and the Linkages between Air Quality and Climate Change, *Chemical Reviews*, 115 (10), 3856-3897, <https://doi.org/10.1021/acs.chemrev.5b00089>, 2015.
- Schiferl, L.D., Heald, C.L., Nowak, J.B., Holloway, J.S., Neuman, J.A., Bahreini, R., Pollack, I.B., Ryerson, T.B., Wiedinmyer, C., Murphy, J.G.: An investigation of ammonia and inorganic particulate matter in California during the CalNex campaign. *J. Geophys. Res.: Atmos.* 119 (4), 1883-1902, <http://dx.doi.org/10.1002/2013JD020765>, 2014.
- Schmelz, E. A., Alborn, H. T., Banchio, E., and Tumlinson, J. H.: Quantitative relationships between induced jasmonic acid levels and volatile emission in *Zea mays* during *Spodoptera exigua* herbivory, *Planta*, 216, 665-673, 2003.
- Seinfeld, J. H. and Pandis, S. N.: *Atmospheric chemistry and physics: from air pollution to climate change*, John Wiley & Sons, New York, 2016.
- Sheppard, L. J., Leith, I. D., Mizunuma, T., Neil Cape, J., Crossley, A., Leeson, S., Sutton, M. A., Dijk, N., and Fowler, D.: Dry deposition of ammonia gas drives species change faster than wet deposition of ammonium ions: evidence from a long-term field manipulation, *Global Change Biol.*, 17, 3589-3607, 2011.
- Shiraiwa, M. and Seinfeld, J. H.: Equilibration timescale of atmospheric secondary organic aerosol partitioning, *Geophys. Res. Lett.*, L24801, 39, <https://doi.org/10.1029/2012GL054008>, 2012.
- Shiraiwa, M., Berkemeier, T., Schilling-Fahnestock, K. A., Seinfeld, J. H., and Pöschl, U.: Molecular corridors and kinetic regimes in the multiphase chemical evolution of secondary organic aerosol, *Atmos. Chem. Phys.*, 14, 8323-8341, <https://doi.org/10.5194/acp-14-8323-2014>, 2014.
- Silva, P. J., Erupe, M. E., Price, D., Elias, J., Malloy, Q. G. J., Li, Q., Warren, B., and Cocker, D. R. III: Trimethylamine as precursor to secondary organic aerosol formation via nitrate radical reaction in the atmosphere, *Environ. Sci. Technol.*, 42, 4689-4696, <https://doi.org/10.1021/es703016v>, 2008.
- Skamarock, W., Klemp, J., Dudhia, J., Gill, D., Barker, D., Duda, M., Huang, X., Wang, W., and Powers, J.: A description of the Advanced Research WRF Version 3, NCAR technical note, Mesoscale and Microscale Meteorology Division, National Center for Atmospheric Research, Boulder, Colorado, USA, 2008.
- Sorooshian, A., Murphy, S.M., Hersey, S., Gates, H., Padro, L.T., Nenes, A., Brechtel, F.J., Jonsson, H., Flagan, R.C., and Seinfeld, J.H.: Comprehensive airborne characterization of aerosol from a major bovine source. *Atmos. Chem. Phys.*, 8, 5489-5520, 2008.
- Stelson, A.W., Friedlander, S.K., and Seinfeld, J.H.: A note on the equilibrium relationship between ammonia and nitric acid and particulate ammonium nitrate, *Atmospheric Environment*, 13(3), 369-371, 1979.
- Stelson, A.W. and Seinfeld, J.H.: Relative humidity and temperature dependence of the ammonium nitrate dissociation constant, *Atmospheric Environment* (1967), 16(5), 983-992, 1982.
- Sun, H., Biedermann, L., and Bond, T. C.: Color of brown carbon: a model for ultraviolet and visible light absorption by organic carbon aerosol, *Geophys. Res. Lett.*, 34, L17813, <https://doi.org/10.1029/2007GL029797>, 2007.

- Sutton, M., Pitcairn, C. E., and Fowler, D.: The exchange of ammonia between the atmosphere and plant communities, *Adv. Ecol. Res.*, 24, 301–393, 1993.
- Suzuki, T., Ohtaguchi, K., and Koide, K.: Application of principal components analysis to calculate Henry's constant from molecular structure, *Comput. Chem.*, 16, 41–52, [https://doi.org/10.1016/0097-8485\(92\)85007-L](https://doi.org/10.1016/0097-8485(92)85007-L), 1992.
- Tang, X., Price, D., Praske, E., Lee, S. A., Shattuck, M. A., Purvis-Roberts, K., Silva, P.J., Asa-Awuku, A., and Cocker III, D. R.: NO₃ radical, OH radical and O₃-initiated secondary aerosol formation from aliphatic amines. *Atmospheric Environment*, 72, 105-112, 2013.
- Tang, Y., Carmichael, G.R., Seinfeld, J.H., Dabdub, D., Weber, R.J., Huebert, B., Clarke, A.D., Guazzotti, S.A., Sodeman, D.A., Prather, K.A., Itsushi Uno, I., Woo, J.-H., Yienger, J.J., Streets, D.G., Quinn, P.K., Johnson, J.E., Song, C.-H., Grassian, V.H., Sandu, A., Talbot, R.W., and Dibb, J.E.: Three-dimensional simulations of inorganic aerosol distributions in east Asia during spring 2001, *J. Geophys. Res.*, 109, D19S23, <https://doi.org/10.1029/2003JD004201>, 2004
- Thompson, J. E., Hayes, P. L., Jimenez, J. L., Adachi, K., Zhang, X., Liu, J., Weber, R. J., and Buseck, P. R.: Aerosol optical properties at Pasadena, CA during CalNex 2010, *Atmos. Environ.*, 55, 190–200, <https://doi.org/10.1016/j.atmosenv.2012.03.011>, 2012.
- Tsai, C.J., Chen, M.L., Ye, A.D., Chou, M.S., Shen, S.H., and Mao, I.F.: The relationship of odor concentration and the critical components emitted from food waste composting plants. *Atmos. Environ.*, 42, 8246-8251, 2008.
- Tuazon, E.C., Carter, W.P., Atkinson, R., Winer, A.M. and Pitts, J.N.: Atmospheric reactions of N-nitrosodimethylamine and dimethylnitramine, *Environmental science & technology*, 18(1), 49-54, 1984.
- Tuazon, E.C., Atkinson, R., Aschmann, S.M. and Arey, J.: Kinetics and products of the gas-phase reactions of O₃ with amines and related compounds, *Research on chemical intermediates*, 20(3-5), 303-320, 1994.
- Tully, F.P., Ravishankara, A.R., Thompson, R.L., Nicovich, J.M., Shah, R.C., Kreutter, N.M. and Wine, P.H.: Kinetics of the reactions of hydroxyl radical with benzene and toluene, *The Journal of Physical Chemistry*, 85(15), 2262-2269, 1981.
- Turlings, T. C., Tumlinson, J. H., and Lewis, W. J.: Exploitation of herbivore-induced plant odors by host-seeking parasitic wasps, *Science*, 250, 1251–1253, 1990.
- Turlings, T. C. and Wäckers, F.: Recruitment of predators and parasitoids by herbivore-injured plants, in: *Advances in Insect Chemical Ecology*, Cambridge University Press, Cambridge, 21–75, 2004.
- Updyke, K. M., Nguyen, T. B., and Nizkorodov, S. A.: Formation of brown carbon via reactions of ammonia with secondary organic aerosols from biogenic and anthropogenic precursors, *Atmos. Environ.*, 63, 22–31, 2012.
- US Environmental Protection Agency (EPA): User's Guide to MOBILE6.1 and MOBILE6.2, Environmental Protection Agency, Ann Arbor, USA, 2003.
- US EPA: Guidance on the use of models and other analyses for demonstrating attainment of air quality goals for ozone, PM_{2.5}, and regional haze, US Environmental Protection Agency, Office of Air Quality Planning and Standards, Research Triangle Park, North Carolina, 2007.
- US EPA: Integrated Science Assessment for Particulate Matter (Final Report). Rep. EPA/600/R-08/139F. D. C, Washington, 2009.

- US EPA: 2014 National Emissions Inventory (NEI) Technical Support Document (TSD), https://www.epa.gov/sites/production/files/2016-12/documents/nei2014v1_tsd.pdf (last access: 12 July 2017), 2017a.
- US EPA: SMOKE v4.5 User's Manual, https://www.cmascenter.org/smoke/documentation/4.5/manual_smokev45.pdf (last access: 12 July 2017), 2017b.
- Varutbangkul, V., Brechtel, F. J., Bahreini, R., Ng, N. L., Keywood, M. D., Kroll, J. H., Flagan, R. C., Seinfeld, J. H., Lee, A., and Goldstein, A. H.: Hygroscopicity of secondary organic aerosols formed by oxidation of cycloalkenes, monoterpenes, sesquiterpenes, and related compounds, *Atmos. Chem. Phys.*, 6, 2367–2388, <https://doi.org/10.5194/acp-6-2367-2006>, 2006.
- Vayenas, D. V., Takahama, S., Davidson, C. I., and Pandis, S. N.: Simulation of the thermodynamics and removal processes in the sulfate-ammonia-nitric acid system during winter: Implications for PM_{2.5} control strategies, *J. Geophys. Res.-Atmos.*, 110, D07S14, <https://doi.org/10.1029/2004JD005038>, 2005.
- Volkamer, R., Jimenez, J. L., San Martini, F., Dzepina, K., Zhang, Q., Salcedo, D., Molina, L. T., Worsnop, D. R., and Molina, M. J.: Secondary organic aerosol formation from anthropogenic air pollution: rapid and higher than expected, *Geophys. Res. Lett.*, 33, L17811, <https://doi.org/10.1029/2006GL026899>, 2006.
- Vutukuru, S., Griffin, R. J., and Dabdub, D.: Simulation and analysis of secondary organic aerosol dynamics in the South Coast Air Basin of California, *J. Geophys. Res.*, 111, D10S12, <https://doi.org/10.1029/2005JD006139>, 2006.
- Walser, M. L., Desyaterik, Y., Laskin, J., Laskin, A., and Nizkorodov, S. A.: High-resolution mass spectrometric analysis of secondary organic aerosol produced by ozonation of limonene, *Phys. Chem. Chem. Phys.*, 10, 1009–1022, <https://doi.org/10.1039/B712620D>, 2008.
- Wang, X., Gao, S., Yang, X., Chen, H., Chen, J., Zhuang, G., Surratt, J.D., Chan, M.N., and Seinfeld, J.H.: Evidence for high molecular weight nitrogen-containing organic salts in urban aerosols. *Environ. Sci. Technol.* 44 (12), 4441–4446, 2010.
- Wang, Y., Zhang, Q. Q., He, K., Zhang, Q., and Chai, L.: Sulfate-nitrate-ammonium aerosols over China: response to 2000–2015 emission changes of sulfur dioxide, nitrogen oxides, and ammonia, *Atmos. Chem. Phys.*, 13, 2635–2652, <https://doi.org/10.5194/acp-13-2635-2013>, 2013.
- Warner, J., Dickerson, R., Wei, Z., Strow, L., Wang, Y., and Liang, Q.: Increased atmospheric ammonia over the world's major agricultural areas detected from space, *Geophys. Res. Lett.*, 44, 2875–2884, 2017.
- Washenfelder, R. A., Flores, J. M., Brock, C. A., Brown, S. S., and Rudich, Y.: Broadband measurements of aerosol extinction in the ultraviolet spectral region, *Atmos. Meas. Tech.*, 6, 861–877, 2013.
- Weber, R. J., Guo, H., Russell, A. G., and Nenes, A.: High aerosol acidity despite declining atmospheric sulfate concentrations over the past 15 years, *Nat. Geosci.*, 9, 282–285, 2016.
- Wei, G., Bhushan, B., and Torgerson, P.M.: Nanomechanical characterization of human hair using nanoindentation and SEM, *Ultramicroscopy*, 105, 248–266, <https://doi.org/10.1016/j.ultramicro.2005.06.033>, 2005.

- West, J. J., Ansari, A. S., and Pandis, S. N.: Marginal PM₂₅: nonlinear aerosol mass response to sulfate reductions in the Eastern United States, *J. Air Waste Manage. Assoc.*, 49, 1415–1424, 1999.
- White, S. J., Jamie, I. M., and Angove, D. E.: Chemical characterisation of semi-volatile and aerosol compounds from the photooxidation of toluene and NO_x, *Atmos. Environ.*, 83, 237–244, <https://doi.org/10.1016/j.atmosenv.2013.11.023>, 2014.
- Wolfram, L.J.: Human hair: A unique physicochemical composite, *Journal of the American Academy of Dermatology*, 48 (6), S106-S114, <https://doi.org/10.1067/mjd.2003.276>, 2003.
- Woodbury, B. L., Gilley, J. E., Parker, D. B., Marx, D. B., and Eigenberg, R. A.: VOC emissions from beef feedlot pen surfaces as affected by within-pen location, moisture and temperature, *Biosystems Engineering*, 134, 31-41, 2015.
- Wright, D. W., Eaton, D. K., Nielsen, L. T., Kuhrt, F. W., Koziel, J. A., Spinhirne, J. P., and Parker, D. B.: Multidimensional gas chromatography – olfactometry for the identification and prioritization of malodors from confined animal feeding operations, *J. Agr. Food Chem.*, 53, 8663–8672, <https://doi.org/10.1021/jf050763b>, 2005.
- Xu, L. and Penner, J. E.: Global simulations of nitrate and ammonium aerosols and their radiative effects, *Atmos. Chem. Phys.*, 12, 9479–9504, <https://doi.org/10.5194/acp-12-9479-2012>, 2012.
- Yao, L., Garmash, O., Bianchi, F., Zheng, J., Yan, C., Kontkanen, J., Junninen, H., Mazon, S. B., Ehn, M., Paasonen, P., Sipila, M., Wang, M., Wang, X., Xiao, S., Chen, H., Lu, Y., Zhang, B., Wang, D., Fu, Q., Geng, F., Li, L., Wang, H., Qiao, L., Yang, X., Chen, J., Kerminen, V.-M., Petaja, T., Worsnop, D.R., Kulmala, M., and Wang, L.: Atmospheric new particle formation from sulfuric acid and amines in a Chinese megacity, *Science*, 361, 278–281, 2018.
- Yarwood, G., Jung, J., Whitten, G. Z., Heo, G., Mellberg, J., and Estes, M.: Updates to the Carbon Bond mechanism for version 6 (CB6), in: 2010 CMAS Conference, October 2010, Chapel Hill, NC, http://www.cmascenter.org/conference/2010/abstracts/emery_updates_carbon_2_010.pdf (last access: 18 August 2017), 2010.
- Ye, X., Ma, Z., Zhang, J., Du, H., Chen, J., Chen, H., Yang, X., Gao, W., and Geng, F.: Important role of ammonia on haze formation in Shanghai, *Environ. Res. Lett.*, 6, 024019, <https://doi.org/10.1088/1748-9326/6/2/024019>, 2011.
- Yeh, H.-S., Cuddihy, R.G., Phalen, R.F., and Chang, I.-Y.: Comparisons of calculated respiratory tract deposition of particles based on the proposed NCRP model and the new ICRP66 model, *Aerosol Sci. Technol.*, 25, 134-140, <https://doi.org/10.1080/02786829608965386>, 1996.
- Yu F. and Luo, G.: Modeling of gaseous methylamines in the global atmosphere: impacts of oxidation and aerosol uptake, *Atmos. Chem. Phys.*, 14, 12455–12464, <https://doi.org/10.5194/acp-14-12455-2014>, 2014.
- Yu, J., Jeffries, H. E., and Sexton, K. G.: Atmospheric photooxidation of alkylbenzenes – I. Carbonyl product analyses, *Atmos. Environ.*, 31, 2261–2280, [https://doi.org/10.1016/S1352-2310\(97\)00011-3](https://doi.org/10.1016/S1352-2310(97)00011-3), 1997.
- Yuan, B., Coggon, M. M., Koss, A. R., Warneke, C., Eilerman, S., Peischl, J., Aikin, K. C., Ryerson, T. B., and de Gouw, J. A.: Emissions of volatile organic compounds (VOCs) from concentrated animal feeding operations (CAFOs): chemical compositions and

- separation of sources, *Atmos. Chem. Phys.*, 17, 4945–4956, <https://doi.org/10.5194/acp-17-4945-2017>, 2017.
- Yuan, J. S., Himanen, S. J., Holopainen, J. K., Chen, F., and Stewart, C. N.: Smelling global climate change: mitigation of function for plant volatile organic compounds, *Trends Ecol. Evol.*, 24, 323–331, <https://doi.org/10.1016/j.tree.2009.01.012>, 2009.
- Zahn, J. A., DiSpirito, A., Do, Y., Brooks, B., Cooper, E., and Hatfield, J.: Correlation of human olfactory responses to airborne concentrations of malodorous volatile organic compounds emitted from swine effluent, *Journal of Environmental Quality*, 30, 624–634, 2001.
- Zhang, H., Surratt, J. D., Lin, Y. H., Bapat, J., and Kamens, R. M.: Effect of relative humidity on SOA formation from isoprene/NO photooxidation: enhancement of 2-methylglyceric acid and its corresponding oligoesters under dry conditions, *Atmos. Chem. Phys.*, 11, 6411–6424, <https://doi.org/10.5194/acp-11-6411-2011>, 2011.
- Zhang, X., Cappa, C. D., Jathar, S. H., McVay, R. C., Ensberg, J. J., Kleeman, M. J., and Seinfeld, J. H.: Influence of vapor wall loss in laboratory chambers on yields of secondary organic aerosol, *P. Natl. Acad. Sci. USA*, 111, 5802–5807, <https://doi.org/10.1073/pnas.1404727111>, 2014.
- Zhang, Y., Seigneur, C., Seinfeld, J.H., Jacobson, M., Clegg, S.L., and Binkowski, F.S.: A comparative review of inorganic aerosol thermodynamic equilibrium modules: similarities, differences, and their likely causes. *Atmos. Environ.* 34 (1), 117–137, 2000.
- Zhao, R., Aljawhary, D., Lee, A. K. Y., and Abbatt, J. P. D.: Rapid aqueous-phase photooxidation of dimers in the α -pinene secondary organic aerosol, *Environ. Sci. Technol. Lett.*, 4, 205–210, <https://doi.org/10.1021/acs.estlett.7b00148>, 2017.
- Zheng, J., Ma, Y., Chen, M., Zhang, Q., Wang, L., Khalizov, A.F., Yao, L., Wang, Z., Wang, X., and Chen, L.: Measurement of atmospheric amines and ammonia using the high resolution time-of-flight chemical ionization mass spectrometry, *Atmos. Environ.*, 102, 249–259, <https://doi.org/10.1016/j.atmosenv.2014.12.002>, 2015.
- Zhou, Y., Zhang, H., Parikh, H. M., Chen, E. H., Rattanavaraha, W., Rosen, E. P., Wang, W., and Kamens, R. M.: Secondary organic aerosol formation from xylenes and mixtures of toluene and xylenes in an atmospheric urban hydrocarbon mixture: water and particle seed effects (II), *Atmos. Environ.*, 45, 3882–3890, <https://doi.org/10.1016/j.atmosenv.2010.12.048>, 2011.
- Zhuang, X., Fiesselmann, A., Zhao, N., Chen, H., Frey, M., and Chen, F.: Biosynthesis and emission of insect herbivory-induced volatile indole in rice, *Phytochemistry*, 73, 15–22, <https://doi.org/10.1016/j.phytochem.2011.08.029>, 2012.
- Zito, P., Doetterl, S. Sajeva, M.: Floral volatiles in a sapromyiophilous plant and their importance in attracting house fly pollinators, *J. Chem. Ecol.*, 41, 340–349, <https://doi.org/10.1007/s10886-015-0568-8>, 2015.